Author:
Paris, Eleonora

Title:
Structural studies of minerals and glasses by X-ray absorption spectroscopy.

STRUCTURAL STUDIES OF MINERALS AND GLASSES BY X-RAY ABSORPTION SPECTROSCOPY

by

Eleonora Paris

A thesis submitted to the University of Bristol in accordance with the requirements of the degree of Doctor of Philosophy in the Faculty of Science, Department of Geology.

January 1996

ABSTRACT

This thesis comprises a series of studies conducted using synchrotron radiation to probe the structure of crystalline and glassy materials of geological interest, and theoretical studies aimed at modelling the experimental results and thereby obtaining an improved understanding of the origins of specific features observed in the experimental spectra. All of the work is in the general field of X-ray absorption spectroscopy (XAS), which can provide unique information concerning the local structure around specific atoms. In the first chapter I provide a brief background concerning general features of synchrotron radiation, the experimental apparatus used, and some theoretical background concerning both XAS in general, and modelling of X-ray Absorption Near-Edge Structure (XANES). Chapter 2 contains the results of a study of densified silica glass by XANES, utilizing absorption spectra for both oxygen and silicon. A decrease of the mean Si-O-Si angle in vitreous silica upon densification from 2.20 to 2.36 gcm^{-3} is supported by multiple scattering calculations using clusters of two shells around the oxygen and silicon atoms; the calculated spectra are in good agreement with experimental spectra and confirm mean Si-O-Si between 130 and 144° for these samples, and a decrease of the mean angle with densification. Chapter 3 provides a comprehensive examination of the titanium XANES for richteritic amphiboles and for a variety of glasses; the unusual occurrence of tetrahedral Ti in amphibole is shown, and mixed coordination (4 to 6 fold) of Ti in glasses, with systematic coordination changes with glass composition and pressure are illustrated. Modelling of Ti K-XANES spectra illustrates and clarifies the effects of coordination and polyhedral distortion on the spectral features. Chapter 4 concentrates on Fe site geometry in orthopyroxene, and shows the importance of considering contributions from both the M1 and M2 sites in understanding the experimental spectra and the possibility of quantify the site occupancy from XANES spectra. The calcium environment in clinopyroxenes is the subject of Chapter 5, again involving both measurements and theoretical models of the factors affecting Ca XANES spectra. The sites of Fe and Mg in the olivine structure are the subject of Chapter 6, with theoretical results showing how differences in site distortion and the effects of pressure and temperature lead to changes in XANES spectra. Chapter 7 focuses on Ni distribution in synthetic potassium richterites, showing how XANES data and theory may be combined to understand Ni distribution in the different crystallographic sites in amphiboles which are too fine-grained to be studied by conventional single-crystal x-ray diffraction studies. The final Chapter (8) documents the development of a new furnace which allows in-situ XAS measurements at high temperatures; the application of this development is illustrated with brief studies of unquenchable phase transitions in Co-melilite, and measurements of Ti XANES spectra in high T silicate melts.

ACKNOWLEDGEMENTS

Due to the nature of the work, studies using synchrotron radiation can not be accomplished without the assistance of others (i.e., it is difficult to have a synchrotron in your laboratory). For experimental assistance, discussions and suggestions, help in sample preparation or providing of samples, and company during long overnight shifts involved in collecting spectra, I thank I. Davoli, G.Della Ventura, D. Dingwell, M.Fanfoni, G. Giuli, A. Marcelli, A. Mottana, J-L. Robert, C.Romano, and F. Seifert. I have also benefited from collaboration with numerous physicist colleagues, both at Frascati and Camerino, who have helped to open my eyes to the intricacies, and the utility, of multiple scattering calculations. These include, but are not limited to, M.Benfatto, M.Berrettoni, A.Bianconi, A.Di Cicco, A. Gargano, C.R.Natoli, S.Stizza, T.A.Tyson, and Wu Ziyu.

The Laboratori Nazionali di Frascati (I), the Bayerisches Geoinstitut of University of Bayreuth (D), the Centro Grandi Apparecchiature of University of Camerino (I) are gratefully acknowledged for hospitality.

DECLARATION

The material presented in this thesis is the result of my own independent research carried out between October 1992 and July 1995 in the Department of Geology, University of Bristol, Dipartimento di Scienze della Terra, Universita' di Camerino, and Istituto Nazionale di Fisica Nucleare Laboratori Nazionali di Frascati, Italy. Any previously published or unpublished work used is given full acknowledgement.

The views expressed in this dissertation are those of the author and not of the University.

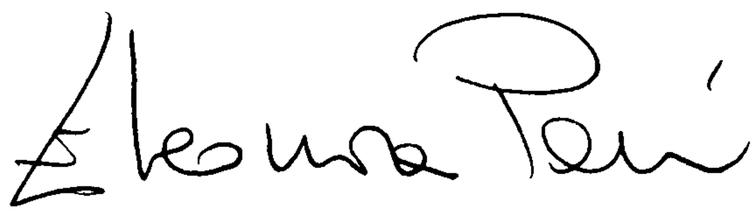

Eleonora Paris

December, 1995

A Mike,
compagno d'avventura

e a Nicholas,
la migliore delle
nostre avventure

TABLE OF CONTENTS

LIST OF FIGURES

LIST OF TABLES

CHAPTER 1. INTRODUCTION AND BACKGROUND

1.1 X-RAY ABSORPTION SPECTROSCOPY: THEORY, METHODS AND EXPERIMENTAL SET-UP

1.1.1 Abstract

This chapter provides a brief description of the characteristics and properties of synchrotron radiation and a description of the synchrotron radiation facility of Frascati (Italy), where the experiments reported here were conducted. The description includes details of the experimental set-up at the X-ray line of ADONE (closed in 1994), with technical details of the equipment as well as of the experimental methods used to investigate the coordination number and local geometrical environment for specific elements in complex systems. Following the experimental details, I provide a brief overview of absorption EXAFS and XANES spectra, their physical meaning, and their use as sources of structural information for crystalline and amorphous systems.

1.1.2 Characteristics of synchrotron light

A charged particle submitted to acceleration radiates and progressively loses its energy. This simple effect, well-known even to beginning students in electromagnetism, represents the theoretical basis for describing and understanding the properties of synchrotron radiation. Lamour, in 1897, showed that the power radiated (P) by a single charged particle submitted to acceleration is given by:

$$P = \left(\frac{2e^2}{3c^3}\right)\left(\frac{dV}{dt}\right)^2 \qquad [1.1]$$

In the case of a particle of mass *m*, forced to move in a circular orbit with velocity ß = V/c, energy *E* and radius of curvature *R*, the relativistic form of expression [1] is

$$P = (2e^2c/3R^2)ß^4(E/mc^2)^4 \qquad [1.2]$$

Because the irradiated power depends inversely on the fourth power of the mass, protons accelerated in a storage ring produce a negligible amount of synchrotron radiation. However, Eqn. [1.2] is not expressed in practical units, so the same expression may be reformulated as:

$$P\ (kW) = 88.47\ E^4\ I/R = 2.654\ B\ E^3\ I \qquad [1.3]$$

where P is the power irradiated by an accelerated electron beam. The current I is measured in amperes, the energy E in GeV, the magnetic field B of the bending magnets in Kgauss, and the curvature radius R of the magnets in meters. The process of successive simplifications may continue according to the purpose to be achieved. Thus,

if we want to know the radiative power emitted by electrons going through a magnetic field for a length L, we may use the formula:

$$P = 1.267 \cdot 10^{-2} E^2 B^2 I L \qquad [1.4]$$

This formula is particularly useful for calculation of the synchrotron radiation coming from insertion devices such as wigglers or undulators, which are used for obtaining higher energy measurements.

For considering the general characteristics of synchrotron light, Fig. 1.1.1 shows the radiation emission pattern for an electric charge submitted to centripetal acceleration. The two cases concern the different spatial distributions of radiation as a function of the velocity of the moving charges.

Case 1: electrons travelling at relatively slow speed have a pattern similar to a doughnut, the center of which coincides with the electron, and the highest symmetry axis with the acceleration direction.

Case 2: when electrons travel at a speed close to the speed of light, the spatial distribution of the emitted radiation is highly collimated in the direction tangent to the orbital plane, in the forward direction of the motion of the electrons.

This extreme collimation is both an advantage and disadvantage of synchrotron radiation. At energies above 1 GeV, the natural collimation of the beam is of the order of about 1 mrad, thus permitting a very high photon flux onto mm-sized samples, even at a distance of 20-30 m from the source. However, this highly favourable property goes hand in hand with extreme difficulty in the alignment: the angular deviation of the beam is of the order of some tens of mrad, which corresponds to a deviation of a few mm from the position of the sample and to the loss of most of the radiation.

The second useful characteristic of synchrotron radiation is its wide spectral range which generally goes from the visible to the X-rays. The parameter defining this property is the critical energy E_C, given by:

$$E_c = 3h'c\tau^3 / 2R \qquad [1.5]$$

where h' is Planck's constant divided by 2π, c is the velocity of light, R is the radius of the bending magnet and τ is a parameter defined by $\tau = E/mc^2$. The critical energy E_c is the value at which the radiated energy is half of the total energy. The critical energy value (in KeV) can be determined in practice from:

$$E_c = 2.218\ E^3 /R = 0.06651\ B\ E^2 \qquad [1.6]$$

In figure 1.1.2 are shown two spectral distributions: one refers to the radiation coming from a bending magnet having energy E = 1.5 GeV and a magnetic field B of 10 kgauss, and the second refers to the radiation coming from a wiggler magnet and shows a wider

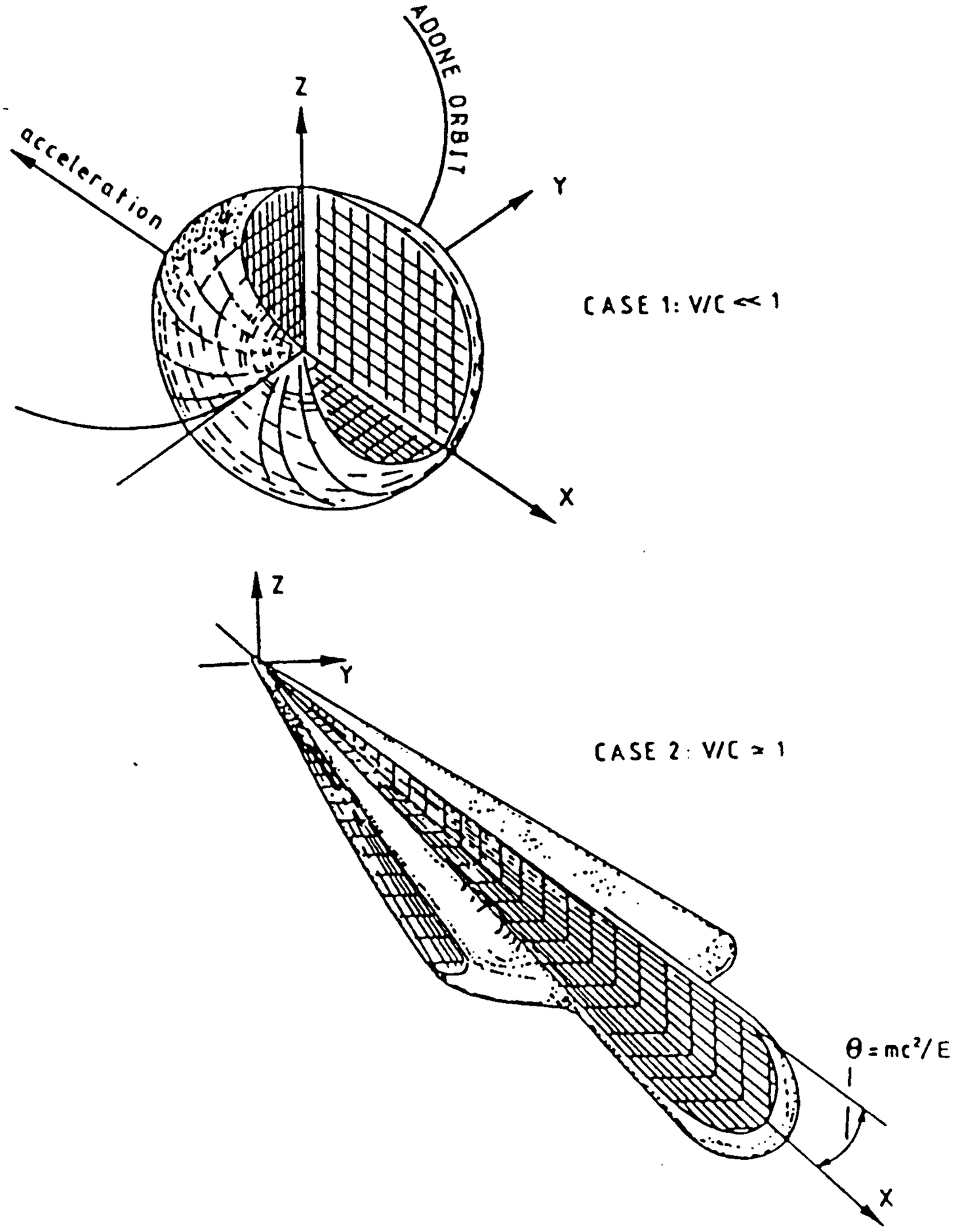

Fig. 1.1.1 Radiation emission pattern foe an electric charge submitted to centripetal acceleration. See the text for explanation of the case I and II (Davoli et al., 1988).

spectral range; the increase of the intensity is due to the fact that along the wiggler axis the magnetic field is higher than that of the bending magnet. Fig. 1.1.3 shows a set of distribution curves from SPEAR. By increasing the kinetic energy of the electrons, the spectral distribution range increases toward the region of hard X-rays, but the flux intensity at lower energies does not increase.

A third, fundamental characteristic of synchrotron radiation concerns its polarization. The emitted radiation is 100% polarized with the electric field lying in the orbital plane of the accelerated electrons. The polarization is only reduced by a slight angular spread in the vertical direction. When many electrons are present the incoherent vertical and radial betatron oscillations resonate in a range of angles for the electron beam at each point in the orbit: this angular divergence reduces the polarization. Fig. 1.1.4 shows the calculated intensity of the perpendicular and parallel polarization for a single electron versus the emission angle for different wavelengths (Winick,1980).

The last characteristic of synchrotron radiation worth mentioning is its pulsing structure. Electrons contained in a storage ring are grouped in bunches whose duration in time is determined by the radiofrequency. As a result, the radiation pulses with a rhythm which is of the order of 10% of the radiofrequency. In the case of ADONE, the radiofrequency power supply is 50 MHz and pulse length is 10 nsec, with a period of about 300 nsec. The pulsing nature of synchrotron light is being used for time-resolved spectral studies measuring the fluorescence times with a precision to the order of 5 picosec; this has found numerous applications in studies of biological materials but has not yet been used extensively for mineralogical applications.

1.1.3. The ADONE facility: experimental set-up

The Program for the Utilization of the Synchrotron Light (PULS) at Frascati made use of the ADONE storage ring (Table 1.1.1) during the period 1979–1994; the ADONE ring is now closed and the associated scientists are working on a new line at the ESRF in Grenoble. The ADONE facility comprised two laboratories: the first one collected its light from a bending magnet and split it into four channels (Fig. 1.1.5), the spectral ranges of which are shown in Fig. 1.1.3; the second laboratory collected its light from a wiggler and split it into three channels, two of which operated in the 3-30 KeV range, and the third one (Fig. 1.1.6), dedicated to lithography, used a white beam with spectral range 1.5-3.5 KeV.

The "X-ray line" collected the radiation emitted over a 1 mrad of the bending magnet sections of ADONE and consisted of a monochromator, two ionization chambers and a measurement chamber (Fig.1.1.7). The storage ring is isolated from the

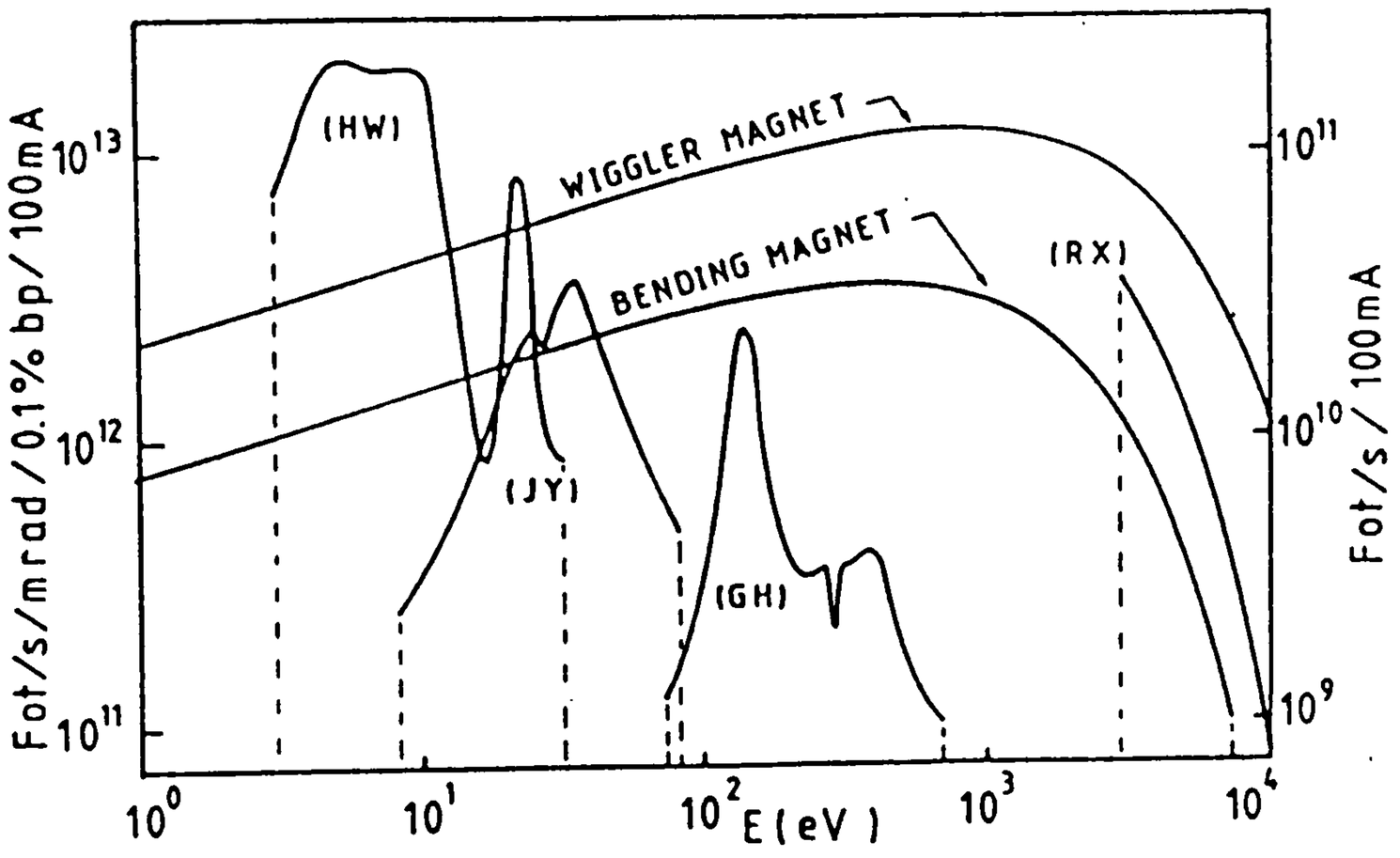

Fig. 1.1.2 Radiation coming from a bending magnet and from a wiggler magnet in ADONE. The transmission curves of the monochromators constituting the lines at Frascati Synchrotron Radiation Facility are also reported: HW= Hilger and Watts, JY= Jobin Yvon, GH= Grasshopper RX= X-rays (Davoli et al., 1988).

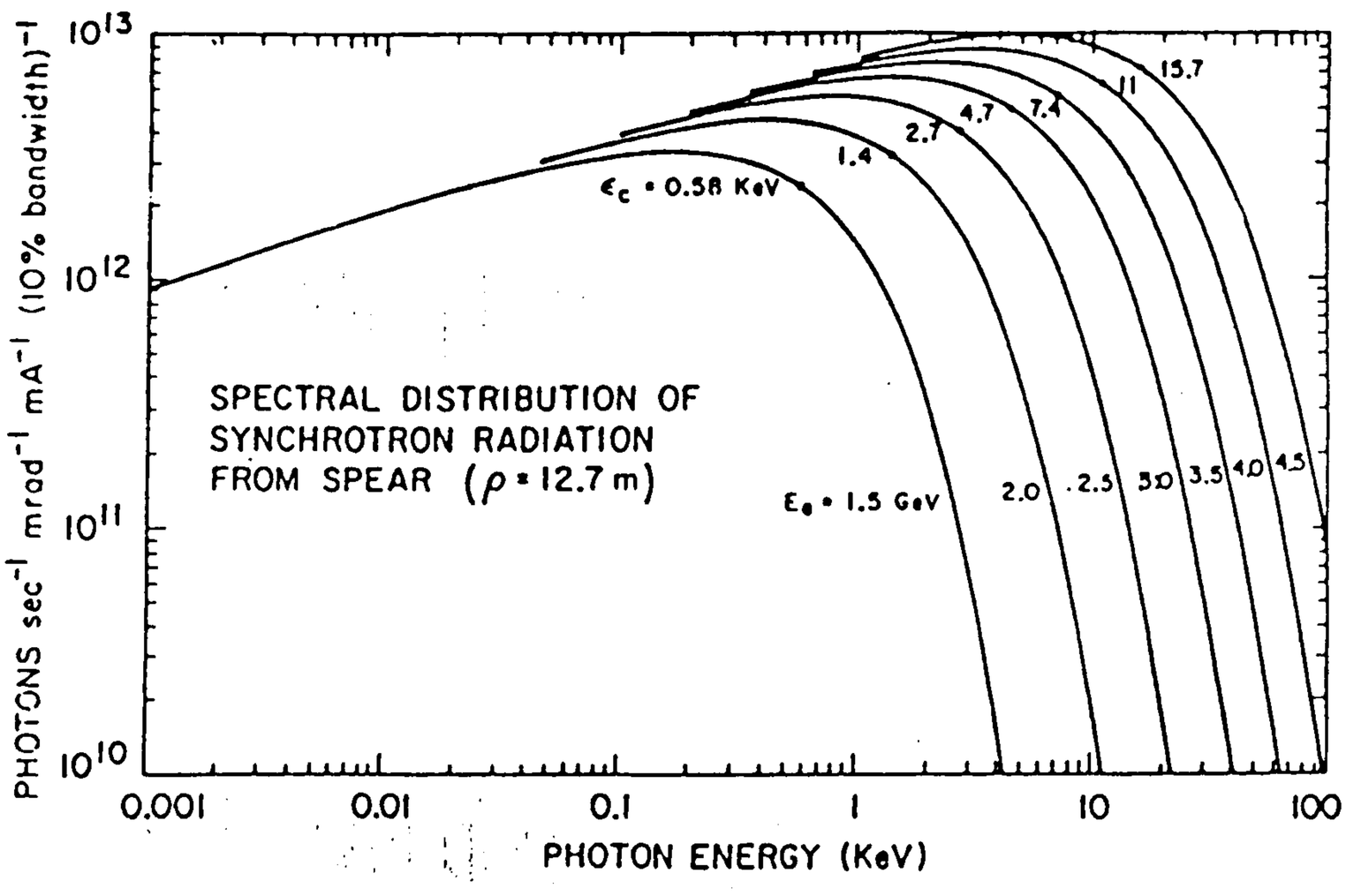

Fig. 1.1.3 Spectral disribution of synchrotron radiation from SPEAR. E_c is the SPEAR operating energy and ε_c is the critical energy (Davoli et al., 1988).

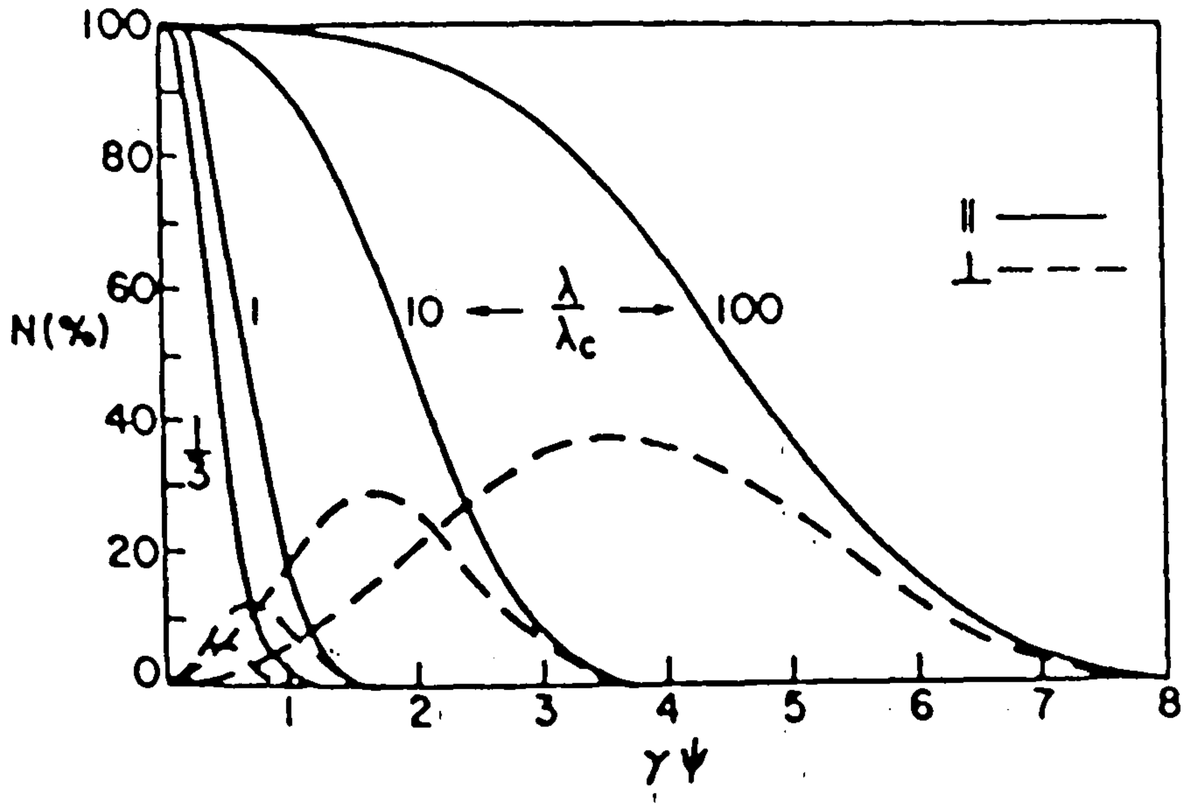

Fig. 1.1.4 Vertical angular distribution of parallel and orthogonal polarization components (Davoli et al., 1988).

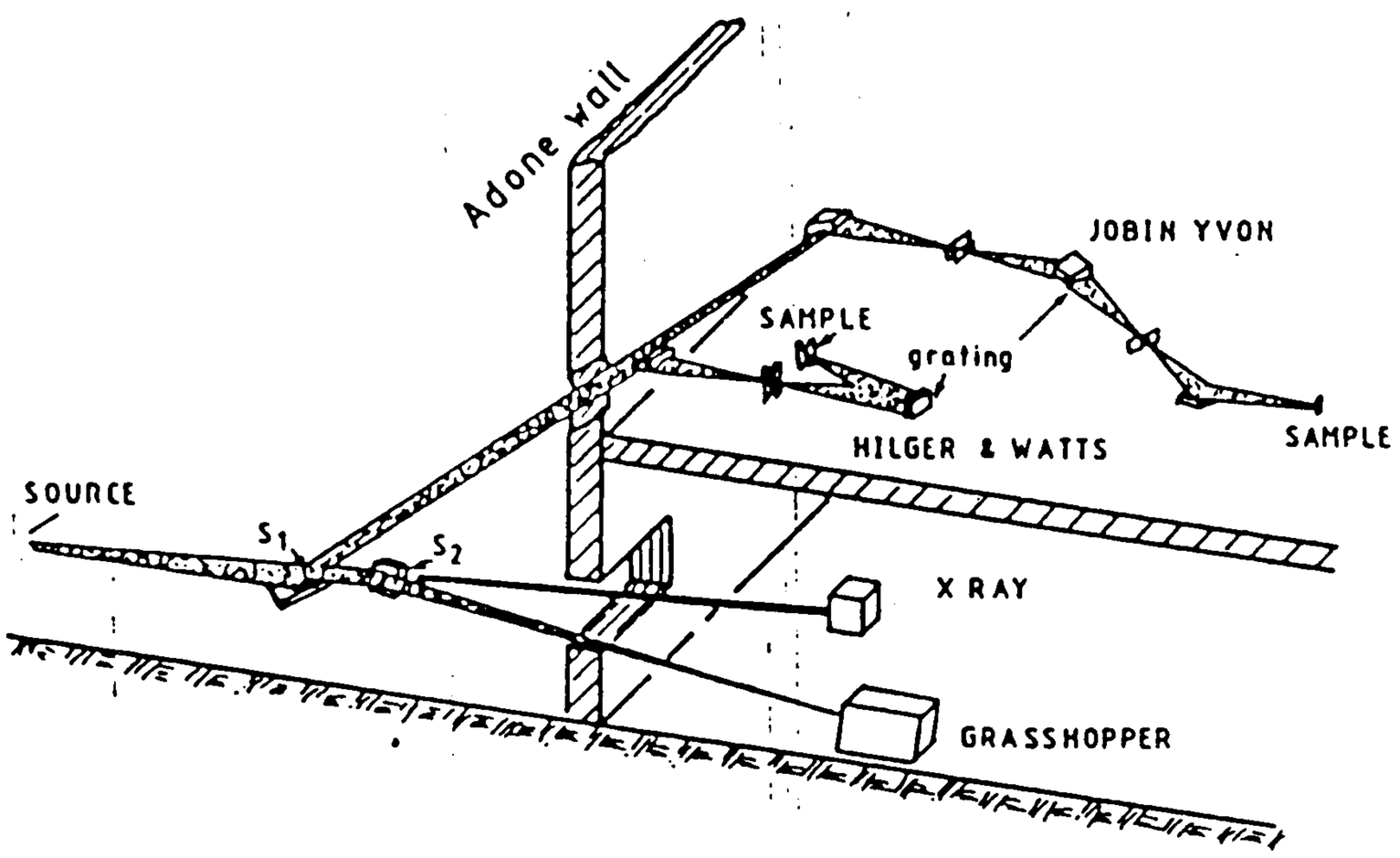

Fig. 1.1.5 Line sketch of PULSat Frascati Synchrotron Radiation Facility (Davoli et al., 1988).

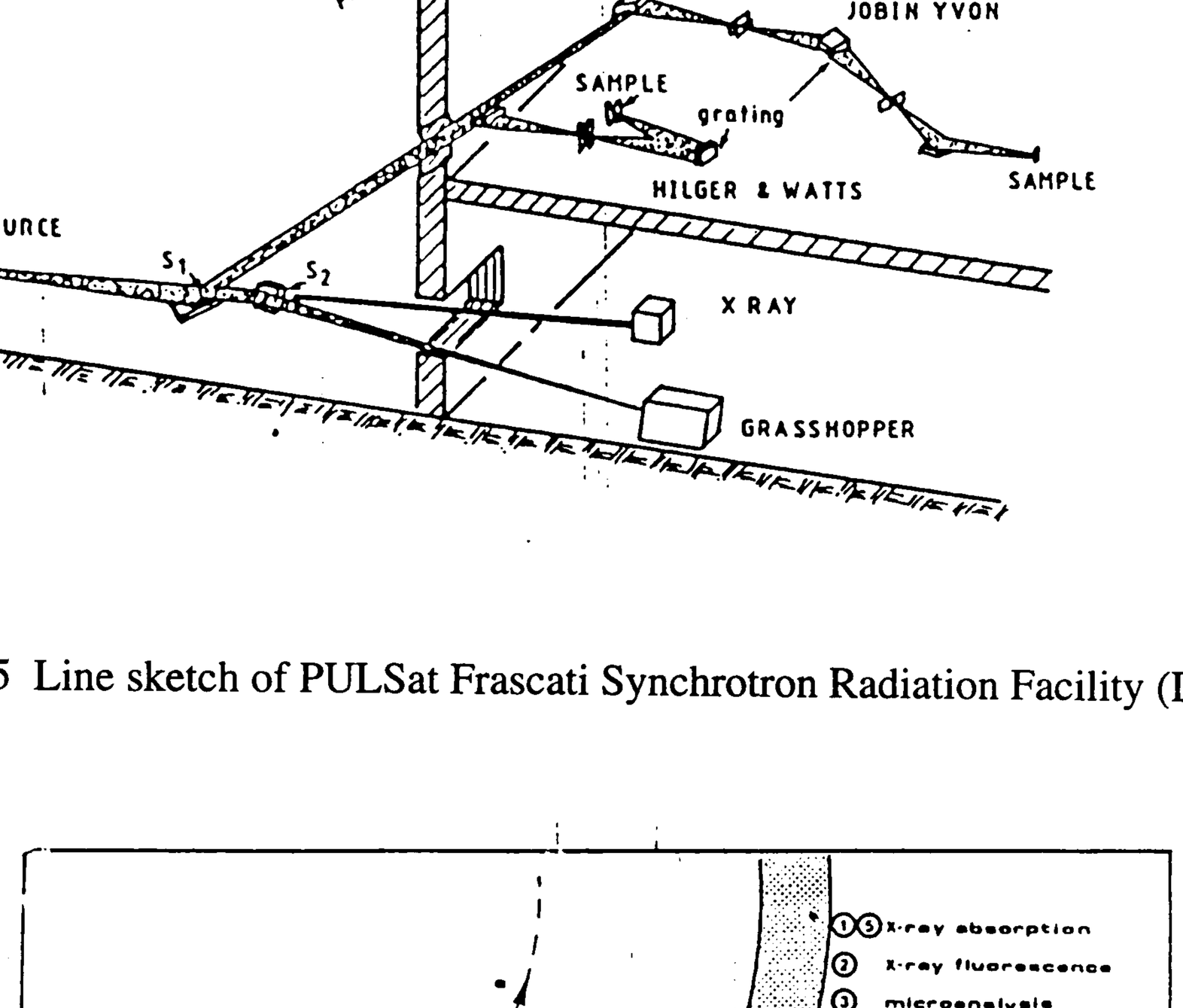

Fig. 1.1.6 Synchrotron Radiation PWA Laboratory (Frascati) using a wiggler magnet as source (Davoli et al., 1988).

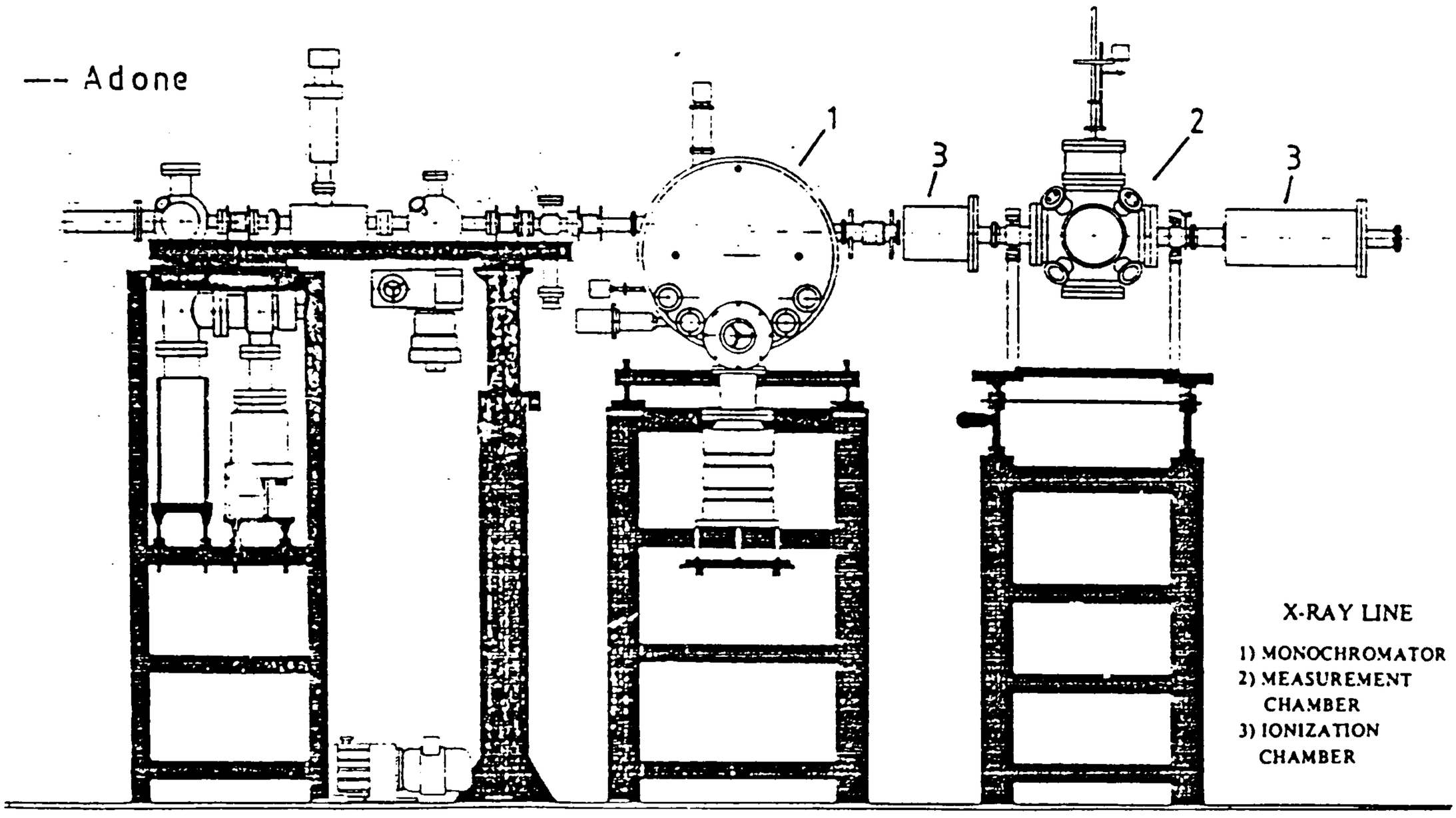

Fig. 1.1.7 X-ray line at the PULS laboratory (Davoli et al., 1988).

monochromator by a beryllium window in order to maintain ultra-high-vacuum conditions (10^{-9} mm Hg). Be has an absorption threshold at about 111 eV and is therefore practically transparent over the entire energy range at which the X-ray line operates (2.7-13 KeV). Consequently, the monochromator, and all the following devices which operate under low vacuum, can be easily opened and closed for maintenance and sample substitution.

The monochromatizing device consists of a single channel-cut crystal, which can be either Si (111) or Si (220) according to the experimental requirements. The resolution of the entire system results from the combination of the crystal and slits used. The double reflection inside the channel-cut allows the beam to move in a vertical plane when the crystal is being rotated. The monochromatization is obtained via the Braggs' law ($n\lambda = 2d\sin\theta$) where n is the reflection order and d is the plane lattice distance and θ is the incidence angle . By varying the incident angle, the exit slit of the monochromator lets rays of different wavelengths pass through (Fig. 1.1.8). A fine adjustment of the second plane reflection makes it possible to filter out the high harmonics or any undesired reflections. However, the main reason for this second reflection is to change the direction of the reflected beam back to the direction of the incident one. In this way the incident and the outcoming beam lie on the same plane and are simply translated to one another by a distance $2D\cos\theta$, where D is the distance between the two faces of the channel-cut. Once the beam is monochromatized, it is directed to the sample through the first ionization chamber which consists of a flat-parallel face condenser contained in a case filled by a suitable gas mixture (Fig.1.1.9). The X-rays passing through this device are photoelectrically absorbed and produce a current in the external circuit, the intensity of which is proportional to the photons passing through the condenser. By using two ionization chambers of this type, and simultaneously measuring the incoming photons and the photons passing through the sample, one gets the absorption spectrum. The ionization chambers are sealed by windows of kapton. Both the ionization chambers and the measurement chamber are supported by a plate which can be translated to follow the movements of the beam coming out from the monochromator.

The measurement chamber is a steel box with several ports. The necessary vacuum is usually achieved by means of a rotary pump, but occasionally one may use a turbine for high vacuum, or, alternatively, one may also fill the chamber with helium to operate at very low energy (less than 5 KeV) and/or with liquid samples. The measurement chamber contains a translational sample-holder, where standards and unknown samples may be studied together without requiring opening of the chamber; this aids obtaining measurements at uniform experimental condition (e.g. energy range, slit, counting rate). All operations are monitored by computer with all data stored in digital form in order to maximizes the quality and reproducibility of the results.

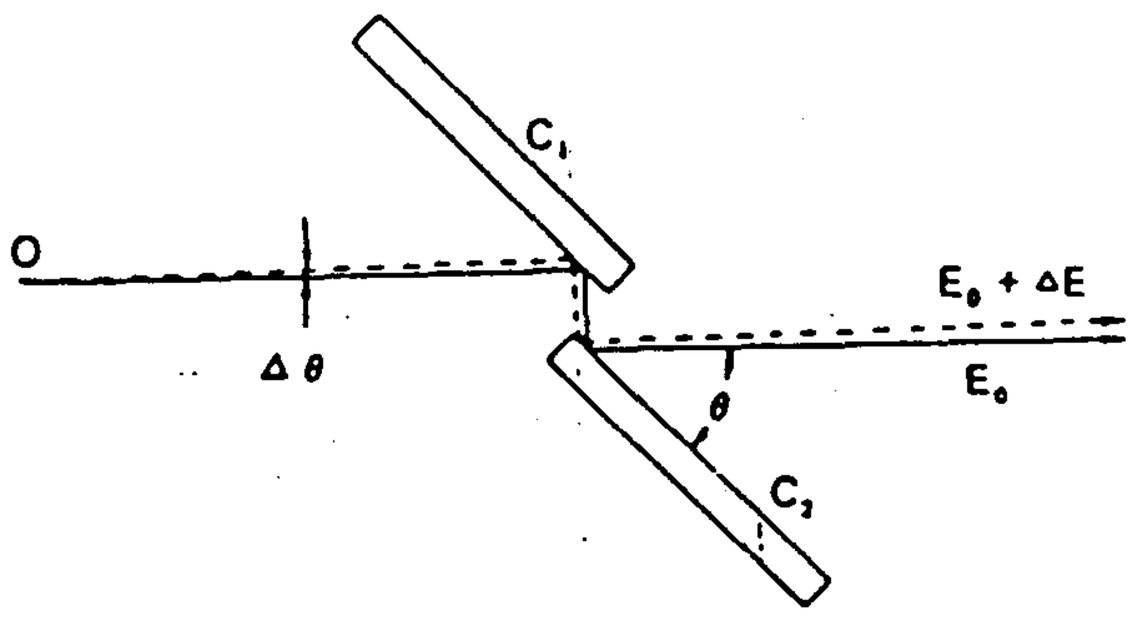

Fig. 1.1.8 Monochromatizing device, obtained with a single channel-cut crystal. C_1 and C_2 crystals, θ angle between the crystal and the beam, E_o energy (Davoli et al., 1988).

Table 1.1.1. Characteristics of ADONE as a synchrotron light source

Maximum energy	E=	1.5	GeV
Bending magnet radius	R=	5	m
Maximum current	I=	100	mA
Energy loss per turn per electron	ΔE=	89.6	keV
Critical wavelength	l_c=	8.28	Å
Critical energy	E_C=	1.5	keV
Total power radiated	P=	8.97	kW
Power available per mrad per observed orbit	P_1=	1.43	w/mrad
Types of available sources		- bending magnet - wiggler (6 poles) - undulator	
Number of lines of the bending magnet		= 4 + (2)	
Number of lines of the wiggler magnet		= 1 + (2)	
Number of lines of the undulator		= 1	
Flux per l = lc		Bending magnet N_1 = 2.4 x 10^{13} (lc = 89 Å)	
fot/sec · mrad · 1% BW		Wiggler magnet N_2 = 1.4 x 10^{14} (lc = 4.3 Å)	
Brilliance at $E = E_C$		6.4 x 10^{14} fot/s, 1% mrad^2/cm^2	
Emission angle at $E = E_C$		= 0.18 mrad	
Number of "bunches" of electrons		N=1 - 18	
Pulse width		=1.2 - 0.3 nsec	
Size of the electron beam		s_x=0.8mm	
		s_y=0.4mm	
Divergence of the beam		s_x=0.2mrad	
		s_y=0.4mrad	

Knowledge of the I and I_o through the ionization chamber allows solution of the equation

$$\mu = \frac{1}{d} \ln(\frac{I_o}{I}) \qquad [1.7]$$

where μ is the absorption coefficient and d is the thickness of the sample and Io and I are the beam intensity after the first and second ionization chambers, respectively. The samples are usually prepared as a powder stuck on a kapton tape or as a self-supporting film of ~1 μm thickness. A more detailed description of this method is given by Mobilio et al. (1982). In addition to transmission measurements it is also possible to make use of the fluorescence (Fig. 1.1.10) of the irradiated sample, measured by a photomultiplier set orthogonally to the incident beam direction. This method is very sensitive for dilute systems and suitable for numerous mineralogical applications.

The second line at ADONE was the GH (Grasshopper) line operating in the range of soft X-rays (40-940 eV; see Chiaradia et al., 1986). This line is considerably more difficult in its use than the previously described X-ray line. The name of the line derives from the resemblance of its monochromator to a "grasshopper" (Fig. 1.1.11). The operating energy range does not permit the use of the Be window, so the entire line is maintained under the same ultra-high-vacuum conditions of the ADONE storage ring (below ~$4 \cdot 10^{-9}$ mm Hg). Details of the Grasshopper monochromator are given in Brown et al. (1978) and only the main characteristics are reported here. The entire apparatus is made of steel and can be heated up to 250°C in order to reach the required 10^{-9} mm Hg vacuum. The optics arrangement requires a fixed outlet slit; for this reason the mirror M1 is spherical in order to be able to focus the source onto the inlet slit S1. This slit moves on the axis of the beam when the grating G is being moved. The holographic grating has 1200 lines/mm and moves following a very precise geometry so that the fixed outlet slit, the inlet slit and the grating itself all lie on a Rowland circle having 1m radius. The beam monochromatized in this way is refocussed onto the sample by a toroidal mirror. The sample is located about 16 m away from the synchrotron radiation source and 2 m from the outlet of the monochromator. The sample-holder assembly permits positioning of the specimen(s) so as to maximize the alignment, and it allows positioning of the samples at different levels for different treatment conditions, both during the set-up stage and the actual measurement; e.g., the sample-holder may be cooled down to the temperature of liquid nitrogen, or heated up to 700°C.

The measurement method in the soft X-ray energy range is the partial yield method (Fig.1.1.12), which determines the number of secondary electrons with low kinetic energy (typically 2 eV) photoemitted by the specimen as a function of the energy of the impinging photon beam. With increasing photon energy, the level of secondary photons increases as a result of Auger processes occurring in the valence bands and, at even higher energies as a result of other processes involving core levels (De Crescenzi

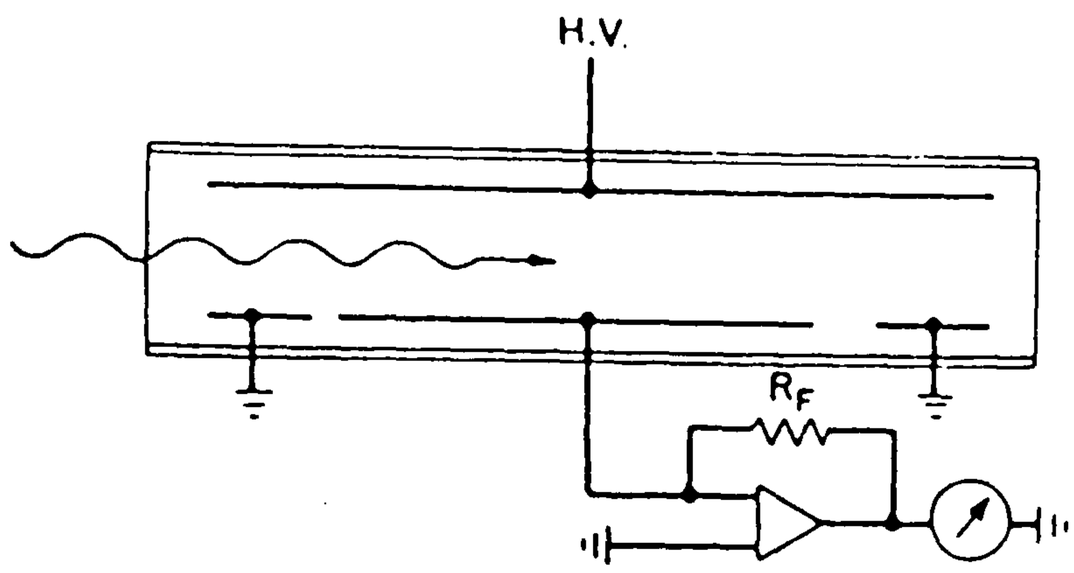

Fig. 1.1.9 Sketch of the working principle of an ionization chamber. HV high voltage, R_F resistance (Davoli et al., 1988).

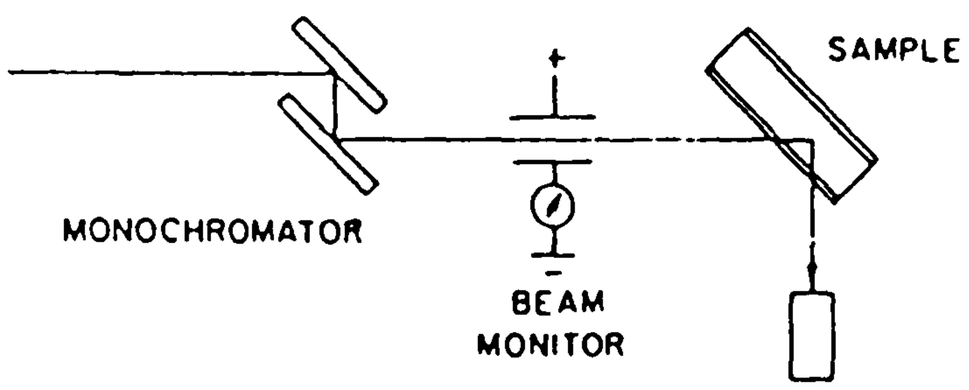

Fig. 1.1.10 Sketch of the fluorescence detection method (Davoli et al., 1988).

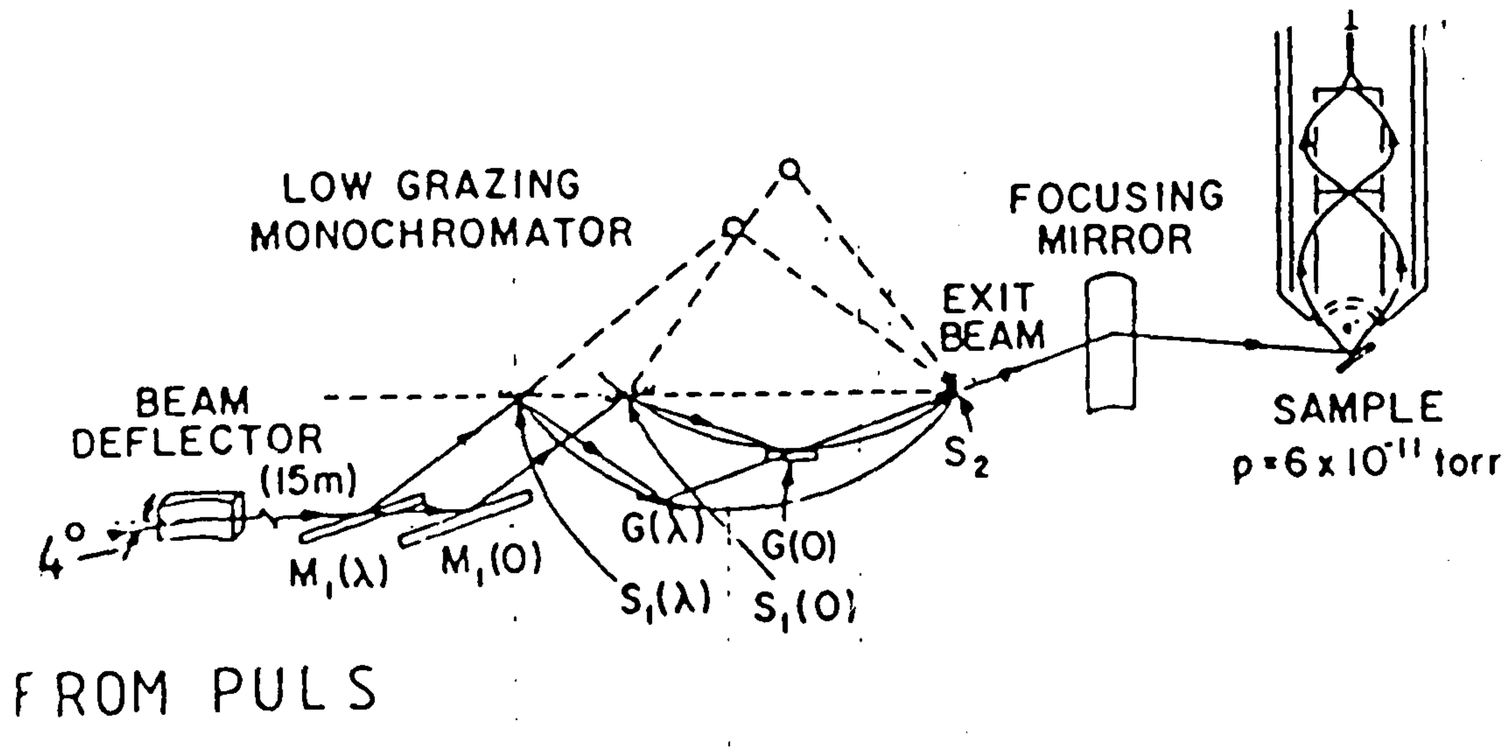

Fig. 1.1.11 Schematic of the Grasshopper monochromator. The main reflection mirror is at 4° incidence. The scheme shows also the double focussing mirror after the exit slit and the CMA double pass used as energy analyser (Davoli et al., 1988).

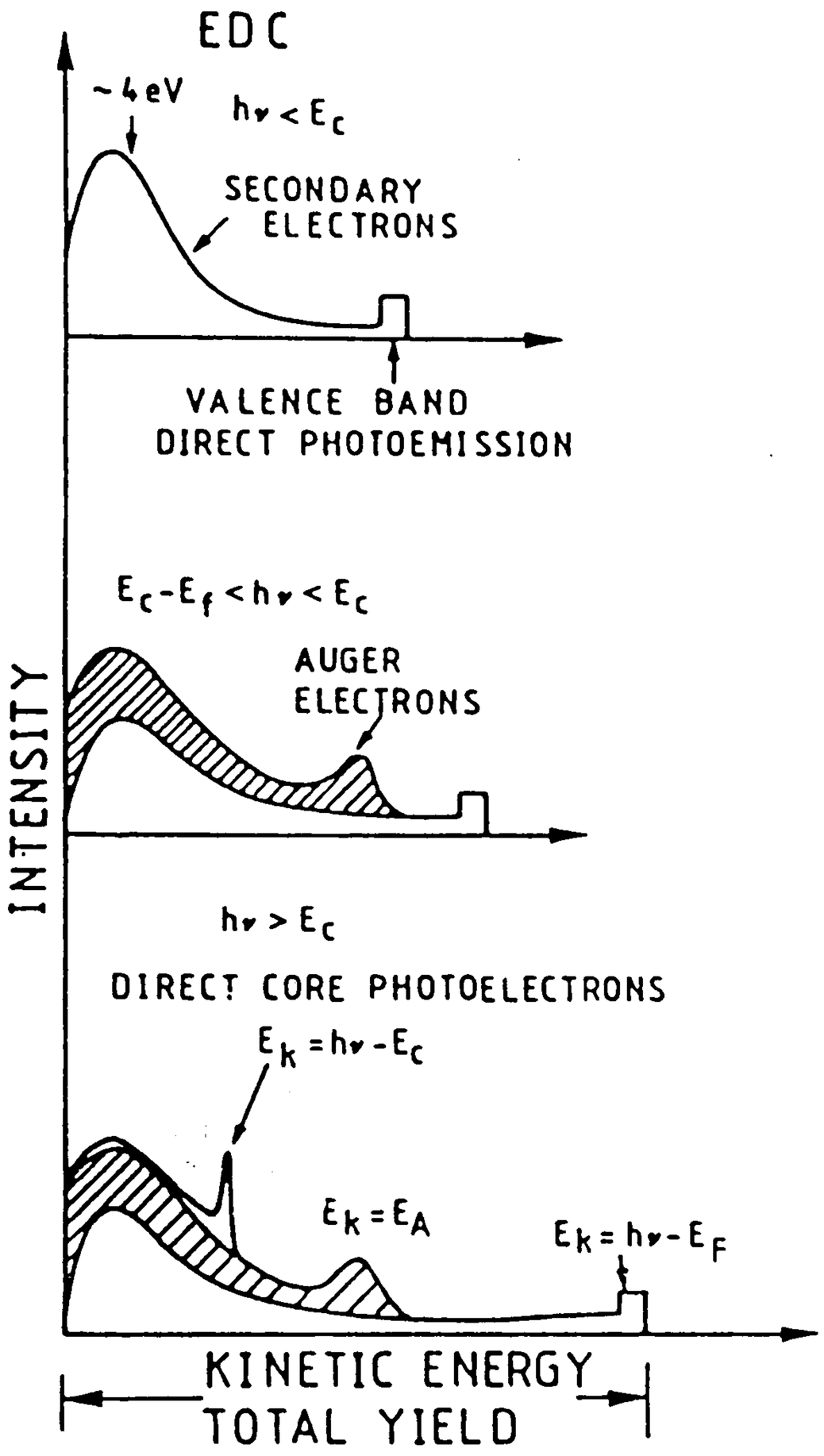

Fig. 1.1.12 Partial yield method (Davoli et al., 1988).

and Davoli, 1983). The apparatus used to collect these electrons is either a custom-made channeltron equipped with a grid selecting electrons or, as in this case, where the same line is used also for photoemission experiments, a double pass CMA which selects electrons photo-emitted in the energy range 10-2000 eV.

1.1.4. Essential features of absorption spectra and their interpretation

The general form of an absorption spectrum is shown in Fig. 1.1.13. The shape is that of a decreasing curve with a sharp jump at the absorption edge, followed by a ripple with amplitude ~3–4 % of the edge intensity.

Two different regions have been distinguished within the spectrum. They are indicated by the acronyms EXAFS (Extended X-ray Absorption Fine Structure) and XANES (X-ray Absorption Near Edge Structure) and, although this division is no longer justified on purely theoretical grounds (Benfatto et al., 1986), they are still commonly used for practical reasons. From an experimental point of view these two regions are separated because they require two separate measurement techniques, differing in sensitivity and resolution. The structures in the region measured for EXAFS are oscillations having periods as long as 10 eV, and consequently the resolution for such measurements is not so critical. On the contrary, the main purpose of XANES studies is to get information from small shifts and/or splittings of peaks in a relatively narrow energy window: for this reason a high resolution is usually required.

Besides the different experimental needs, the XANES and EXAFS features arise from different processes described by different theoretical models. When the energy of the impinging photon is greater than the energy required to excite an electron located in a given orbital (K, L_1, L_2, L_3, ...) of the investigated atom, the electron leaves the atom and moves towards the continuum with a kinetic energy which is equal to the difference between the incident photon energy and the energy of the ionization threshold. In the EXAFS region (which extends from 50 to 600 eV or more above the edge), according to the semiclassical model describing the physical radiation, the photoemitted electrons have kinetic energies which are high enough to interfere only once with their nearest neighbours. Consequently, the information the EXAFS spectrum can give only regards the average distance between the absorbing atom and its nearest neighbours. Quantitative data are extracted from this information by means of the Fourier analysis of only the periodic wavy portion of the EXAFS region (see Teo and Joy, 1979 for a full explanation).

Interpretation of near edge (XANES) structures is much more complex than that of EXAFS oscillations, mainly because the low energy of the ejected photoelectron increases the scattering cross section by interfering many times with the neighbouring atoms, before leaving the cluster (i.e., this is a multiple scattering process). This part of the absorption spectrum is therefore very sensitive to the details of the geometrical

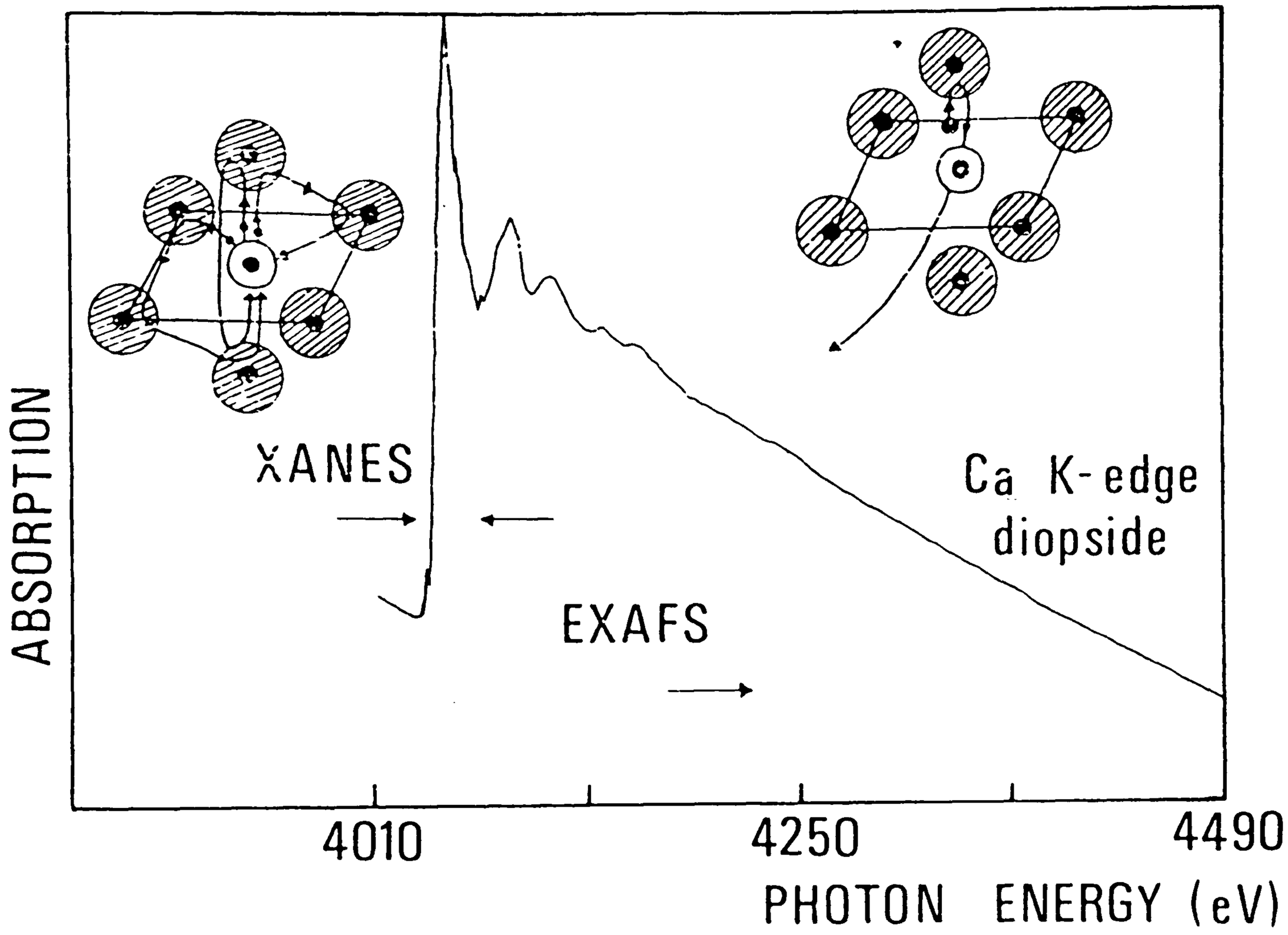

Fig. 1.1.13 Ca K-edge absorbing spectru for diopside. The insets show the semiclassic models explaining the single scattering and the multiple scattering rocesses (Davoli et al., 1988).

environment around the absorbing atom; this feature has been the subject of extensive study since the first investigations in the 1980's. As the work described in this thesis involves measurements and theoretical models of XANES spectra the collection and interpretation of such spectra is described in more detail in the following section.

1.2 GENERAL PRINCIPLES AND METHODS IN XANES SPECTROSCOPY

1.2.1 Abstract

Recent developments of the XANES (X-ray Absorption Near Edge Structure) technique are reported. This spectroscopic method may contribute considerably to the structural study of systems without long range order and in a more specific way to the determination of the local environment of atomic species in dilute solid solution. Low energy features of X-ray Absorption spectra contain information related to the distance from the absorbing atom to its first nearest (pair distribution function), as well as additional information on factors such as site distortion in the region near the photoabsorber.

1.2.2 Introduction

The local structural distortions around the sites of impurities in dilute solid solutions have largely been inferred from their effects on the intensities of diffraction peaks and from the associated diffuse scattering. The diffraction technique, powerful in determining the crystallographic structure and in the evaluation of the site distance of crystalline systems, is less informative for the study of highly dilute systems or systems without long range order. It is thus evident that techniques sensitive to disordered systems are welcome among scientists interested in structural distortions caused by small impurities into compounds forming solid solution. The advent of high intensity synchrotron radiation sources has promoted the development of the spectroscopic techniques dealing with X-rays. Techniques like EXAFS and XANES provide direct information concerning the atomic environment around a selected atom and give information on both structural and electronic characteristics. EXAFS spectroscopy is already supported by a well developed theoretical background (Sayers et al.,1971) and is widely used for a variety of inorganic compounds where elements occur both as trace and major components in crystalline or amorphous solids. For a general review see the Geochemistry section of Hodgson et al. (1984).

In the last decade, together with the extensive use of EXAFS, a considerable effort has been dedicated to the identification and understanding of the structures present in the first 50 - 60 eV of the absorption spectrum, the so called "XANES region". The

sensitivity of this energy region to the electronic state and the geometrical arrangement of the enviroment around the absorbing atom has been well known since the late 1970s (e.g., Natoli et al.,1980; Kutzler et al.,1980; Bianconi et al.,1978; Belli et al.,1980) but the use of the observed spectral features was generally limited to qualitative interpretation or to simple comparative analysis with reference to standard materials with known structures (Bianconi 1981; Bianconi et al.,1982).

The low energy part of the absorption spectrum is divided into the "edge region", which extends ~10 eV above the very first core ionization energy, and the true XANES region, which goes from +10 eV up to +50–60 eV. Fig. 1.2.1 shows the vanadium K-edge of two different stoichiometric oxides. From this it is possible to distinguish the difference of the edge region dominated by the white line and the XANES region dominated by the multiple scattering resonances. The chemical shift in the edge region is related to the effective charge of the vanadium ion, whereas the features near 10 eV are related to structural differences.

In the "edge region" the photoelectron kinetic energy is sufficiently low to yield an inelastic scattering with the valence electrons. The structures observed in the edge region are mainly due to transitions to bound states and therefore mainly reflect the electronic character. The physical origin of the absorption features in this region is different for different classes of materials: bound multiple-scattering resonances in molecules, core excitons in ionic crystals, unoccupied local electronic states in metals and insulators, atomic-like resonances, many-body effects and multielectron configuration interactions in solids (e.g., Bianconi, 1981).

In XANES, like in EXAFS spectroscopy, the structural information is due to the scattering of the excited photoelectron by the neighbouring atoms (elastic scattering), but in the EXAFS region the photoelectron has a very small cross-section and is backscattered weakly by the neighbouring atoms. The electron undergoes only a single-scattering process and as a consequence of this the information is related to the pair distribution function. In the XANES region the weak kinetic energy of the photoelectron compels it to bump many times into the neigbours atoms. This multiple scattering process (Fig. 1.2.2) makes XANES a method highly sensitive to the geometrical environment and it is therefore possible to use XANES spectra to get information which goes beyond the pair distribution function, such as angles between atomic bonds and relative distances of the neighbouring atoms.

Recently, XANES analysis has developed into a more quantitative method, starting from the finding that structures in the low part of the absorption spectrum are due to multiple scattering resonances within a small atomic cluster of neighbouring atoms (Benfatto et al., 1986; Natoli & Benfatto 1986; Natoli, 1987). The development of detailed theoretical models to describe such processes has allowed significant progress in the interpretation of XANES spectra, as described further below.

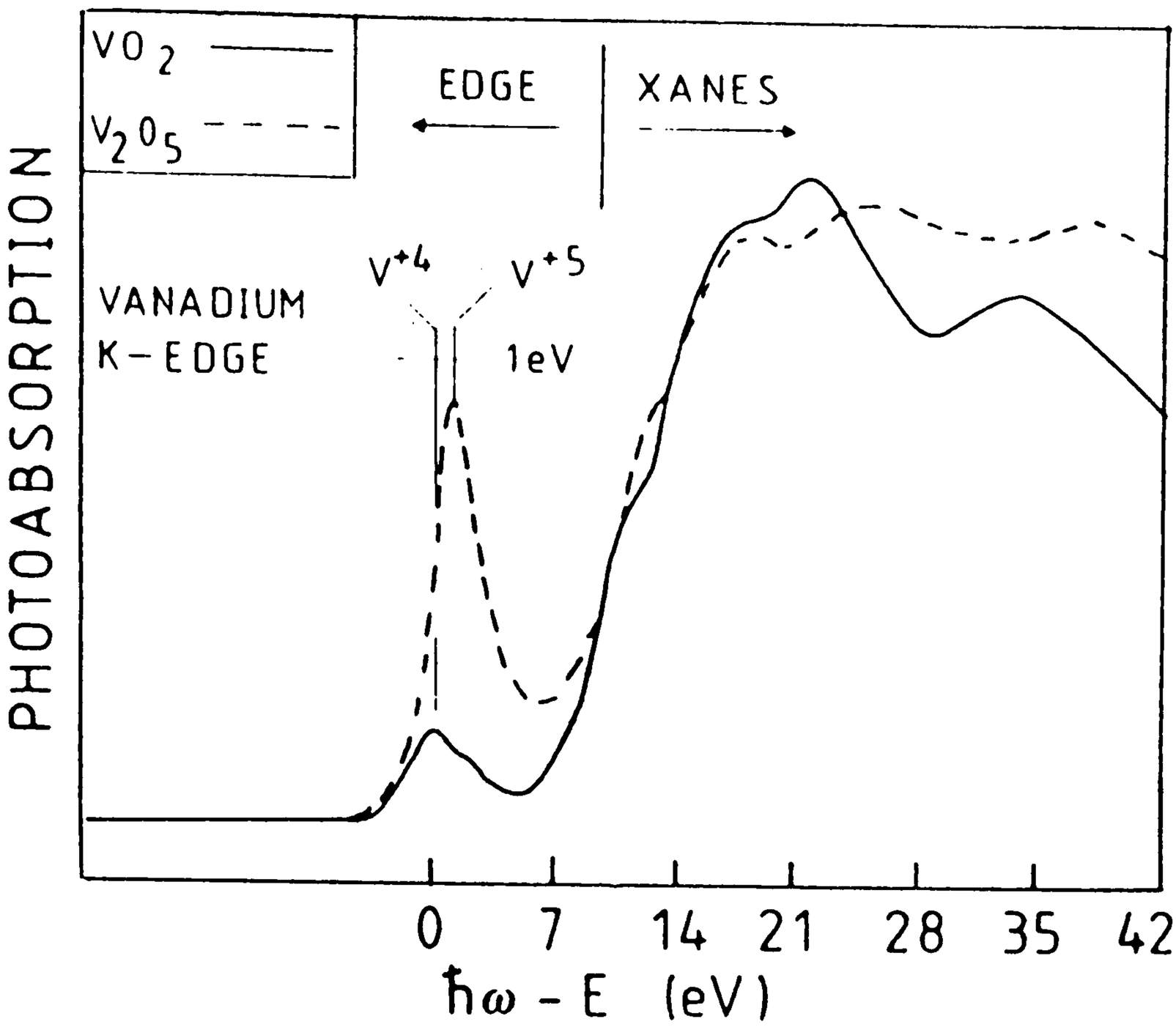

Fig. 1.2.1 XANES spectrum at the K-edge of V measured in two different vanadium oxides (Davoli & Paris, 1990).

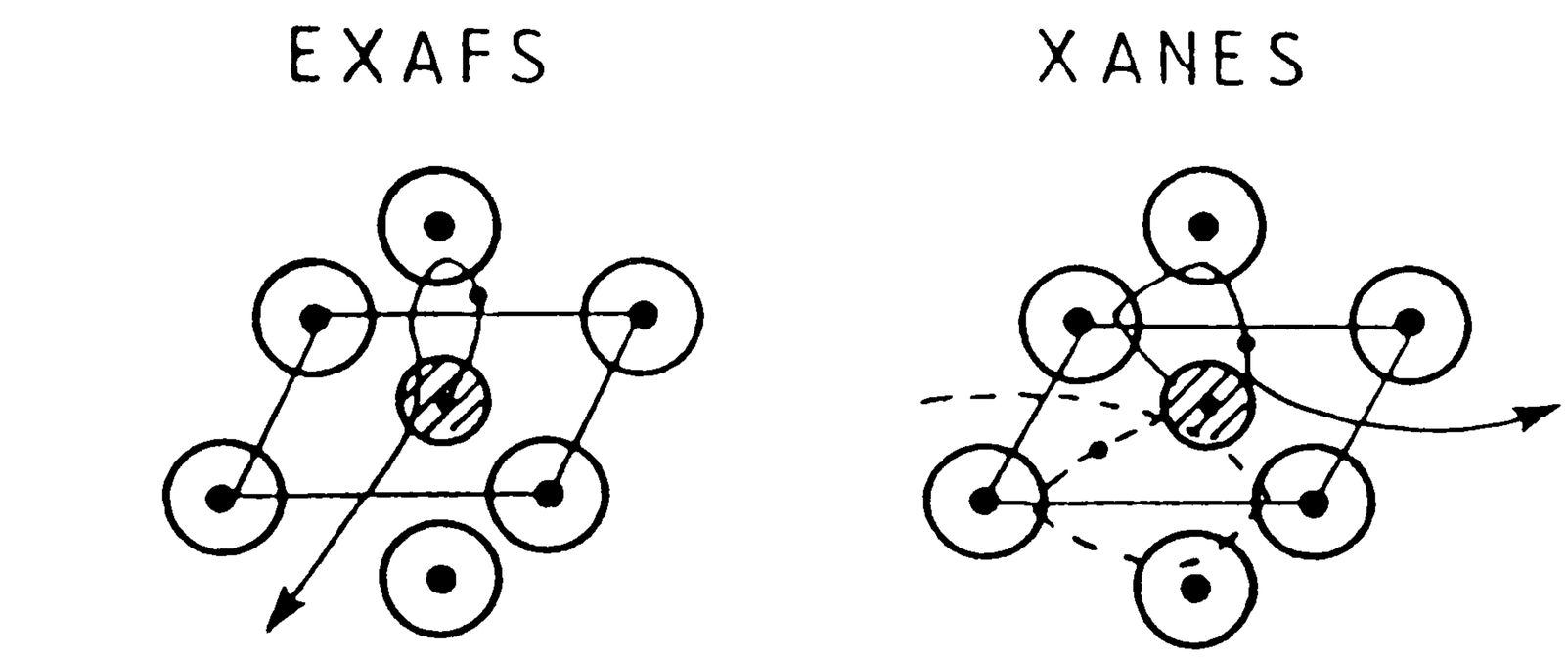

Fig. 1.2.2 Schematic view of the single (left side) and multiple (right side) scattering processes, showing two different pathways (Davoli & Paris, 1990).

1.2.3 Experimental requirements

1.2.3.1 *General considerations*

As has been briefly indicated, different energy regions may be identified in an absorption spectrum of a selected edge. Although this distinction has wide margins depending on the system studied, for the experimentalist it is important to know which part of the spectrum is interesting in order to optimize the monochromatization and detection systems. In fact, in the EXAFS energy region, where the amplitude of the oscillations never exceeds 3–4 % of the edge jump, a high photon flux of the incoming beam is necessary, even at expense of resolution, because the period of the oscillations is only 5 or 6 eV. In contrast, in the XANES region high resolution is of crucial importance because information on the electronic nature may be extracted even from very small variations in the energy position ($\Delta E \approx 0.2$ eV) or from peak splitting. The photon flux is of secondary importance because the examined resonance structures are generally very intense.

The monochromator usually used in studies of the X-ray energy region is of the "channel-cut" type. The energy bandwidth ΔE of this device is determined by the angular divergence $\Delta\theta$ and by the crystal monochromator rocking curve. In synchrotron radiation beam lines the angular divergence depends on the electron optics of the storage ring, which from the point of view of the "user" is a fixed parameter. Therefore resolution can be improved only by changing the monochromator crystal or its reflection plane.

Particular attention must be given also to sample preparation, because radiation leakage affects the intensity of the absorption peaks and reduces the intensity of the measured structures. The sample thickness should be exactly calculated, knowing the stoichiometric composition of the sample itself, its density ρ (given in g/cm^3), and its mass attenuation coefficient μ_m (expressed in terms of cm^2/g).

If we consider an X-ray beam of intensity I with a unit cross section crossing a sample with density ρ, the intensity will decrease along the path dx according to

$$\frac{dI}{I} = -\mu_m \rho dx \qquad [1.8]$$

If $I = I_0$, integration gives

$$I = I_0 \exp[-\mu_m \rho x] \qquad [1.9]$$

where ρx is the planar density expressed in terms of $[g/cm^2]$.

Generally we need to know the thickness of the sample, the type of atomic species it is composed of, and the energy of the selected edge. The expression of the $\mu_m(\omega)$ in terms of the atomic attenuation coefficient $\mu_a(\omega)$ is given by:

$$\mu_m^{Total}(\omega) = \frac{N_A \mu_a^{'}(\omega)}{\sum C_i \cdot A_i} = \frac{\sum \mu_m^i \cdot C_i \cdot A_i}{\sum C_i \cdot A_i} \qquad [1.10]$$

where N_A is Avogadro's number, C the weight fraction of the atomic species in the studied molecule, A the atomic weight and i indicates the number of the n different atomic species present in the molecule. Consequently, thickness is given by

$$x = \frac{1.5}{\rho \mu_m^T} = \frac{1.5 \sum C_i A_i}{\rho \sum \mu_m^i C_i A_i} \qquad [1.11]$$

where the factor of 1.5 comes from an estimation deduced by the study of thickness effects (Heald & Stern, 1977; Stern & Kim, 1981).

A calculation carried out for various amounts of leakage (Fig. 1.2.3) suggests that samples should be prepared with a thickness such that μx is ≤ 1.5. However, accurate calculation of thickness is required only where thickness effects are suspected. In any case, measuring samples with various thicknesses will permit extrapolation of the absorption to zero thickness: this is the only procedure appropriate to reduce the effects due to the contingent pin-holes and the unavoidable inhomogeneity of the sample.

1.2.3.2 *Detection method*

The detection method depends mostly on the energy range of the selected edge and on the atomic species concentration. In the hard X-ray energy region (above 3000 eV), for samples where concentration of the selected atomic species is greater than 10^{-3} g, transmission is the most used technique to measure the absorption coefficient μ. According to Eqn 1.9, where the thickness x of the sample is known, the absorption coefficient is determined by measuring the intensites of the incident and transmitted photon beam. The loss of intensity of the transmitted beam is due to the absorption by the electron of the selected core level. The photoionization chambers required to detect the photon flux are simply flat condensers filled by a suitable gas mixture. In this way photons passing through the gas create ion pairs, making the current of an external circuit increase. Beside the normal transmission method, schematically shown in Fig.1.2.4, other detection systems have been used, but a little more sophisticated explanation is required.

The inner shell photoionization process may be described as a two-step process: at first the radiation excites a core electron-hole pair, then in a second step the recombination process takes place. Among the many possible recombination channels, the most

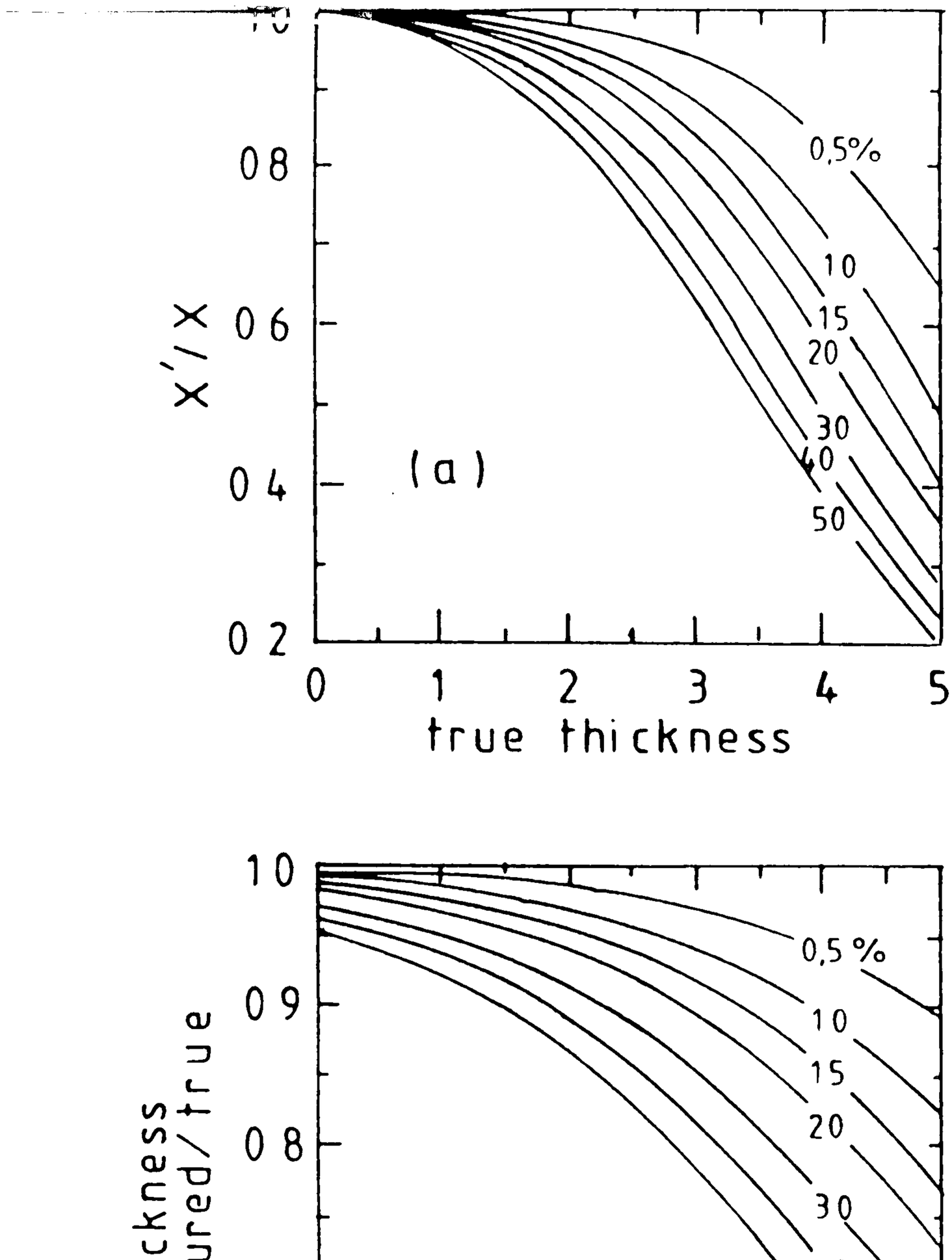

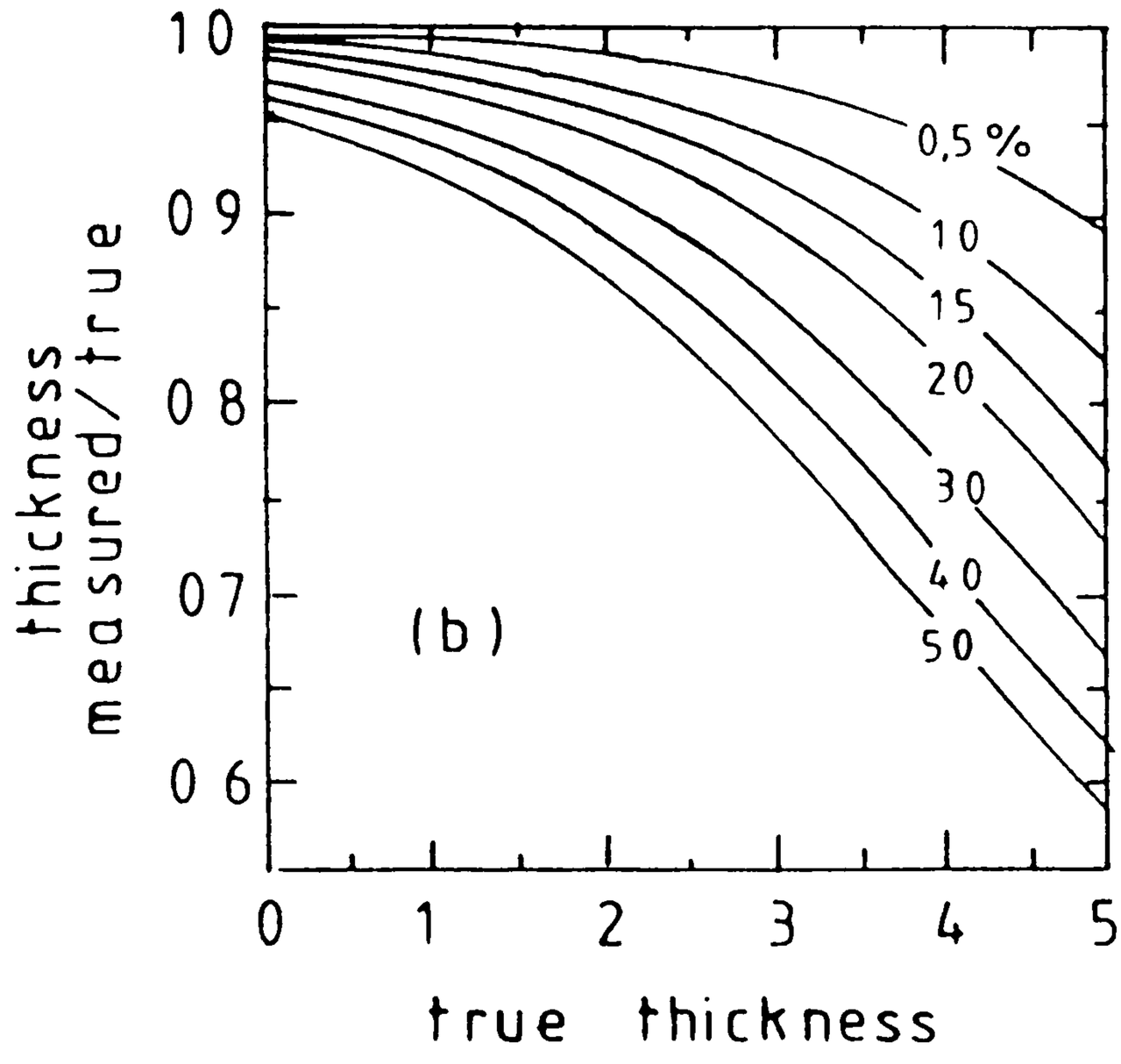

Fig. 1.2.3 Reduction of the χ'/χ with the measured thickness/true thickness ratio (Davoli & Paris, 1990).

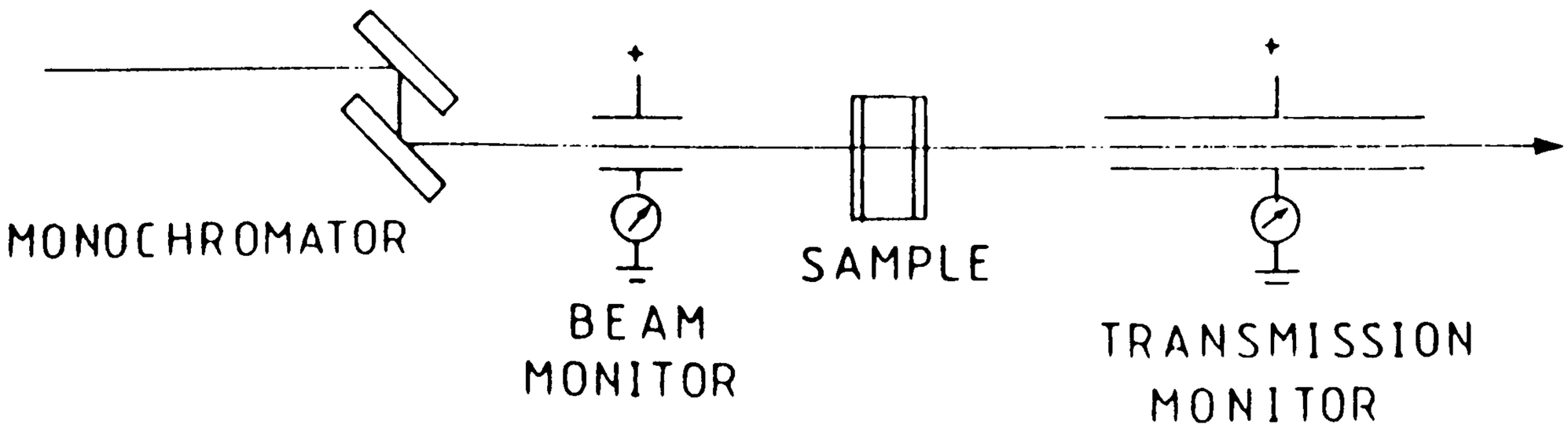

Fig. 1.2.4 Sketch of the set-up for X-ray absorption measurements by transmission mode (Davoli & Paris, 1990).

probable in the hard X-ray region is the direct radiative core-hole decay which produces X-ray fluorescence lines. The availability of very good photon detectors makes this technique suitable to detect absorption signals coming from atoms in very dilute samples, while the high photon energy of the fluorescence lines makes the technique bulk sensitive. Figure 1.2.5 shows a sketch of a setup designed to record absorption spectra in the fluorescence mode.

In the soft X-rays region, where the energy of photons is less than ~4000 eV, the recombination channels following the atomic excitation are dominated by the production of photoelectrons and Auger electrons. Fig.1.2.6 shows the energy distribution of the electron photoemitted by the sample onto which a monochromatic radiation shines (Stohr et al., 1984). This electron detection system utilizes a Cylindrical Mirror Analyzer (CMA) mounted according to a reflection geometry (Fig. 1.2.7). This device is normally used in surface spectroscopy, but it is also possible to gather information coming from the bulk of the studied sample (i.e. involving a surface layer thicker than 10 Å). The electrons photoemitted originate from the bulk or from the surface according to a universal curve which exhibits only one minimum at about 5 Å and around 100 eV. By selecting different energy windows we may have different types of "yield". So if we optimize the detector only for "Secondary" electrons we have a bulk sensitive spectroscopy with the resolution given by the monochromator. With this technique, the sensitivity is not very high because the signal to background ratio is poor. In addition, the "Total Yield" is a bulk sensitive method with a low signal to background ratio because it collects all the electrons coming out from the sample. The only advantage with respect to the "Secondary" yield is the simple experimental set up.

1.2.4 Theoretical interpretation of XANES

The Multiple Scattering Theory (MST) can explain the features of the total absorption spectra, starting from Fermi´s golden-rule. The expression of the total absorption cross-section can be written as:

$$\sigma(\varepsilon) = 4\pi^2\varepsilon\alpha\sum_f |\psi_f|p\cdot D|\psi_i|^2\,\delta(\varepsilon-E_f-E_i) \qquad [1.12]$$

where $\psi_{i,f}$ are the initial and the final state wave functions, ε the photon energy, p the polarization vector, E_i and E_f the energy of initial and final state, D the dipole transition operator and $\alpha = 1/137$ the fine structure constant. Many different approaches can be used to calculate expression [1.12] (e.g.Natoli, 1984), but each of them leads to the same numerical results. In the work reported here a Green's function approach has been used because it is the most suitable for obtaining structural information (Durham et al., 1982; Lloyd & Smith, 1972). Further deatails are given in Davoli and Paris (1990).

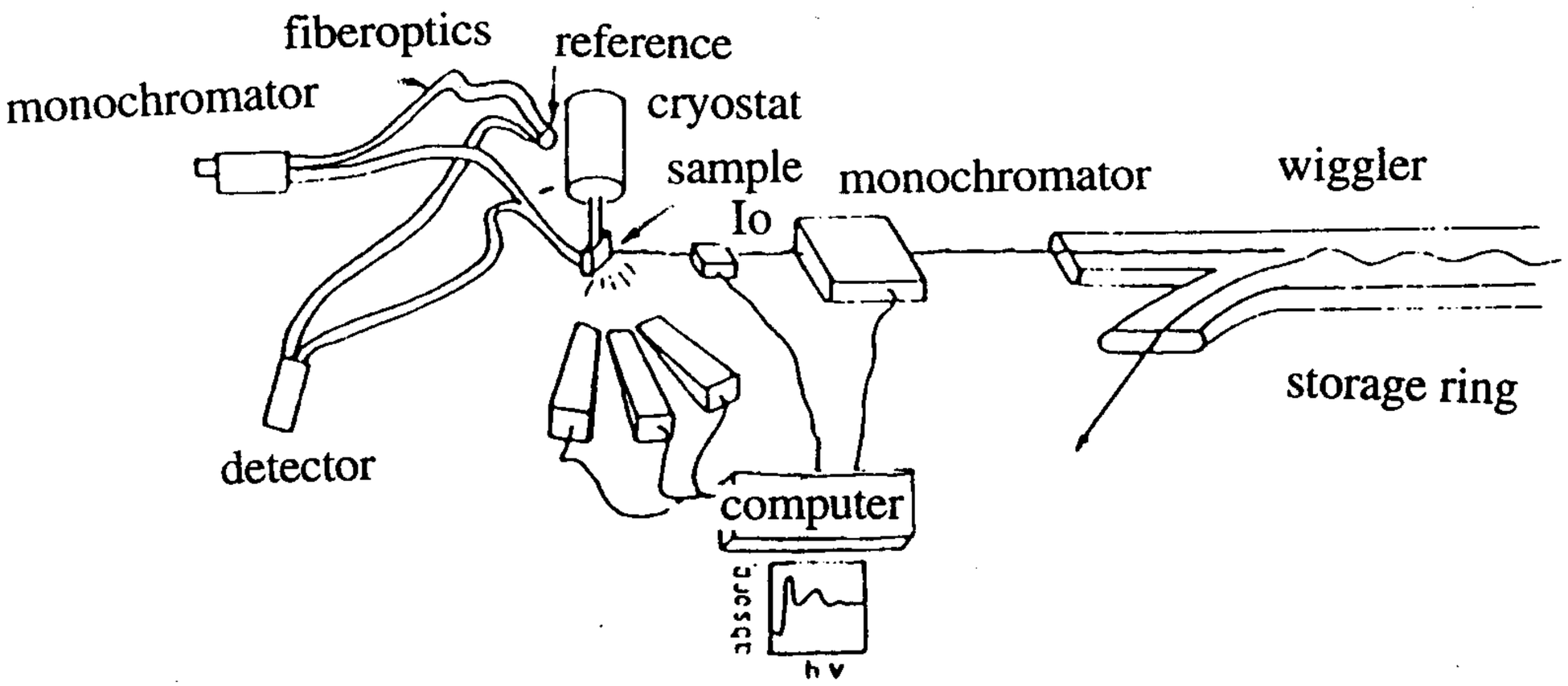

Fig.1.2.5 Schematic view of a beam line for X-rays absorption experiments using a wiggler as the X-ray source, and fluorescence as the detection system.

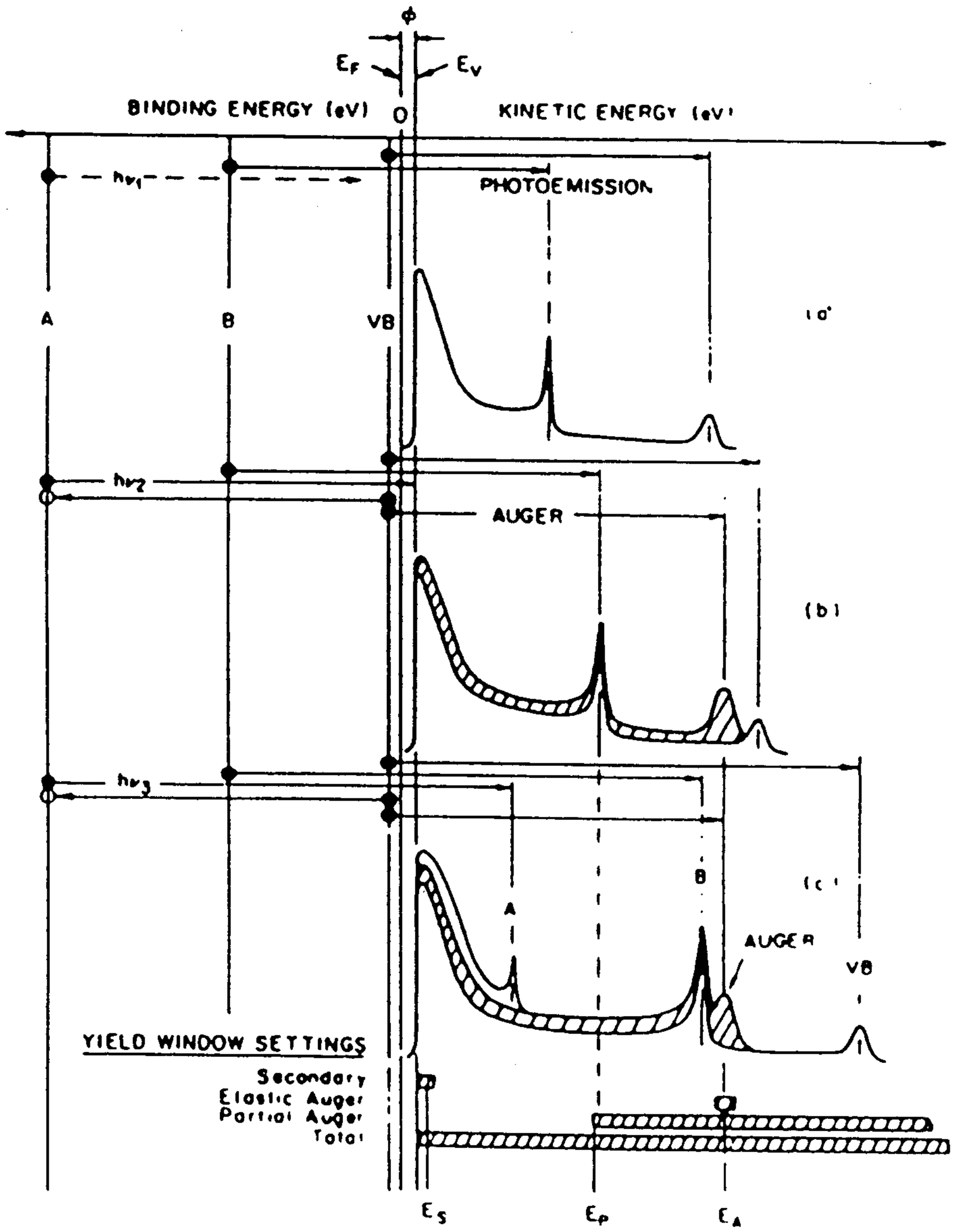

Fig.1.2.6 Schematic photoemission spectra for different excitation energies. The contributions to photoemission spectra by different channels are shown.

At low energy, where all the paths are equally important and give only global information, a relation between energy position of the continuum resonance and bond length between the absorption atom and its nearest neighbours is given by (Heald & Stern, 1977; Stern & Kim,1981):

$$(E_r - V)\, R^2 = C_r = \text{const.} \qquad [1.13]$$

where E_r is the energy position of the peak, R is the bond length between the absorbing atom and its first neighbours in the real space, and V is an average interstitial potential typical of the particular cluster under investigation. In this expression the quantity V is not measurable directly. To overcome this difficulty, we can subtract a similar expression calculated for pre-edge features due to transitions to bound states (like antibonding states of 3d character in the case of metal oxides) (Bianconi et al., 1982). This expression is:

$$(E_b - V)\, R^2 = C_b = \text{const.} \qquad [1.14]$$

The result of the subtraction is:

$$(E_r - E_b)\, R^2 = \text{const} \qquad [1.15]$$

where E_b is the energy of the transition to bound states. Now all quantities are experimentally measurable.

1.2.5 Experimental verification

In this section I briefly present some results confirming the conclusions reached in the previous section. Consider the relationship of the energy position of the continum resonance to the bond length between the absorbing atom and first neighbours as indicated by Eqn. [1.15]. In Fig. 1.2.8, the calcium K-edges of a set of natural pyroxenes with different Ca concentration are shown; note the shift of major intensity from C_2 for Ca-poor samples to C_1 for Ca-rich samples. These samples belong to the solid solution series diopside ($CaMgSi_2O_6$) - jadeite ($NaAlSi_2O_6$), along which Na substitutes for Ca in the M2 site. From XANES analysis a distortion of the polyhedron around the site was found as a function of the Ca content, attributable to compression of the site in a selected direction while the average distance remained unchanged. Such a selective compression was not detectable with other techniques. The experiment was performed at the Frascati Synchrotron Radiation Center utilizing the "PULS" X- ray line (Mobilio et al.,1982) with a Si [111] single-cut crystal as monochromator. The spectra were collected in the transmission mode using two ionization chambers filled by a suitable gas mixture. Details on this experiment and its interpretation can be found in Davoli et al., (1987) and simulation of the spectra is reported in Chap. 5.

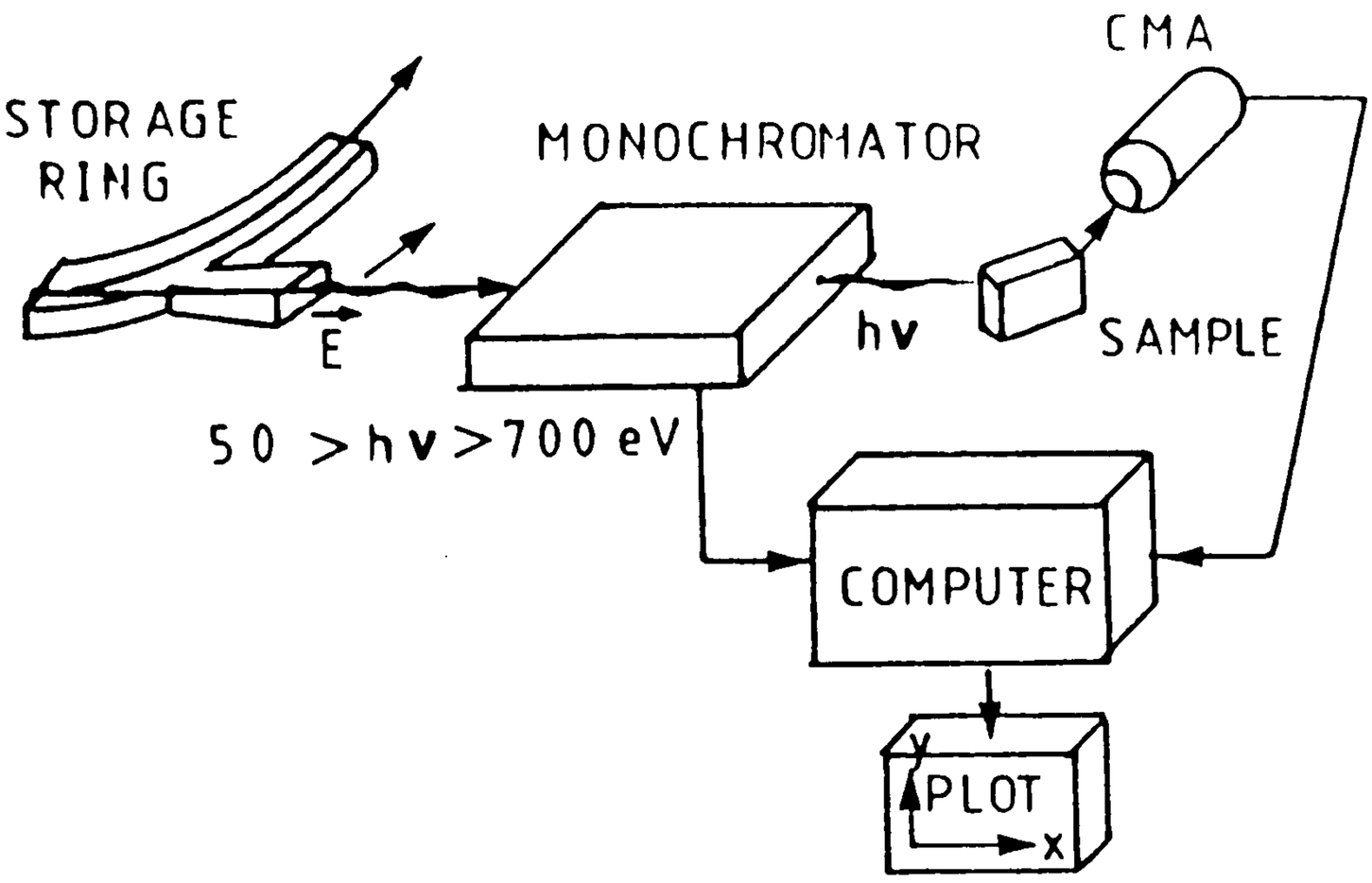

Fig. 1.2.7 Experimental set-up for soft X-ray detection. The absorption is measured by detecting the emitted electron via an electron analyzer set at the selected energy (Davoli & Paris, 1990).

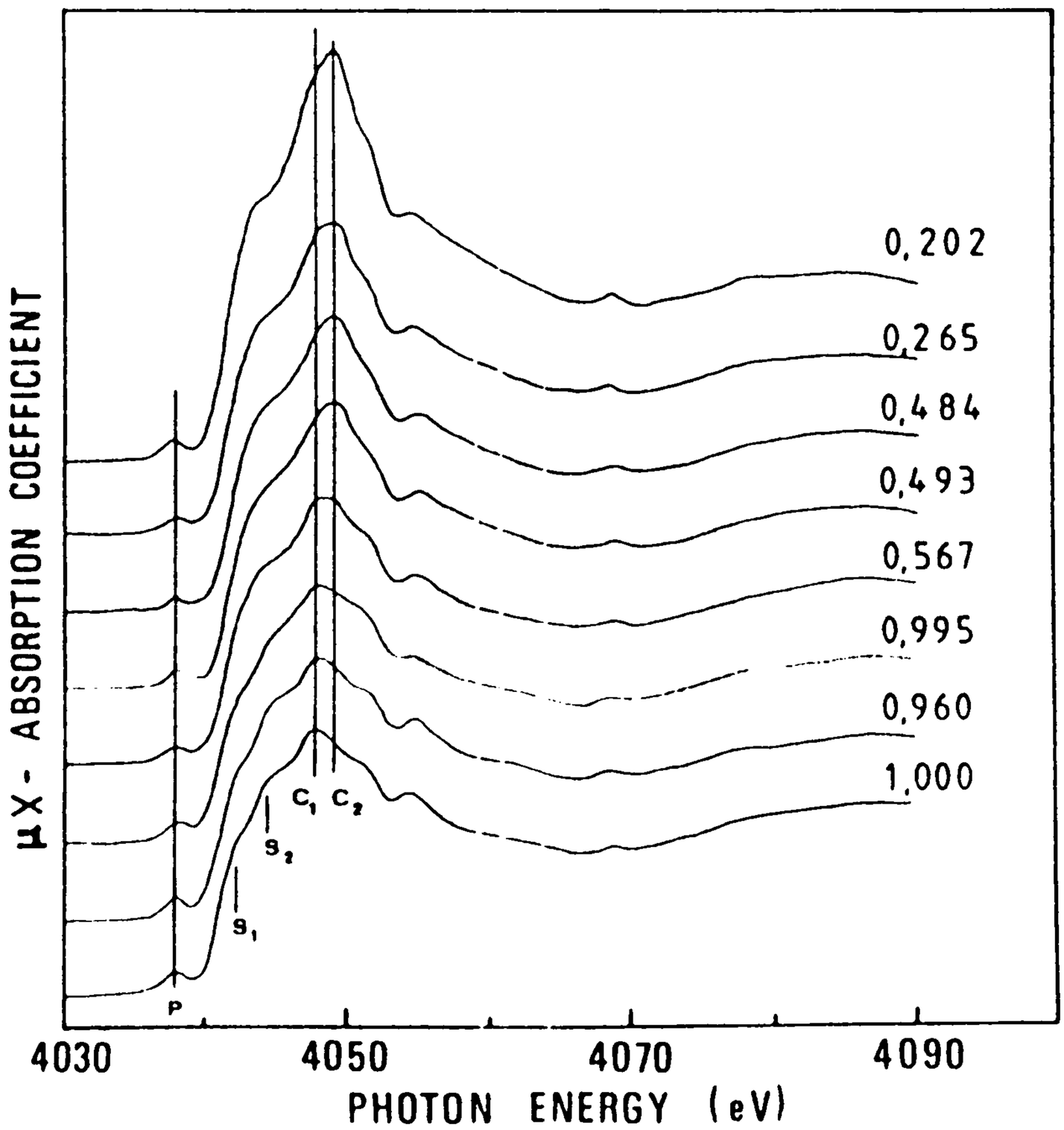

Fig. 1.2.8 XANES spectra at the Ca K-edge. Numbers next to each curve indicate the Ca content of the M2 site (Davoli & Paris, 1990).

A second illustrative example is provided by the case of the Mn K-edge absorption of $(MnO_4)^-$ and $[Mn(OH_2)_6]^{2+}$ complexes in aqueous solution (Benfatto et al., 1986). The aqueous solutions have been chosen in such a way as to obtain clusters in which it was possible to remove the effects of undesirable high order shells. The two complexes (both forming stable molecules) are characterized by having the Mn ion in different coordination: the $[Mn(OH_2)_6]^{2+}$ one has an octahedral coordination, with a Mn-O average distance of about 2.17 Å, whereas the $(MnO4)^-$ one has a tetrahedral coordination with a Mn-O average distance of about 1.63 Å. High resolution was achived by using a Si(220) channel-cut monochromator and an entrance slit of 0.5 mm. The only treatment of the raw data was the subtraction of the pre-edge absorption background.

The comparison between the two absorption spectra, normalized to the atomic absorption at very high energy, is shown in Fig. 1.2.9. After rescaling the energy so as to correct the different metal-ion effective distances, and to normalize the amplitude taking into account the different number of the first neighbours, the two spectra show the same behaviour only in the region where the photoelectron probes the pair correlation function (EXAFS region). This is a clear indication that information about high-order correlation functions and the geometrical arrangement of the absorbing atom environment are contained in the spectra below 160 eV from the edge.

In order to get a deeper insight into the interpretation of the XANES energy region the theoretical absorption coefficients for both the complexes was calculated. The experimental data were then then analyzed using the concepts described previously in the theoretical section. To evaluate the atomic phase shifts, the real part of the energy -dependent Hedin-Lundvquist potential has been used. The potential was constructed by using the electron density obtained for the muffin-tin approximation. Finally the calculated spectra have been convoluted by a Lorenzian broadening function with an appropriate energy-dependent width so as to take into account the core-hole lifetime, the experimental resolution, and the energy-dependent damping of the electron in the final state.

Figure 1.2.10 shows the comparison between the experimental and theoretical spectrum of the $[Mn(OH_2)]^{2+}$ complex. The quantity $\alpha_F{}^c$ is the calculated absorption coefficient obtained by exact inversion of the Multiple Scattering series and the superscript c indicates the convolution as previously described. Fig. 1.2.11 shows the breakdown of the α_F in terms of partial contributions for n up to 4. The sum $\alpha_0+\alpha_2$ is already a good approximation of total absorption coefficients for energies greater than 40 eV. This is a clear indication that the EXAFS regime starts at this point and is due to a fortuitous cancellation of the α_3 and α_4 contributions, both of which are quite sizeble

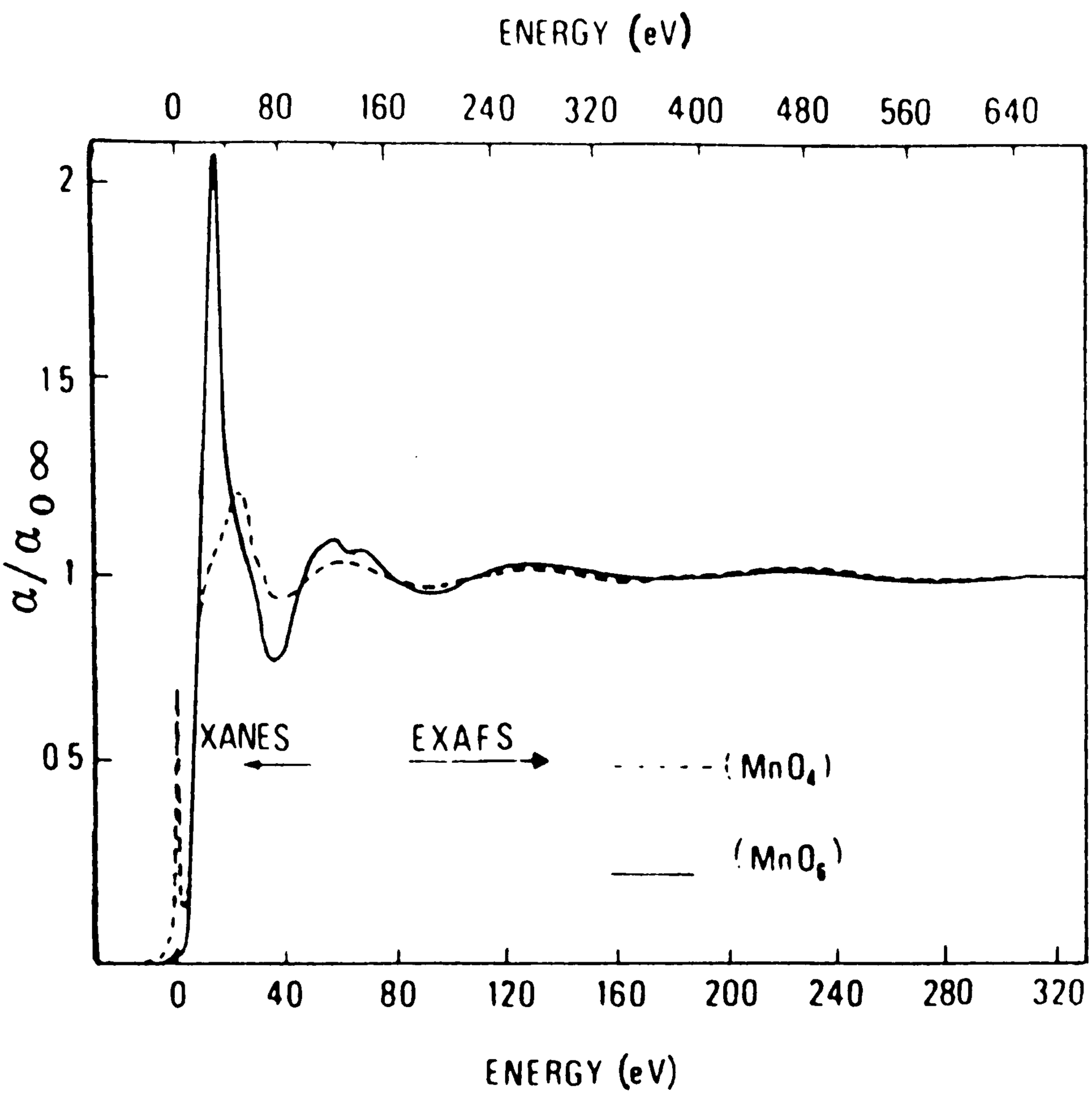

Fig. 1.2.9 Comparison between the experimental spectra of $(Mn(OH_2)_6)^{2+}$ and $(MnO4)^-$ compounds. The uppermost energy scale refers to the $(MnO4)^-$ curve (Davoli & Paris, 1990)

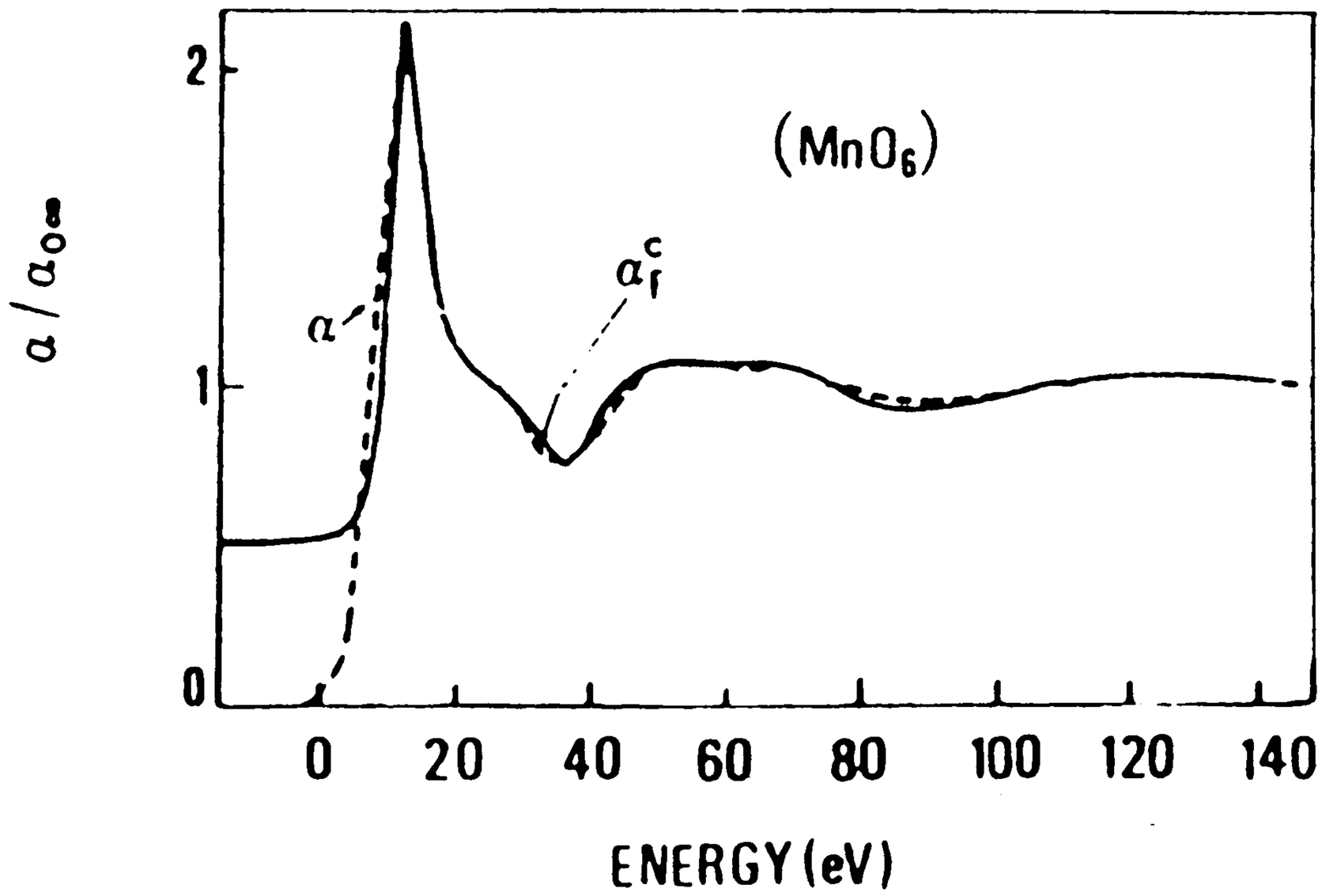

Fig. 1.2.10 Comparison between theoretical (solid line) and experimental spectra for the $(Mn(OH_2)_6)^{2+}$ complex (Davoli & Paris, 1990).

figs 1.2.9 and 1.2.10

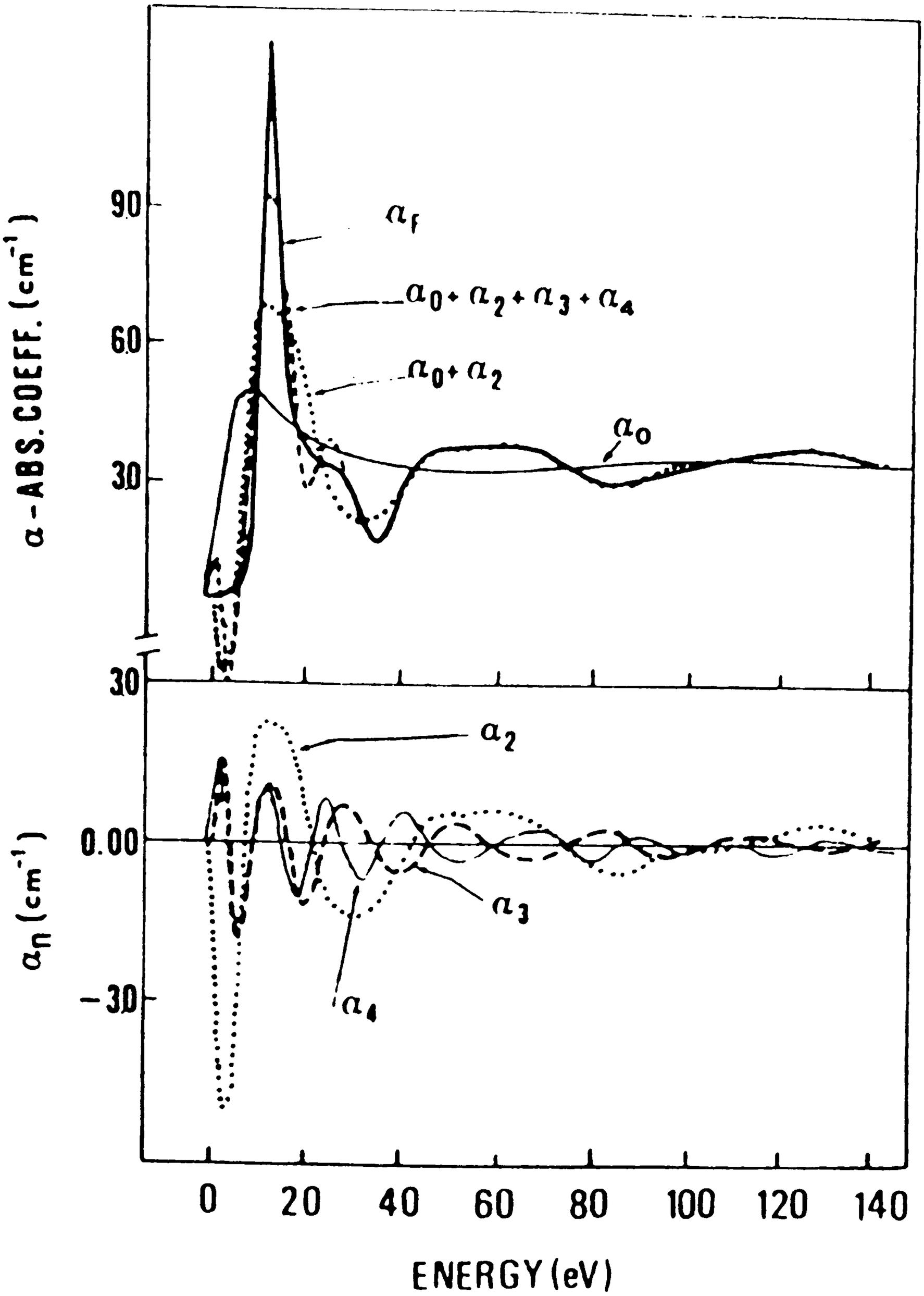

Fig. 1.2.11 Breakdown of the total theoretical cross-section of the $(Mn(OH_2)_6)^{2+}$ complex in terms of partial contributions (Davoli & Paris, 1990).

and of the same order of magnitude as the EXAFS signal in the whole energy range considered (as shown in the bottom panel of Fig. 1.2.11). The explanation of this behaviour lies in the geometry of the cluster (presence of two collinear paths of order 3 and 4) and in the particular value of the l=1 phase shift of the absorbing atom in the range 40–80 eV. Below 40 eV all the Multiple Scattering contributions are important and, due to the geometry of the cluster, they happen to be all in phase at one particular energy with the result of forming peak A. In this interpretation peak A is a shape resonance.

Results and interpretations for the $(MnO_4)^-$ cluster, treated in the same way as the $(Mn(OH)_2)^{2+}$ complex, are shown in Figs.1.2.12-13. In this case contribution α_3 is in a good agreement with the total absorption coefficient in the range 50-140 eV (i.e.the sum $\alpha_0+\alpha_2+\alpha_3$ must be considered), while higher order terms are negligible. However, high order MS signals are essential to obtain features below 50 eV. The breakdown approach shows a continuous merging of the MS regime into the EXAFS regime, with a merging interval ranging from 50 to 150 eV.

From this consideration it is clear that only in the case of the tetrahedral $(MnO_4)^-$ cluster it is possible to extract the α_3 contribution from the experimental spectrum, measuring in this way the length of the triangular path Mn-O-O-Mn by means of Eqn. [1.13]. The point can be stresses that this signal is proportional to the first peak of the three-body correlation function. By exploiting the knowledge of the first two terms of the series, we have then subtracted the calculated $X_2 = 1 + \chi_2^1$ contribution, conveniently convoluted, from the experimental spectrum normalized to α_0. The resulting signal is compared with the calculated α_3 in Fig. 1.2.12. The agreement is striking, thus confirming this interpretation. More details of the procedure used are given in Garcia et al. (1986) and Ruiz Lopez et al. (1988) where the same results have been obtained for the chromate cluster $(CrO_4)^{2-}$ and for a ferrocene compound.

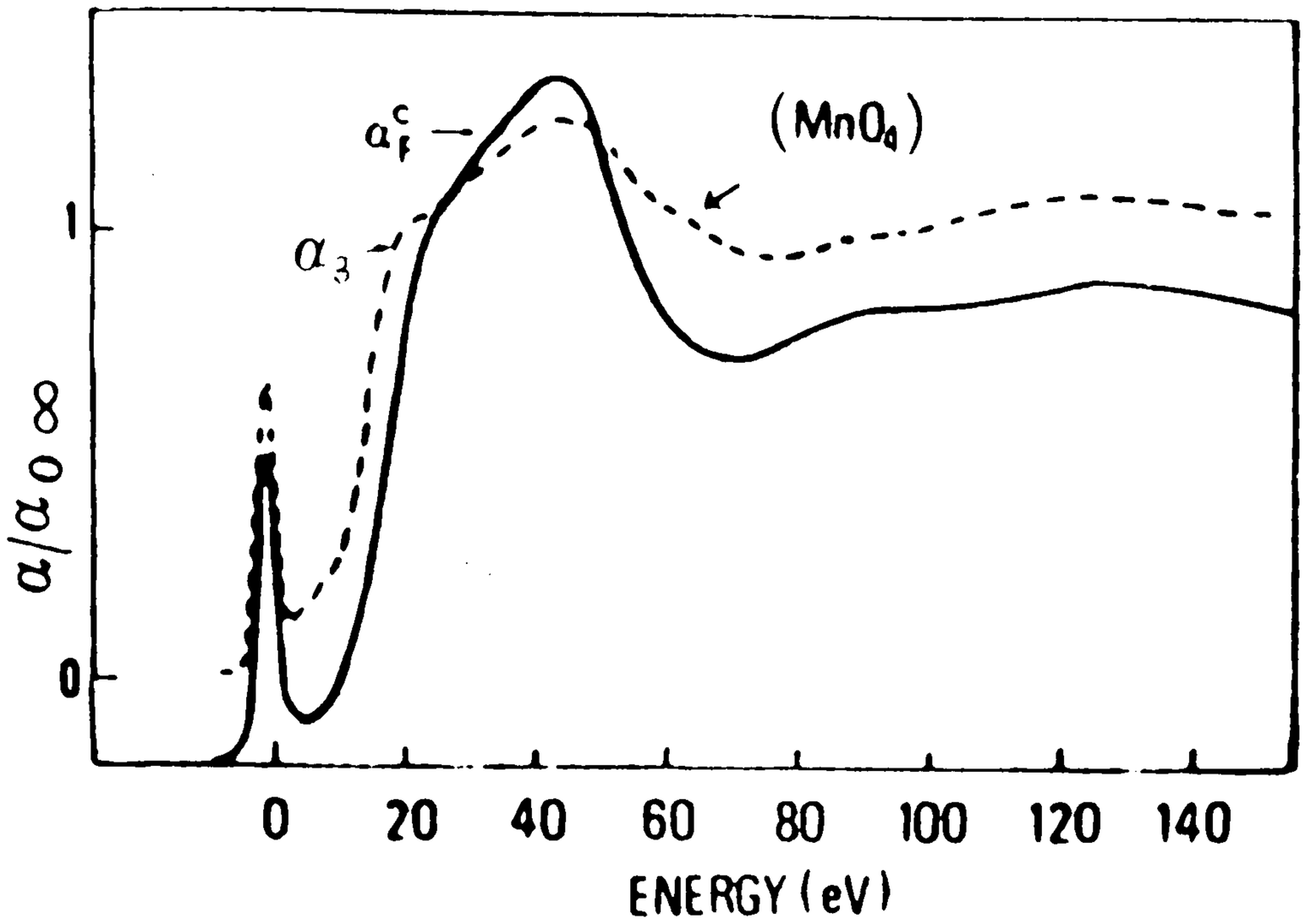

Fig. 1.2.12 Comparison between theoretical (solid line) and experimental spectra for the $(MnO_4)^-$ complex (Davoli & Paris, 1990).

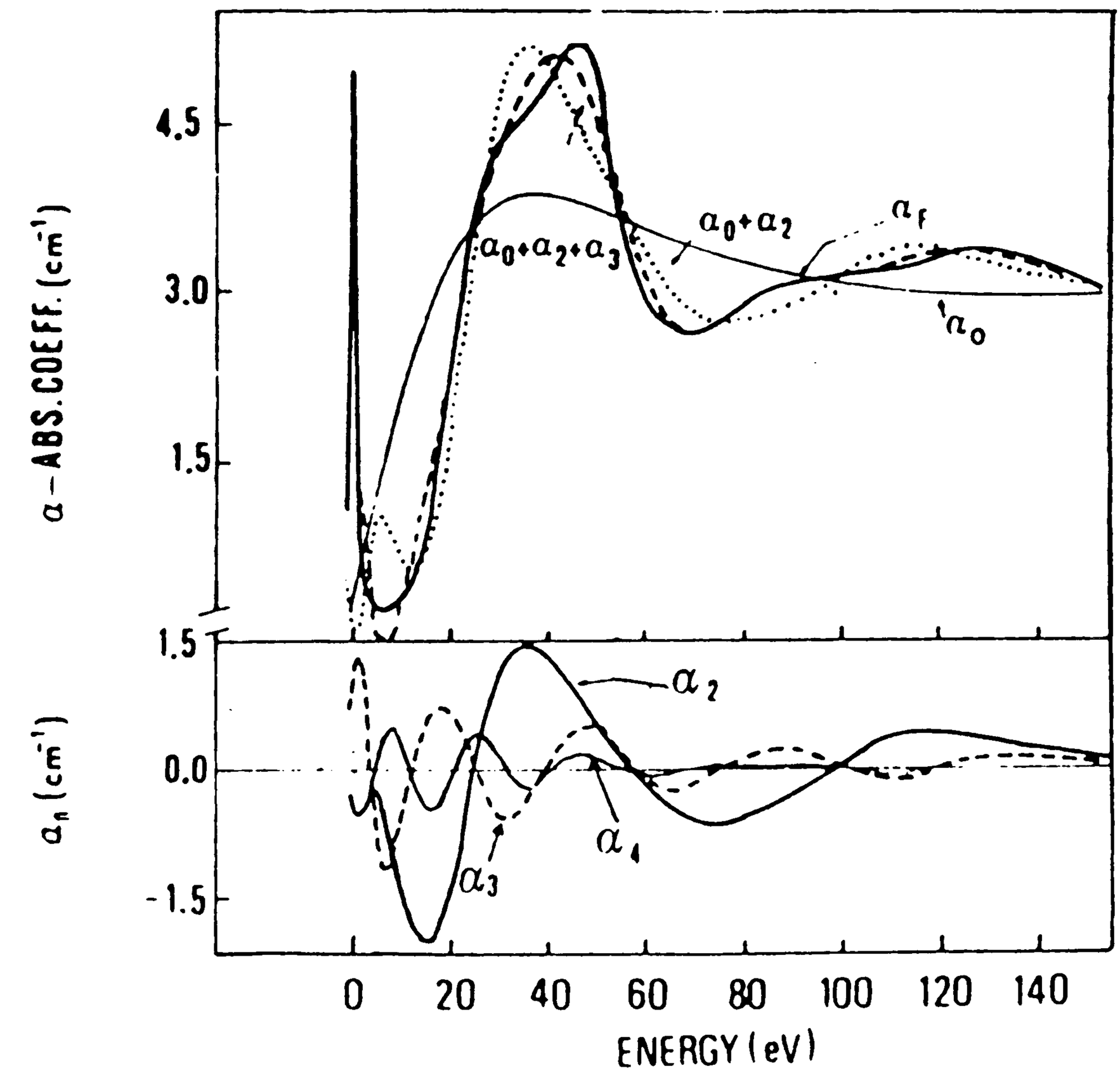

Fig. 1.2.1.13 Breakdown of the total theoretical cross-section of the $(MnO_4)^-$ complex in terms of partial contributions (Davoli & Paris, 1990).

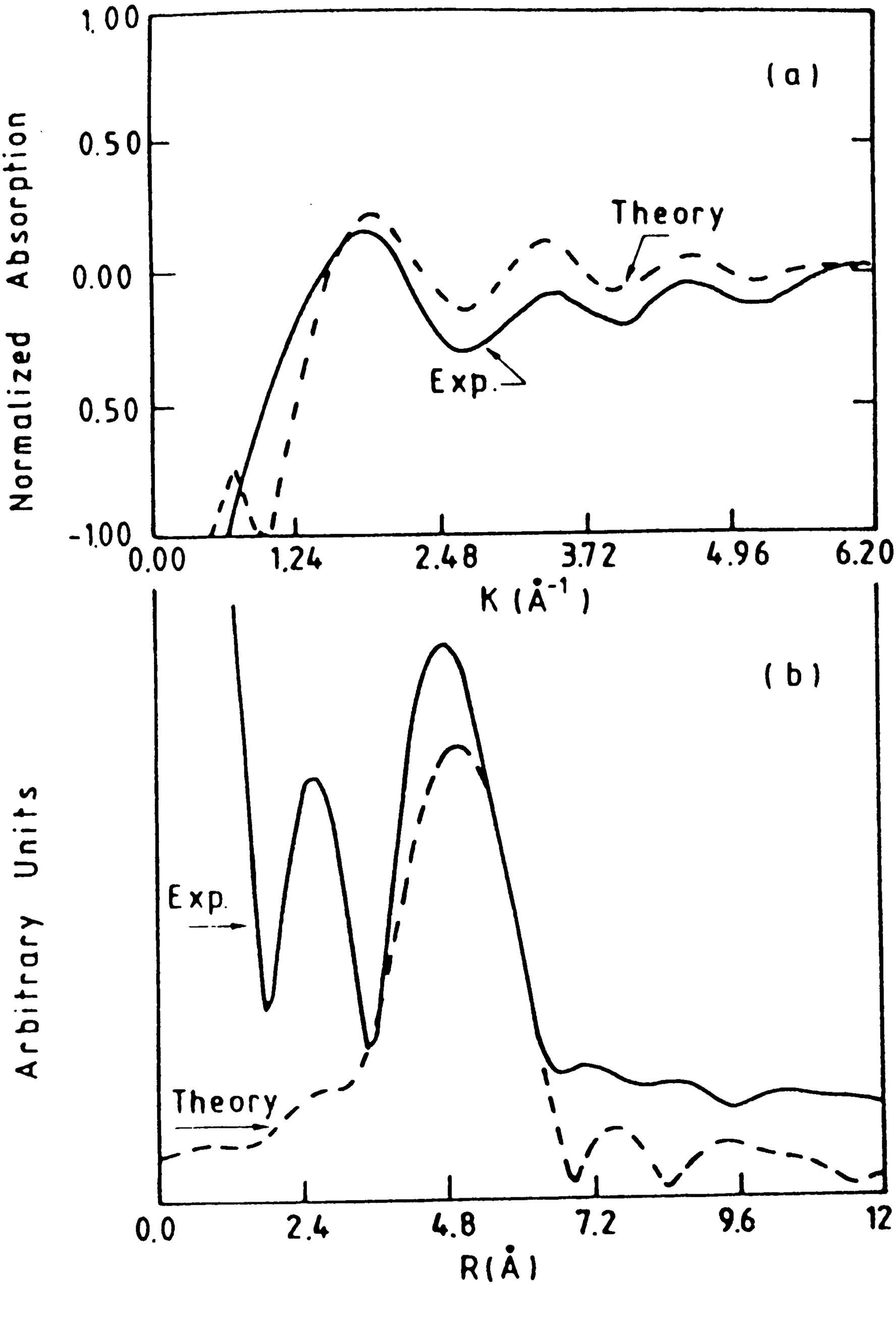

Fig. 1.2.1.14 Theoretical and experimental signals due to the triangular path Mn-O-O-Mn. In the bottom drawing the related Fourier transforms are shown (Davoli & Paris, 1990).

CHAPTER 2. STUDY OF SILICA GLASS BY XANES

2.1 STRUCTURE OF DENSIFIED VITREOUS SILICA BY SILICON AND OXYGEN XANES SPECTRA AND MULTIPLE SCATTERING CALCULATIONS.

2.1.1 Abstract

The decrease of the mean Si-O-Si angle in vitreous silica upon densification from 2.20 to 2.36 g cm^{-3} has been followed by oxygen and silicon K-edge XANES spectroscopy. Multiple scattering calculations using clusters of two shells around the oxygen and silicon atoms are in good agreement with experimental absorption spectra and confirm mean Si-O-Si between 130 and 144° for these samples, and a decrease of the mean angle with densification. The experimental spectra also exhibit features due to scattering at outer (>2) shells around the photoabsorbers.

2.1.2 Introduction

Vitreous SiO_2 may be considered the simplest model substance for a multicomponent oxide glass. Its behaviour as a function of pressure and temperature may therefore shed some light on structural variations in other highly polymerized but chemically more complex silicate glasses and melts such as acidic magmas. Furthermore, a full comprehension of the properties of vitreous SiO_2 and their structural causes is essential for its use in industrial and technological application.

Vitreous silica exhibits a three-dimensional network structure of corner-sharing SiO_4 tetrahedra (Si-O distance *ca.* 1.61 Å) forming mostly six-membered rings (Kubicki and Lasaga, 1988). The structural disorder is thought to be mostly caused by variations of the Si-O-Si angle and only to a minor extent by the presence of smaller or larger numbers of tetrahedra per ring. The Si-O-Si angle distribution is therefore of prime importance for characterization of the structural state of vitreous SiO_2.

Bell and Dean (1972) calculated, from random network theory, a mean Si-O-Si angle of 153°. This calculation, supported by the experimental work of Da Silva et al., (1974), was subsequently modified by Gaskell and Tarrant 1974), who found an angle distribution centered at 144° with a standard deviation of 8.5° in agreement with results by Mozzi and Warren (1969). In contrast, Raman and infrared spectroscopic studies (Seifert et al., 1982, 1983; Velde and Couty, 1987) indicate the presence of rings of tetrahedra (possibly with different numbers of tetrahedra or differing in the degree of puckering) each having a distribution of Si-O-Si angles but different mean values. This observation might also explain the asymmetry in the Si-O-Si angle distribution postulated by the work of Gaskell and Tarrant (1980), Mitra (1982) and Kubicki and Lasaga (1988).

Vitreous SiO_2 can be recovered in a partially unrelaxed (densified) state after compression at elevated temperatures and pressures (Höfler and Seifert, 1984); i.e., it does not return to its normal 1 bar, room temperature density of about 2.20 g cm^{-3}, but retains densities up to about 2.6 g cm^{-3}, depending on the P-T conditions of treatment. Therefore, the effect of densification upon the structure of vitreous silica can be conveniently determined at ambient conditions. In the low pressure range, the compression mechanism cannot be due to a variation of the stiff Si-O mean bond distance but must be assigned to changes in the Si-O-Si bridging angle or the number of tetrahedra per ring, or a combination thereof. Raman spectroscopic studies (Seifert et al., 1983; McMillan et al., 1984), molecular dynamics calculations (Kubicki and Lasaga, 1988) and LCAO calculations (Murray and Ching, 1989) support this view of a decrease of the mean Si-O-Si angle with compaction.

X-ray absorption near edge structure (XANES) is a sensitive and selective tool for studying local environments of atoms and could, therefore, contribute to a characterization of the compaction mechanism of vitreous SiO_2, in particular when also modelled by multiple scattering calculations. In a preliminary work (Marcelli et al., 1985) it was shown that the XANES at the oxygen K-edge is sensitive to the variation of the oxygen bridging angle, but the limited number of atoms used in these calculations and the consequent misfit between theory and experiment did not allow further conclusions.

Here I present the analysis of the experimental XANES spectra at both the silicon and oxygen K-edges and compare them to theoretical results for different geometries obtained by changing the Si-O-Si angle. The clusters used here have been extended to two shells around each photoabsorber, resulting in better correspondence between calculated and experimental spectra than observed by Marcelli et al. (1985).

2.1.3 Experimental

Type II vitreous silica (<200ppm H_2O) was permanently densified at a range of pressures at 1173 K for 10 min in sealed silver capsules in a piston-cylinder press and quenched under pressure. Pressures of 5, 10, 15 and 20 kbars resulted in 1 bar-densities of 2.23, 2.24, 2.31 and 2.36 gcm^{-3}, respectively. The same starting material, annealed at 1025 K, 1atm has a density of 2.20 gcm^{-3}, and this material was used as a reference sample; the densest sample studied here thus correspond to 7% densification.

The X-ray measurements have been performed at the Synchrotron Radiation Facility of Frascati (Italy) and at LURE-Orsay (France). Both facilities provide radiation in the soft X-ray energy range. At Frascati, the so-called grasshopper (Chiaradia et al., 1986) beam line has been used to study the oxygen K-edge between 520 and 570 eV (resolution 2.2 eV) whereas the transmission EXAFS beam line equipped with a double-crystal InSb monochromator served for the study of the Si K-edge in the energy range 1830–1870 eV, with energy resolution about 0.5 eV. Absorbance has been calculated

from the ratio of intensities in ionization chambers placed in the incident and transmitted beam, respectively. At LURE, the soft X-ray beam line equipped with an InSb monochromator served for recording Si K-edge spectra in the range 1830 to 2000 eV. The detection technique was partial electron yield, and a freshly vapour-deposited copper film was used for the reference structureless total yield signal I_o. Particular attention has been paid to keep measurement conditions rigorously identical from one sample to the other. The energy range, the energy step size, the statistics and most important, the thickness of the samples (weighed and deposited on a Millipore membrane) are critical for observing the small differences in the spectra of different samples.

2.1.4 Theoretical considerations

All calculation reported here are based on the one-electron multiple scattering (MS) theory (Benfatto et al., 1986; Natoli and Benfatto, 1986; Benfatto and Natoli 1987). The Coulomb part of the potential is built up by superimposing neutral atom charge densities obtained from the Clementi and Roetti (1974) tables and by using the Z+1 approximation for the final state. For the exchange-correlation part of the potential, the ordinary X_α energy independent one is used and the muffin-tin radii are chosen according to the Norman (1974) criterion. A 10% overlap between contiguous spheres has been allowed to simulate atomic bonds. The clusters used are formed by two shells around the photoabsorber; i.e., they contain 9 atoms for both the oxygen and the Si edges, and the silicon-oxygen distance has been taken to be 1.61 Å in all calculations. For the case of an Si-O-Si angle of 144° the atomic coordinates have been taken from the crystallographic data of α-quartz (Levien et al., 1980).

In order to make the comparison of the calculated spectra with the experimental results, the calculations have been convoluted with a Lorentzian broadening function of an energy dependent width given by $\Gamma(E)=\Gamma_c+\Gamma_{exp}+\Gamma_x(E)$. The core hole width ($\Gamma_c$=0.15 and 0.46 eV for the oxygen and silicon K-edge, respectively) was taken from McGuire (1970). The quantity Γ_{exp} represents the experimental resolution for the two edges. The energy-dependent $\Gamma_x(E)$ is linked to the electron mean free path $\lambda_x(E)$ by the relation (Müller et al., 1982)

$$\Gamma_x(E) = 2h\left(\frac{2E}{m}\right)^{\frac{1}{2}} \lambda_x^{-1}(E) \qquad [2.1]$$

where the electron mean free path is given by the following universal relation

$$\lambda_x(E) = 0.54\, E^{0.5} + \frac{1430}{E^2} \qquad [2.2]$$

which is the best fit of several experimental results. In the above expression E is in eV and the mean free path is in Å.

2.1.5 Results and discussion

To overcome the limitation of the previous analysis (Marcelli et al., 1985) and to complete the XANES study of this set of densified vitreous silica samples the experimental XANES data at both the oxygen and silicon K-edges are reported together with a new set of calculations for both edges based on a geometrical cluster formed by nine atoms around each photoabsorber.

For the analysis of the oxygen K-edge, the calculated XANES is compared to the experimental spectra of the starting material and the most densified sample in Fig. 2.1.1. The theoretical curve is the weighted average of different curves, each of them obtained using a cluster geometry with different Si-O-Si angles (θ = 130.5, 144, 160 and 174° weighted according to the angle distribution given by Gaskell and Tarrant (1980) and Dupree and Pettifer (1984)). This procedure is justified because disorder in vitreous SiO_2 is essentially caused by variations in the Si-O-Si angle. The basic assumptions in this calculation are that the width of the angle distribution remains constant and that no significant amounts of penta-coordinated Si are formed (Stebbins, 1991) in this pressure range in pure SiO_2. The two experimental curves, on the other hand, are quite similar to each other except for a small but significant and reproducible red shift of about 0.7 eV of peak C in the densified sample. They also closely match the theoretical curve, but peak B is slightly stronger than in the calculated curve.

For a better understanding of the origin of the various peaks in the XANES spectra a set of four theoretical curves is reported in Fig. 2.1.2. They are obtained by changing the Si-O-Si angle in the geometrical cluster, but contrary to the theoretical spectrum in Fig. 2.1.2, the convolution has been omitted for clarity. The presence of peak B is now obvious; it changes neither in intensity nor energy with a variation in the Si-O-Si angle. However, its intensity is not enough to reproduce, after convolution, the experimental data. This suggests that there are additional contributions present coming from further shells, although these are strongly quenched by structural and thermal disorder. This would be expected because upon increase of the photon energy of the incoming beam the mean free path value of the electron escaping from the absorber atom will rapidly decrease. In fact, this value is quite high at the energy position of peak B and reaches a minimum, at about 4.5 Å, at the energy position of peak C. Finally, Fig. 2.1.2 demonstrates that the main effect of a decreasing Si-O-Si angle is a shift of peak C towards lower energies. The total shift amounts to only 2.8 eV and, as shown on the inset, is most pronounced in the angle range 144 to 160°. Unfortunately, the position of peak C is not a sensitive, quantitative measure of the mean Si-O-Si angle mostly because of the structure in the convoluted theoretical spectra and the experimentally observed spectra, but to some extent also due to the poor signal-to-noise ratio.

Calculated and measured silicon K-edge spectra for three samples densified at different pressures are shown in Fig. 2.1.3. The curves are very similar but they do

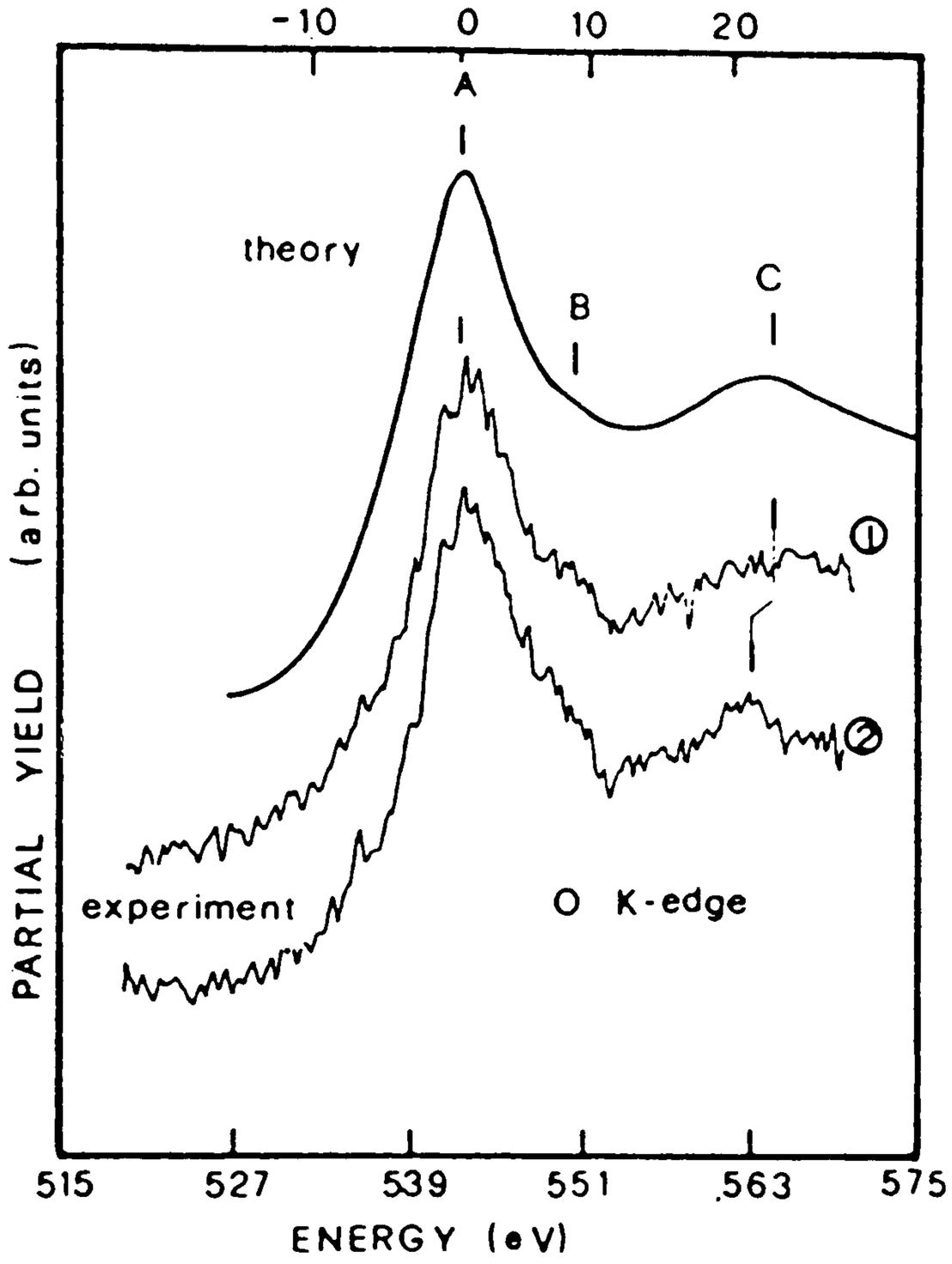

Fig. 2.1.1 Comparison between theoretical and experimental XANES data related to the O K-edge. The experimental curve 1 is that of the undensified starting material, whereas curve 2 refers to the sample having a density of 2.36 gcm^{-3}. All curves have been aligned to peak A.

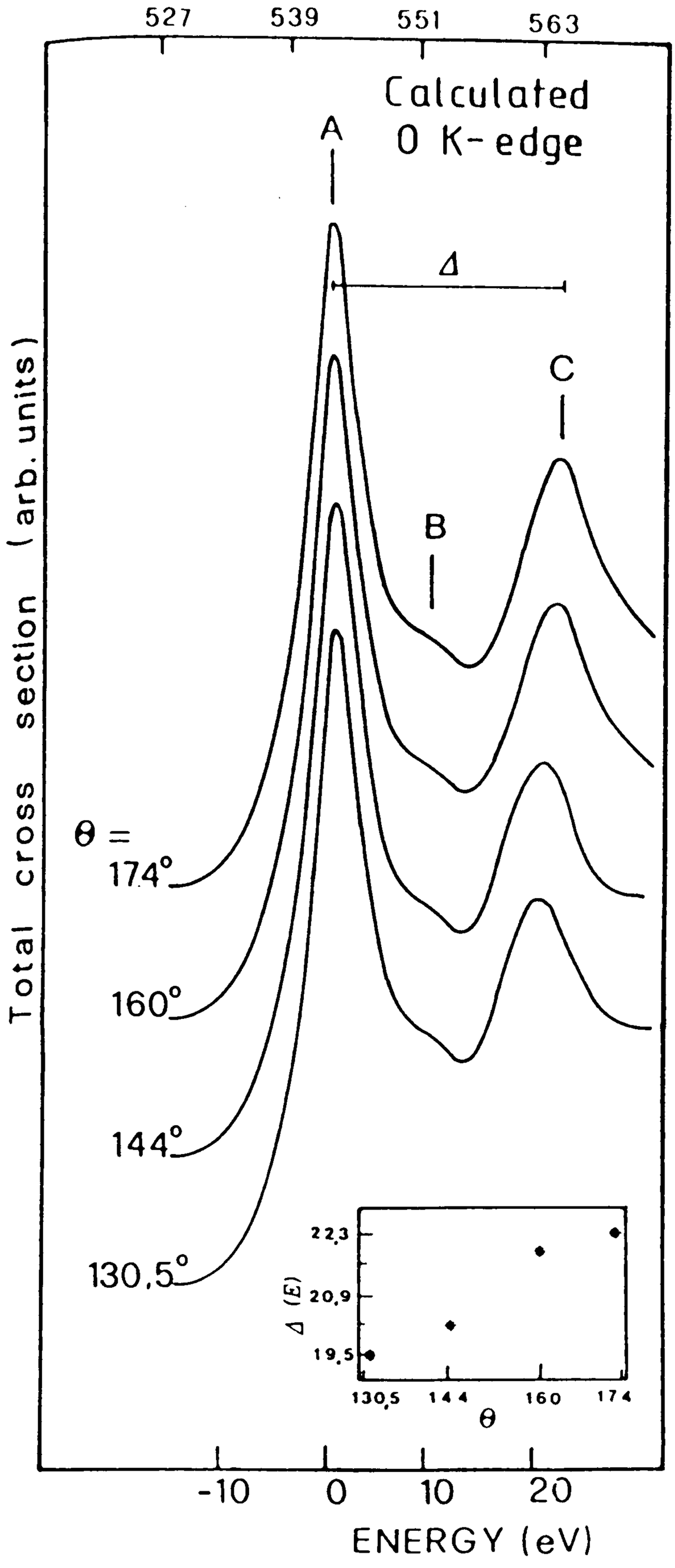

Fig. 2.1.2 A set of theoretical absoption curves at the O K-edge obtained for different values of the Si-O-Si angle theta. The inset shows the energy separation between peaks A and C. The energy scale is relative to the position of peak A.

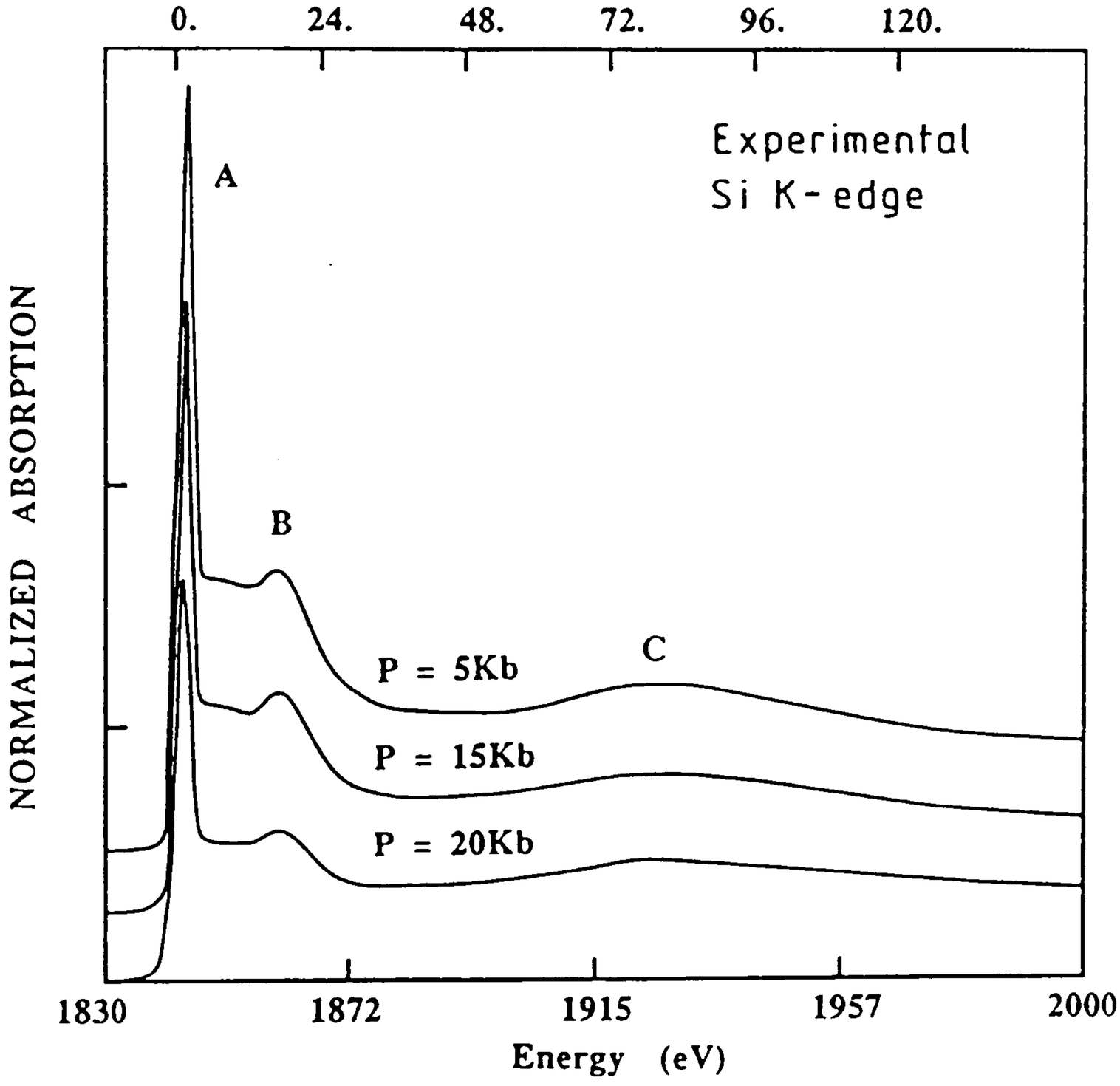

Fig. 2.1.3 Comparison between experimental data at the Si K-edge of three different vitreous SiO_2 samples compacted at the pressures indicated in the text. A, B and C indicate the main features of the spectra.

show small differences in the region labelled *b*. Very high resolution measurements in this critical energy range for a set of five variably densified samples are shown in Fig. 2.1.4. A small modification in the peak position, just above the noise level, is evident, with the peak moving towards higher energy with increasing densification. Moreover, the intensity of the main peak A, calculated with respect to the foot point labelled *a* in Fig. 2.1.4, decreases with synthesis pressure by more than 15%. The intensity ratio I_A/I_a changes from 2.10 to 1.73 from 1 bar to 20 kbars synthesis pressure. This effect, which is also observable in the spectra reported in Fig. 2.1.3 is probably due to the increasing *p* character of the electronic states in the continuum.

Calculated spectra for the silicon K edge, produced from a geometrical cluster with different Si-O-Si angles, are shown in Fig. 2.1.5. Going from larger to smaller Si-O-Si angles the peak B grows and, at the same time, the peak C disappear. The weak structure labelled *b* in the experimental spectra is not reproduced by the calculations. This is not surprising because, as mentioned before in the discussion of the oxygen K-edge spectra, this structure lies in the energy region where contributions from atoms farther out than the second shell are important; such features could not be considered in a sphere of 5 Å radius as used in the calculations. The nature of the b structure can be explained by considering the spectrum of crystalline SiO_2 (A.M. Flanck, P. Lagarde, private communication) which also exhibits several peaks in the same energy region. In spite of the crystallinity of their sample, the intensity of these structures is very weak, in accordance with peak *b* in the glass spectra.

2.1.6 Conclusions

In conclusion, the oxygen and silicon K edges have two features in common:
(1) the glass model used for the calculations of the theoretical XANES spectra of SiO_2 reproduces the experimental data very well. The calculations demonstrate that the best agreement is achieved for mean Si-O-Si angle between 130.5 and 144°, in agreement with the work by Gaskell and Tarrant (1980) and Kubicki and Lasaga (1988);
(2) the modification of the Si-O-Si angle induced by the densification is evident from both edges, but the small degree of densification (about 7%) produces only minor changes in the spectra and a minor decrease of the Si-O-Si angle. This is consistent with the notion by Seifert et al., (1983) who estimate, from Raman spectroscopic studies, that the average Si-O-Si angle decreases by only a few degrees in this range of densities, as well as the same conclusion obtained by molecular dynamics calculations by Kubicki and Lasaga (1988). Furthermore, changes in Si-O-Si angle in quartz in this pressure range are of the same order of magnitude (Jorgensen, 1978); Ogata et al., 1987);
(3) the effects of scattering from shells farther out than the second shell are seen in both edges.

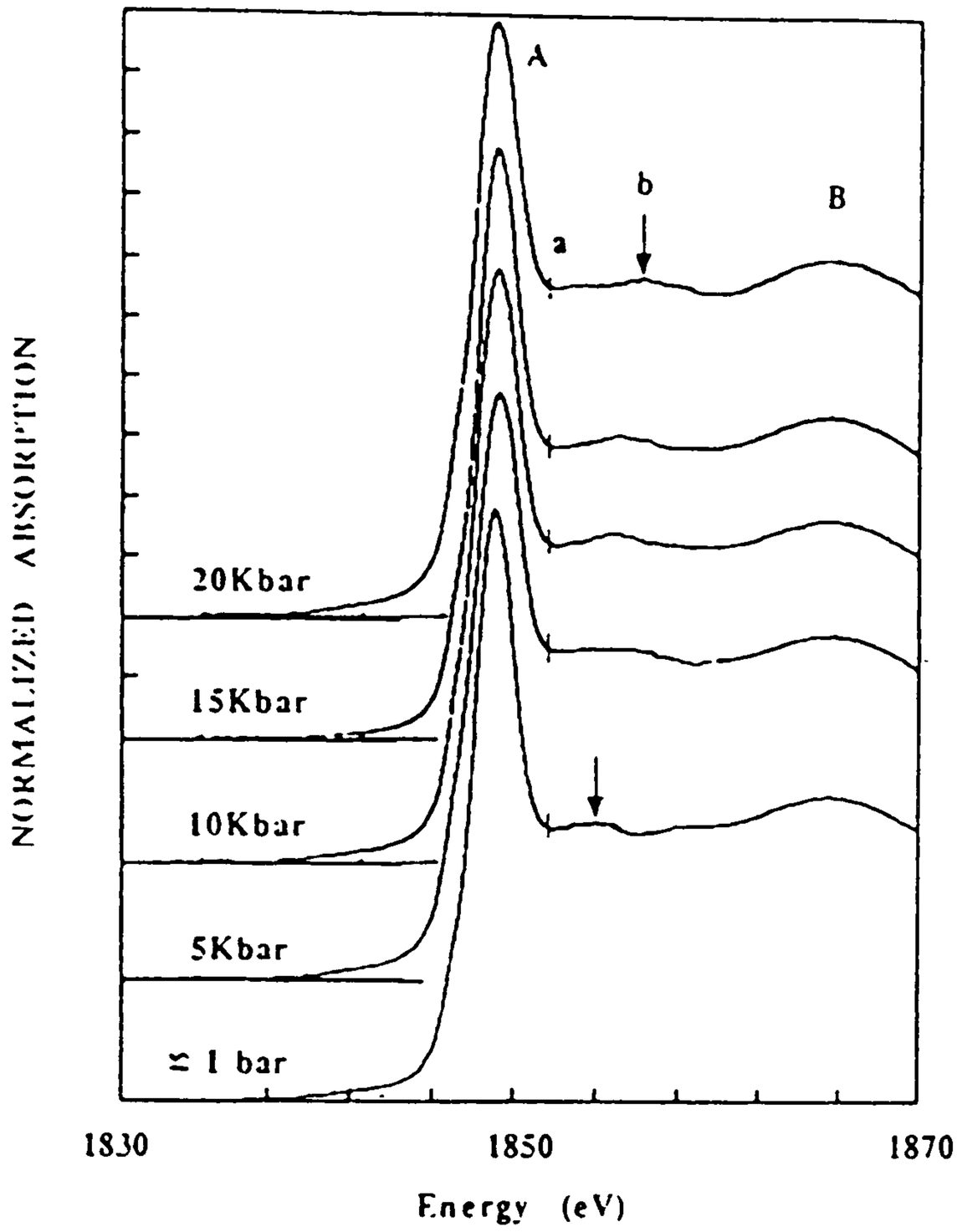

Fig. 2.1.4 Comparison between experimental data at the Si K-edge for five vitreous SiO_2 samples with different degree of densification (indicated by the synthesis pressures). The lowermost curve refers to the starting material. All the spectra have been collected with very high energy resulution of 0.2 eV. The arrows indicate the only feature that exhibits a shift with density.

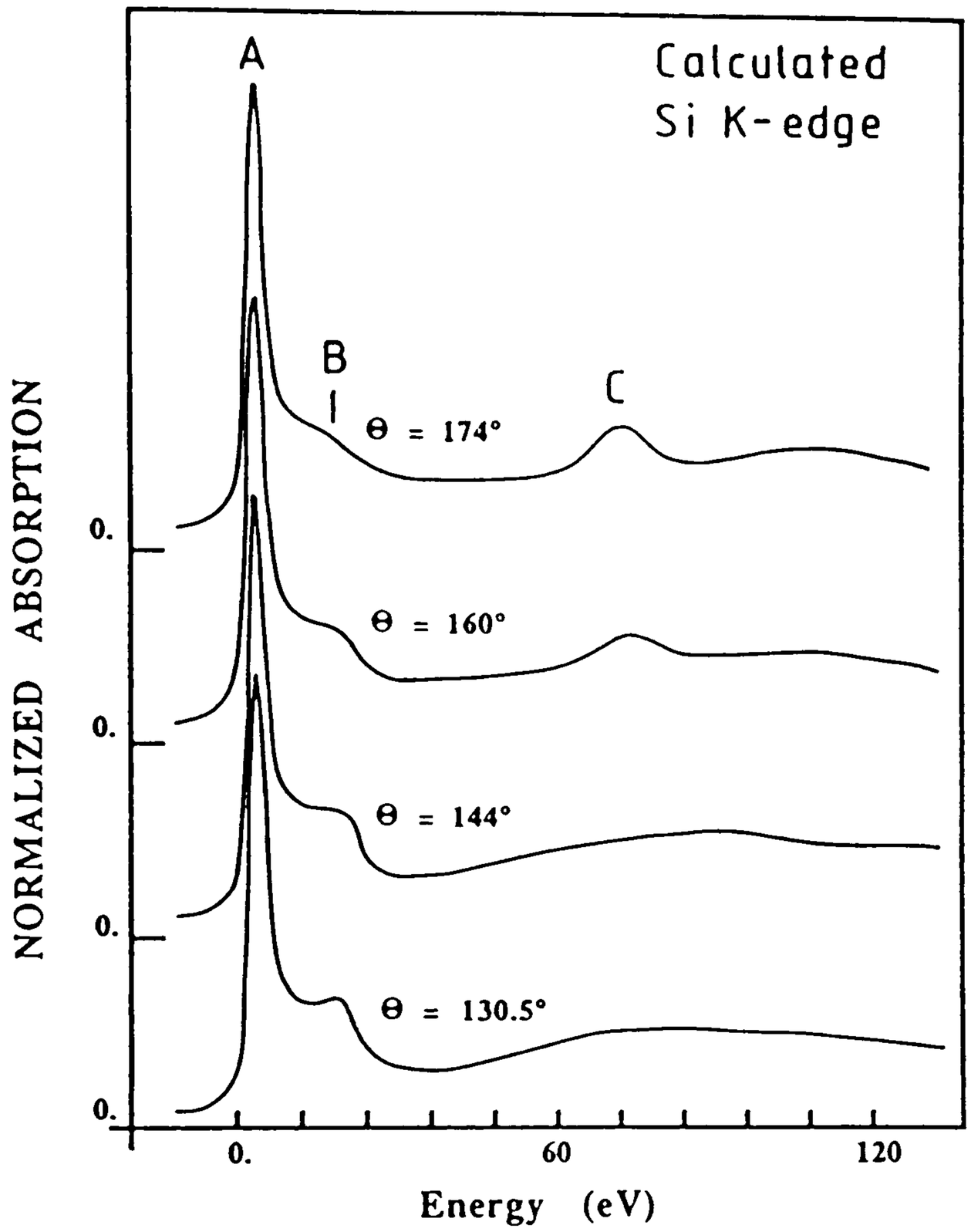

Fig. 2.1.5 A set of theoretical absorption curves at the Si K-edge obtained for different values of the Si-O-Si angle theta. The energy scale is relative to the position of peak A.

CHAPTER 3. TITANIUM IN MINERALS AND GLASSES

3.1 TITANIUM VALENCE AND COORDINATION IN SYNTHETIC RICHTERITE – Ti-RICHTERITE AMPHIBOLES.

3.1.1 Abstract

Synthetic amphiboles of the richterite–Ti-richterite series have been examined by synchrotron X-ray absorption spectroscopy to determine the oxidation state and coordination of Ti in their structure. The Ti K-edge in the amphibolites is displaced to energy values higher than that of Ti metal (4966.0 eV) and consists of several components. In addition, the spectra begin with a single and strong pre-edge feature characteristic of Ti^{4+} in tetrahedral coordination. The different components of the edge are constant in position throughout the series, but vary in shape and intensity. Multiple and single scattering features suggest that Ti^{4+} in these synthetic amphiboles resides in a single tetrahedral site having <Ti-O>= 1.84 Å, probably T(2).

3.1.2 Introduction

The mode of incorporation and the valence of titanium in silicates have been matters of debate for some time. Titanium in terrestrial minerals is normally tetravalent and predominantly in octahedral coordination (Hartman, 1969; Hawthorne, 1981). However, Czamanske & Atkin (1985) and Wagner & Velde (1986) have reported microprobe evidence suggesting that significant Ti may enter the tetrahedral (T) sites of alkali and alkali-calcic amphiboles to compensate for deficiency in the usual four-fold coordinated cations (Si^{4+}, Al^{3+} and Fe^{3+}).

The mechanism by which Ti can enter the T sites of amphiboles are several, but the most straightforward is direct isovalent substitution of Ti^{4+} for Si^{4+}. In order to test the feasibility of this mechanism, Della Ventura & Robert (1988) synthetized amphiboles along the K-richterite -Ti-K-richterite series and obtained single phases up to about 70 mol% Ti-K-richterite end-member. This result indicates that Ti can enter the amphibole structure in amounts not yet documented in nature. On the basis of stoichiometry, unit-cell variation and spectroscopic evidence (FTIR and Raman), Della Ventura et al. (1991) concluded that the Ti in their synthetic K-richterites is present as Ti^{4+} in tetrahedral coordination. Additional support for their conclusions was provided by preliminary X-ray absorption spectroscopic studies (Mottana et al., 1990; Paris et al., 1990). The structure of several natural titanian richterites have been also solved by single-crystal X-ray diffraction methods (Oberti et al., 1992). In these studies, Ti was found to be present in both four-fold and the more common six-fold coordination. Here I present new X-ray absorption spectroscopy (XAS) results for Ti in the K-richterite - Ti-K-richterite

amphiboles synthetized by Della Ventura & Robert (1988). XAS can give direct information on Ti valence, coordination, and Ti-O distances. Such information can be used to constrain the crystal-chemical role of Ti in the amphibole structure. Near-edge structure spectroscopy (XANES) gives indication on the immediate environment of the absorbing atom, and is particularly suited to discriminate among different oxidation states of transition elements (Bianconi, 1988; Bianconi et al., 1988; Brown et al. 1988; Davoli & Paris, 1990). Extended X-ray absorption fine structure spectroscopy (EXAFS), on the other hand, provides information on average distances between the absorbing atom and its nearest neighbours, as well as the extent of long-range order interactions (Wong, 1986; Waychunas et al., 1986; Calas et al., 1987; Brown et al., 1988).

Spectroscopic techniques are needed because the synthetic amphiboles are too fine-grained to allow structural examination by single-crystal X-ray diffraction. Moreover, the amount of Ti (from 1.84 to ~4 wt% Ti metal) is dilute in these complex structure, and only the use of a high energy, high flux X-ray source such as provided by synchrotron light provides a sufficiently sensitive means to examine the Ti environment.

3.1.3 Materials

Syntheses were done at $P(H_2O)$=0.1 GPa and 800°C using conventional hydrothermal techniques and Morey-type hot-seal externally-heated vessels. Oxidation state conditions were near the Ni-NiO buffer (NNO) and thus all all Ti should be in the 4+ valence state (Della Ventura & Robert, 1988). Six nominal compositions, covering the entire range from end-member potassium-richterite, $KNaCaMg_5[(OH)_2Si_8O_{22}]$ (RI), to end-member potassium-titanium-richterite, $KNaCaMg_5[(OH)_2TiSi_7O_{22}]$ (TiRI), at 20 mol% intervals were run simultaneously (Della Ventura & Robert, 1988).

The material here examined ranges in composition from $RI_{80}TiRI_{20}$ to Ri_0TiRI_{100}. However, only samples containing 20, 40 and 60 mol% TiRI are homogeneous amphiboles (Della Ventura et al., 1991). Samples $RI_{20}TiRI_{80}$ and RI_0TiRI_{100}, the nominal potassium-titanium-richterite end-member, contain minor impurities. Among these, I identified (by X-ray powder diffraction) priderite (Dubeau & Edgar, 1985), inferred to be $K_2MgTi_7O_{16}$ on the basis of the starting composition and of SEM-EDAX analyses. In the RI_0TiRI_{100} sample, SEM showed three grains of titanite [$CaTiSiO_5$]. All run products having nominal compositions exceeding $RI_{40}TiRI_{60}$ contain an amphibole with cell parameters which are slightly greater than those of the $RI_{40}TiRI_{60}$ homogeneous phase; these extrapolate to composition about $RI_{30}TiRI_{70}$, which is the substitutional limit at the P-T conditions of the syntheses (Della Ventura et al., 1991).

The TiO_2 used as reference materials are a certified 99.8% pure reagent in the rutile structure (Ventron, batch 88221), and an analytical reagent grade powder in the anatase structure (British Drug House Chemicals, cf. Howard et al., 1991).

3.1.4 Methods

X-ray absorption spectroscopy was done at Frascati National Laboratories (LNF) on the PULS line, which is derived from the ADONE synchrotron ring *via* a bending magnet. Set-ups and methods were described elsewhere (Davoli et al., 1988) and can be summarized as follows: Si (111) channel-cut monochromator, calibration against a certified standard Ti metal foil (EXAFS materials) taking the first inflection point as 4966.0 eV, transmission mode, gas detectors for both I_0 and I_1.

For XANES, the Ti K-edge was scanned at 0.2 eV steps over the range 4940-5050 eV, using 0.5 mm slits to give a resolution of 0.5-0.6 eV. Experimental data were background corrected using a polynomial function and intensities were normalized using the XANES high-energy side at 5027 eV (+60 eV; Bianconi, 1981). The energies of the observed features were determined from derivatives, and the intensities were determined as ratios of the normalized absorption values at the observed maxima to the 5027 eV value.

For EXAFS measurements the energy range 4860-5700 eV was scanned with steps of 3 and 1 eV, respectively before and after the edge, using 1.5 mm slits. Information from the EXAFS spectra was extracted by first subtracting the background, taking into account the absorption step and using a third-degree polynomial function. E_0 was taken at 4966.6 eV. The radial distribution function was calculated over the k range 2.5-11 $Å^{-1}$ where the effects are considered to be due only to EXAFS oscillations, using n=2 in the function $chi(k)K^n$ to give a larger weight to the high-k part of the spectrum, where signal decreases as a function of the back-scattering amplitude and of the thermal factor $e\ exp(-s^2k^2)$. A Hanning windowing function (Dk=0.2 $Å^{-1}$) has been used to avoid truncation effects at the transformation limits. The first shell in the radial distribution function corresponding to the Ti-O distance was then Fourier-transformed back into k space and fitted to the theoretical chi(k) calculated for a cluster composed of tetrahedrally-coordinated Ti and O. The *ab initio* calculation method of Mustre de Leon et al. (1991) has been used to obtain Ti-O and Ti-Ti phases and amplitude parameters. These have been preliminary used and tested on the standards, rutile and anatase. The results obtained show perfect agreement with the values obtained from XRD (Shintani et al., 1975; Howard et al., 1991), and this supports the validity of applying the same method to the unknown samples.

To overcome preferred orientation of the synthetic amphiboles crystals, several types of sample preparations were tried including a mixture of the sample with BN or a deposition of the material on a membrane. Batches of five interchanged samples (one of them being always the rutile standard) were run repeatedly to test for the accuracy of the results.

3.1.5 Results

The Ti K-edge measured in all the amphiboles is slightly shifted from the first inflection point of the K-edge of Ti metal at 4966.0 eV. The entire edge can be separated into three main regions, related to different physical effects: the pre-edge, the edge crest, and the above-crest region with the onset of EXAFS oscillation (Fig.3.1.1).

The pre-edge is usually considered to be related to dipole- forbidden 1s-3d bound-state transitions to unfilled levels having predominantly metal character (Balzarotti et al., 1980; Elmi et al., 1984; Dumas & Petiau, 1986; Waychunas, 1987; Waychunas & Brown, 1990), although other explanations have also been proposed (Grunes, 1983; Bianconi, 1988; Uozumi et al., 1992). In all these amphiboles, it consists of a single, sharp and intense feature (A) at 4969.8 $\pm$ 0.1 eV (Table 3.1.1; Fig.3.1.1). However, I do not rely so much on this absolute location because of the known difficulty in reproducing accurately the energy position of the channel-cut monochromator (cf. Waychunas & Rossman's, 1983, plea for a [4]Fe^{3+} spectroscopic standard). Of notice is that the pre-edges of rutile and anastase standards (Table 3.1.1; see also Fig.3.1.2) are triplets showing the same profiles and the same spacing between their peaks as those reported by Waychunas (1987, Table 2). There is a systematic displacement between his and this sets of data (+1.0 eV), but it may arise from the different fitting methods, and is well within the normal inter-laboratory error.

The pre-edges of all the amphibole spectra are unusually strong, particularly when compared with the three weak peaks occurring in the pre-edge regions of rutile and anastase. Pre-edge intensities increase slightly with increasing total Ti content of the samples, although they are not proportional to the nominal mol% TiRI of the solid solutions (Table 3.1.1).

The edge crest region is believed to reflect the multiple scatterings of the photoelectron emitted by the absorbing atom, thus giving information on the configuration of the polyhedron formed by the first nearest neighbours around the absorber (Kutzler et al., 1980; Bianconi, 1981, 1988; Waychunas et al., 1986; Davoli et al., 1987, 1988). In the amphiboles (Fig.3.1.1), it consists of three or more features, two of them on the steeply rising slope of the absorption edge, and the third being the edge crest. This shape is consistent with Waychunas' (1987) findings in a variety of minerals, but with several differences. The first feature (B) is a shallow shoulder the position of which shows up only when plotting the first derivative: in all these samples, it is at *ca.* 4976 eV, with *ca.* 0.3 intensity. The second feature (C) is a small peak at 4983.1 $\pm$ 0.2 eV on the rising slope of the edge. This peak always occurs at the same energy, but it becomes weaker and less well resolved in sample $RI_{80}TiRI_{20}$, and changes into a shoulder in the nominal RI_0TiRI_{100} composition. The edge crest (D) is at 4989.6$\pm$0.3 eV in homogeneous amphiboles, and at 4989.9 eV in the run products containing excess Ti-

Table 3.1.1 Characteristic features of Ti K XANES spectra of synthetic richterites and of standard rutile and anatase.

Nominal Composition	A		B	C		D		E	
	E(eV)	I	E(eV)	E(eV)	I	E(eV)	I	E(eV)	I
RI0TiRI100*	4969.9	0.67	4976	4983.3	1.06	4989.8	1.39	5003.4	1.45
RI20TiRI80+	4969.7	0.61	4976	4983.2	1.10	4989.9	1.45	5003.6	1.44
RI40TiRI60	4969.9	0.78	4976	4983.1	1.22	4989.9	1.64	5003.8	1.67
RI60TiRI40	4969.7	0.66	4976	4983.1	1.21	4989.5	1.56	5004.0	1.56
RI80TiRI20	4969.9	0.52	4976	4982.9	1.03	4989.2	1.39	5003.6	1.37
rutile@	4967.9	0.06	4980	4986.0	1.53	4990.6	1.56	5002.8	1.50
	4970.5	0.21							
	4973.4	0.19							
anatase#	4966.9	0.10	4977	4985.2	1.57	4993.6	1.38	5001.5	1.47
	4970.1	0.16				4998.3	1.45		
	4972.6	0.16							

* amphibole coexisting with priderite and titanite
+ amphibole coexisting with priderite
@ also a hump at 5019.3 eV with I 1.10
# also a hump at 5016.3 eV with I 0.98
NB. All features standardized for energy against the first inflection point of Ti metal foil at 4966.0 eV, with intensities normalized to 1 at 5027 eV.

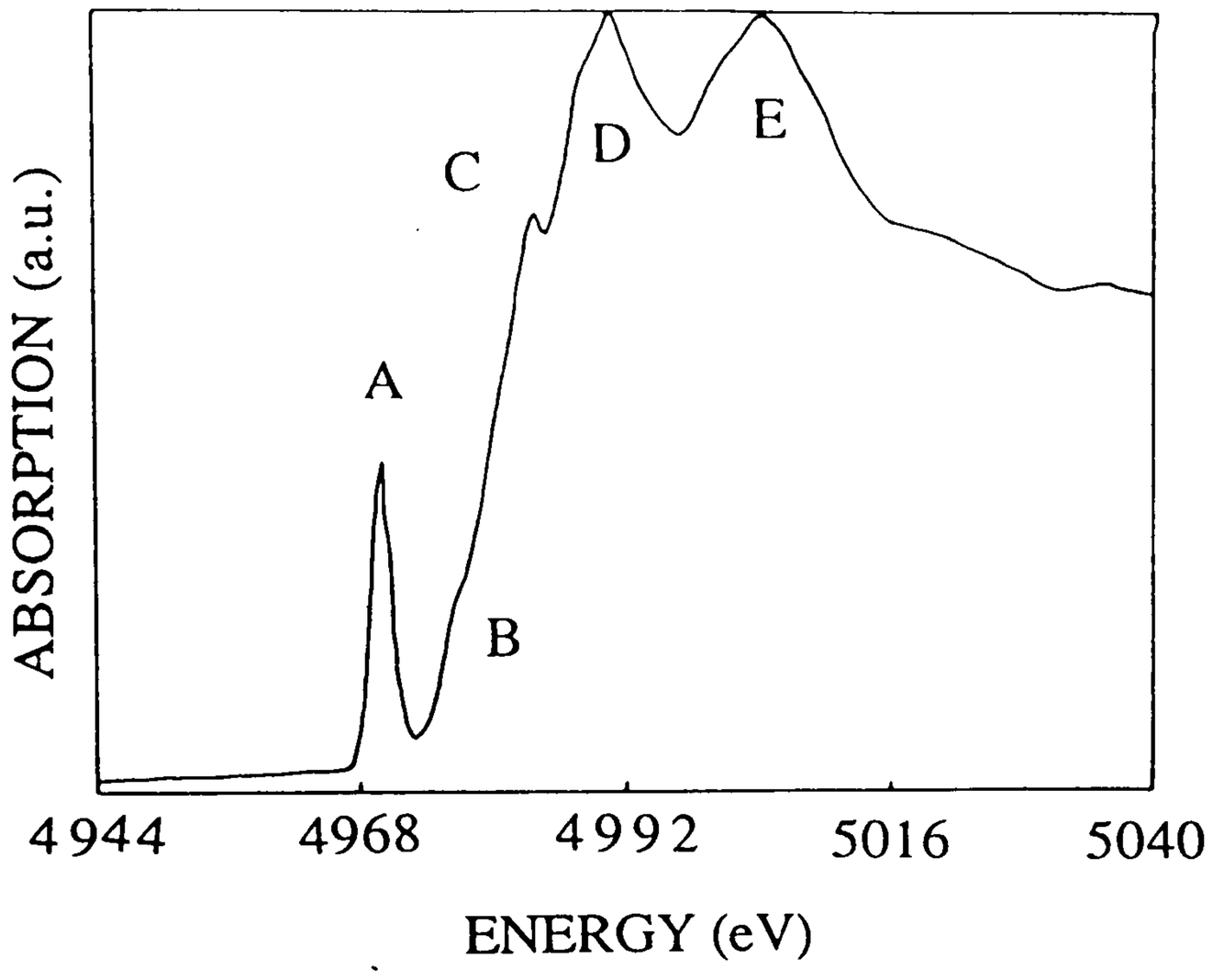

Fig. 3.1.1 XANES spectrum of Ti-richterite $RI_{40}TiRI_{60}$ taken at the Ti K-edge. The spectrum is normalized at the high energy side (5027 eV). The letters correspond to different parts of the spectrum (pre-edge, edge, above-edge regions).

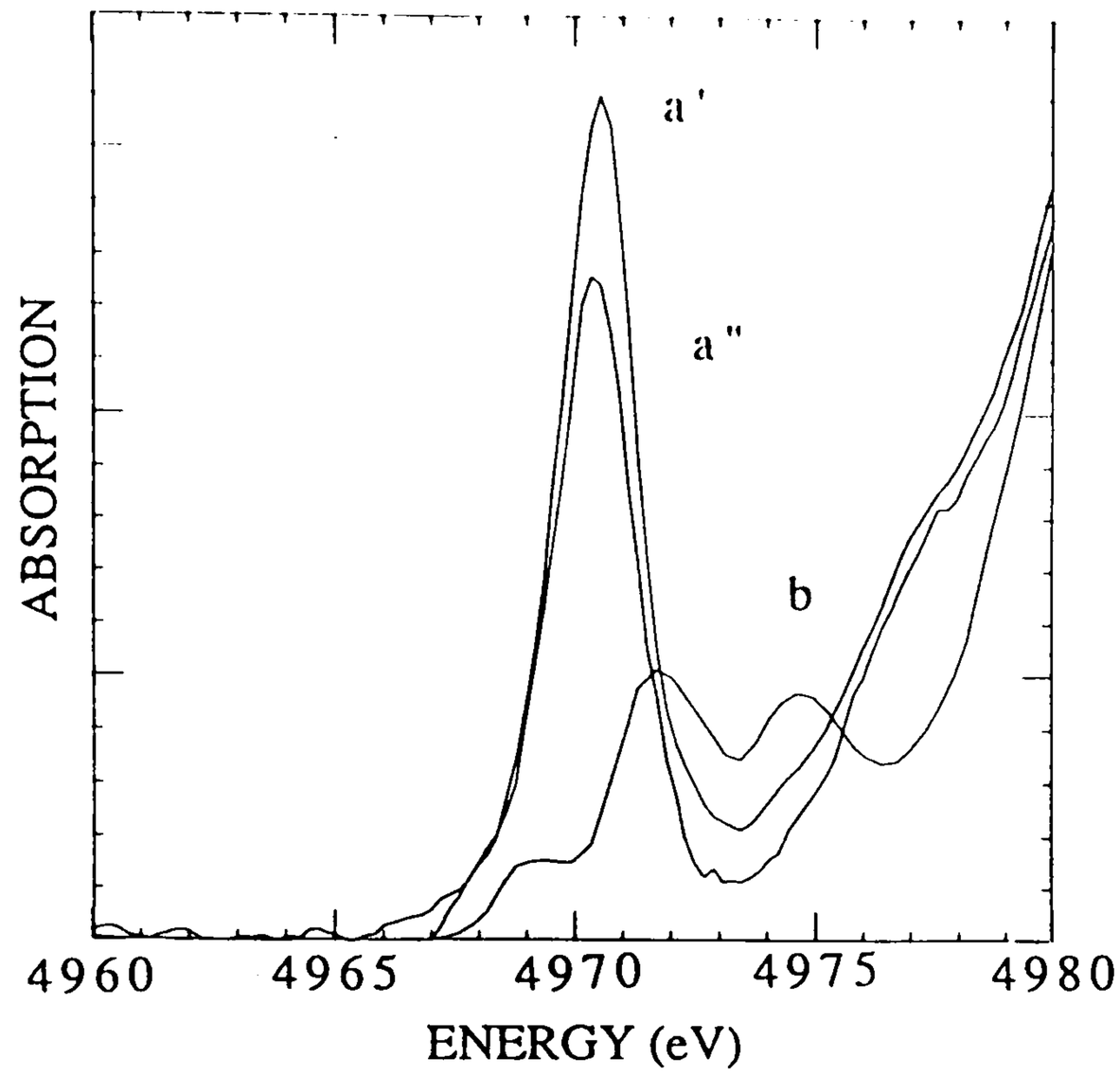

Fig. 3.1.2 The pre-edge region of single phase Ti-richterite $RI_{80}TiRI_{20}$ (a") and of nominal end-member RI_0TiRI_{100} (a') compared to that of TiO_2 (rutile) standard (b).

phases. The crest shifts slightly in energy (although by an amount that barely exceeds the resolution) and changes in intensity with composition (Table 3.1.1).

The region following the edge crest reflects transition from multiple scattering of a photoelectron displaced by the incident photon. In these samples it consist of a large, rounded and symmetric feature (E) at 5003.7 $\pm$ 0.3 eV (Table 3.1.1), and, possibly, a hump at *ca.* 5020 eV, which can be related to beginning EXAFS oscillations (see later). The intensity of E with respect to the edge crest, D, changes with composition: it is lower in $RI_{80}TiRI_{20}$, equal for $RI_{60}TiRI_{40}$, higher for $RI_{40}TiRI_{60}$, nearly the same for $RI_{20}TiRI_{80}$, and higher again for the nominal RI_0TiRI_{100} end-member (Table 3.1.1).

The Fourier transform (Fig.3.1.3) of the EXAFS oscillations of all amphiboles shows one predominant peak, followed by other progressively weaker peaks. We relate the first peak to the average distance from the absorber, titanium, to the backscattering first neighbour, oxygen; the second one to the interaction between Ti and second neighbours (Si, Ti), while the following peaks probably reflect more distant interactions, but cannot be assigned properly. For the first shell, the comparison between the theoretical chi(k) calculated for Ti-O and the back-transformed chi-functions from the experimental data is quite satisfactory (Fig.3.1.4), giving a Ti-O distance of 1.84 $\pm$ 0.02 Å. The Debye-Waller factor is 0.006 $Å^2$, a value that Brown et al. (1988, p.486, however referring to Fe) consider to be typical of a good order of the absorber in silicates and oxides.

Attemps to fit the second shell with either Ti-Ti and Ti-Si theoretical chi(k) and obtained good but not completely satisfactory agreements for both at *ca.* 3.07 Å distance. The best fit is obtained when combining both signals. Therefore the second peak of the radial distribution is probably due to contributions from more than one neighbour.

3.1.6 Discussion

Three types of information can be deduced from XAS study of crystalline and amorphous compounds: (1) valence of the element investigated; (2) coordination number; (3) average distance from the backscattering surrounding atoms.

For the first point, pre-edge location is considered to be indicative of the oxidation state of transitional elements. However, literature data on Ti are equivocal in this respect. Grunes (1983) claims a +6.8 to +9.8 eV shift in passing from Ti^0 (as in Ti metal) to Ti^{4+} (as in TiO_2). On the other hand, Waychunas (1987) indicates an average -2.0 eV shift from Ti^{4+} (rutile) to Ti^{3+} (Ti_2O_3, with the corundum structure), and supports his statement further by comparing the edge positions of several Ti^{4+}-bearing silicates to that of $NaTiSiO_6$, a synthetic pyroxene with octahedrally-coordinated Ti^{3+}.

The location of the amphibole pre-edge presented here is close to the values given for Ti^{4+} in other crystalline compounds. However, the negative displacement shown by the pre-edges of the amphiboles with respect to the middle peak of the rutile pre-edge is

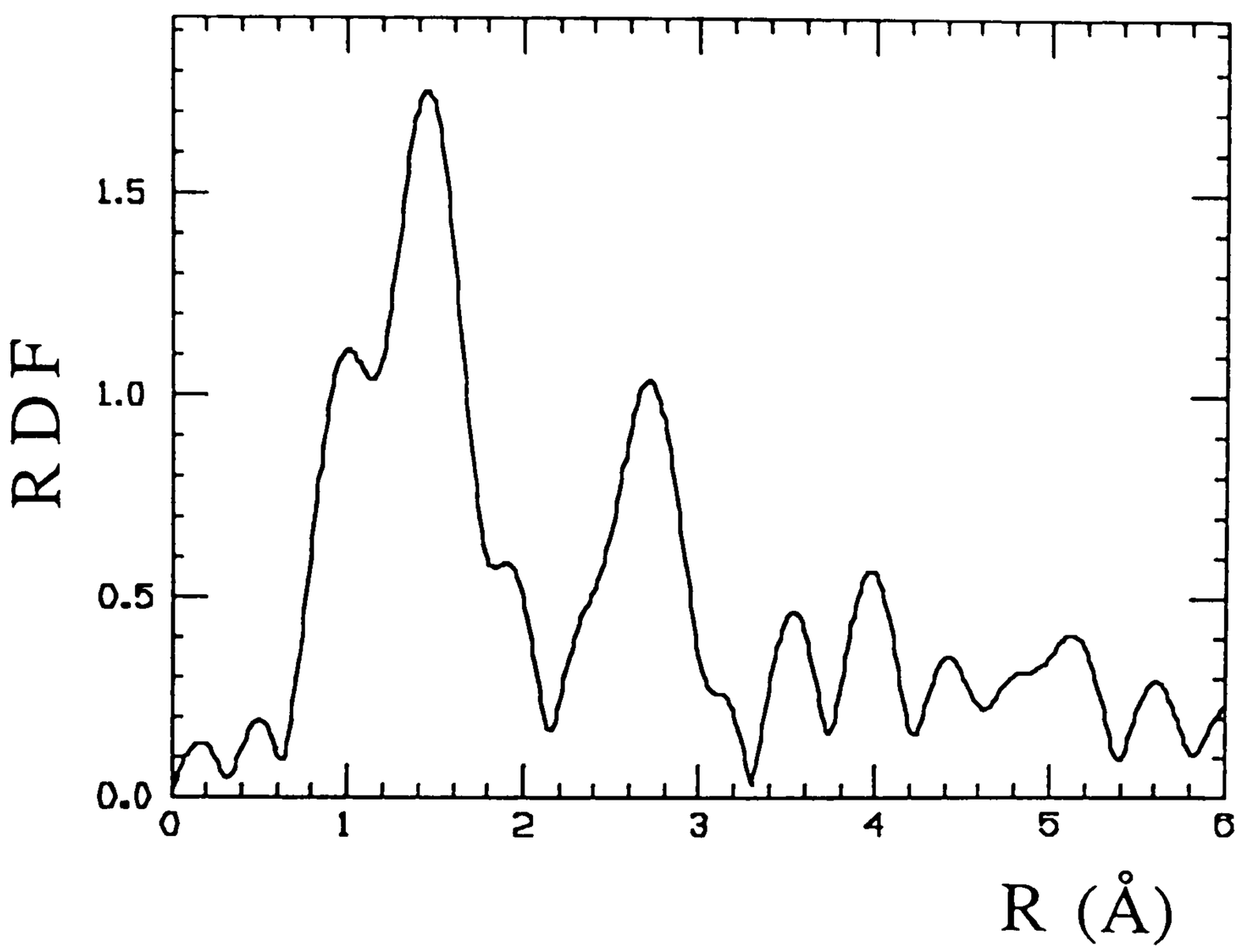

Fig. 3.1.3 Fourier transform of the EXAFS part of the Ti-richterite $RI_{80}TiRI_{20}$ spectrum. The first intense peak corresponds to the <Ti-O> distance; the second peak to more complex interactions with the second-shell neighbours. See text for discussion.

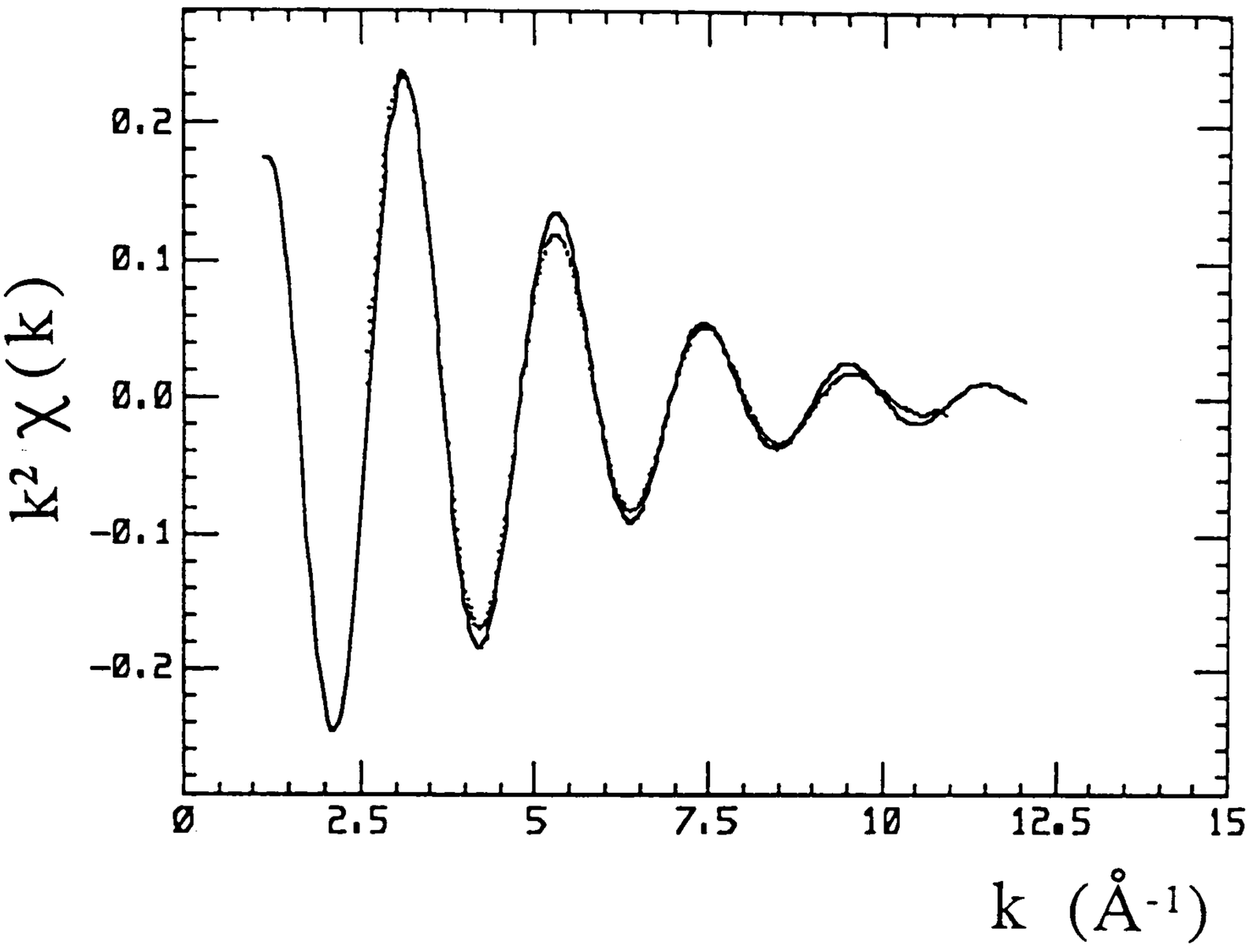

Fig. 3.1.4 Comparison between the theoretical $\chi(k)$ for a single Ti-O shell (C.N.=4, R=1.84 Å) and the signal obtained by Fourier filtering of the first coordination shell in sample $RI_{80}TiRI_{20}$.

almost half the displacement observed by Waychunas (1987) between TiO_2 and α-Ti_2O_3, which he interpreted as due to change in valence of Ti from 4+ to 3+. I do not disagree with Waychunas' (1987) general statement, but I do not believe that it applies to this case, in view of the oxidising conditions at which the syntheses were done. More significantly, the pre-edge value for barium orthotitanate, Ba_2TiO_4, a compound where Ti is rigorously four-valent, is the same as that for Ti_2O_3 (Waychunas, 1987). Thus, whereas a -2 eV shift may indicate Ti^{3+} in simple Ti-oxides, a negative shift does not necessarily correspond to Ti^{3+} in more complex structures such as Ti-bearing amphiboles and Ba_2TiO_4. An additional, non-sophisticated but nevertheless useful piece of evidence for estimating the valence of Ti is colour (Ihinger & Stolper, 1986): all these amphiboles are white, whereas synthetic $NaTi^{3+}Si_2O_6$ is dark emerald-green (Prewitt et al., 1972).

Regarding coordination, the single, sharp, intense pre-edge feature in the amphibole spectra is identical to that in Ba_2TiO_4, the only crystalline inorganic compound in which Ti^{4+} has been determined by single-crystal structure refinement to be in tetrahedral coordination (Bland, 1961). This strongly suggests that Ti^{4+} in richteritic amphiboles is in tetrahedral coordination (Mottana et al., 1990). Similar but slightly broader pre-edges occur in Ba_2TiO_4-TiO_2 mixtures (Maier & Frahm, 1989) and in synthetic solid solutions of TiO_2 containing high amounts of TaO_2 (Poumellec et al., 1986). Moreover they occur in the organic crystalline compound $Ti[N(CH_3)_2]_4$ (Yarker et al., 1986), and in several Ti-bearing glasses (Greegor et al., 1983, 1984; Elmi et al., 1984; Dumas & Petiau, 1986; Yarker et al., 1986; Calas et al., 1987; Maier & Frahm, 1989). They are in definitive contrast with the multiple pre-edges shown by all crystalline compounds in which Ti is in octahedral coordination, such as rutile, ilmenite, anatase, neptunite, titanite, schorlomite and many others (Greegor et al., 1984; Dumas & Petiau, 1986; Waychunas, 1986, 1987; cf. Table 3.1.1).

In general, a high intensity of the pre-edge such as that measured in these amphiboles is considered to be strongly indicative of a confined environment which, in the case of 3d transition elements, has always been related to their being in tetrahedral coordination (Bianconi et al., 1985; and, specifically for Ti: Dumas & Petiau, 1986; Yarker et al., 1986; Maier & Frahm, 1989; see Mottana et al., 1990). From the intensity of the pre-edge observed in their glasses, Dumas & Petiau (1986) even compute the amount of Ti in tetrahedral versus octahedral coordination.

On closer inspection, can be noted that, as long as X-ray diffraction indicates that the synthesis products are single-phase amphiboles, the pre-edges measured are sharp and single. However, in the definite three-phase assemblage produced from the nominal $TiRI_{100}$ composition, there is a slight asymmetry consistent with the position of the most intense peak of the triple pre-edge shown by the [6]-coordinated Ti of rutile and anastase.

In order to verify this, I compare in Fig. 3.1.2 the rutile pre-edge features with those of two of the run products. The pre-edge of the unquestionable single phase $RI_{80}TiRI_{20}$ amphibole is a single and sharp peak at 4969.8 eV. That of rutile consists of a triplet, as already reported: the three peaks are all weaker than the single peak of $RI_{80}TiRI20$, the middle one at 4970.5 eV being the strongest, the third one at 4973.4 eV being the second strongest, and the first one at 4967.9 eV being the weakest and broadest. Finally, the pre-edge of the nominal composition $TiRI_{100}$, which contains priderite and titanite plus an amphibole of composition about $RI_{30}TiRI_{70}$, consists of a strong sharp feature at 4969.9 eV, plus a weak shoulder at 4971 eV. From these observations, can be inferred that a small amount of Ti-bearing impurities is present and interferes with amphibole by exhibiting a pre-edge characteristic of Ti in octahedral coordination. SEM observations indicates *ca.* 3 vol% priderite to be present in this sample. Although the abundance is low, the high Ti content (56.50 wt%) contributes significantly to the spectra.

Additional information on coordination number, N, is usually extracted from the EXAFS spectrum. The fit of the experimental data leads to N = 3.5; this is slightly lower than expected, but certainly in better agreement with a four-fold than a six-fold coordination. For comparison, the anastase standard gives N= 5.2. Therefore, in all considerations that follow it is assumed that Ti^{4+} is in tetrahedral coordination in these amphiboles.

As for distance, EXAFS indicates that Ti in richteritic amphiboles is 1.84 Å away from its backscattering first neighbour, oxygen. This distance is in good agreement with the value 1.82 Å which would be expected from simple addition of the ionic radii (Shannon, 1976), but significantly exceeds the average Ti-O determined by crystal structure refinement on barium orthotitanate Ba_2TiO_4 (Bland, 1961: <Ti-O>= 1.71 Å, with the two shortest Ti-O bonds of the tetrahedron 1.63 and 1.64 Å, and the two longest bonds 1.75 and 1.82 Å, respectively). However, it agrees well with the first shell distance 1.82 Å recently measured on barium orthotitanate by EXAFS (Henderson et al., 1991) and with the Ti-O distances 1.823-1.834 Å measured on defect $Ni^{2+}(Ti,Si)^{4+}O_4$ spinels containing tetrahedral Ti by neutron powder diffraction (Lager et al., 1981). On the other hand, <Ti-O> distances in TiO_2 polymorphs are significantly longer: 1.955 Å for rutile (Shintani et al., 1975), 1.946 Å for anastase (Horn et al., 1972), and 1.959 Å for brookite (Baur, 1961). In general, <Ti-O> distances for all compound in which Ti is rigorously in six-fold coordination are in the range 1.95-1.96 Å, and occasionally longer (Greegor et al., 1984; Waychunas, 1987).

The measured Ti-O distance also provides stronger evidence than does colour for there being no significant trivalent Ti in these amphiboles. Using ionic radii of Ti^{3+} and O^{2-} (Shannon, 1976) indicates a bond distance of 2.07 Å: much longer than the measured value. Only in the rare compounds in which Ti is in four-fold coordination are <Ti-O>

distances as short as that measured in richteritic amphiboles; this is another strong indication that Ti occurs at the tetrahedral sites. Data on natural richterites determined by single-crystal X-ray diffraction cannot be of help to this point, because their measured Ti-O distances (1.597-1.698 Å: Oberti et al., 1992) average the contribution of Ti with that of the predominant Si (and occasionally Al and Fe^{3+} also).

Of all the other effects that can be observed in Fig. 3.1.3, the only relevant one is at *ca.* 3.07 Å, which we interpret as due to interaction effects of Ti with second shell neighbours. This distance permits surmising which tetrahedron of the double-chain is occupied by Ti. To this aim I used as reference the atomic distances in the structure of a natural [4]Ti^{4+}-bearing richterite determined by single-crystal X-ray diffraction. The chosen sample is R(7) from W. Kimberley, Australia (Oberti et al., 1992); this is closest in composition to RI_{80}TiRI20 and has almost all Ti in tetrahedral coordination (0.270 a.p.f.u. [4]Ti^{4+}, plus 0.050 [6]Ti^{4+}). All possible distances were calculated for the T(1) and T(2) central atoms and the following was found:

a) 3.08 Å : T(1)-T(2);
b) 3.15 Å : T(2)-M(4);
c) 3.18 Å : T(2)-O(4);
d) 3.20 Å : T(1)-M(1) and T(1)-M(3).

The distance measured from EXAFS agrees well with a) and indicates interaction between the central atoms of two neighbouring tetrahedra. Given the bulk composition of the run products, where the tetrahedral double chain contains less than 1 Ti for every 10 Si ($Si_{7.3}Ti_{0.7}$ a.p.f.u.), the most likely contribution to the observed peak should be from Si. However, comparison between the theoretical chi(k) for Ti-Si at 3.07 Å distance with the experimental signal shows that the agreement is good but not perfect, as does also the comparison for a Ti-Ti pair with the same characteristics. Only a combination of the two contributions improves the fit with the measured signal.

3.1.7 Conclusion

(1) Titanium can be incorporated in the structure of synthetic richteritic amphiboles by the direct isovalent substitution $Ti^{4+} = Si^{4+}$ at the tetrahedral sites only.

(2) The EXAFS spectra of these synthetic amphiboles shows Ti to be at 1.84 Å distance from its first nearest neighbour, oxygen, and at 3.07 Å from the second shell.

(3) The spectra do not offer clear indication for exact location of Ti in the tetrahedral double chain, but the measured Ti-O distance suggest the least confined T(2) site as the likely site of Ti in the amphiboles examined here. However, the spectra also show a second peak that may indicate a minor disorder, i.e. a hint for some Ti also in the T(1) site.

4) The conclusion about the tetrahedral location of Ti in richterite can be extended from these synthetic samples to natural amphiboles. Supporting evidence includes

Czamanske & Atkin's (1985) and Wagner & Velde's (1986) systematic observations about the crystal chemical relationship of Si, Al, Ti, Fe3+ in many alkali and alkali-calcic amphiboles of different origin, and on the single-crystal X-ray diffraction refinements of Oberti et al. (1992).

Studies on synthetic and natural amphiboles open again the question about the role that Ti has in petrogenesis, and particularly in the formation of certain high-K, high-Ti magmatic rocks such as lamproites, with which richteritic amphiboles are usually associated.

3.2 X-RAY ABSORPTION STUDY OF TI-BEARING SILICATE GLASSES

3.2.1 Abstract

Ti K-edge XANES spectra have been collected on a series of Ti-bearing silicate glasses with metasilicate and tetrasilicate compositions. The intensity of the pre-edge feature in these spectra has been found to change with glass composition and varies from 29 to 58 % (normalized intensity) suggesting a variation in structural environment around the absorbing atom. The pre-edge peak intensity increases for the alkali titanium tetrasilicate glasses from 35% to 58% in the order Li < Na < K <Rb, Cs, whereas for the metasilicate compositions there is a maximun for the K-bearing glass. The pre-edge peak intensity remains constant for the alkaline earth titanium metasilicate glasses, Ca and Sr (34%) but increases slightly for Ba (41%). As the intensity of this feature is inversely correlated with coordination number, consideration of the correlation between pre-edge intensity data for the investigated glasses with those of materials of known coordination number leads us to infer that the average coordination number of Ti in these glasses ranges from 4.8 to 5.8. Large alkali cations appear to stabilize a relatively low average coordination number for Ti in silicate melts. The Ti structural environment results appear also to vary as a function of SiO_2 content whithin the K_2O-TiO_2-SiO_2 system.

Numerous studies of the physical properties of Ti -bearing silicate melts provide clear evidence of a variable coordination number of Ti, consistent with the interpretation of the present XANES data and complementary density measurements. These and other property determinations are compared with the present spectroscopic observations in an attempt to relate structure and properties in these melts which contain a major component with variable coordination number.

3.2.2 Introduction

An understanding of the relationship between properties and structure of silicate melts is the central objective of a large body of research in the glass, and other materials, important for metallurgical and geological sciences. The incentive for spectroscopic studies of silicate melts in the geological sciences rests especially upon the promise that the understanding of silicate melt structures will allow predictions to be made about the physical and chemical behavior of silicate melts during igneous petrogenesis. Thus, it is this construction of predictive relationships between structure and properties of silicate melts that is the general goal of studies of silicate melt structure.

In the structural investigation of silicate melts, in their liquid or glassy state, a commonly used strategy for the delineation of significant trends in melt structure is to vary systematically the composition of a melt that has been chosen from a system with a relatively small number of components. This approach has been adopted in this study.

Another aspect of studies of silicate melt structure concerns the case of cations present in a range of coordination geometries which exhibit variable coordination numbers. Such behavior is temperature-, pressure- and composition-dependent and can be described by a homogeneous equilibria between two or more coordination geometries, involving the stabilizing cations of interest. Several cations are thought to occupy a mixture of sites with different coordination number in silicate liquids and glasses over large ranges of pressure, temperature or composition (e.g., Si, Xue et al., 1989; Al, Ohtani et al., 1985; Ge, Itié et al., 1989; Fe, Virgo and Mysen, 1985; B, Riebling, 1967; Ti, Johnson and Carmichael, 1987; Mn, Kohn et al., 1990; Ni, Galoisy and Calas, 1993; Co, Keppler and Rubie, 1993). In the present study I have chosen the example of Ti to illustrate how coordination number changes can influence the structure and properties of silicate melts.

The incentive for the choice of Ti was the observation that the partial molar volume of Ti depends on melt composition in high temperature silicate melts at (Lange and Carmichael, 1990; Dingwell, 1992a). Additionally, heat capacity and compressibility data appear to show anomalous behavior which could indicate a mixed coordination number (Richet and Bottinga 1985; Lange and Navrotsky, 1993; Webb and Dingwell, 1994). Considerations of these properties were also supplemented by seemingly contradictory proposals for the coordination of Ti in silicate melts by previous workers (see review by Mysen, 1988).

In this study I present the results of an investigation of the composition-dependence of the coordination of Ti in glasses quenched from 1 atm, high temperature liquids in air. In companion work (Paris et al., 1994; Seifert et al., 1994) the effects of pressure and temperature have been investigated for selected compositions. I have employed the element-specific technique X-ray absorption near-edge structure (XANES) spectroscopy to investigate the Ti K-edge spectra of these glasses. Transition metals show, due to their electronic structure, a sensitive dependence of the XANES features on coordination number and site distortion. The principle spectroscopic variable is the intensity of the pre-edge feature, calibrated against mineral standards. This feature has been correlated with a shift in the average coordination number of Ti in the glass samples, and it is concluded that large alkali cations stabilize a lower average coordination number of Ti in silicate melts.

3.2.3 Experimental

The starting materials for the present investigation were powder mixtures of the requisite proportions of oxides and carbonates. The composition of the investigated samples was based on a tetrasilicate and a metasilicate stoichiometry plus TiO_2. The general formulae are $X^{n+}_{2/n}TiSi_4O_{11}$ and $X^{n+}_{2/n}TiSiO_5$ (where X is Li, Na, K, Rb, Cs, Ca, Sr, and Ba); an $Al_2O_3.TiO_2.4SiO_2$ composition was also studied. The melts were prepared by fusion of oxides and carbonates in platinum crucibles in a $MoSi_2$ box furnace

at temperatures ranging between 900 and 1650°C. Glass samples were quenched by pouring onto a steel plate. The products of these fusions have been used for experimental determination of the density, viscosity and compressibility of the liquids at superliquidus temperatures (Dingwell, 1992a; 1992b; Webb and Dingwell, 1994). Poured glass samples were stored in a dessicator until use in structure and property determinations.

The chemical compositions of the glasses have been determined by solution-based inductively coupled plasma atomic absorption spectroscopy (ICP-AES) and electron microprobe methods (Table 3.2.1). Deviations from nominal composition are minor. Under extreme conditions of low oxygen fugacity, high temperature or composition, Ti may occur in a partially reduced state (Ti^{3+}) in silicate melts (e.g., Schreiber et al., 1984). The low temperature and high oxygen fugacity of synthesis of the studied samples minimizes the possibility of reduced Ti occurring in these samples. The composition and totals of the chemical analyses indicate all the Ti is present as Ti^{4+}. Oxidation during the quench might however have affected the state of Ti in these glasses. One extra constraint is provided *in situ* by a weight-loss test performed at 1000°C for the Cs-bearing metasilicate melt. A few grams of this sample were weighed into a crucible and melted at 1000°C in air, suspended from a balance. No weight loss was observed. Subsequent reduction in a $CO+CO_2$ gas flow also failed to produce a weight loss. Had the $TiO_2 = Ti_2O_3 + 1/2O_2$ reaction been stoichiometrically significant then the weight loss in this melt, with 33 mole % TiO_2 equivalent, would have been easily measureable (cf. Fe in Dingwell, 1990a). The arguments for the alkali-bearing melts are however difficult to extend to the Li- and Al-bearing tetrasilicate melts. These exhibited a blue colour most likely arising from the presence of a trace of Ti^{3+}. The subsequent interpretation of the spectra of these two samples reveals nothing extraordinary with respect to the rest of the sample set (see below); nevertheless, the results for these two samples must be treated with caution.

All glass samples have been checked under the optical microscope for the possible presence of TiO_2 crystalline phases and revealed to be crystal-free. The absence of crystalline material can be assessed also from the XANES spectra, since even a small amount of TiO_2 crystals would be easily detected by strong resonances in the XANES region and the features typical of rutile and anatase in the pre-edge region (e.g., see Chapter 3.1; Paris et al., 1993).

The X-ray absorption spectra of powdered glass samples have been collected at the PULS X-ray line of the Frascati Synchrotron Radiation Facility (Italy). The absorption spectra were recorded at room temperature in transmission mode at the titanium K edge using a Si(111) channel-cut crystal as the monochromator. The XANES spectra have been recorded in a range of energy of 100 eV through the absorption edge with steps of 0.2 eV and overall resolution of 1 eV. A Ti-metal foil (EXAFS Materials, 4966.0 eV)

TABLE 3.2.1. Analysed glass compositions.

X_2O, XO	TiO_2	SiO_2	total
<u>tetrasilicate</u>			
7.8(Li)	23.5	68.8	100.1
15.5(Na)	19.5	63.6	98.6
21.6(K)	18.1	58.0	97.7
36.5(Rb)	16.2	47.9	100.6
43.3(Cs)	13.2	39.1	95.6
<u>metasilicate</u>			
30.5(Na)	39.6	29.2	99.3
39.9(K)	34.9	24.8	99.6
57(Rb)	24.7	18.0	99.7
67(Cs)	19.6	14.4	101.0
29.0(Ca)	40.4	30.6	100.0
43.1(Sr)	32.6	24.6	100.3
48.5(Ba)	27.5	22.5	98.5

alkali-bearing glasses by ICP-AES; alkaline earth-bearing glasses by electron microprobe (see Dingwell, 1992 for analytical details); metasilicate analyses reproduced from Dingwell (1992)

was used for energy calibration and to verify experimental reproducibility. Possible changes in Ti oxidation state were investigated by comparing the first derivative calculated for each spectrum to check for chemical shift effects. The samples have been prepared by smearing the powder obtained by grinding glass fragments in a agate mortar onto a kapton tape. Homogeneity and thickness of the samples were taken in consideration to insure a good signal/noise ratio. Standard materials consisted of natural and synthetic Ti-bearing compounds, all well-characterized by X-ray diffraction methods (Table 3.2.2). Experimental data have been reduced by subtraction of the background, followed by normalization of intensity to the high energy side of the spectra (at 5027 eV) in order to avoid the influence of multiple scattering effects. Peak intensities and half-widths have been evaluated by standard fitting method using Lorenzian curves and least-squares procedure (Table 3.2.3).

3.2.4 Glasses and melts

The structural information frozen into glasses on quenching from high-T liquids corresponds to the glass transition temperature for the combination of glass chemistry and quench rate (Richet and Bottinga, 1986; Brandriss and Stebbins, 1987; Dingwell and Webb, 1990; Ihinger, 1991; Keppler, 1992; Mysen and Frantz, 1992, Lange and Navrotsky, 1993). Inasmuch as the present measurements were performed on glasses quenched from high temperature liquids I must emphasize that the spectra of these glasses provide data on the structure of the silicate liquids that was quenched in at the glass transition. This range of temperature is approximately 500-600°C for the combination of the present compositions and experimental quench rates (Dingwell and Webb, 1990) with the consequence that considerable relaxation or backreaction of any temperature-dependent changes in melt structure could have occurred between the dwell temperatures of synthesis (above 1000°C) and the glass transition temperatures. Also, as the viscosity-temperature relationships of the various compositions are not identical (Dingwell, 1992b), the possibility exists that the structures are not quenched in at identical glass transition temperatures. Both of these effects can be relegated for the present melts to a minor role in influencing the comparisons to follow because *in situ* study of the temperature dependence of the spectra of one chosen melt composition indicates a very weak dependence of structure on temperature (Seifert et al., 1994).

TABLE 3.2.2. Pre-edge peak (P) intensities for reference compounds.

sample	**N**	**C.N.**	**P I (%)***	**reference**
benitoite	1	6	6	Waychunas (1987)
titanite	2	6	16	this work
anatase	3	6	17	this work
ilmenite	4	6	18	Waychunas (1987)
rutile	5	6	21	this work
neptunite	6	6	33	Waychunas (1987)
brookite	7	6	33	Waychunas (1987)
narsarsukite	8	6	38	this work
Ba-fresnoite	9	5	55	Behrens et al. (1990)
Sr-fresnoite	10	5	62	Behrens et al. (1990)
$CsAlTiO_4$	11	4	72**	Behrens et al. (1990)
Ba_2TiO_4	12	4	75	Behrens et al. (1990)
Ti-ricthterite	13	4	78	Paris et al. (1993)
Ba_2TiO_4	14	4	84	Greegor et al. (1983)
Ba_2TiO_4	15	4	88	Yarker et al.(1985)

* all values normalized at 5027 eV according to Paris et al. (1993)

** normalized intensity evaluated by comparison with n.12, due to the Cs L edge interference

TABLE 3.2.3. Spectral features and calculated coordination number of the glasses.

glass	PI(%)	CN	PE (eV)	CE (eV)	DE(eV)
<u>metasilicate composition</u>					
Na	47	5.2	4970.9	4990.0	5003
K	55	4.9	4971.0	4987	4999
Rb	29	5.8	4971.6	4989.7	5003
Cs	36	5.6	4971.2	4986.5	-*
Ca	34	5.6	4970.7	4987.3	4999.3
Sr	34	5.6	4970.3	4986.7	4999.1
Ba	41	5.4	4970.6	4986.9	4999.3
<u>tetrasilicate composition</u>					
Li	35	5.6	4970.6	4987.5	4999.9
Na	43	5.3	7970.3	4987.6	5000.4
K	52	5.0	4970.2	4986.1	4998.1
Rb	58	4.8	4970.4	4986.0	5000.0
Cs	58	4.8	4970.2	4986.1	-*
Al	43	5.3	4970.6	4990	5003.3

PI = normalized pre-edge peak P intensity; CN = calculated average coordination number using the equation given in the text; PE = peak P energy; CE peak C energy; DE = peak D energy; * interference by Cs L-edge

3.2.5 Results

The XANES part of the absorption spectrum provides information on the oxidation state of the absorber and on structural details such as the coordination number of the absorbing atom and the geometry, bond angles and distances relative to the surrounding anions (in this case, oxygens) (Brown et al., 1988).

A XANES spectrum is traditionally divided into two regions; the pre-edge region where the features are determined by electronic transitions to empty bound states and the XANES region *sensu stricto* where the multiple-scattering effects are predominant. The combined study of these effects, together with the analysis of the EXAFS oscillations, can provide detailed information on the local geometry of the ligands around the absorber. However, the multiplicity of Ti environments in the types of materials under investigation, and recent advances in the modelling of theoretical XANES spectra (e.g., see Chap. 1.2, 3.4) lead to focussing the attention on the XANES part of the spectra.

The peak located in the pre-edge region (from now on to be referred to as peak P) has been related, in transition elements, to the electronic transition 1*s*-3*d* (Waychunas, 1987). This transition is forbidden when the absorber site symmetry is *Oh* (perfectly regular octahedron) whereas it becomes partially allowed when *d-p* orbital mixing is produced, e.g. by polyhedral distortion and consequent change of symmetry or change of coordination polyhedron. The *d-p* mixing produces an increase of probability for the transition to occur and an increase of the peak P in the spectrum; peak P would have zero intensity in a perfectly regular octahedral symmetry. The intensity of this peak is related to the electronic structure of the atom and, for transition elements, to the number of electrons in the *d*-orbitals, decreasing systematically as the 3*d*-orbitals are filled (Lytle et al., 1988) and being very high for Ti. In fact, when titanium is located in a tetrahedral site, the change in orbitals distribution and symmetry produces a considerable *d-p* mixing giving a strong increase of the peak P intensity (Bianconi et al., 1985). For titanium, the changes in the XANES spectra as a function of the coordination number and local geometry around the absorber provide infomation on the geometrical environment around the absorber (Table 3.2.2). In the case of a transition element in a glass, the XANES spectrum is dominated by the resonances produced by the scattering effects of the first shell of atoms around the absorber and the absence of long-range order makes the effects due to shells farther then the first almost negligible. For crystalline materials, the XANES region is more complex due to the presence of resonances produced up to the fifth shell of coordination, as a function of cluster symmetry and composition (Kitzler, 1993). However, even for crystalline materials, the first coordination shell mostly affects the near-edge region, as shown by multiple scattering (MS) calculations performed at the iron K-edge for pyroxenes (see Chap. 4).

The experimental Ti K-edge XANES spectra for alkali-titanium metasilicate and alkaline-earth-titanium metasilicate samples are grouped in Figs. 3.2.1 and 3.2.2

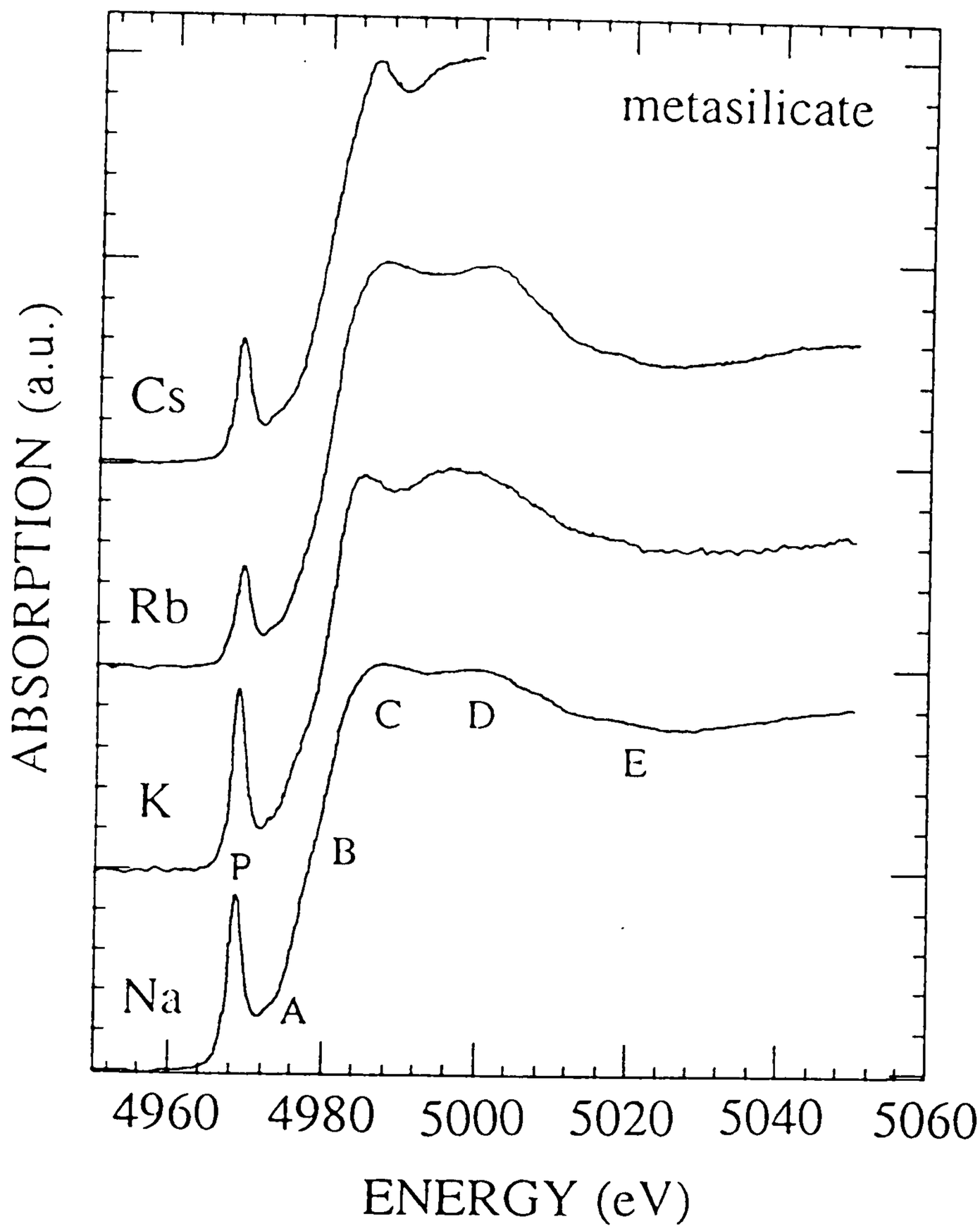

Fig. 3.2.1 Ti K-edge XANES spectra for alkali-bearing glasses of metasilicate composition. A variation of the intensity of the pre-edge peak with composition is evident. This variation is interpreted as resulting from a change in average coordination number.

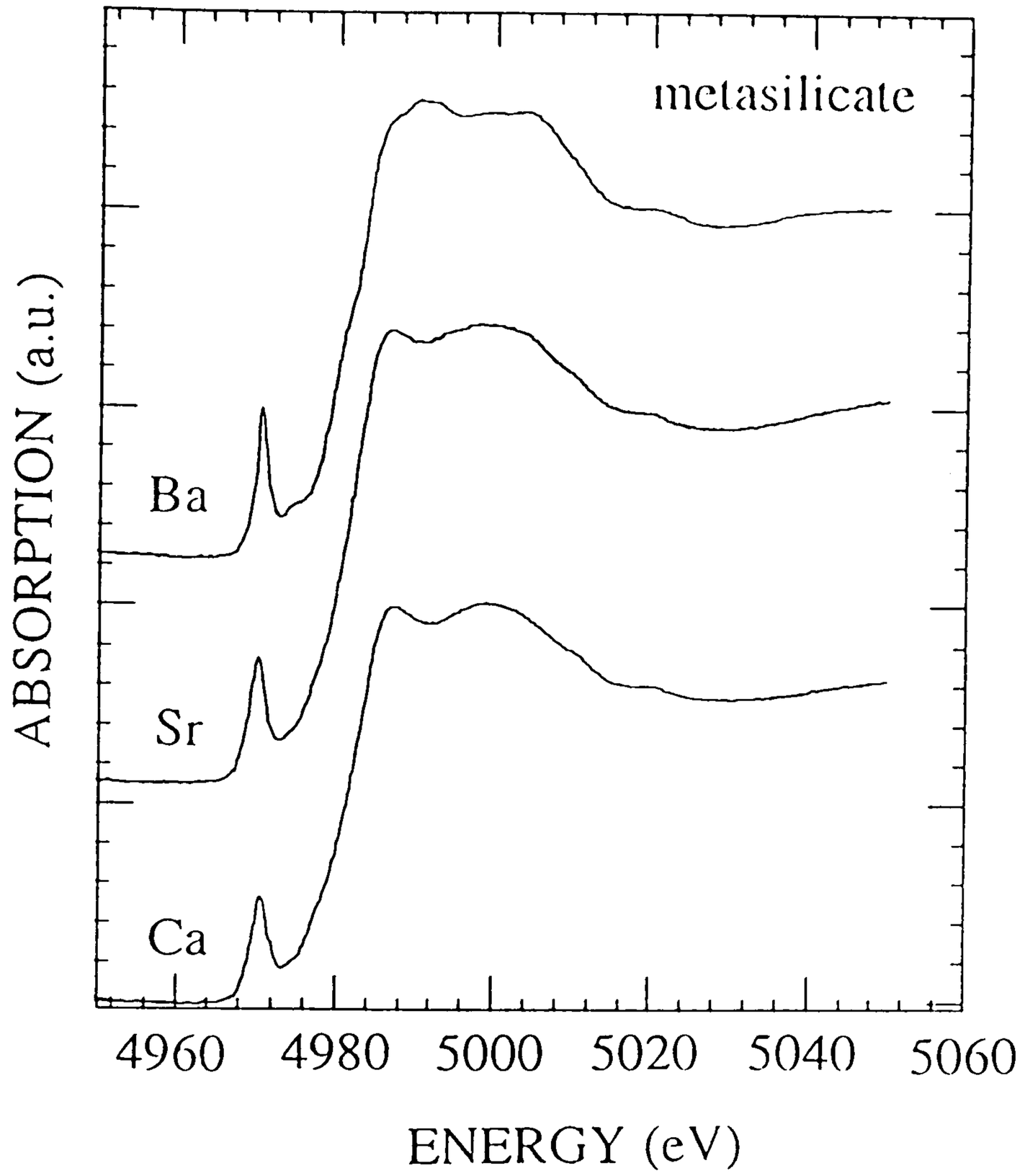

Fig. 3.2.2 Ti K-edge XANES spectra for alkaline earth-bearing glasses of metasilicate composition. The variation of the intensity of the pre-edge peak with composition is minor. The pre-edge intensity exhibited by these samples is interpreted as resulting as resulting from an average coordination number near 6 for all the glasses.

respectively. The pre-edge region is composed of a peak P and two small peaks (A and B) not present in all the spectra, whereas the absorption region presents two strong resonances (C and D) followed sometimes by a bump (E). Energy position and intensity of the XANES features are reported in Table 3.2.3. All the spectra show similar resonances in the region around the absorption edge, but they differ strongly for the intensity of the pre-edge peak (P) (Figs. 3.2.1 and 3.2.2). In fact, the peak P for metasilicate glasses increases in intensity from Na (47%) to K (55%) and decreases again for the Rb sample (29%). The spectra of the alkaline earth-bearing glasses exhibit only minor variations, with the pre-edge peak being 34% for the Ca- and Sr-glasses but increasing to 41% for the Ba-glass. In Fig. 3.2.3 the XANES spectra of alkali-titanium tetrasilicate glasses are reported, showing that the pre-edge intensity increases from 35% (Li) to 58% (Cs) (Table 3.2.3).

Given the relationship between the pre-edge peak intensity and the local geometry around the absorber, the P intensity data for all the samples have been compared with data for a series of inorganic crystalline materials (oxides, titanates and silicates). The standards were chosen from analyzed Ti compounds where Ti is exclusively bonded to O (since differnt anions produce a different degree of covalency that modifies the *p* character of the final state thus affecting the P intensity) and and where Ti is present in a variety of coordination numbers (4, 5 and 6) and geometries (regular and distorted octahedra, tetrahedron, trigonal bipyramid) (Table 3.2.2). All of the samples are structurally well characterized both by XAS and XRD and, as expected, the pre-edge peak shows strong variations in intensity as a function of the coordination number (Table 3.2.2), being very high for tetrahedral coordination (72-88%), intermediate for 5-coordination (55-62%) and low (0-38%) for octahedrally coordinated Ti. The uncertainty in these data can be judged from the fact that octahedral samples 2, 3 and 4 have been reported in the literature (Waychunas, 1987) with the same values as those reported here, whereas the tetrahedral compound Ba_2TiO_4 is reported with a difference in values up to 13%. This difference is possibly due to uncertainties concerning purity of the analyzed samples and/or to interlaboratory error. For octahedrally-coordinated titanium, the range of variation in the observed pre-edge peak intensity can be been related to polyhedral distortion, with the more intense pre-edge peak resulting from samples with less regular sites (Waychunas, 1987). Not enough data are available for similar considerations of the 4- and 5-coordinated materials, due to the preference of Ti^{4+} for octahedral environments and the small number of crystalline compounds with different coordination numbers.

Comparison with the standards suggests that some of the alkali-bearing metasilicate glasses, which show the highest pre-edge peak heights, have lower average coordination number than the alkaline-earth-bearing metasilicate glasses, whose pre-peak heights are lower and similar to those typical of the standards containing octahedrally coordinated Ti.

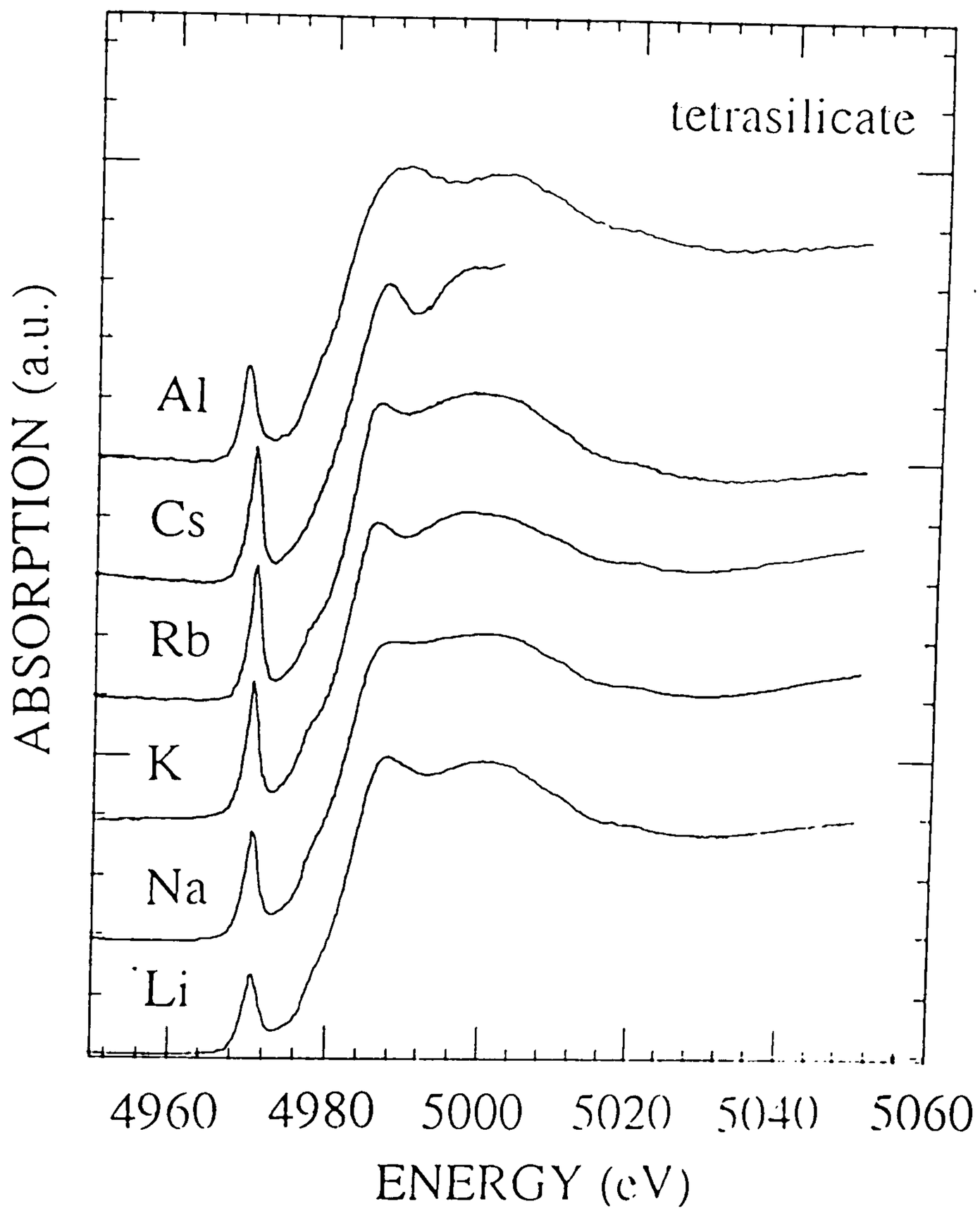

Fig. 3.2.3 Ti K-edge XANES spectra for alkali-bearing glasses of tetrasilicate composition. A variation of the intensity of the pre-edge peak with composition is evident. This variation is interpreted as resulting from a change in average coordination number. Also included in this figure is the spectrum of the Al-bearing sample, separately discussed in the text.

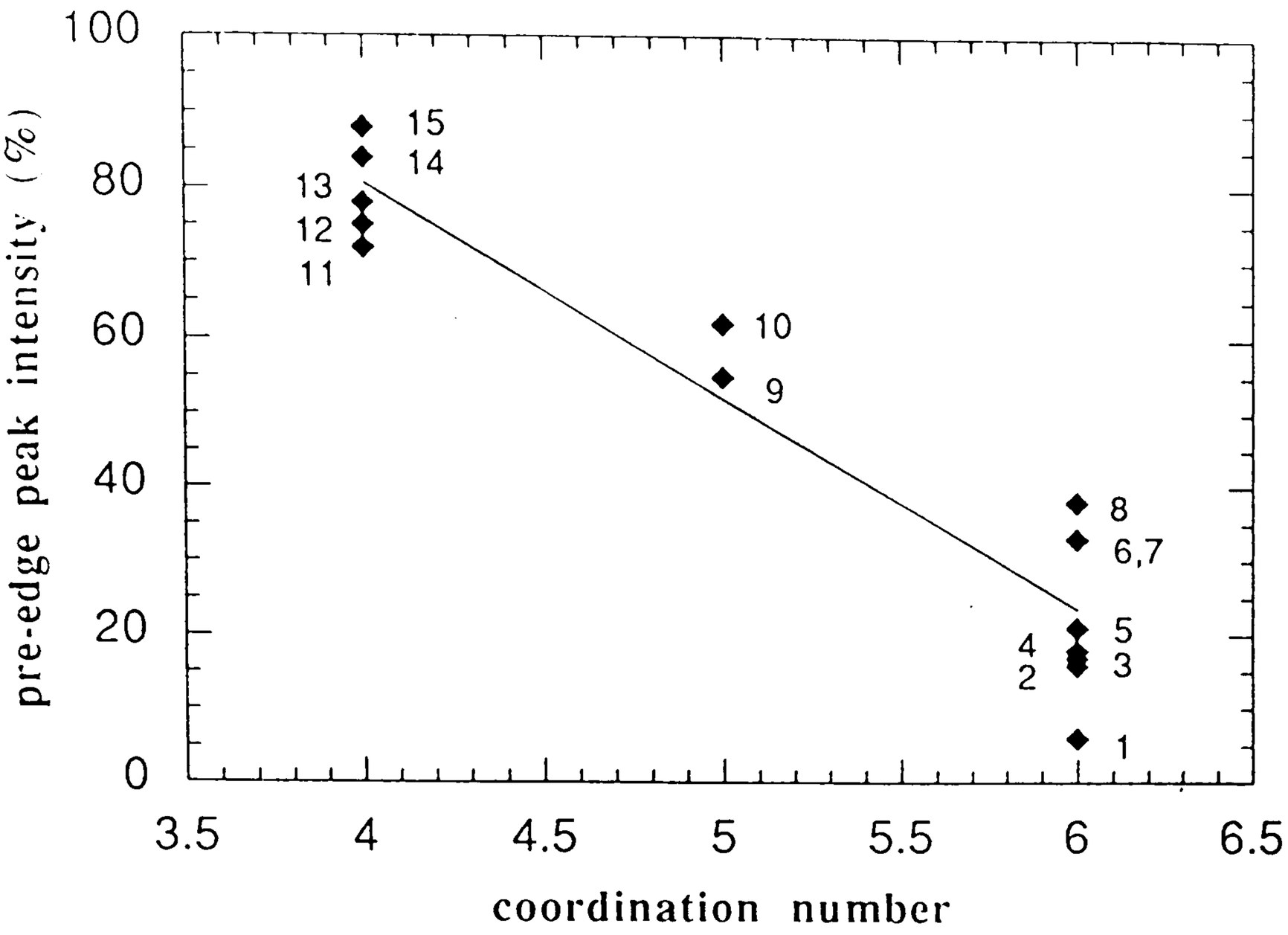

Fig. 3.2.4 The relationship between coordination number and pre-edge intensity for a number of crystalline reference materials (numbers as in Table 3.2.2). This relation is used to estimate an average coordination number for unknown samples.

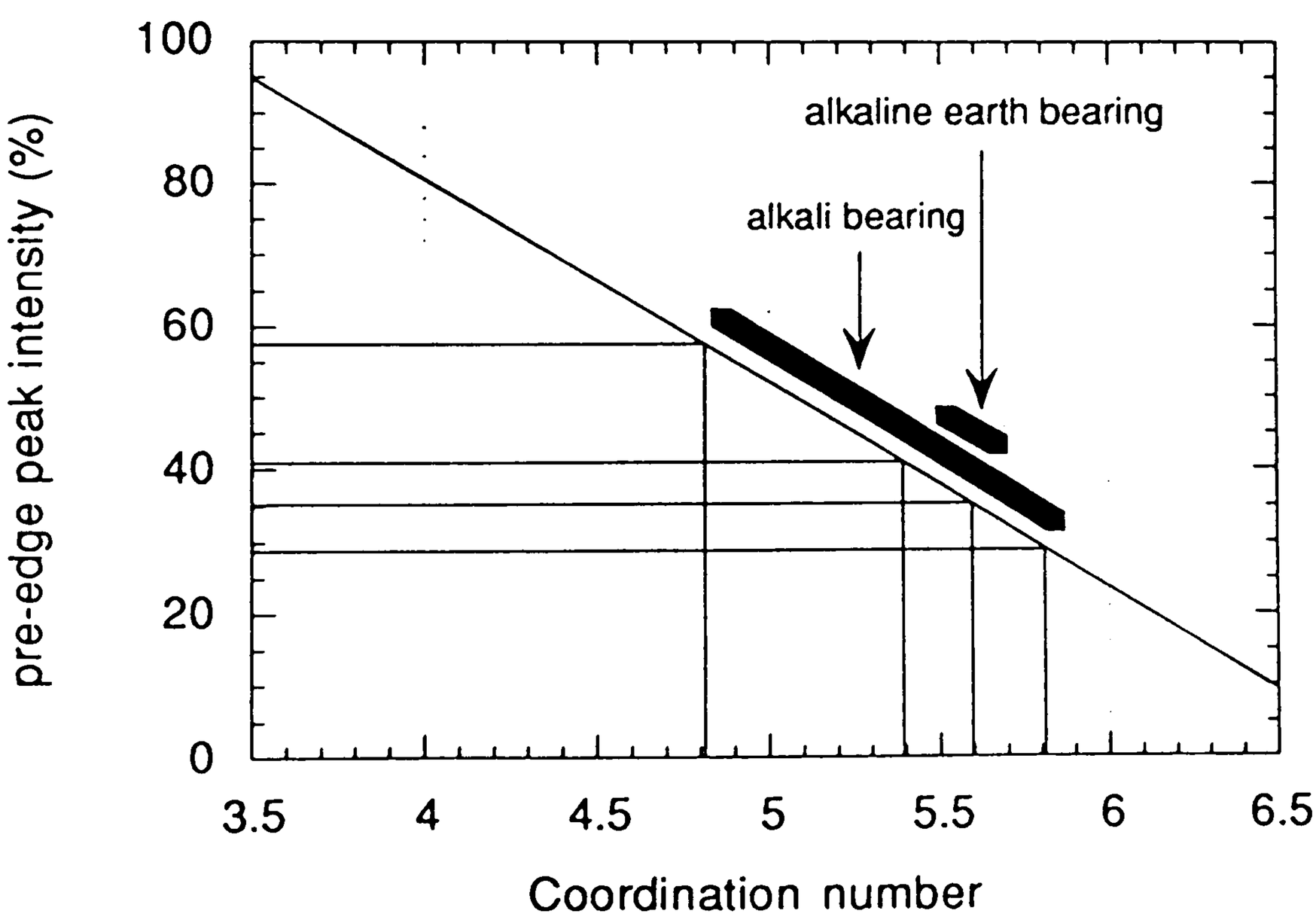

Fig. 3.2.5 The derivation of average coordination number for all the glasses investigated in this study based on the regression presented in Fig. 3.2.4. The range of average coordination number is from 4.8 to 5.8 for the alkali titanium silicate glasses and restricted to 5.4 to 5.6 for the alkaline earth silicate glasses.

Fig. 3.2.4 shows a roughly linear trend between the intensity data obtained for the standards and their coordination numbers; linear regression of the data yields

$$IP = -28.57 \cdot CN + 194.9$$

where CN is the average coordination number and IP is the normalized intensity of the pre-edge peak P; the correlation coefficient R = 0.95. Assuming that the correlation between the coordination number and the intensity of the pre-edge peak P obtained for crystalline materials can be applied to glasses, I can now try to estimate the average coordination number for the amorphous samples. This assumption is well supported by the comparison with the coordination number obtained by neutron diffraction (Yarker et al., 1985) on a glass of composition intermediate between the samples studied here, which has also been analyzed by XAS. The coordination number obtained for this glass is 4.82±0.02 that is in reasonable good agreement with the value 4.7 calculated using the above equation and the experimental IP peak intensity value of 62% (renormalized for comparison with the other spectra).

The calculated (average) coordination numbers for these glasses (Table 3.2.3) are all between 4.8 and 5.8. However, in Fig. 3.2.5 I show that these glass data, derived from the regression given above, lie at consistentantly higher average coordination number for the alkaline-earth silicate glasses (5.4-5.6) and in a lower but larger range of CN for alkaline silicate glasses (4.8-5.8). The CN range is slightly lower for alkali tetrasilicate glasses (4.8-5.6) if compared with the metasilicate compositions (4.9-5.8). Also, in Figs. 3.2.1 and 3.2.2 the absorption peak D of XANES experimental spectra exhibits for some samples a small shift toward higher energies, suggesting an increase of the bonding and a decrease of the mean Ti-O bond length in passing from Li to Cs and from Ca to Ba. This supports the general idea of decreasing average coordination number as a function of increased cation size in each series of glasses. Thus, the XANES features appear to be particularly sensitive to the coordination of Ti in these glasses and this will be subsequently discussed in the interpretation of the spectra.

Further support for the application of the correlation between CN and P peak intensity to the determination of Ti local environment comes from the results obtained by MS calculations performed at the Ti K-edge on small clusters reproducing tetravalent titanium surrounded by oxygens in different types of coordination numbers and geometries (see Chap 3.4). The theoretical spectra obtained by using clusters of this type have been used to study of the local environment of transition elements in aqueous solutions (Garcia et al. 1986) and can be applied also to glasses, since in both cases only the contribution of the first coordination shell is expected because of the strong disorder of the more distant ligands. The MS calculations show that each geometrical environment produces characteristic features in the edge region and that the peak P increases in intensity in passing from 6 to 4-fold (Paris et al., 1994). It also increases, to a lesser extent, for the octahedral clusters as a function of polyhedral distortion, in

agreement with the trend observed for crystalline compounds. The variation of P as a function of local geometry in the theoretical spectra further supports the validity of this equation and its application to average CN estimation. The comparison with the theoretical spectra also suggests that Ti is present in these glasses in three different geometries, tetrahedron, trigonal bipyramid and distorted octahdron, whose combination in the glasses is strongly composition-dependent. For example, Li-glass spectrum (Fig. 3.2.3) can be reproduced by linearly combining the distorted octahedron and the trigonal bipyramid theoretical spectra in the equal proportions (Paris et al.,1994). This combination gives the exact IP value of the experimental spectrum and reproduces the other resonances (B, C and D) as well, with a CN value (5.5) in good agreement with that independently obtained via the equation (5.6) (Paris et al., 1994). The Li-glass spectrum is not reproduced by combining other geometries (like a tetrahedron and an octahedron) or by using other proportions. Application of this approach to the entire set of spectra needs to consider the contribution from tetrahedral titanium, as the other spectral features (A, B, C, D) suggest that in some of these glasses it plays a more important role than in others. A more detailed investigation of Ti XANES spectra by MS calculation needs to be undertaken.

Finally, to check for the oxidation state, the energy position of the absorption edge has been measured by computing the first derivative of each spectrum. A chemical shift about +2eV is generally observed in titanium compounds (Waychunas, 1987) and reported as characteristic of the change in oxidation state from Ti^{3+} to Ti^{4+}. This shift is evaluated in details only if a reference material is used for calibration. In this case a Ti metal foil has been measured to evaluate the energy position of the glasses spectra. The results show that there is no shift in energy between the spectra: all of them are consistent with the presence solely of Ti^{4+}. However, the slight bluish colour of the Li- and Al-bearing samples suggest a minor presence of Ti^{3+} in these glasses, below the sensitivity of the XAS method, since no energy shift has been detected (note however that concentrations of Ti^{3+} on the order of 10–100 ppm may be enough to yield colored glasses).

3.2.6 Discussion

The variations in pre-edge intensity of the XANES spectra of these Ti-bearing silicate glasses is interpreted here in terms of a variation in the average coordination number of Ti in the glass structure. The values of the calculated coordination numbers (based on the regression of Fig. 3.2.4 and presented in Fig. 3.2.5) are clearly non-integer valued. I interpret this observation, together with several other lines of evidence discussed below, to be a consequence of a homogeneous equilibrium in these glasses between different coordination states of Ti. Thus the coordination number quoted in Table 3.2.3 is labelled as "average coordination number". It is not intended here to

establish a topological stability of the fractional coordination numbers quoted here, rather they are taken to represent the average of two or more coordination states of Ti in these glasses, most likely 4 and 6 or 4, 5 and 6.

A further observation from the comparison of the metasilicate and tetrasilicate series of glasses can be made for the Cs, Rb, K and Na-bearing glasses. The relative intensity of the pre-edge is not the same for both compositions (Table 3.2.3). For the Na-bearing glasses the pre-edge decreases with increasing SiO_2 content whereas for the K-bearing glasses it is almost constant and for the Rb- and Cs-bearing glasses it decreases strongly with decreasing SiO_2. Variation of the relative intensity of the pre-edge in the TiO_2-SiO_2 system has also been observed by Greegor et al. (1983). They observed an initial increase in the pre-edge intensity with the addition of TiO_2 to SiO_2 up to 2 wt.% a constant pre-edge intensity up to the addition of 7.5 wt.%, and then a subsequent decrease in the pre-edge intensity with further addition of TiO_2 beyond this to 14.7 wt.%. According to my preferred interpretation, these trends reflect differences in the average coordination number with melt composition. In fact such trends must exist if the equilibrium between the Ti coordination species is a homogeneous one involving other melt components. The relative pre-edge intensity data presented here for the alkali meta- versus alkali tetrasilicate compositions can been interpreted as extensions of the trends observed by Greegor et al. (1983) into the respective alkali-bearing ternary systems. According to the forgoing discussion the observation of similar pre-edge intensities for the K metasilicate and tetrasilicate compositions must be fortuitous in that the pre-edge is predicted to be in general composition dependent within the ternary. Support for this comes from data reported by Yarker et al. (1986) on the glass composition $K_2TiSi_2O_7$, intermediate between the two compositions analyzed here. The pre-edge intensity reported for this composition yields an average coordination number of 4.7 from the regression presented here, in good agreement with the value 4.82±0.2 reported by Yarker et al. (1986) from their combined neutron diffraction and XAS study. Interestingly, the pre-edge intensity of their glass is much higher than the data for the tetra- and metasilicate compositions and thus supports the notion that a maximum in pre-edge intensity (and by inference a minimum in average coordination number) occurs as a function of composition within the K_2O-TiO_2-SiO_2, just as is seen for the TiO_2-SiO_2 binary. It is known that the stability of the low coordinated, high pre-edge species is alkali specific and thus the stability as a function of SiO_2 content can be individual as well. I would only add that according to this interpretation the pre-edge intensity in all ternary alkali-bearing systems must eventually decrease as the pure TiO_2 component is approached.

There are three additional lines of evidence that independently support the proposed homogeneous equilibrium between coordination states of Ti. Firstly, the value of the pre-edge intensity, in addition to being a function of composition (both SiO_2 content and

alkali identity), is also a smooth continuous function of pressure (Paris et al., 1994) and possibly temperature (Seifert et al., 1994). The continuous composition-, temperature- and pressure-dependence of the pre-edge intensity is the type of behavior expected for a homogeneous equilibrium with finite values of enthalpy and volume, the latter of which results in the pressure-dependence observed by Paris et al. (1994). I propose that the continuous composition-, pressure- and temperature-dependence of the pre-edge intensity results from the subequal proportions of differing coordination polyhedra that are implied by the non-integer average coordination numbers obtained in this study. Finally with regard to this point, the pressure-dependence of the proposed equilibrium is in the direction favouring higher coordination at higher pressure. Although the entropic consequences of a putative coordination shift from 4 to 6 coordination are ambiguous, the volume consequences are clear. The shift in coordination from 4 to 6 should result in a volume reduction per oxygen atom. This is consistent with the observed pressure-induced shift of Ti to lower pre-edge intensity and independently consistent with volume measurements described next.

The second type of evidence favouring the interpretation of speciation proposed above lies in the available physical property data for melts of metasilicate composition. Specifically, the density of melts of the titanium metasilicate composition have been determined and the partial molar volume of the TiO_2 component has been calculated for each using the available densities of the respective Ti-free metasilicate melts from sources in the literature. The calculated partial molar volume of TiO_2 (estimated at 1000°C) rises from 23.9(5) cm^3/mol in the $CaTiSiO_5$ melt to 28.5(5) cm^3/mol in the K_2TiSiO_5 composition. The results of these density determinations have been interpreted to reflect a change in the coordination of Ti from a relatively low-volume polyhedron in the alkaline earth-bearing melts to an increasingly large-volume polyhedron or combination of polyhedra in certain alkali-bearing melts. This interpretation is consistent with the interpretation of the pre-edge intensity data from this study.

Further physical property data also point to an anomalous behavior of the TiO_2 component in the temperature dependent properties of equilibrium Ti-bearing silicate liquids. Richet and Bottinga (1985) have demonstrated that that portion of the heat capacity of silicate melts contributed by temperature-dependent configurational changes, the so-called "configurational heat capacity", which is derived by subtracting the glassy value of the heat capacity from the measured value above the glass transition, is anomalously large and temperature-dependent for titanium-bearing alkali silicate melts in comparison with Ti-free alkali silicates. The anomalously large configurational heat capacity observed above the glass transition can be attributed to a temperature-dependent reaction involving the coordination of Ti in the Ti-bearing melts. Similarly, Lange and Navrotsky (1993) have emphasized that the T-dependence of the configurational entropy of alkali titanosilicate liquids is anomalously large at temperatures just above the glass

transition but becomes similar to that of Ti-free alkali silicate melts at temperatures of approximately 1000°C. The observation that the anomalous configurational heat capacity disappears at high temperature might indicate that the reaction approaches completion at high temperature. The data for the temperature dependent shift of the pre-edge intensity for a Rb-titanosilicate melt (Seifert et al., 1994) can be interpreted to indicate a subtle temperature-dependent coordination shift of Ti which is complete at such high temperatures.

Property data constraining the coordination number of Ti also come from recent ultrasonic determinations of the bulk modulus of alkali and alkaline earth titanium silicate liquids of the metasilicate composition (Webb and Dingwell, 1994). Preliminary data from these melts indicate that the compressibility of the partial molar volume of TiO_2 component is strongly dependent on composition. This is an anticipated consequence of varying the proportions of two or more coordination states of Ti in silicate liquids as a function of composition. The K and Na titanium metasilicate melts, in particular, show a large decrease in bulk modulus compared with equivalent alkali disilicate compositions (those with Ti replaced by Si). This sensitivity for the K and Na-bearing melts is tentatively interpreted to result from the differing proportions of differing coordination states of Ti in those melts. Further, the pressure-dependence of the pre-edge intensity (Paris et al., 1994) implies that a coordination shift is occurring with pressure and the variable compressibility of the 1 atm liquids is consistent with this observation.

The third line of evidence consistent with the interpretation of variable pre-edge intensity as a consequence of changes in the average (non-integral) coordination number of Ti in the silicate melts comes from analogous interpretations of other types of spectroscopic data for Ti and for other cations in silicate melts. Previous studies of the coordination of Ti in silicate glasses have been undertaken in a variety of systems using a number of different spectroscopic techniques (e.g. neutron scattering, Wright et al. 1977; vibrational spectrsocopy Takahashi et al., 1977; Furukawa and White, 1979; Mysen et al., 1980; Kusabiraki, 1986; X-ray absorption spectroscopy, Greegor et al., 1983; Sandstrom et al., 1980; Yarker et al., 1986). Previous spectroscopic studies of the structural role of Ti in silicate glasses have been interpreted to indicate a composition-dependence of the coordination number of Ti and the presence of both 4 and 6-fold coordinated of Ti in certain compositions. Of special interest in the present context are the studies of Wright et al. (1977), Hanada and Soga (1980) and Yarker et al. (1987). Wright et al. (1977) conducted a neutron scattering study of $K_2Si_2TiO_7$ glass, obtaining an average bond length of 1.95 Å. They concluded that the average coordination number of Ti in this composition is 5.2. Hanada and Soga (1980) conducted a study of the chemical shift of the Ti Kß X-ray emission spectra for glasses in the Na_2O-TiO_2-SiO_2 system, and observed a composition-dependence of the wavelength-shift which they interpreted to represent an increasing proportion of tetrahedrally-coordinated Ti with

increasing Ti content to 33 mol% TiO_2; higher TiO_2 contents showed a decrease. Their Figure 1 indicates an average coordination number near 5.2. Finally, as noted above, Yarker et al. (1987) have interpreted their neutron diffraction and XAS data in terms of a non-integer (i.e., average) coordination number of 4.8.

Previous discussions of the structural role of TiO_2 in silicate melts have returned repeatedly to distinguishing between the possibilities that (1) the anomalous coordination of Ti in large-alkali silicate glasses is due to an extreme distortion of an octahedral coordination, or (2) the anomalous coordination results from a proportion of lower coordination species. What distinguishes these two possibilities has to do with the definition of a coordination number for Ti in these melts. Variations in partial molar volume of TiO_2 by up to 20% with variable melt composition have been observed, and a pre-edge feature in the XANES spectra which shows variations corresponding to a range of average coordination number from 4.8 to 5.8. These data seems easiest to reconcile with the interpretation of a changing average coordination number of Ti in these melts. I have chosen to describe this structural degree of freedom as a homogeneous reaction between lower and higher coordinate species, dependent on composition, temperature and pressure. These species may be greatly distorted and the definition of a coordination number may be blurred. Thus whether one chooses to interpret the pressure-, temperature- and compositional features of these spectra as a reaction between coordination polyhedra of regular geometry or between species of varying degree of distortion of an octahedron, one must explain the large molar volume difference between the species. This term is large enough to lead us to conclude that the best description of the homogeneous equilibrium occurring in these melts yields an effective shift in the coordination number of TiO_2.

3.2.7 Conclusions

The coordination of Ti in simple ternary silicate melts can be described by a composition-dependent average coordination number between 4 and 6. The presence of large alkali cations reduces the proportion of high coordinate Ti species, presumably by shifting a homogeneous equilibrium involving variously coordinated Ti species. The variation in the average coordination number of Ti is reflected in a composition-dependence of physical properties such as density, heat capacity and compressibility. The equilibrium appears to be pressure- and temperature-dependent as well. Average non-integral coordination of cations in silicate melts may well be the rule rather than the exception.

3.3 STUDY OF PRESSURE-INDUCED COORDINATION CHANGE OF TITANIUM IN SILICATE GLASS BY XANES

3.3.1 Abstract

The effect of pressure on Ti coordination in glasses of $K_2TiSi_4O_{11}$ composition, quenched isobarically from liquids equilibrated at T=1600°C and high pressure (5–30 kbar) has been investigated by X-ray absorption spectroscopy (XAS). The XANES spectra collected at the Ti K-edge clearly show a variation with synthesis pressure that is related to changes in the geometrical environment around the Ti atoms. By comparison with spectra of standard materials, the XANES spectra from the glasses suggest a relatively low average coordination number (near 5) in low pressure samples and a higher coordination number (near 6) in higher pressure samples. The combination of XANES data with density and compressibility measurements supports the presence of a mixture of 6-, 4- and/or 5-coordinated Ti geometries in the 1 bar glass, and an increasing proportion of 6-coordinated Ti in the glasses synthesized at higher pressures.

3.3.2 Introduction

The influence of cationic coordination on the silicate melt physical properties has been widely discussed in the literature (Bottinga et al., 1982; Bottinga, 1985; Rigden et al., 1984; Stolper and Ahrens, 1987). Perhaps the most direct consequence is the effect of cationic coordination on melt density (Waff, 1975). A variable coordination number can influence the contribution of a melt component to the melt density through the different volumes corresponding to the coordination states. Additionally, the existence of a homogeneous equilibrium, dependent on temperature and pressure, between two coordination states of a cation, can drastically influence the values of thermal expansivity and compressibility of the melt. For these reasons and due to the importance of predicting melt densities at high pressures (e.g., Stolper et al., 1981), the pressure dependence of the coordination of cations in silicate melts has been the subject of several investigations. The TiO_2 component in silicate melts has been demonstrated to exhibit a partial molar volume and compressibility that is dependent on composition (Johnson and Carmichael, 1987; Lange and Carmichael, 1990; Dingwell, 1992), and investigation of silicate glasses quenched from liquid at 1 atm pressure, suggests that the average coordination number of Ti in silicate melts may be composition-dependent (Dingwell et al., 1994). Thus it is appropriate to investigate the dependence of the structural role of Ti on pressure of synthesis or density. I have chosen a melt with an apparent low average coordination number of Ti at 1 atm (Dingwell et al., 1994) in the expectation that its compression will induce a significant increase in the average coordination number.

X-ray absorption spectroscopy (XAS) can provide element-specific structural data, even at very low concentration of the selected element in both crystalline and amorphous

materials (e.g., Calas and Petiau, 1973; Brown et al., 1988; Kohn et al., 1990; Galoisy and Calas, 1993). XANES spectra (X-ray Absorption Near Edge Structure) are recorded through an energy range from the pre-edge to about 70 eV after the edge. This region is dominated by multiple scattering effects between the absorber and its near neighbours and has been shown yield information on the coordination and local geometry around the selected absorbing atom (Davoli and Paris, 1990). XANES spectra can also give information about the oxidation state of the absorber since different oxidation states produce a shift of the absorption edge (chemical shift) (Brown et al., 1988).

In this work, XANES spectra have been collected on a set of glass samples with the same chemical composition, that have been quenched from different pressures. The observed differences in the spectra are compared with the results of density measurements obtained on the same samples.

3.3.3 Materials and methods

The 1 atm preparation and analysis of the $K_2TiSi_4O_{11}$ glass starting material has been described in Dingwell et al. (1994). For the purposes of the present investigation bubble- and crystal-free cylinders (4.8 mm diameter) of this glass were drilled from the 1 atm fusion products and cut to lengths of 10 mm. These cylinders were loaded into Pt capsules (5 mm dia.) and sealed by welding. The sealed capsules were surrounded by Al_2O_3 powder and packed into talc-pyrex-graphite cylindrical assemblies for a 1.25cm piston cylinder apparatus. The high pressure syntheses were performed at 1600° C and pressures of 5, 10, 15, 20, 25 and 30 kbar, respectively. Pressure has been calibrated against the polymorphic transitions in $CaGeO_3$ and Mg_2GeO_4 (Ross et al., 1986; Ross and Navrotsky, 1987) and a pressure correction of -18(±2) % of nominal pressure for piston-in conditions was obtained.

The samples were held at the high temperature, high pressure condition for 1-2 hours and then quenched isobarically in a few seconds from the run temperature to a few hundred degrees by switching off power to the furnace. The quenching rate is thus on the order of 50-100° C/sec. This quenching rate is more rapid than that experienced by the 1 atm sample, but the difference in cooling rate (perhaps 1 log unit) should not lead to significant changes in the fictive temperature of the glasses. Estimation of the activation energy of structural relaxation in these melts indicates that a maximum shift of 30° C is expected at the different cooling rates. The effect of pressure on the glass transition for these samples is unknown. I cannot exclude that a significant variation in spectra results from the effect of pressure on the glass transition or fictive temperature of the quenched glasses. However, preliminary determinations of the temperature dependence of the pre-edge peak intensity, determined *in-situ* (see Chap. 8) indicate that only minor variations (1-2%) can be expected to result from shifts in fictive temperature.

The assumption of thermal equilibration in these samples at the time-temperature-pressure conditions of the experimental dwell time is reasonable given the low viscosities of these melts at such temperatures. The extent of relaxation of the melt density to lower temperatures and/or pressures is not known. I have measured the glass densities in order to quantify the density dependence of the spectra of these glasses.

X-ray absorption spectroscopy measurements have been carried out at the PULS X-rays line of the Frascati synchrotron ADONE (Italy). The XAS spectra have been collected in transmission mode using a Si (111) channel-cut crystal as monochromator and keeping the sample chamber in high vacuum. The samples were prepared by grinding glass fragments in a agate mortar and then smearing the powder on a kapton tape taking care of the thickness and homogeneity of the sample to obtain a good signal-to-noise ratio. To ensure the reproducibility of the measurements and for checking for the oxidation state of the samples, energy calibration has been performed using a standard Ti metal foil (EXAFS Materials, 4966.0 eV). The XANES spectra have been collected at energies of 100 eV to 70 eV after the absorption edge with an energy step of 0.2 eV and overall resolution of 1 eV. After subtraction of the background with a linear function, all the XANES spectral intensities have been normalized at high energy (5027 eV) to avoid the influence of multiple scattering effects. Peak energy position and intensity has been evaluated by curve-fitting procedure, using Lorentzian curves. First derivatives of the spectra have been calculated to determine the energy position of the absorption edge, to check for possible chemical shifts and to verify the oxidation state of the samples.

Several XRD-characterized crystalline materials have been used as reference compounds, including synthetic rutile, anatase, narsarsukite and a natural titanite; a group of literature data has been used as comparison and to investigate the relationship between spectral features and Ti coordination. The standards were chosen to be representative of the widest range of different coordination numbers and polyhedral geometries of oxygen-coordinated tetravalent titanium compounds. The collected data are summarized in Table 3.2.2 and have been used to calculate a regression curve for quantitative estimation of the coordination numbers in the glasses using the pre-edge peak intensity.

3.3.4 Results

3.3.4.1 *XANES data*

The XANES region is particularly sensitive to the local environment around the photoabsorber and thus provides information concerning the average overall shape of the site; i.e., type of coordination polyhedron, presence of distortion, symmetry of the site (Brown et al., 1988). For transition elements, and in particular for titanium due to its electronic structure, the utility of XANES spectra is enhanced by a pre-edge resonance whuch shows a dramatic change in intensity with changes in polyhedral geometry around the absorber (Waychunas, 1987). The intensity variation of the pre-edge peak (labelled P

in Fig.3.3.1 and in the following) is related to the electronic transition 1*s*-3*d*, that is forbidden in centrosymmetrical sites (e.g., regular octahedron) but partially allowed in non-centrosymmetrical polyhedra (e.g., tetrahedron; Waychunas, 1987). Different polyhedral geometries produce a different overlapping of the orbital wave-functions and intermediate intensity of the pre-edge peak P (e.g., distorted octahedron, trigonal bipyramid, tetragonal pyramid; Paris et al., 1994), and this peak is therefore a good indicator of the prevalent geometry in the material under investigation.

The XANES spectrum of the uncompressed $K_2TiSi_4O_{11}$ glass is shown in Fig. 3.3.1 (curve R). It shows an intense pre-edge peak at 4971.6 eV (peak P), followed by a shoulder at about 4978 eV (A) and two asymmetric maxima in the region of the absorption edge, respectively at 4986.3 eV (B) and 4997.6 eV (C) (Table 3.3.1). Given the sensitivity of the peak P to changes in coordination geometries of the target atom it can thus give information on the coordination number when calibrated with standards of known Ti coordination. A very intense pre-edge peak (72-88%) has been found to be characteristic of tetrahedrally-coordinated Ti (e.g., Ba_2TiO_4; Yarker et al., 1985) whereas the same pre-edge peak has intermediate intensity (55-62%) in compounds with 5-fold Ti (e.g. $Sr_2TiSi_2O_8$, Behrens et al., 1990) (Dingwell et al., 1994). In compounds with octahedrally-coordinated titanium the pre-edge peak is even less intense and varyies in intensity between 6% (benitoite, regular octahedron; Fischer, 1969) and 38% (narsarsukite, distorted octahedron: Peacor and Buerger, 1962); this range of values results from differences in site symmetry and polyhedral distortion (Waychunas, 1987; Dingwell et al., 1994; Paris et al., 1994). From the comparison with the standards, the glass at room pressure, with pre-edge peak intensity (IP) of 58%, has an average coordination number (CN) close to 5, in good agreement with previous studies on similar glass compositions (Dingwell et al., 1994; Yarker et al., 1986).

Fig. 3.3.1 shows the variation of the XANES spectra with pressure, up to 30 kbar. XANES resonances energy positions and intensities, evaluated by curve fitting, are reported in Table 3.3.1. Minor variations affect the resonances B and C at increasing pressures, whereas the spectra exhibit a strong decrease of the pre-edge peak P intensity (IP) with pressure, passing from 58% at room pressure to 29% at 30 kbar. The IP variation with pressure is clearly non-linear (Fig. 3.3.2), being very small up to 5 kbar, large between 5 and 20 kbar, and almost flat at higher pressure. From comparison with reference compounds, the decrease in peak P intensity in these glasses is consistent with an increase in the average coordination number at increasing pressure. In fact, the peak P intensities in the highest pressure samples are comparable with those characteristic of 6-fold coordinated standards. Support for this interpretation comes also from developments of the theoretical XANES calculations (e.g., Natoli et al., 1990) and the modelling of titanium polyhedral geometry by multiple scattering calculations. These calculations, using clusters of a few oxygen atoms around titanium to simulate the Ti

local environment in a glass, allow discrimination of the contributions to the total spectrum coming from different geometrical environments and they support the presence of more than one Ti-coordination geometry in the glass structure (see Chap. 3.4).

In an attempt to better quantify the average coordination number using the observed variations in the pre-edge, data for all the titanium standards reported from the literature have been plotted versus coordination number (see Chap. 3.2) and a linear regression fit to these data has been used to estimate average coordination numbers for the samples quenched from high pressures. Although an approximation, the utility of this approach is supported by comparison with glasses whose CN has been independently determined to be in good agreement with the calculated values (section 3.2; Yarker et al., 1986). The application of a relationship obtained on crystalline compounds to glasses is not unrealistic considering that the resonance under consideration (peak P) is mostly due to interaction with the first coordination shell and it is therefore not affected by long-range order structural effects like other XANES resonances. A similar trend of the variation of CN with IP is also shown by theoretical spectra of a suite of Ti and O clusters reproducing different geometries (Chap. 3.4; Paris et al.., 1994). Applying the observed CN vs. IP correlation to the high pressure glasses yield estimated coordination numbers varying from 4.9 for the room pressure spectrum to 5.7 for the spectra for the highest pressure samples (Table 3.3.1). Fig. 3.3.4 shows the range of calculated average coordination numbers at the different pressures for the present samples. The calculated values support the idea of a lower average coordination number, close to 5, for the room pressure sample and a coordination number close to 6 for the high pressure samples, in full agreement with the more qualitative observation made by simple comparison with standard material.

Another observation regarding the pre-edge region of the spectra concerns the peak P full-width at half-maximum values (FWHM) that show an increase from 2.0 to 2.8 eV with increasing pressure. In crystalline compounds, as well as in glasses, narrower peaks have been found to be related to tetrahedrally coordinated Ti (e.g., (e.g.Ba_2TiO_4, 1.5 eV: Greegor et al., 1983) whereas larger FWHM values can been related either to the presence of a mixture of 4- and 6-coordinated Ti (e.g. diopside, 3.5-3.8 eV: Quartieri et al., 1993), or to a prevalent 6-coordinated distorted titanium environment whose pre-edges generally have larger FWHM (e.g.kaersutite, 2.7 eV; Lopez et al., 1993). However, in silicate glasses, in the case of a mixture of 4- and 6-coordinated Ti (Greegor et al., 1983) the spectrum also shows a strong increase of peak C (as well as P) with increasing of the tetrahedral component whereas this effect does not occur in the case of octahedral environments, as confirmed by MS calculations (Paris et al., 1994). The observation of these combined effects is therefore useful to discriminate

Table 3.3.1. Characteristics of XANES resonances, calculated average coordination numbers and density data for the set of glasses at different pressures.

P(kbar)	EP(eV)	IP	CN	EB(eV)	EC(eV)	D(g/cm^3)
0.001	4970.9	58	4.8	4986.3	4997.6	2.538±0.002
5	4971.0	57	4.8	4986.6	4999.2	2.553±0.001
10	4971.0	47	5.2	4986.9	4997.9	2.592±0.002
15	4971.1	35	5.6	4987.0	4997.9	2.477±0.001
20	4971.1	32	5.7	4986.6	4998.3	2.722±0.007
25	4971.1	30	5.8	4986.9	4998.1	2.802±0.03
30	4970.9	29	5.8	4987.0	4998.8	2.820±0.05

EP = peak P energy position ; IP = peak P normalized intensity; CN = calculated average coordination number, using the equation given in the text; EB = peak B energy position; EC = peak C energy position; D = measured density;

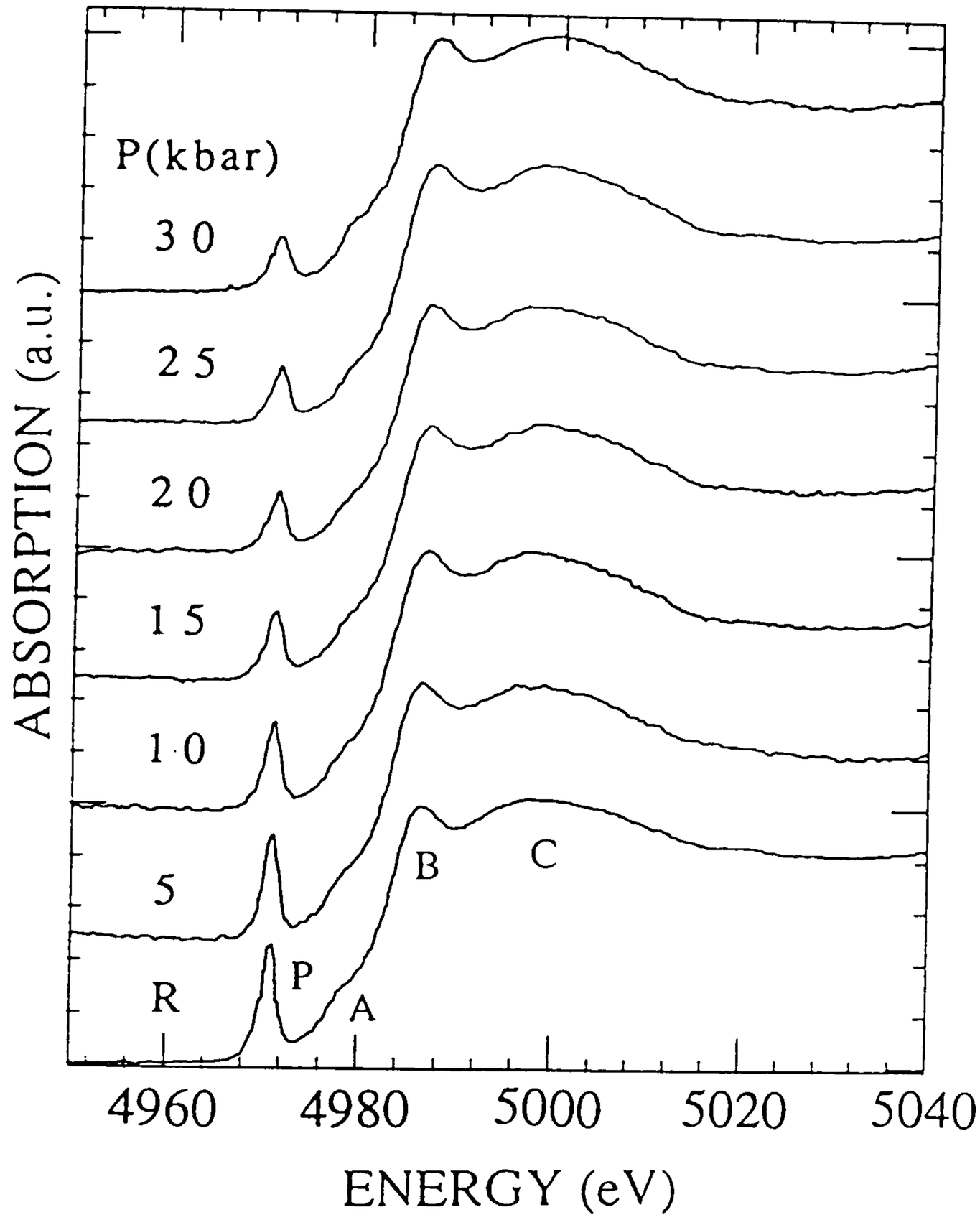

Fig. 3.3.1 Ti K-XANES spectra of $K_2TiSi_4O_{11}$ glasses quenched from different pressures. The main resonances are shown and labelled according to the text (P pre-edge peak, A, B, C). The intensity of peak P decreases strongly with the increasing pressures, suggesting an increase of the Ti average coordination number with pressure.

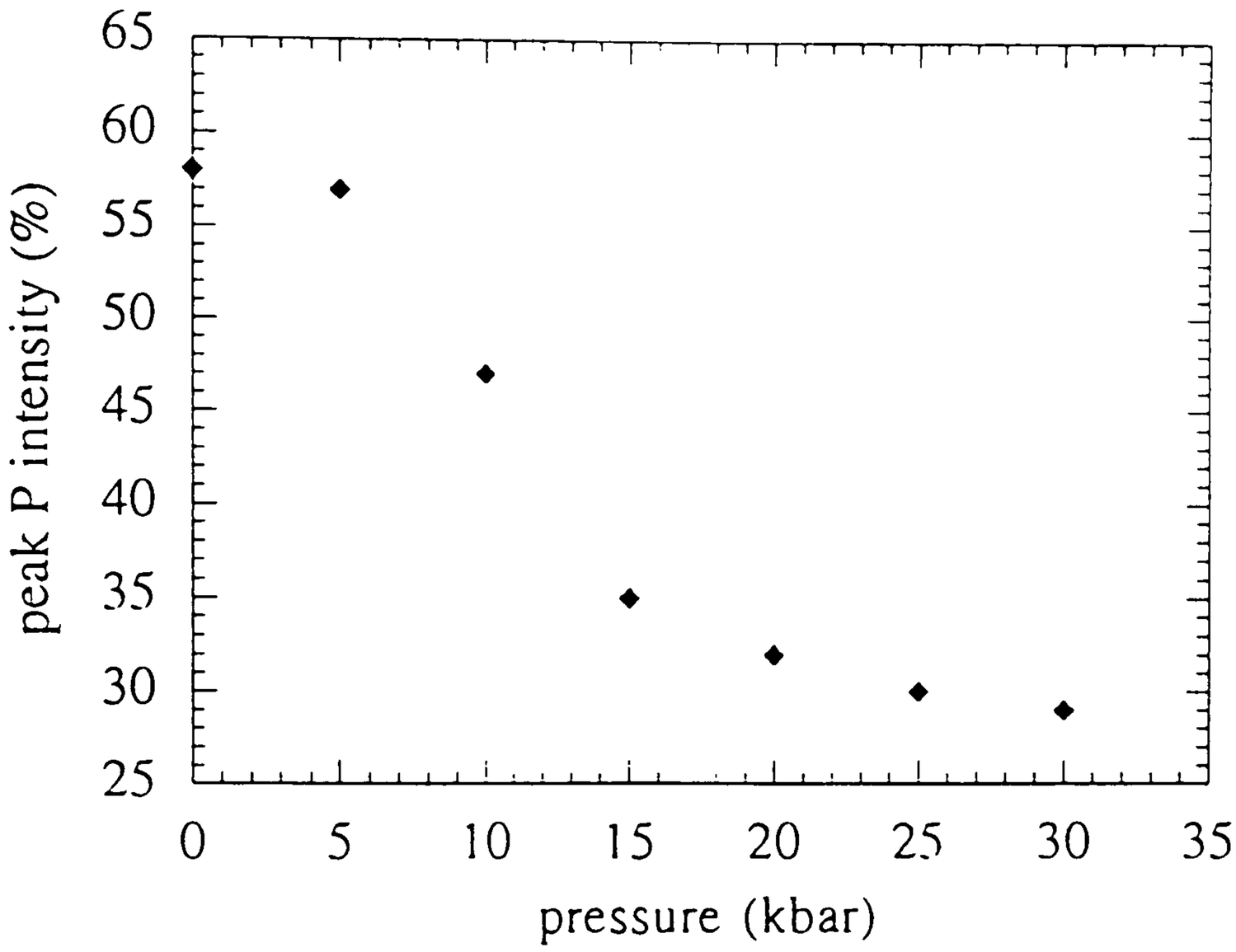

Fig. 3.3.2 Non-linear variation of pre-edge peak P intensity (IP) with pressure up to 30 kbar. The IP values (expressed in %) are normalized to high energy. A major decrease of the IP values occurs between 5 and 20 kbar, with little change above 25 kbar.

between the two possibilities. The FWHM value of 2.0 eV reported for 5-coordinated Ti in glass studied by Yarker et al (1986) is in agreement with the FWHM value for the room pressure spectrum and supports the interpretation of an average CN of 4.8. The increase of FWHM values I observe suggests therefore an increase of the octahedral component with pressure, as the FWHM value approach those of a distorted 6-coordinated environment (Lopez et al., 1993); the presence of minor amounts of other geometries cannot be ruled out. More precise understanding of the correlation between FWHM and structural environment requires further investigation. The detailed analysis made by Waychunas (1987) on a suite of octahedrally-coordinated Ti crystalline compounds also shows the pre-edge peak to be composed of different lines which appear to be symmetry dependent. The limited number of Ti compounds with other geometries other than octahedral does not allow similar investigations to be applied to them.

The energy position of the absorption edge gives an indication of the oxidation state of the material under investigation, if energy calibration is determined by using reference materials (Brown et al., 1988). However it has been shown that there is a large uncertainty in the determination of Ti oxidation state, due to the small shift in energy observed between Ti^{3+} and Ti^{4+} (about 2 eV) and also due to the "structure" effect that influences the resonances energy position (Waychunas 1987). In this study, a Ti metal foil (4966.4 eV) has been used for energy calibration. First derivatives of both the first inflection point of the spectrum and the inflection point at the edge ramp have been taken into consideration and the values scatter around 4970.1±0.1 and 4977.2±0.5, respectively. If the pre-edge peak P energy position considered as the most reliable measure of oxidation state (Waychunas, 1987), the samples show an energy shift of 4.5-4.7 eV with respect to Ti metal (Table 3.3.1). These values are consistent with the presence of tetravalent titanium but it is interesting to observe that they are much higher than those found for crystalline compounds in both tetrahedral (3.5 eV, Ba_2TiO_4; Yarker et al., 1986) and octahedral coordination (2.0-3.5 eV; Waychunas, 1987; Lopez et al., 1993). Instead, they are consistent with the values found for glasses (3.8-4.6 eV, Greegor et al., 1983; 4.8 eV, Yarker et al., 1986), suggesting not only a bond-length effect but also a structure-dependence of the energy of the pre-edge feature, similar to the case for crystalline silicates and oxides (Waychunas, 1987). For the purpose of this work however, it is important to note that no pressure-induced changes in the oxidation state were detected in the set of samples. However, given the large uncertainty of the method at this energy, up to 10% Ti^{3+}/Ti_{tot} could be present but not detected (Waychunas, 1987). On the other hand, absence of anomalous colour of the glasses is a good indications that the presence of even small amounts of Ti^{3+} can be excluded.

3.3.4.2 *Density data*

The measured density data for the studied glasses synthesized at different pressures are reported in Table 3.3.1. Fig.3.3.4 shows that the density increases slightly at low pressure then more steeply between 10 and 25 kbar and then less steeply again at the highest pressures. This behaviour suggests that the Ti environment reacts very rigidly at low pressures (<10kbar), followed by a dramatic change in the structure between 10 and 25 kbar and minor variation at higher pressures (>25kbar). This general variation of density versus pressure is consistent with the notion of a homogeneous equilibrium between the various coordination states of Ti which goes to near completion at P > 25 kbar. It is worthwhile to note that the pattern of density variation with pressure (Fig.3.3.4) is very similar to that of pre-edge peak intensity (Fig.3.3.2), suggesting a close correlation between density and Ti structural environment for these glasses.

3.3.5 Discussion and conclusions

The effect of pressure on the coordination state of cations of geological interest and their analogues have been studied with a variety of methods. In general, the conclusion has been reached that either there is little or no coordination change or it is unquenchable to room pressure. For example, for SiO_2 glasses it is has been shown that an increase in pressure up to 30 kbar produces no changes of the Si-O bond-length of the network-forming tetrahedra but produces instead a decrease of the intertetrahedral angles (Seifert et al., 1983; Davoli et al., 1992). Highly sensitive NMR investigations have identified the presence of several percent of more highly coordinated Si again from pressures much higher than those accessed in this work (Stebbins and McMillan, 1989; Xue et al., 1989). Only one report of a pressure induced coordination change of Al exists to date, that of Ohtani et al. (1985). An early investigation of Fe, Ga and Ge in silicate glasses quenched from pressures up to 30 kbar (Fleet et al., 1984) indicated no evidence for quenchable coordination shifts of those three cations. That study used X-ray absorption data for Ga and both XANES and EXAFS revealed no evidence for a coordination shift for synthesis pressures up to 25 kbar. More recent in-situ studies of coordination have illustrated a pressure-induced coordination shift of Ge at much higher pressures than those investigated here (Durben and Wolf, 1991). For GeO_2 glasses, in-situ high-pressure XAS studies have shown a transition from 4-fold to 6-fold coordination at ~70kbar and it has been found to be similar to that occurring in crystalline GeO_2 (i.e. from quartz-like phase to rutile-like phase) (Itié et al., 1989). Recently, Keppler and Rubie (1993) have pointed out that pressure produce changes of coordination for Ni and Co in doped albite glasses quenched from 100 kbar and 2900°C. Using crystal-field spectroscopy they found that Co and Ni, which seemed to be respectively tetrahedral and in a mixture of very distorted octahedral and tetrahedral sites at room pressure (cf. Galoisy and Calas, 1993) become octahedral at high pressure.

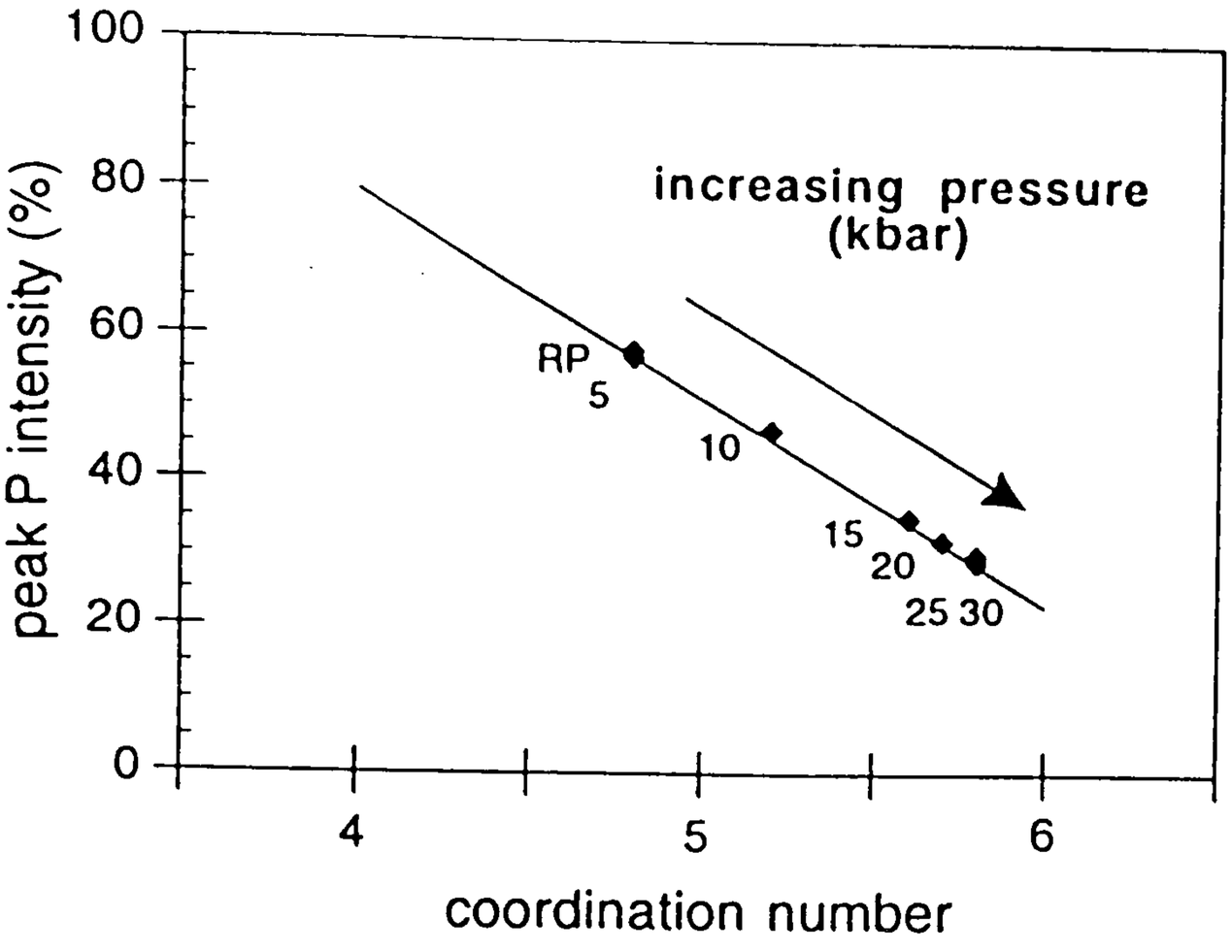

Fig. 3.3.3 Range of variation of average coordination numbers, as calculated from the equation of Dingwell et al. (1994), increasing from 4.8 for the room pressure glass to 5.8 for the highest pressure glass (30 kbar).

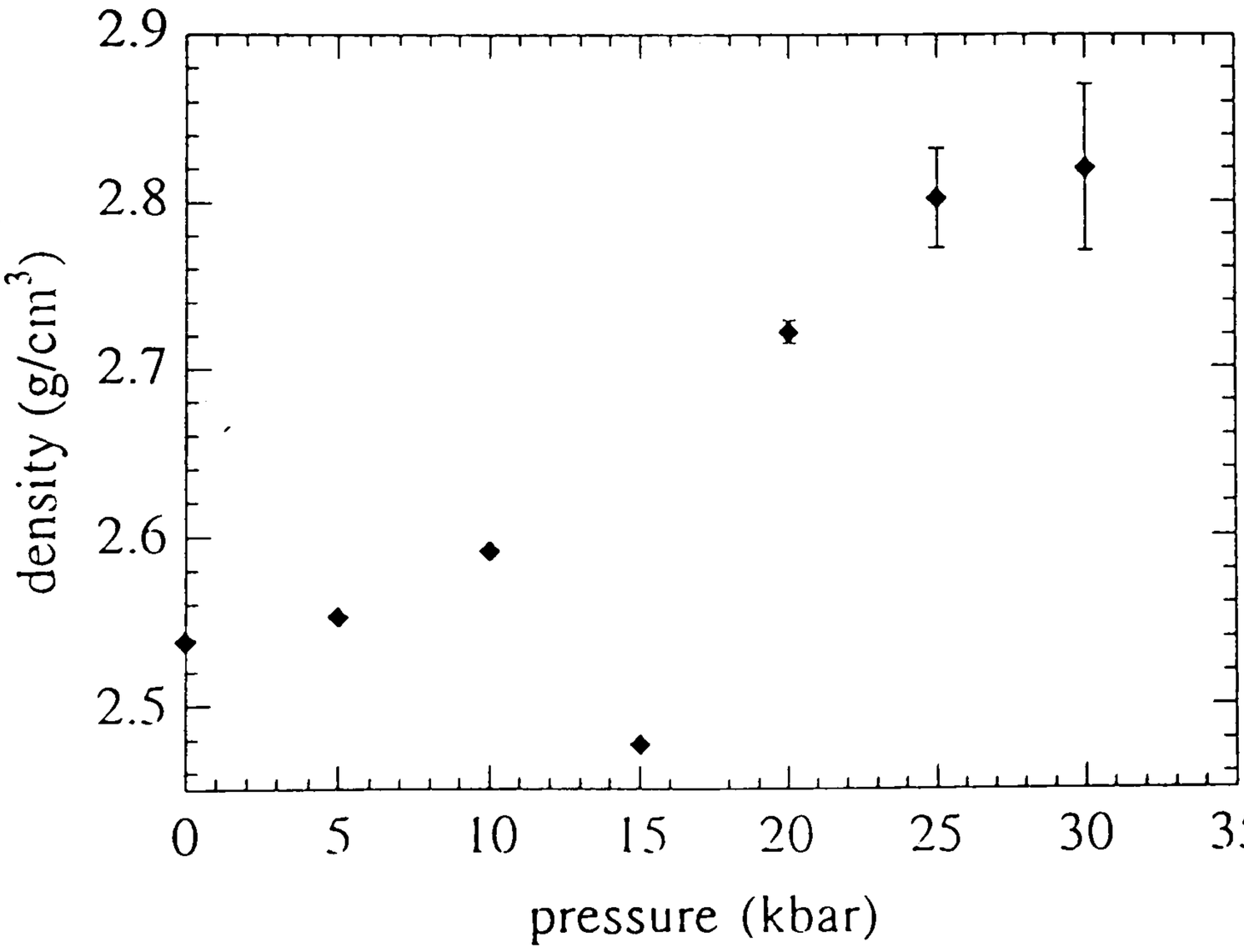

Fig. 3.3.4 Variation of measured glass density with synthesis pressure. The density increases also non-linearly, suggesting a rigid structural response at low pressure followed by a dramatic change between 5 and 25 kbar. (The 15 kbar sample disintegrated during the quench such that no suitably large fragments remained for accurate density determination.)

Previously, no information was available on the influence of pressure on titanium-bearing silicate glasses. The predominance of a distorted octahedral environment around Ti atoms at the higher pressures, determined mainly by comparison with mineral standards XANES data and also confirmed by a preliminary EXAFS analysis which yields an average bond length of 1.95(±.02)Å for the sample treated at 30 kbar. The pressure dependence of Ti coordination inferred in the present study is qualitatively different from all of the above cases in that a large (quenchable) shift in average coordination number occurs over a moderate range of pressure relevant to the petrogenesis of magmas in the crust and mantle.

3.4 APPLICATION OF MULTIPLE SCATTERING CALCULATION TO THE STUDY OF TITANIUM LOCAL GEOMETRY IN SILICATE GLASSES

3.4.1 Abstract

Multiple scattering calculations have been used to study the effects of coordination number, geometry, symmetry and polyhedral distortion on titanium XANES spectra. The calculations show the influence of each of these parameter on Ti K-edge XANES spectra and in particular they illustrate the significant influence of polyhedral distortion. The small clusters used for the calculations represent some possible geometries of titanium atoms in silicate glasses, where Ti is coordinated by oxygen and is found to be in different geometrical environments, mainly as a function of glass composition.

3.4.2 Introduction

The structural role of titanium in silicate glasses of various composition has been spectroscopically investigated by XANES (Chap. 3.2; Yarker et al., 1986; Greegor et al., 1983). Titanium local geometry has been found to vary as a function of the glass/melt composition and this behavior has important geological as well as technological implications because of potential effects on the physical properties of silicate melts and glasses. In glasses, as well as in crystalline compounds (Behrens et al., 1991), Ti coordination number (CN) has been found to vary between 4 and 6 and the changes observed in the XANES spectra as a function of CN and local geometry indicate a need to investigate in detail the structural role of Ti by using multiple scattering (MS) calculations.

3.4.3 Results and discussion

The simulation of the XANES spectra is based on the one-electron multiple-scattering (MS) theory of Lee and Pendry (1975), and takes advantage of the refinements to the theory and computational methods progressively introduced by Natoli et al. (1980), Durham et al. (1982), and Natoli and Benfatto (1986).

Fig. 3.4.1 shows the variation in the calculated Ti K-edge XANES spectra in passing from CN=4 to CN=6 for clusters containing Ti^{4+} coordinated by 4, 5 and 6 oxygens. In transition elements like Ti an intense pre-edge peak is produced by the electronic transition 1s-3d (Waychunas 1987). This transition does not occur when Ti is in a regular octahedral site (Fig.3.4.1a; e.g.benitoite (Waychunas 1987)) whereas it becomes partially allowed when it is in a non-centrosymmetrical site like a tetrahedron (Fig.3.4.1d; e.g.Ba_2TiO_4 (Behrens et al. 1991)). For all the clusters, the changes in local geometry also produce variations of the shape of absorption resonances in the edge region. Two different geometries are reported for 5-fold Ti^{4+}, both found in mineral

standards and in glasses: a square pyramid (Fig.3.4.1b) (Nyman et al., 1978) and a trigonal bipyramid (Fig.3.4.1c). They show a strong change in the pre-edge peak intensity which is higher for the bipyramid cluster due to the hybridization of the ground state (Kuiper et al., 1989) and the different overlapping of the orbital wave-functions in the two clusters.

The effect of polyhedral distortion in octahedrally coordinated Ti is shown in Fig.3.4.2. Curve (a) is the regular octahedron and in curve (b) it is shown the effect of a tetragonal symmetrical distortion of the cluster, producing a shift of the absorption edge towards low energy, due to the Ti-O bonds along z-axis being longer than those on the xy-plane. Curves (c), (d) and (e) show the spectra obtained by using clusters with increasingly asymmetrical Ti-O bonds along the z-axis. Asymmetrical distortion yields spectra with a pre-edge peak which grows as a function of the asymmetry of the z-axis bonds, and a shoulder on the rising part, evident in curves (d) and (e). This feature is always present in experimental spectra of octahedrally coordinated compounds (Waychunas 1987).

Following the results obtained by fitting experimental pre-edges using spectra of standard materials with different CN (Behrens et al., 1991), the spectra of glasses of different composition have been simulated using theoretical spectra. Fig.3.4.3 shows the the results from linear combination of the theoretical spectra of a distorted octahedron (Fig.3.4.2e) and a trigonal bipyramid (Fig.3.4.1c). Similar geometries have been found to occur in silicate glasses containing other transition elements like Co and Ni (Keppler 1992; Galoysi and Calas 1993). The best fit with the experimental spectra (Fig.3.4.3a and 3.4.3c) is obtained when combining the theoretical spectra in proportions respectively 25:75 (Fig.3.4.3b) and 50:50 (Fig.3.4.3d). The agreement with experimental spectra suggests that a more quantitative evaluation of Ti distribution in different geometries by XANES calculations is possible.

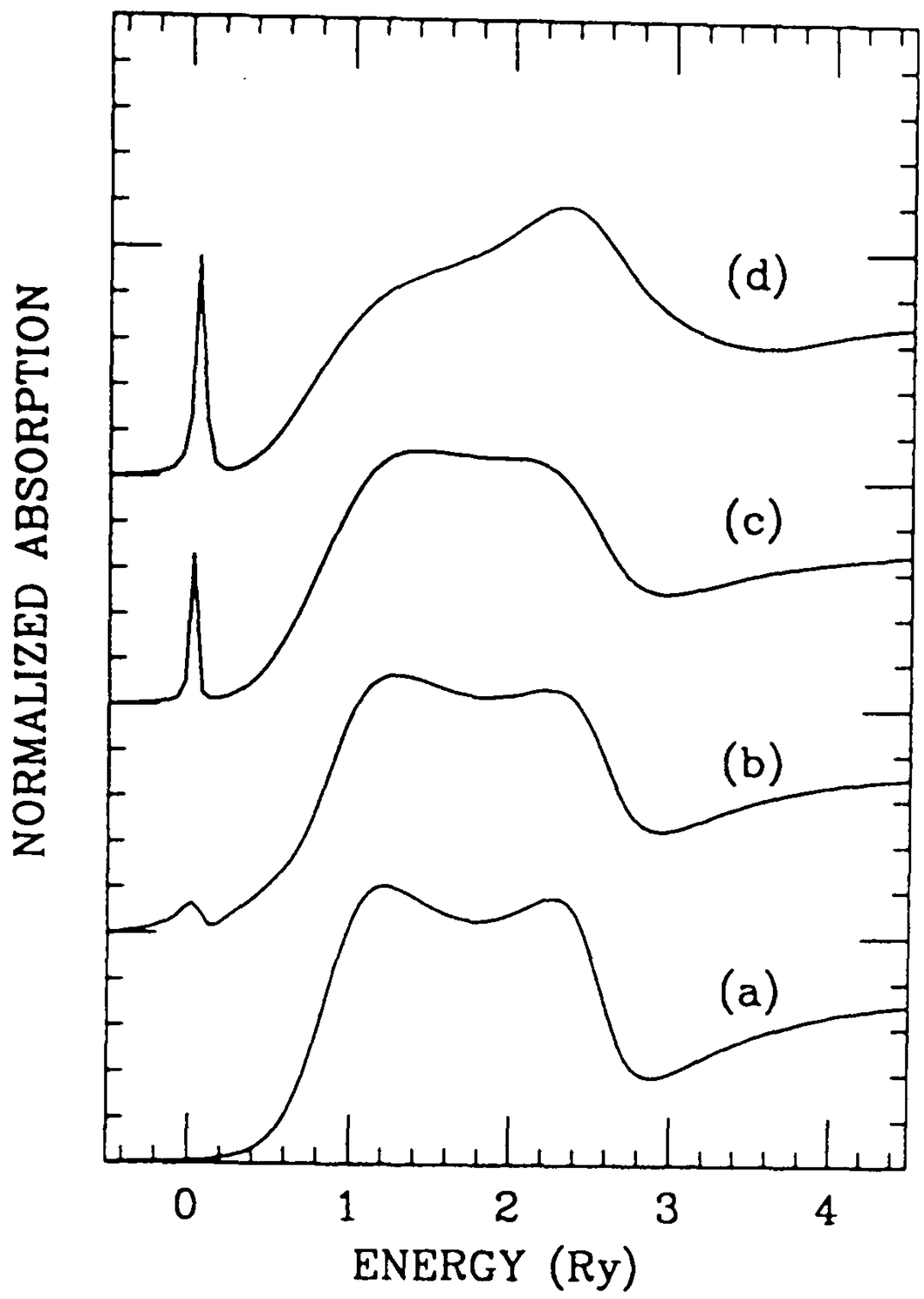

Fig. 3.4.1 Theoretical XANES spectra at the Ti K-edge for different clusters: (a) octahedron, CN=6; (b) square pyramid, CN=5; (c) trigonal bipyramid, CN=5; (d) tetrahedron, CN=4.

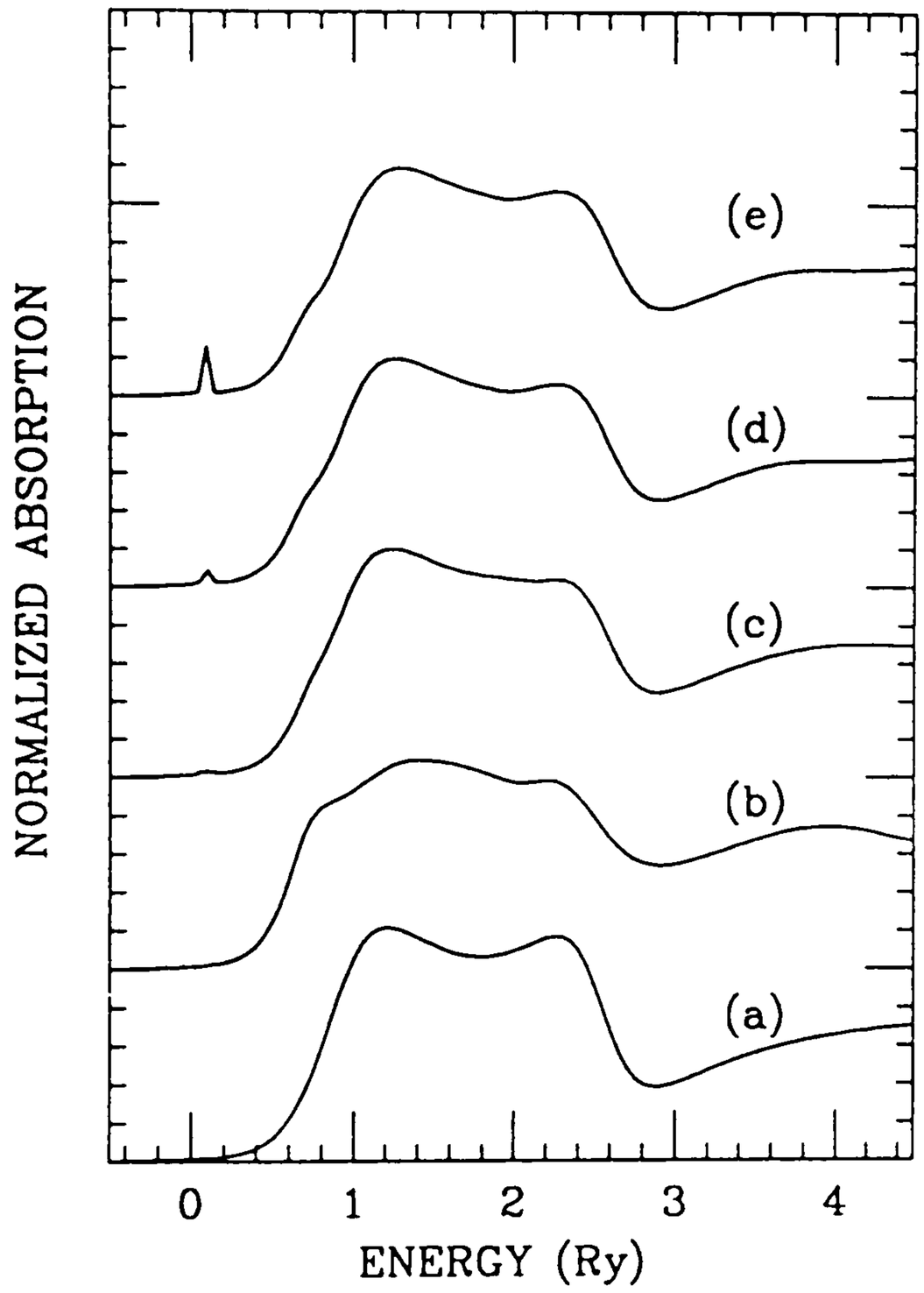

Fig. 3.4.2 Computation of Ti K-edge XANES spectra using an octahedral cluster with different types of distortion: (a) regular octahedron; (b) tetragonal distortion; (c), (d), (e) increasing degree of asymmetrical distortion along the z-axis.

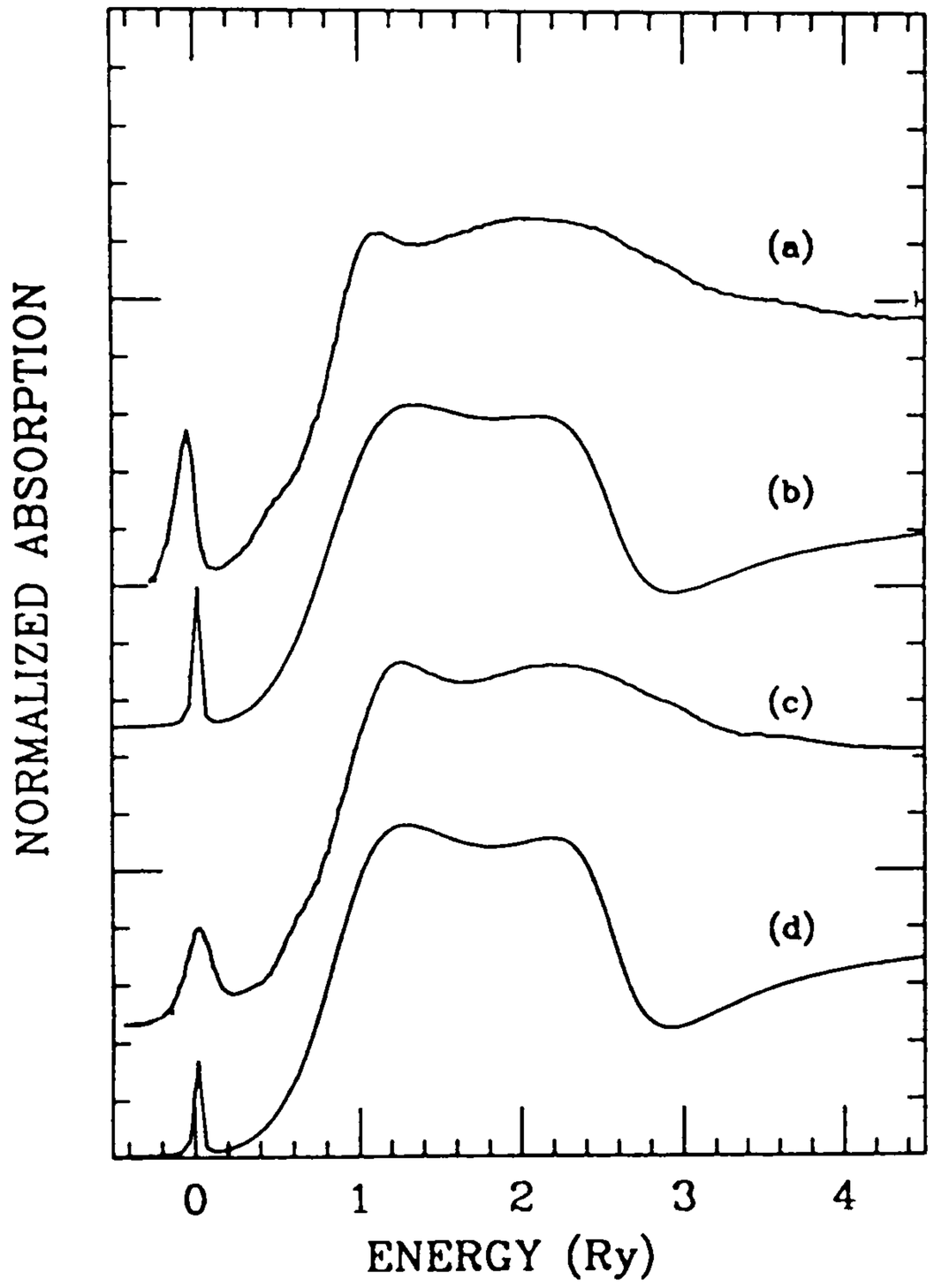

Fig.3.4.3 Experimental XANES spectra of the Ti K-edge in silicate glasses ((a) $K_2TiSi_4O_{11}$ glass; (c) $Li_2TiSi_4O_{11}$ glass (see Chapter 3.3)) compared with theoretical spectra obtained by linear combination of distorted octahedron and trigonal bipyramid in different proportions ((b) 25:75; (d) 50:50)

CHAPTER 4. FE SITE GEOMETRY IN ORTHOPYROXENES

4.1 IRON SITE GEOMETRY IN ORTHOPYROXENE: MULTIPLE SCATTERING CALCULATIONS AND XANES STUDY

4.1.1 Abstract

The iron site geometry in orthopyroxenes (OPX) and synthetic FeO has been investigated by XANES spectroscopy. Multiple scattering calculations have been used to determine how the iron polyhedral geometry affects the absorption spectra. The results demonstrate that this approach is effective in determining the site geometry around the absorbing atom, allowing the assignment of features in the XANES spectrum to specific structural aspects of the coordination environment. In the case of orthopyroxene this method allows discrimination between the multiple scattering contributions to the absorption spectrum due to the two octahedral sites *M1* and *M2* of the OPX structure. The results obtained with the MS calculation were used to evaluate the effects of polyhedral distortion, symmetry changes and iron site occupancies on the experimental spectra. The results indicate a more quantitative way to interpret XANES experimental spectra and give insights into the interpretation of site geometries of more complex or unknown structures and amorphous materials.

4.1.2 Introduction

X-ray absorption spectroscopy (XAS) is an element specific spectroscopic technique which can provide structural information on the atomic environment around a selected absorbing atom in both crystalline and amorphous materials (e.g., Bianconi 1988; Binsted at al., 1986; Bianconi et al., 1982). EXAFS (Extended X-ray Absorption Fine Structures) and XANES (X-ray Absorption Near-Edge Structure) give information on oxidation state of the absorbing atom, bond-distances and coordination numbers and site geometry (Brown et al., 1988). In particular, it has been found (Durham et al., 1982) that much information on the local geometry around the selected atom can be extracted by analyzing the structures of the absorption spectrum at a few tens of electron volts above the absorption edge (the XANES region). The XANES spectra can provide information on the oxidation state of the absorber, the polyhedral coordination, and also information on the degree of distortion for non-regular sites (Garcia et al., 1989). These capabilities make XAS spectroscopy strongly complementary to X-ray diffraction methods.

Particularly when studying XANES spectra of transition elements, a comparison with structurally well-characterized standards is the method traditionally used to distinguish, in a first approximation, between a tetrahedrally- and an octahedrally-

coordinated absorbing atom (Waychunas et al., 1983; Henderson et al., 1993). Although effective, this fingerprint method cannot give detailed information on the geometry of the site or its degree of distortion, especially when the materials under investigation have structures significantly different from those of the standards. The multiple scattering (MS) processes in this part of the absorption spectrum are mostly responsible for the presence of these features, but the correlation and/or unequivocal attribution of MS resonances to structural details is still the subject of active research. Moreover, it is still not clearly understood what the effects are on the XANES spectrum produced by different groups of atoms situated at different distances from the absorber ("structure effect"), how the symmetry of the site influences the spectrum and to what extent it is possible to recognise polyhedral distortion from the XANES spectrum.

The purpose of this paper is to show how a more quantitative evaluation of XANES spectra can be obtained through application of multiple scattering (MS) calculations, using in this case the example of Fe in orthopyroxene. Due to the recent developments of the XANES theory (Tyson, 1992), theoretical calculation of the XANES spectra can now be performed, based on the one-electron multiple scattering theory, and the calculated spectra can be used to evaluate the effects of site geometry on experimental XANES spectra (Paris et al., 1992; Giuli et al., 1993). Here I present some examples of interpretation of experimental iron K-edge XANES spectra based on the results obtained from multiple scattering calculations at the iron K-edge. We focus the attention on iron in octahedral coordination using as a starting point the simple structure of iron oxide. We then extend the analysis to the iron environments in minerals with more complex structures, using orthopyroxenes as an example. In orthopyroxenes the presence of iron in two distinct octahedral sites makes the XAS study much more complicated, the absorption spectrum being due to contributions from Fe atoms both in *M1* and in *M2*. Since the samples whose spectra used in this paper have been previously well characterized by other methods (XRD, Mössbauer; Anovitz et al., 1988) as well as XAS (Mottana et al., 1991) we can use here the available information on both site occupancy and structural data to test the theoretical models.

4.1.3 Experimental

The orthopyroxene and FeO XANES spectra reported here are have been analyzed and described in detail by Mottana et al. (1991) and the experimental methods will be only briefly summarized. X-ray Absorption spectra have been collected using the ADONE storage ring of the Frascati (Italy) synchrotron radiation center, working at 1.5 GeV and with a beam current in the range 30-100 mA. The Fe K-edge XANES spectra were recorded in transmission mode at the X-ray experimental station of the PULS laboratory using a channel-cut Si (111) single crystal as the monochromator (Davoli et al., 1988). The analyses were performed using 0.5 mm entrance slits giving an energy resolution of

about 1 eV. A Fe-metal foil (by EXAFS Materials, Fe K-edge at 7112 eV) was used to ensure a consistent energy calibration for all the samples and to verify iron oxidation state. Sample preparation involved smearing finely powdered samples on a kapton tape, taking special care in checking the homogeneity and the samples thickness, to avoid pinhole effects and ensure a good signal to noise ratio. The spectra have been reduced by subtraction of the background and normalized to the high energy side of the spectra. Peak intensities have been evaluated by standard gaussian fitting.

A synthetic sample has been used for FeO XAS data collection, after a preliminary characterization by X-ray diffraction (XRD) analysis. The orthopyroxenes XANES spectra have been recorded (Mottana et al., 1991) using a natural sample (original name M32b) analyzed at room temperature and after heating at 900° C in a gas mixing furnace at controlled oxygen fugacity (Anovitz et al., 1988). The samples had been chemically characterized by microprobe and Mössbauer spectroscopy to determine iron concentration, Fe site occupancies and oxidation state. The samples were found to be almost Fe^{3+} free and no iron oxidation was detected after the heating process.

4.1.4 Theory

The computations of the XANES spectra were carried out using the multiple scattering model (Durham et al., 1982; Natoli,1984; Natoli and Benfatto, 1986; Tyson et al., 1992). Muffin-Tin (MT) potentials with X-alpha exchange terms were constructed for the various clusters using relativistic atomic charge densities. Given these MT potentials, the total cross sections including all multiple scattering paths for the atoms involved were calculated using the extended continuum scheme in which all of the final states are treated on equal basis as a part of the continuum.

Examples of the application of this method to solid systems are the calculations at the Na K-edge in NaCl (Gunnella et al., 1990) and the study by Sainctavit et al. (1986) on the S and Zn K-edges in sphalerite, ZnS. It has been found that the main limitation of the model is the non-physical partitioning of the potential into spherical regions around each atom and a constant region in between them. In general, by experience, one cannot obtain very accurate relative intensities of XANES peaks. However, for compact structures such as those reported in the literature (Gunnella et al., 1990; Sainctavit et al., 1986) the relative intensities obtained in the calculations are very close to those seen in the experimental spectra and, in particular, for NaCl and ZnS accurate peak intensities and splittings have been obtained.

Using this model gives results with realistic energy spacings between resonances. Obtaining greater accuracy will require the elimination of the MT approximation and the use of self-consistent (SCF) potentials. In particular, by using SCF potentials (Tyson et al., 1992) one typically finds errors on the order of 2 eV in peak separations. The "sharpness" of the features observed in the computed spectra depends on the use of MT

potentials, the absence of experimental resolution limits and core-hole broadening, which will account for a total width of 2 eV. In this work we did not broaden the calculated spectra to take into account these factors in order to better exhibit even the minor features in the calculated spectra. For absorption edges of light elements (i.e. oxygen) it is important to include SCF potential since a significant portion of the charge of the atom is outside of the core. However, at increasing Z, the Z+1 approximation to the potential becomes more and more accurate. From experience on a variety of elements, I found that for the transition elements the inclusion of SCF potential does not modify greatly the intensities or splitting of the XANES features. Therefore, in the case of iron K-edge, the major uncertainties arise from use of the MT potential approximation.

4.1.5 Multiple Scattering Calculations

4.1.5.1 *The FeO case*

Synthetic FeO has been chosen as a starting case to study the site geometry of Fe atoms located in a single undistorted octahedral site. Like other divalent oxides (MnO, CoO), FeO crystallizes with the high-symmetry halite structure (*Fm3m*) and it represents therefore a rather simple starting point for both geometrical and computational reasons: geometrically because in FeO iron is in a single regular octahedral site, and computationally because the high symmetry reduces the computation time required by the complexity of MS calculations.

An evaluation of the geometry of the polyhedral sites can be expressed in terms of quadratic elongation (Q.E.) and angle variance (A.V.), as calculated by Robinson et al. (1971). The unique octahedral iron polyhedron in FeO has real local *m3m* symmetry (O_h on the basis of crystal-field model) and a calculated Q.E. equal to 1.0000, indicating perfect regularity with six equal Fe-O bond lengths of 2.155 Å and no angular distortion (Table 4.1.1) (Foster and Welsh, 1956; Smyth and Bish, 1988). However, in spite of the regularity of this site, Mössbauer spectra of wüstite samples show splitting of the singlet, which should be still consistent with a regular octahedron, but suggesting that at least some of the Fe^{2+} sites can be distorted (McCammon and Price, 1985).

The experimental FeO XANES spectrum collected at the Fe K-edge is shown in Fig. 4.1.1a, where the energy scale has been rescaled using as zero the energy value of the first derivative maximum. There is a single peak (in the following referred to as A) at 8 eV, a peak (B) at 25 eV, a small shoulder (C) at about 40 eV, a large peak (D) at 55 eV and a bump at about 100 eV (E). A small bump (A') is also evident in the low energy side of the main peak A in the experimental spectrum and its presence suggests a minor geometrical distortion around the absorbing atoms in the synthetic FeO. This effect is

Table 4.1.1: Atoms composing the clusters used for MS calculations.

	FeO	OPX-M1	OPX-M2
	Fe	Fe1	Fe2
	O (2.155)	O (2.085)	O (1.987)
	O (2.155)	O (2.086)	O (2.023)
	O (2.155)	O (2.122)	O (2.123)
	O (2.155)	O (2.128)	O (2.161)
	O (2.155)	O (2.193)	O (2.455)
	O (2.155)	O (2.195)	O (2.589)
CN	6	6	6
PS	m3m	1	1
m	2.155	2.135	2.223
D	0	0.110	0.602
s	0	0.049	0.243
Q.E.	1.0000	1.0088	1.0700
A.V.	0	28.7	181
	Fe (3.048)	Fe2 (2.995)	Si (2.881)
	Fe (3.048)	Fe2 (3.069)	Fe1 (2.995)
	Fe (3.048)	Fe1 (3.141)	Fe1 (3.069)
	Fe (3.048)	Si (3.216)	O (3.099)
	Fe (3.048)	Fe2 (3.271)	Si (3.145)
	Fe (3.048)	O (3.293)	Fe1 (3.271)
	Fe (3.048)		Si (3.299)
	Fe (3.048)		
	Fe (3.048)		
	Fe (3.048)		
	Fe (3.048)		
	Fe (3.048)		
	Fe (3.048)		
	O (3.733)	Si (3.296)	Si (3.330)
	O (3.733)	Si (3.331)	Si (3.419)
	O (3.733)	Si (3.341)	O (3.515)
	O (3.733)	O (3.379)	O (3.555)
	O (3.733)	Si (3.443)	Si (3.640)
	O (3.733)	Si (3.556)	O (3.675)
	O (3.733)	O (3.651)	O (3.675)
	O (3.733)	O (3.667)	Si (3.758)

Fe1 iron atoms in M1 site, Fe2 iron atoms in M2 site; in brackets distances from the absorbing atom Fe (Å); CN coordination number; PS point symmetry; m average bond distance (Å); D difference between longest and shortest distance (Å); s standard deviation of the distances (Å); Q.E. quadratic elongation; A.V. angle variance (deg^2)

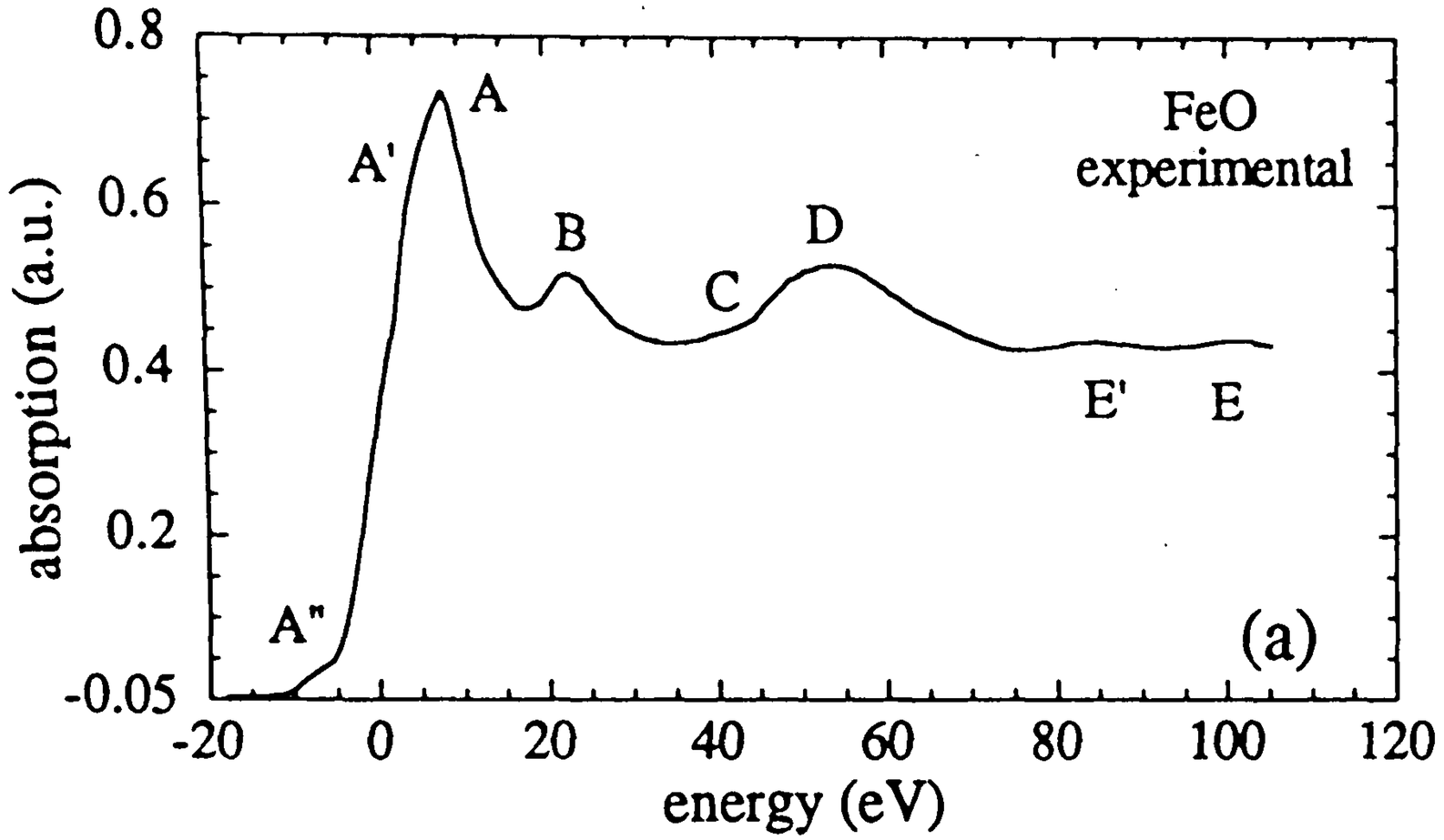

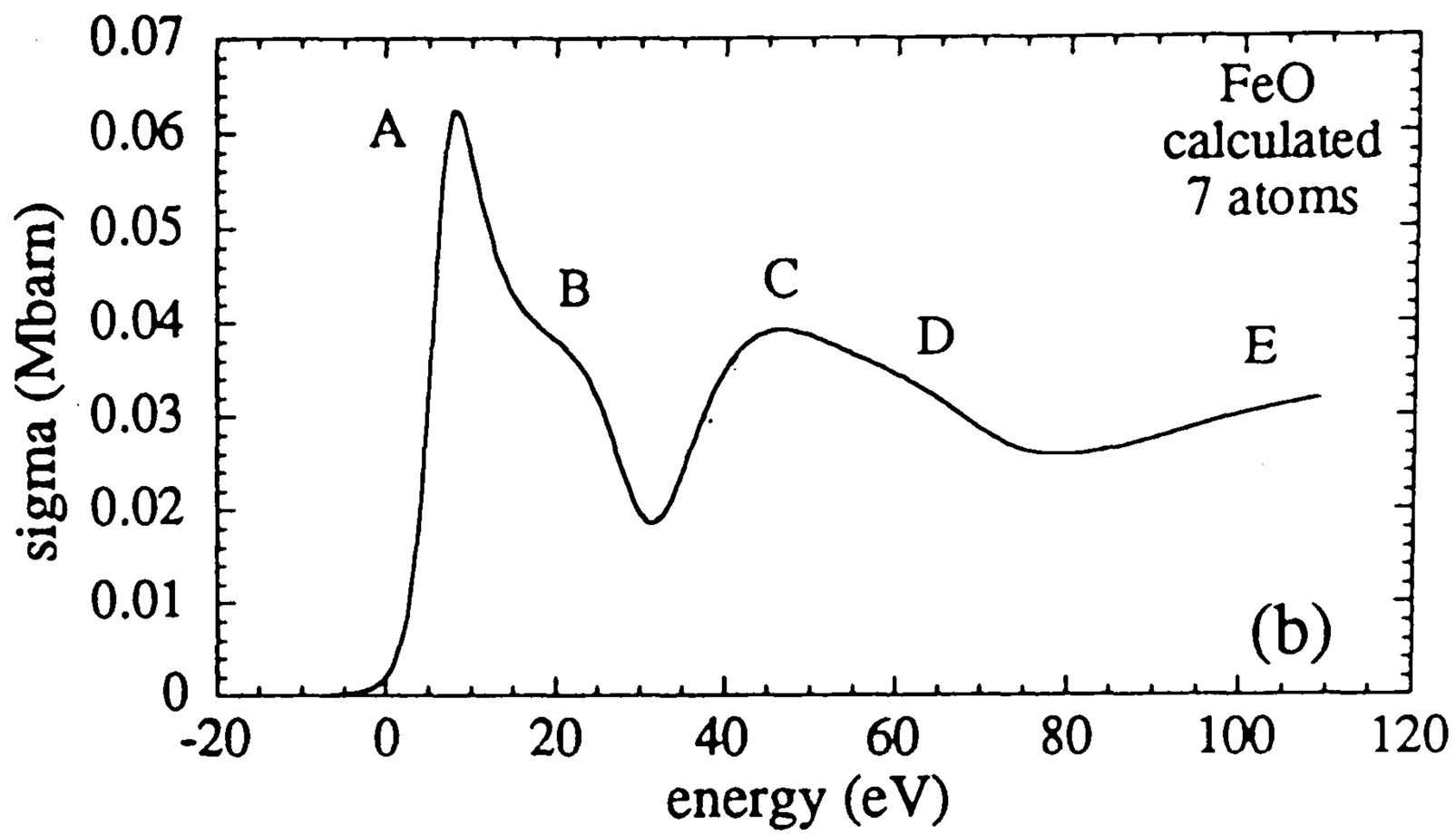

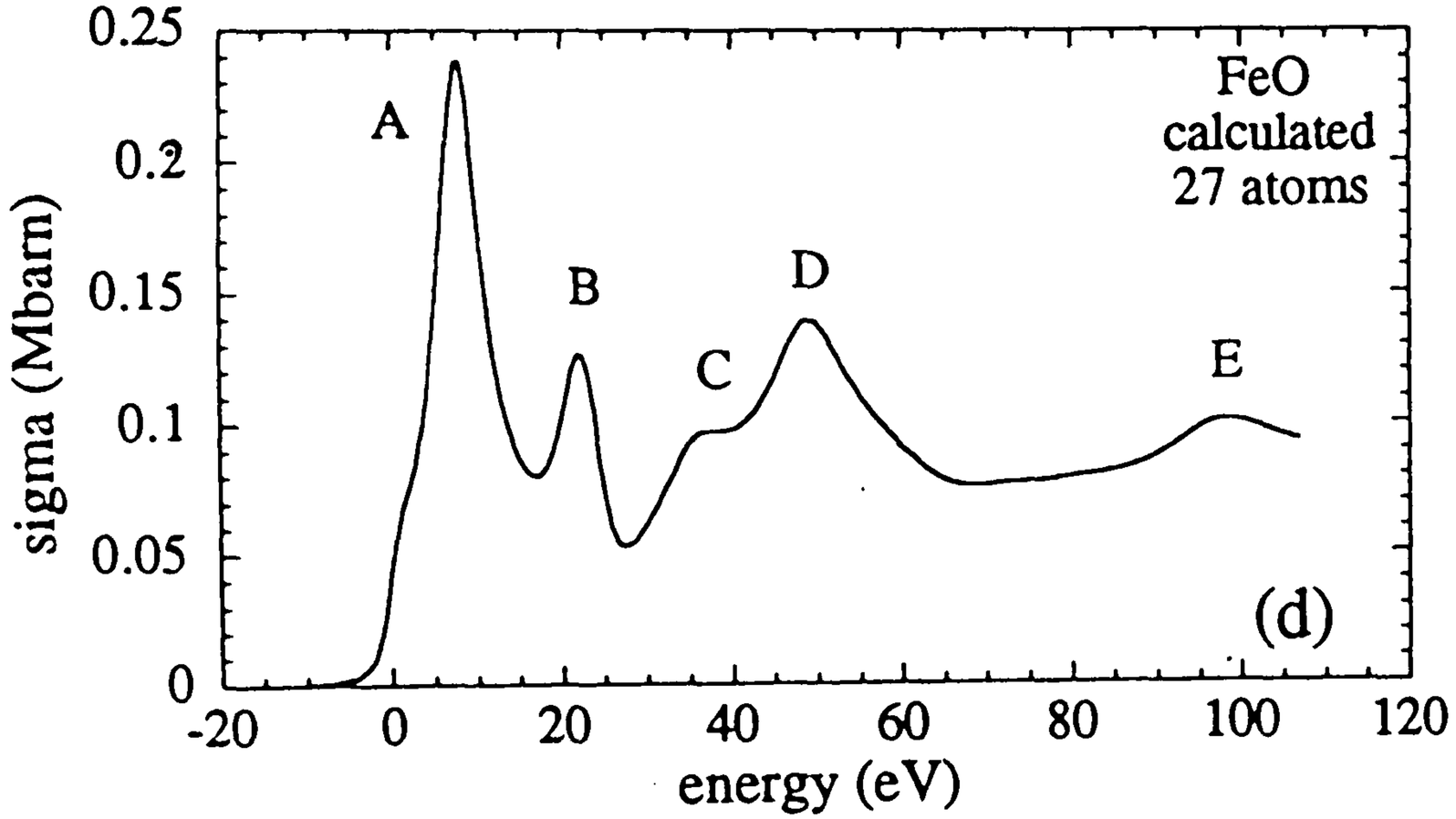

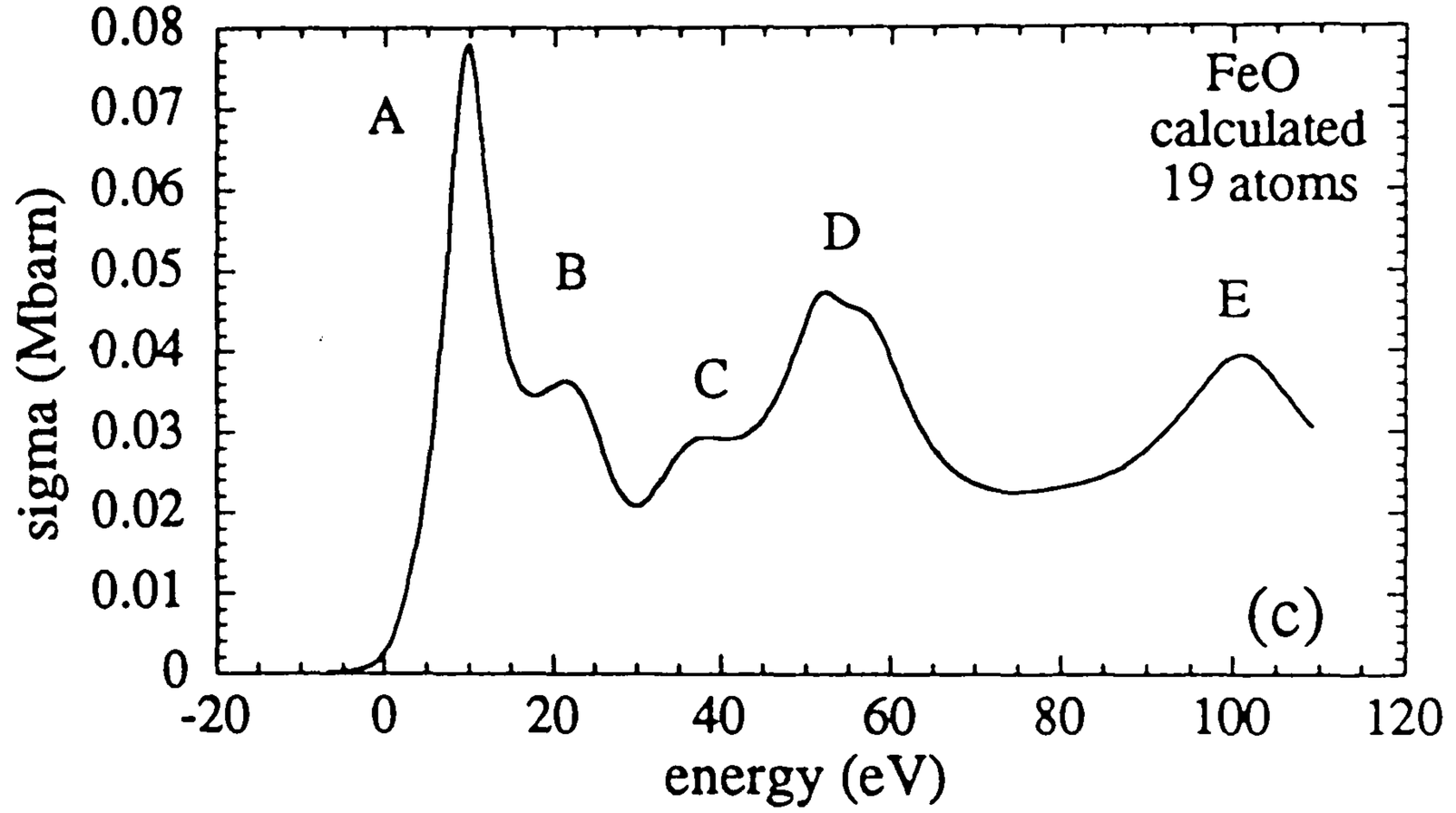

Fig.4.1.1 **a–d.** FeO case. **a** experimental XANES spectrum at the Fe K-edge (Mottana et al. 1991), showing the peaks A″, A′, A, B, C, D, E′, E. **b** XANES FeO calculated spectrum (Fe K-edge) using a cluster of 7 atoms. **c** a cluster of 19 atoms. **d** a cluster of 27 atoms

probably due to non-stoichiometry reasons: in fact, vacancies in the FeO structure can be charge-compensated by the presence of Fe^{3+} ions which would tend to cluster and produce short-range order (Waychunas, 1983).

In general, the XANES absorption spectrum due to transition elements in a single regular octahedral site is characterized by a unique symmetrical peak at a few eVs beyond the absorption threshold (Waychunas et al., 1983; Jackson et al., 1987). Concerning the pre-edge part of the XANES region, a low-intensity peak (A''), as found in the FeO experimental spectrum (Fig. 4.1.1a) is consistent with the presence of an almost regular octahedral site and/or presence of minor quantities of Fe^{3+}. The presence of the pre-edge peak is related, in fact, to transitions to *3d* levels. Since this transitions are dipole-forbidden in O_h symmetry when a transition element is in a regular octahedral coordination there is no peak in the pre-edge region, but it appears when polyhedral distortion takes place. As an extreme case, an intense pre-peak is present when Fe atoms are tetrahedral coordination (Lytle et al., 1988) due to the presence of transitions from a_1 to t_2 energy levels which are electric dipole allowed in T_d symmetry.

In Fig.4.1.1 the experimental spectrum is compared with multiple scattering calculations carried out on clusters of different sizes (Figs. 4.1.1b,1c,1d). The calculations have been performed by building clusters using the structural refinement by Foster and Welch (1956) and progressively adding atoms, which in the FeO structure are grouped for symmetry reasons at the same distance from the absorber.

The smallest cluster used for the FeO MS calculations is composed of an iron atom as the photoabsorber, surrounded by 6 octahedrally coordinated oxygens, all located at a distance of 2.155 Å (Fig.4.1.1b). In spite of the small number of the atoms involved in the calculations, the theoretical spectrum shows reasonable agreement with the overall shape of the experimental XANES spectrum. The spectrum shows a main resonance A followed by smaller features B, C and D located at higher energy. Adding the second shell, composed of 12 iron atoms at 3.048 Å, to the cluster produces a number of features (Fig. 4.1.1c), due to the large number of atoms of the same type added to the cluster and to the high scattering power of iron atoms at this energy. In particular, compared with the smaller cluster model (Fig.4.1.1b), peak A and B increase in definition, C and D assume a more complex configuration being composed of several resonances and a new peak (E) appears at about 100 eV from the absorption threshold.

The third shell added to the cluster is composed of 8 oxygens located at 3.733 Å from the central Fe atom (Fig.4.1.1d). The effects on the calculated spectrum due to the enlargement of the cluster size are less significant compared with the effects of adding the second shell (Fig.4.1.1c). This is mostly due to the lower scattering power of oxygen compared to iron at this energy, and also to the smaller number of atoms added to the cluster. As a result, there are no modifications for the A peak, whereas B and C become

much more defined, D merges into a single symmetric peak at lower energy, E becomes broader, and a shoulder appears at the low energy side of the main peak A.

In order to eliminate the effects of charge transfer, we first computed a 3-shells potential (27 atoms). Using this 3-shells potential, XANES spectra for 1, 2 and 3-shells clusters were computed. In this way, when one increases the cluster size in the computations, the changes seen are only due to MS contributions, i.e. structural effects. In Fig.4.1.2 the comparison between calculated spectra with a 1-shell cluster potential (Fig.4.1.2; a) and a 3-shells cluster potential (Fig.4.1.2; b) is shown. The spectrum (b) indicates that if charge transfer effects are eliminated the intensities are in better agreement with the experimental intensities.

The comparison between the final calculated spectrum (Fig. 4.1.1d) and the experimental (Fig.4.1.1a) indicates that the shape of peak A is dominated by the multiple scattering contribution of the first shell of oxygens around the absorber. Moreover, adding more than three shells of atoms does not change much the shape of the calculated FeO spectrum, but it only sharpens the features that are already present in the 3-shell calculation (Kitzler, 1992). This is also demonstrated from the calculation of larger clusters for the isostructural compound MnO (Chaboy et al., 1992), up to a maximum of 5 shells around the absorber and 39 total atoms.

4.1.5.2 *The orthopyroxene case*

The MS calculations performed on the FeO structure give an example of the influence of structural details on XANES spectra with increasing cluster size around the absorbing atom. The same method has been applied to more complex mineral structures, characterized by iron located in more than one site.

The orthopyroxene structure (OPX) has been chosen for this study due to the presence of two distinct octahedrally coordinated sites, *M1* and *M2* (Sasaki et al., 1982). As a starting point we consider the extreme case of ferrosilite (Table 4.1.1), where the two sites differ in two aspects: a) average *M*-O distance, which in ferrosilite is 2.135 Å for *M1*-O and 2.223 Å for *M2*-O.

b) degree of local symmetry. Although the real local symmetry is 1 for both, *M1* is a fairly regular octahedron that closely approximates the O_h symmetry (*m3m*), with each of the coordinating oxygens being linked to one silicon atom (Burns, 1970). However, on the basis of optical and Mössbauer studies *M1* is assumed to approximate the D_{4h} symmetry (Steffen et al., 1988), although C_{3h} has been recently proposed (Van Alboom et al., 1993). Also *M1* has a smaller polyhedral volume and a shorter mean Fe-O bond length than *M1*2(Table 4.1.1) which not only has a larger volume and a longer mean Fe-O bond-length but it is much more distorted than *M1* (Table 4.1.1). With all the bond-lengths different, the *M2* site has C_1 point symmetry but optical absorption data have shown that Fe^{2+} has a higher electrostatic pseudo-symmetry so that the site *M2*

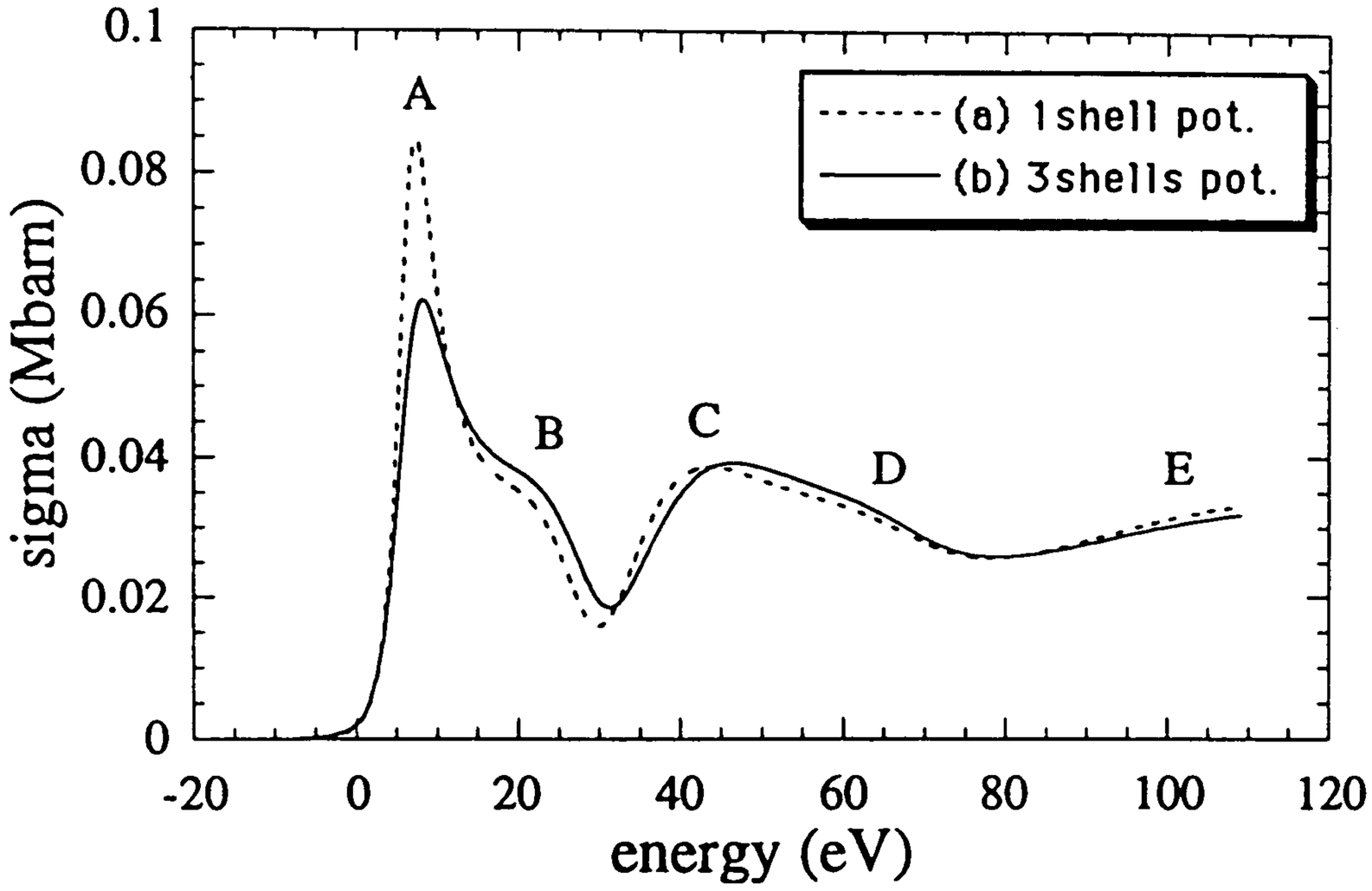

Fig. 4.1.2 The FeO 7-atoms cluster calculated using a 1-shell potential (a), compared with the same cluster calculated using a 3-shell potential (b), (see text for explanation).

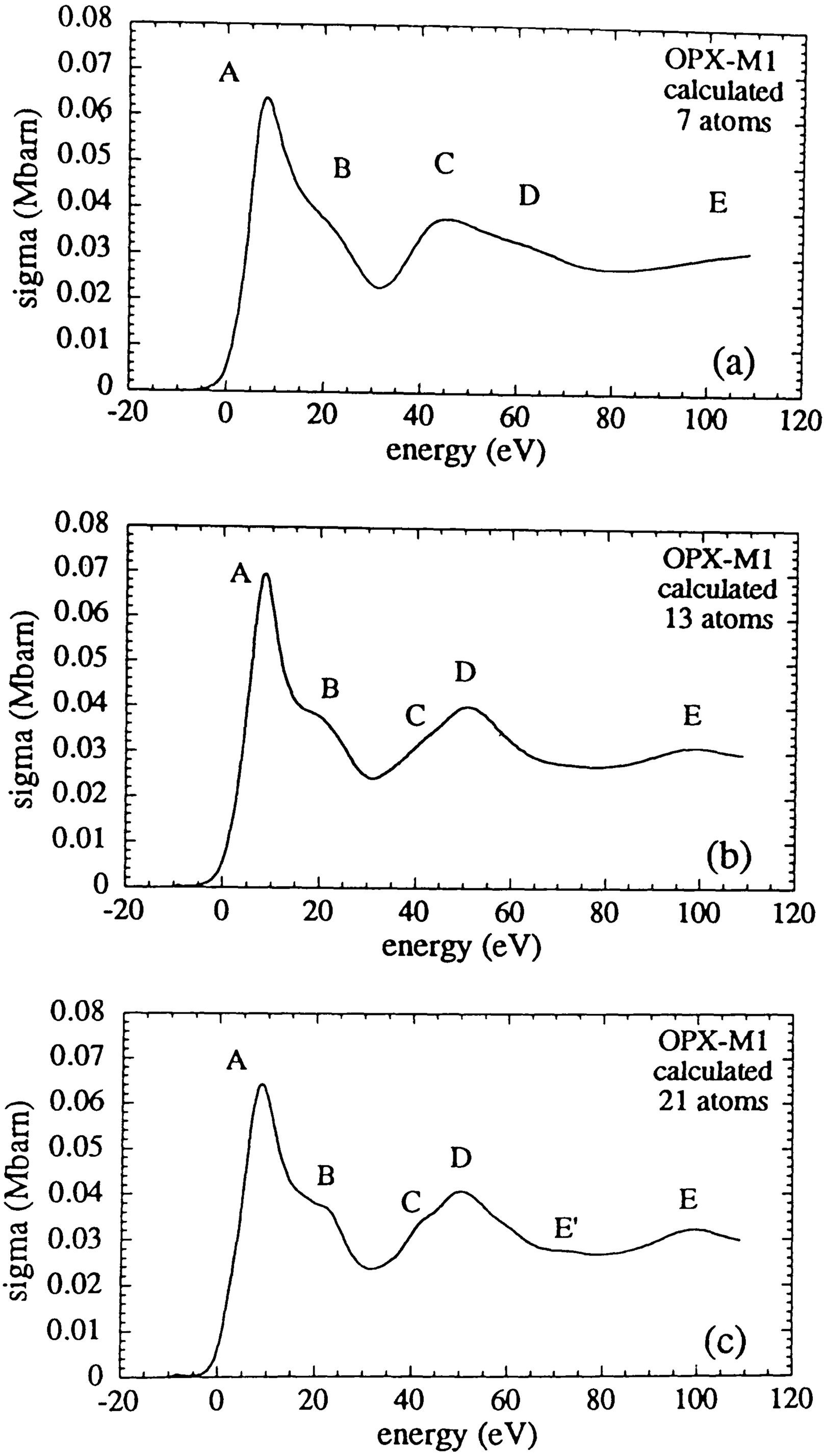

Fig. 4.1.3 The orthopyroxene M1 site multiple scattering calculations. (a) 1-shell cluster, composed of 7 atoms with iron as the absorber and 6 oxygens, (b) cluster composed of 14 atoms, (c) cluster composed of 20 atoms. Cut-off distance 3.555Å. Potential calculated using a 50 atoms cluster.

approximates the C_{2v} ($mm2$) symmetry (Goldman and Rossman, 1977; Van Alboom et al., 1993) if the six bonds are considered as distributed in three orthogonally oriented pairs.

The presence of two structurally different sites both occupied by Fe atoms implies that the orthopyroxene XANES experimental spectrum is the weighted sum of the absorption cross sections of the two sites. Therefore, in order to evaluate the effects due to site geometry and discriminate the contributions due to each site, the multiple scattering calculations must be carried out twice, by locating the Fe absorber either in *M1* or in *M2* and then adequately combining the spectra as a function of site occupancy.

Two different clusters of atoms have been used for these calculations. The differences in the cluster composition involve the cluster being built around Fe respectively in *M1* and *M2*, which have different oxygen geometry in the first coordination shell, and also differences in the structural distribution of next-near neighboring atoms within the same cut-off distance. For these calculations, it has been assumed in the beginning that the clusters are built up of Fe, Si, and O only, i.e. the ferrosilite stoichiometry has been used. It will be shown later that replacement of Fe by Mg in the *M* sites surrounding the Fe absorber chosen as the origin for the calculation only has negligible effects on the shape of the absorption spectra in the region near the edge.

4.1.5.2.1 *M1 site*

Calculated spectra for the *M1* site using clusters with different sizes are shown in Fig.3. The spectrum in Fig.4.1.3a was obtained using a cluster of 7 atoms, with Fe as the absorber and six oxygens, located according to the data obtained from the ferrosilite structural refinement by Sasaki et al. (1982) (Table 4.1.1). The calculated spectrum for the *M1*-site cluster is very similar in its overall shape to the one obtained with the same number of atoms for FeO. This similarity agrees with the expectations, given the low degree of distortion of the orthopyroxene *M1* site. However, when compared with the FeO spectrum (calculated using a perfectly regular octahedron, Fig.4.1.1b), the *M1* spectrum (Fig.4.1.3a) shows a slight increase in peak A half-width; this small difference is more apparent in the derivatives of the spectra. The presence of an additional MS resonance in the *M1* cluster, on the low energy side of the A peak, is indicated by the second derivative of the calculated spectrum; this feature is absent in the derivative of the FeO cluster (Fig.4.1.4). This MS contribution is thus present in *M1* model although it compromised by the presence of peak A is only obvious in derivative spectra; this results mainly from the 1.8eV resolution attained for the MS calculations spectra.

The curves in (b) and (c) in Fig.4.1.3 have been obtained for the *M1* site using clusters with a larger number of atoms, respectively 13 and 21 and a cut-off distance at

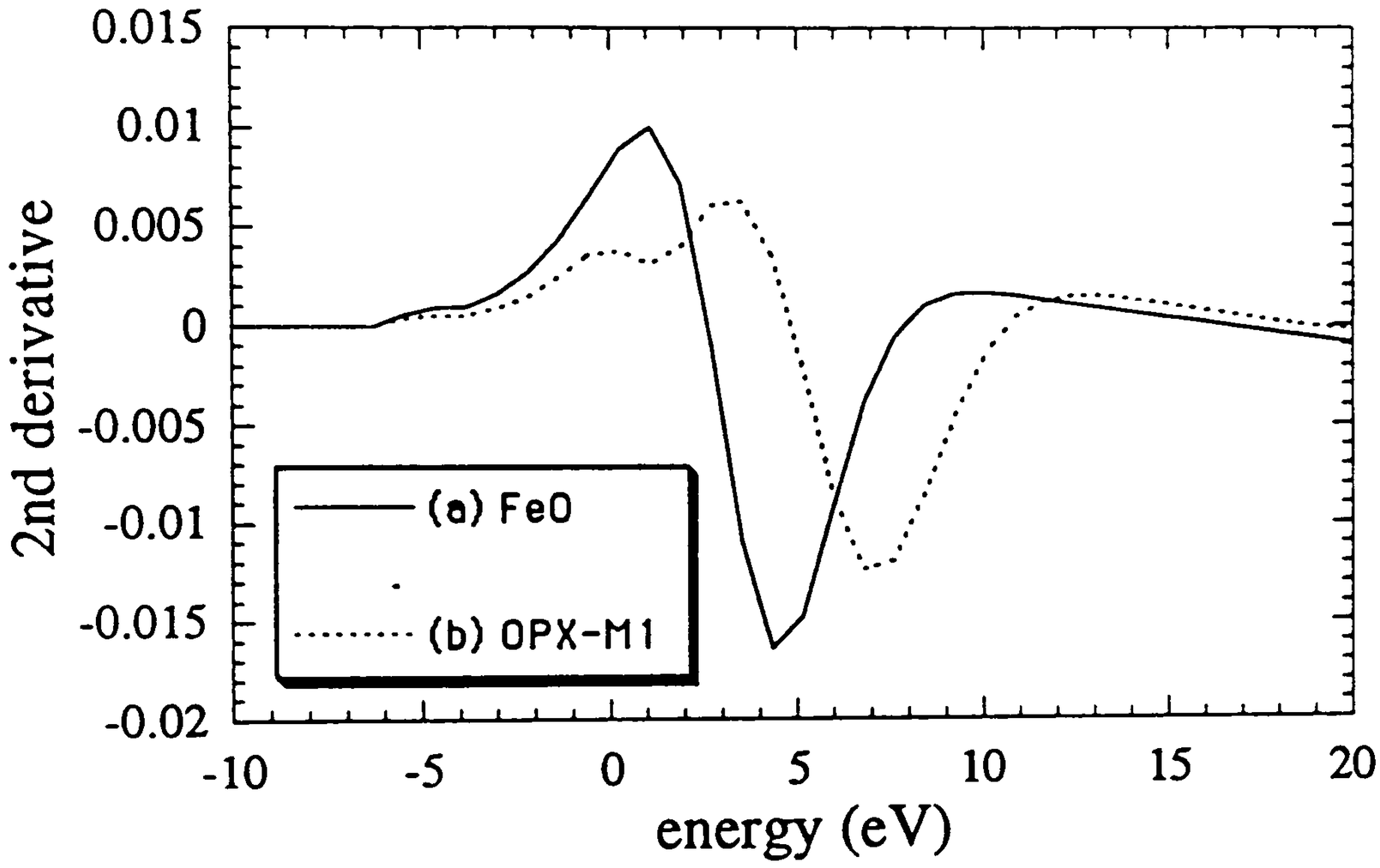

Fig. 4.1.4 Second derivative calculated for the 1-shell cluster of FeO (a) and the same size cluster of OPX-M1 (b), showing the presence of an additional peak due to the lower symmetry of this cluster.

3.667Å. The potential was calculated on a cluster of 50 atoms and a cut-off distance of 5.017Å. The calculated spectra (Fig. 4.1.3b,3c) show that increasing the number of atoms involved in the calculations for this site produces only minor changes in the spectra, mainly a small increase in definition for B, C, E peaks and the appearance of E' peak. A comparison with the FeO clusters shows that there is strong similarity in peak positions between *M1* (Fig.4.1.3) and FeO model spectra (Fig. 4.1.1). In fact as shown at Table 4.1.1, the group of atoms included in the *M1* second cluster (Fig. 4.1.3b) is mainly composed of iron atoms, with a few silicon and oxygen atoms. This makes the cluster very similar in composition to the FeO second shell cluster (Fig. 4.1.1c), which is composed of only iron atoms. The OPX-*M1* cluster spectrum does not change (except for the peaks C and D) with increased cluster size, due to addition of oxygen and silicon atoms (Fig.4.1.3c). Elements with different scattering powers also located at different distances could explain the presence of only weak additional effects observed, i.e. the peaks C, E and E' in passing from the spectrum (b) to the spectrum (c) of Fig.4.1.3. On the contrary, in the FeO structure the atoms are added in groups distributed as sphere of only one element (oxygen or iron) at the same distance from the absorber producing therefore strong focusing effects.

4.1.5.2.2 *M2 site*

The results of MS calculations performed for the OPX-*M2* site are shown in Fig 4.1.5. The curve (a) in Fig.4.1.5 was obtained for *M2* using a cluster composed of 7 atoms, as for FeO and OPX-*M1*, representing the polyhedron of oxygens around the iron atom. The potential used in the calculations was obtained from a cluster of 53 atoms with a cut-off distance of 4.99Å. The spectrum shows a large deviation from the spectra previously obtained for the other clusters of the same size. The peak A is split into two components A and A', and there are major differences in the overall shape of the spectrum compared with the FeO and OPX-*M1* site calculated spectra. These features are undoubtedly due to the presence of a highly distorted site and reflect the MS contributions coming from different Fe-O bond distances.

In the *M1* site the difference (Δ) between the longest and the shortest bonds in the octahedron is 0.110 Å and the six Fe-O bonds have almost a continuous distribution in this range of values; this produces an unique peak in the calculated spectrum, as previously shown. In contrast, in *M2*, Δ is 0.602 Å and this is large enough to allow the detection of two well resolved peaks in the calculated spectra. In the smaller cluster (Fig.4.1.5a) the peaks A and A' can be tentatively be related to the MS contributions of the extreme pair of Fe-O bonds in the highly distorted *M2* site (1.987-2.023Å the shortest; 2.455-2.589Å the longest; Table 4.1.1). The energy difference between the peaks A and A' in the calculated spectrum is 5.5 eV, this value can be related to a difference in

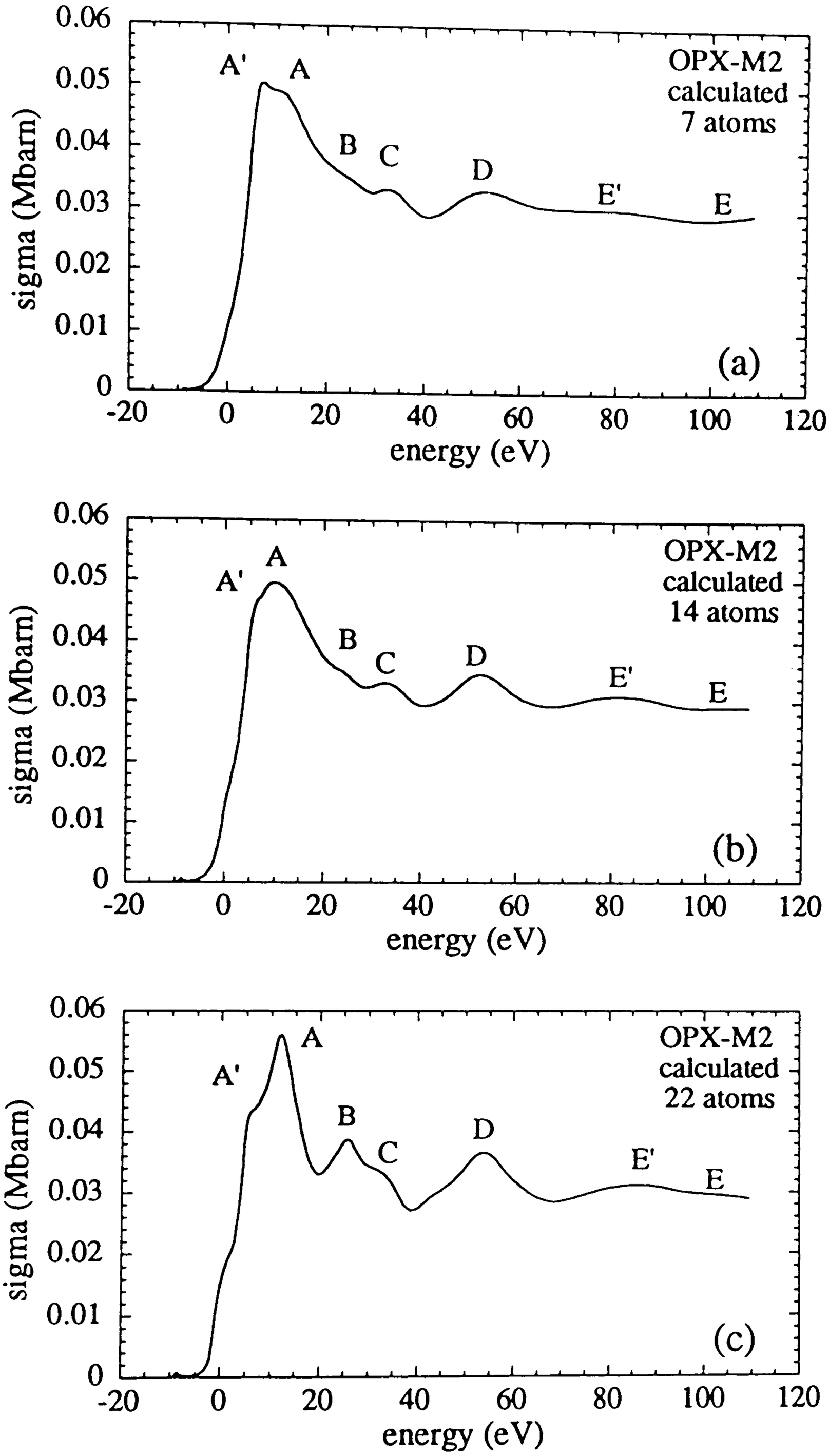

Fig. 4.1.5 The orthopyroxene M2 site multiple scattering calculations. (a) 1-shell cluster, composed of 7 atoms with iron as the absorber and 6 oxygens, (b) cluster composed of 14 atoms, (c) cluster composed of 22 atoms. Cut-off distance 3.75Å. Potential calculated using a 53 atoms cluster.

Fe-O bond-lengths following the general rule, valid for small clusters, for the relationship in the edge region between the peak energy position and the interatomic distance.

$$(E_r - E_b)\, d^2 = \text{const.} \qquad [4.1]$$

where E_r is the energy of the XANES resonances, E_b the energy of the bound state and d the interatomic distance (Natoli, 1984). Using this relationship, the energy difference gives a difference in bond-length of 0.6 Å which is in agreement with the values expected for this site, as determined from XRD structural refinement (Table 4.1.1).

An interpretation based on symmetry arguments is also possible. Starting from the high symmetry example (FeO, O_h) one has p-like final states which are degenerate in energy. In reducing the symmetry to the approximated D_{4h} symmetry (OPX-*M1*) each p-like final states is split into two components (A_{2u}, E_u). If the symmetry is further reduced to C_{2v} (OPX-*M2*) the p-like states are split into three components (A_1, B_1, B_2). In fact, this is what we observe for the main absorption lines of the three calculations. For FeO there is only one main line, which in the case of *M1* becomes broadened and has been shown to consist of two peaks which are resolved in the derivative, whereas in the more distorted *M2* site the reduction in symmetry causes the splitting of the p-like states to become observable.

With increasing cluster size, the *M2* site calculated spectra show quite strong variations if compared with the smaller cluster. Fig. 4.1.5b shows the calculated curve relative to a group of 14 atoms, composed of iron, silicon and oxygen atoms (Table 4.1.1). A lower number of iron atoms and a higher number of silicon atoms in the cluster used for the calculation has a strong influence on the shape of the curve. This effect is most enhanced in the curve of Fig.4.1.5c that is obtained using the largest cluster (22 atoms, cut-off distance 3.758Å), where there are more oxygen atoms than silicon if compared with the *M1* cluster of the same size. In particular, increasing the size of the cluster yields an increase of the intensity of peak A' and all the other peaks are better resolved although no new features appear.

4.1.6 Discussion

The knowledge of the effects that the local geometry around the iron atoms produced in the XANES calculated spectra when the sites are considered separately can now be used to interpret the experimental XANES spectra. Since the total spectrum is the sum of contributions coming from the iron atoms in both *M1* and *M2* sites, to obtain the total calculated spectrum and test the model it is necessary to know the relative occupancy of each site to better weight their contributions to the total spectrum. In the Fe-Mg orthopyroxene structure iron atoms prefer to occupy the *M2* site, which is larger and more distorted than *M1* (Burnham et al., 1971). However, when heated at high

temperature and at controlled oxygen fugacity to prevent iron oxidation, the orthopyroxenes exhibit a redistribution of the Fe^{2+} atoms and the *M1* site is progressively enriched in Fe^{2+} as a function of temperature (Virgo and Hafner, 1969). This effect, well documented by Mössbauer spectroscopy and XRD (e.g., Domeneghetti and Steffen, 1992) has been shown also by XAS on a OPX sample heated at four different temperatures and characterized both by Mössbauer and XANES spectroscopy (Anovitz et al.,1988; Mottana et al., 1991). A variation of the intensity of the main absorption peaks in the OPX-XANES spectra has been found and interpreted as due to the changes in the octahedral site occupancy (Mottana et al., 1991).

To reproduce the OPX experimental spectra we performed a linear combination of the calculated spectra of the two single sites using site occupancy data obtained by Mössbauer spectroscopy (Anovitz et al., 1988). To avoid effects due to different chemical environments around the Fe sites, we choose to use the same OPX sample, at ambient conditions and after heating at 900°C, to have the maximum variation of site occupancy. The XANES experimental spectra for either the natural (Fig.4.1.6a) or the heated samples (Fig.4.1.7a) show that the main multiple scattering resonance is split into two components, A at higher energy and A' at lower energy, with an energy separation of 5.5 eV and variable intensities. The intensity of peak A' in the experimental XANES spectra of the unheated sample is very low when Fe^{2+} is almost all in *M2* (X_{Fe}^{M1}=0.053, X_{Fe}^{M2}=0.723, Anovitz et al., 1988), whereas in the heated sample, where Fe^{2+} fills the *M1* site as well (X_{Fe}^{M1}=0.220, X_{Fe}^{M2}=0.556, Anovitz et al.,1988) the peak A' increases in intensity if compared with A (Mottana et al., 1991).

The calculated spectrum corresponding to the unheated OPX sample, shown in Fig.4.1.6b, was obtained by locating 10% of the Fe^{2+} in *M1* and 90% in *M2*, following the Mössbauer occupancy data. In Fig.4.1.7 is shown the comparison between the heated OPX experimental XANES spectrum, where *M1* also has been partially filled by Fe^{2+}, and the corresponding calculated spectrum. In this case the sum of the MS calculations for the two sites has been obtained assigning a 30% weight to the *M1* site and a 70% to the *M2* site. The calculated spectra show good agreement with the experimental spectra. All of the main structures of the measured spectra are well reproduced in energy position (A, A', B and C) although the calculated spectra show in general sharper peaks as already discussed in the theory part. This "sharpness" is somehow useful and allows us to enhance the MS contributions due to atoms or groups of atoms and, for example, to attribute the peaks B and C (which are not resolved in the experimental spectra due to the presence of structural contribution over the cut-off distance of ~3.8 Å chosen for the calculation) mainly to the contributions due to the *M2* site (Fig. 4.1.5c). Particularly in the edge region, the peaks A and A' agree with those of the experimental data. This agreement is better shown by the comparison of the A/A' intensity ratios between the experimental and calculated spectra: for the heated sample both ratios are equal to 1.04,

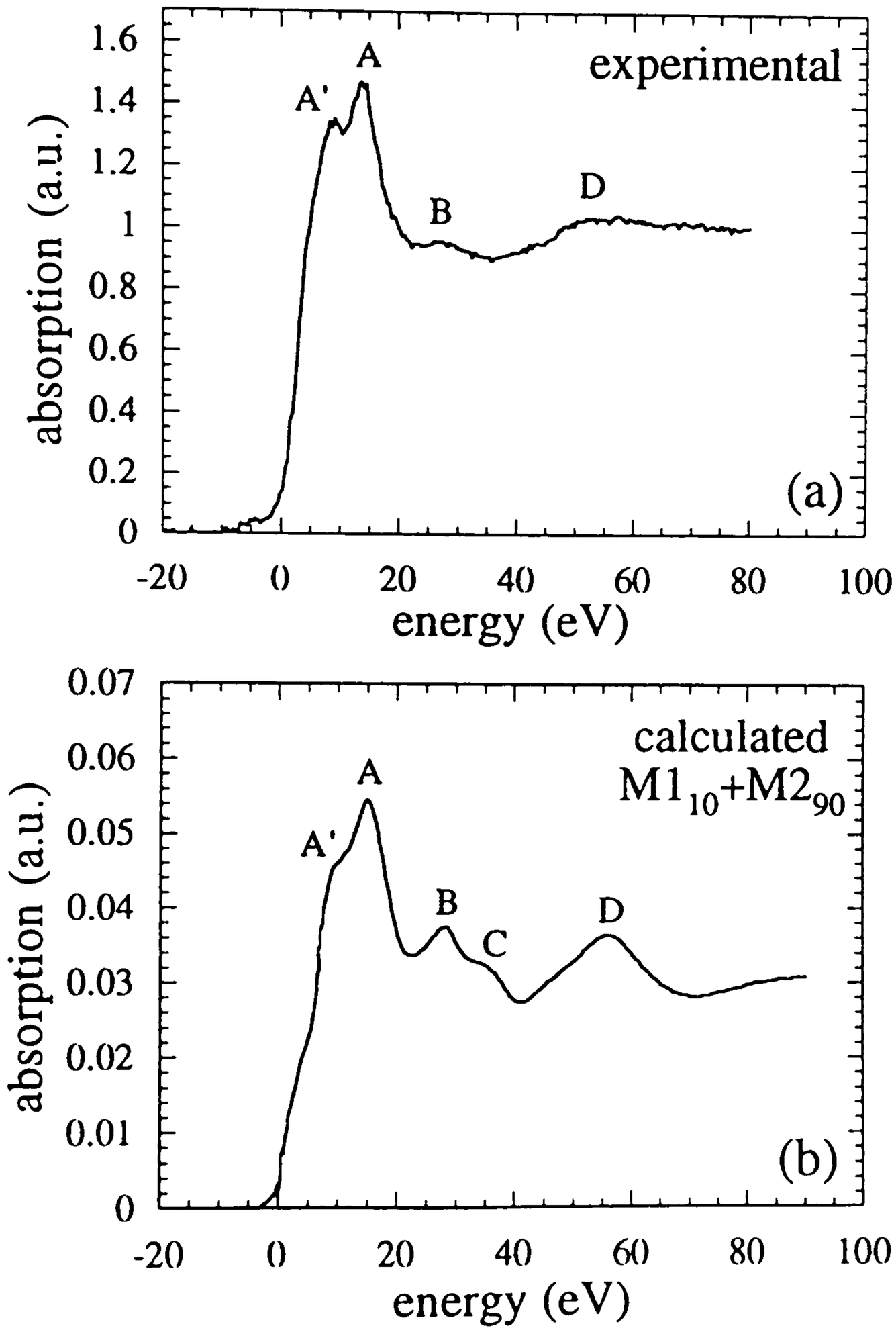

Fig. 4.1.6 Fe K-edge XANES spectrum of a orthopyroxene natural sample (Mottana et al., 1991) (a) compared with a calculated spectrum (b) obtained by combination of the MS contributions of the two sites M1 and M2 in proportion of 10:90.

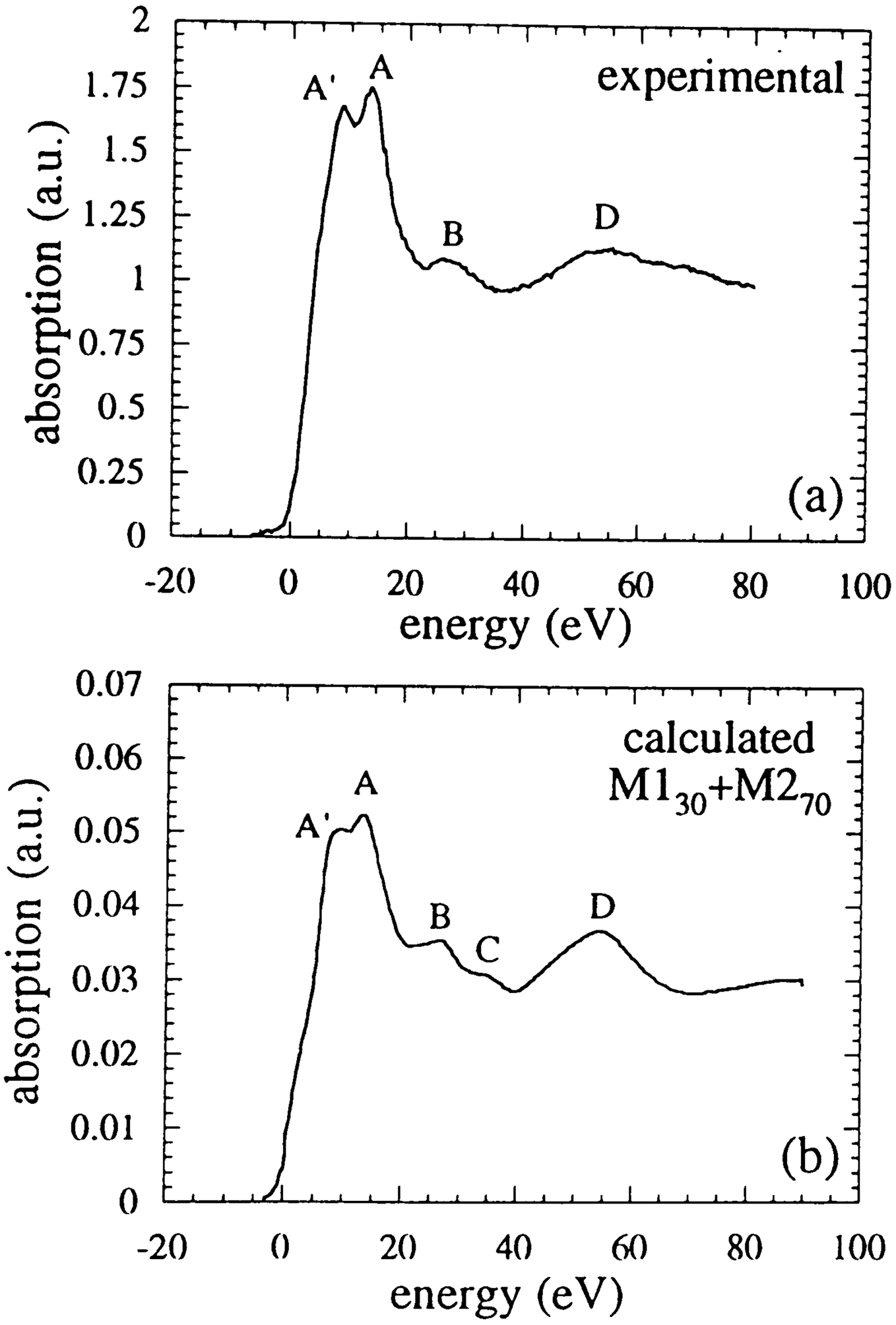

Fig. 4.1.7 Fe K-edge XANES spectrum of a orthopyroxene natural sample heated at 900°C producing a variation of the site occupancy (Mottana et al., 1991) (a) compared with a calculated spectrum (b) obtained by combination of the MS contributions of the two sites M1 and M2 in proportion of 30:70.

whereas for the natural OPX the correlation is not so striking, with A/A'=1.09 for the experimental and 1.18 for the calculated spectrum. This suggests that very low amounts of iron in *M1* and peak resolution may play an important role in affecting the peak intensity and its evaluation.

Looking for a precise evaluation of the correlation between XAS spectra and site occupancy in orthopyroxenes is beyond the purpose of this work, dealing only with the modelling of XANES spectra by MS calculations. However, the orthopyroxene case suggests an interesting possibility of combining experimental and theoretical XANES for a more quantitative evaluation of Fe (or other elements) site occupancies. Application of this method needs further verification, consisting of systematic XANES analysis of series of synthetic samples, fully characterized by XRD, Mössbauer spectroscopy and MS calculations (Mottana et al., 1994).

In the need of simplifying this theoretical approach to a complex structural problem, in a first, gross approximation we assumed that the orthopyroxenes samples were pure ferrosilite end-members. This, in the case of the natural samples we used as comparison is obviously misleading, because the composition of the OPX sample is not a pure ferrosilite end-member (x=0.776; $Mg_{2-x}Fe_xSi_2O_6$). This approach is due to the necessity of considering Fe as the absorbing atom located at the center of the cluster, with all the structural adjustments in the structure related to the presence of iron instead of Mg (i.e. larger octahedral volume, higher site distortion). To verify how the presence of Mg substituting Fe^{2+} in the OPX structure influences the XANES spectra, we recalculated a *M1* cluster after substituting two of the Fe^{2+} atoms present in the second shell cluster by two Mg atoms, and leaving the central Fe absorbing atom and the rest of the cluster unaltered. We choose to substitute the Fe atom in *M1* (Fe1 at 3.141 Å from the absorber) because Mg preferentially occupies the *M1* site and one of the Fe atoms in *M2* (Fe2 at 2.995 Å from the absorber) because it is the closest to the absorber and therefore gives the strongest MS effects. Larger substitution of iron atoms would affect the bulk chemical composition, moving it too close the enstatite end-member. As shown in Fig. 4.1.8, comparison of the Mg-bearing *M1* spectrum (broken line) with the original Fe-*M1* spectrum (solid line) shows that the presence of Mg atoms does not influence much the XANES spectrum in the region near the absorption maximum but only in the region around 50 eV.

The simple substitution of two Fe atoms with Mg in the ferrosilite structure does not take into consideration the structural variations occurring when passing from the Fe end-member to the Mg end-member. However, this type of simplified approach is still satisfying when considering some points. The first one concerns the variation of the Fe-site average bond-distance with composition: the variation of the average bond-length is related to the energy position of the maximum absorption resonance (Natoli, 1984) and not to its overall shape, so the main difference we expect in the spectra is a shift in energy

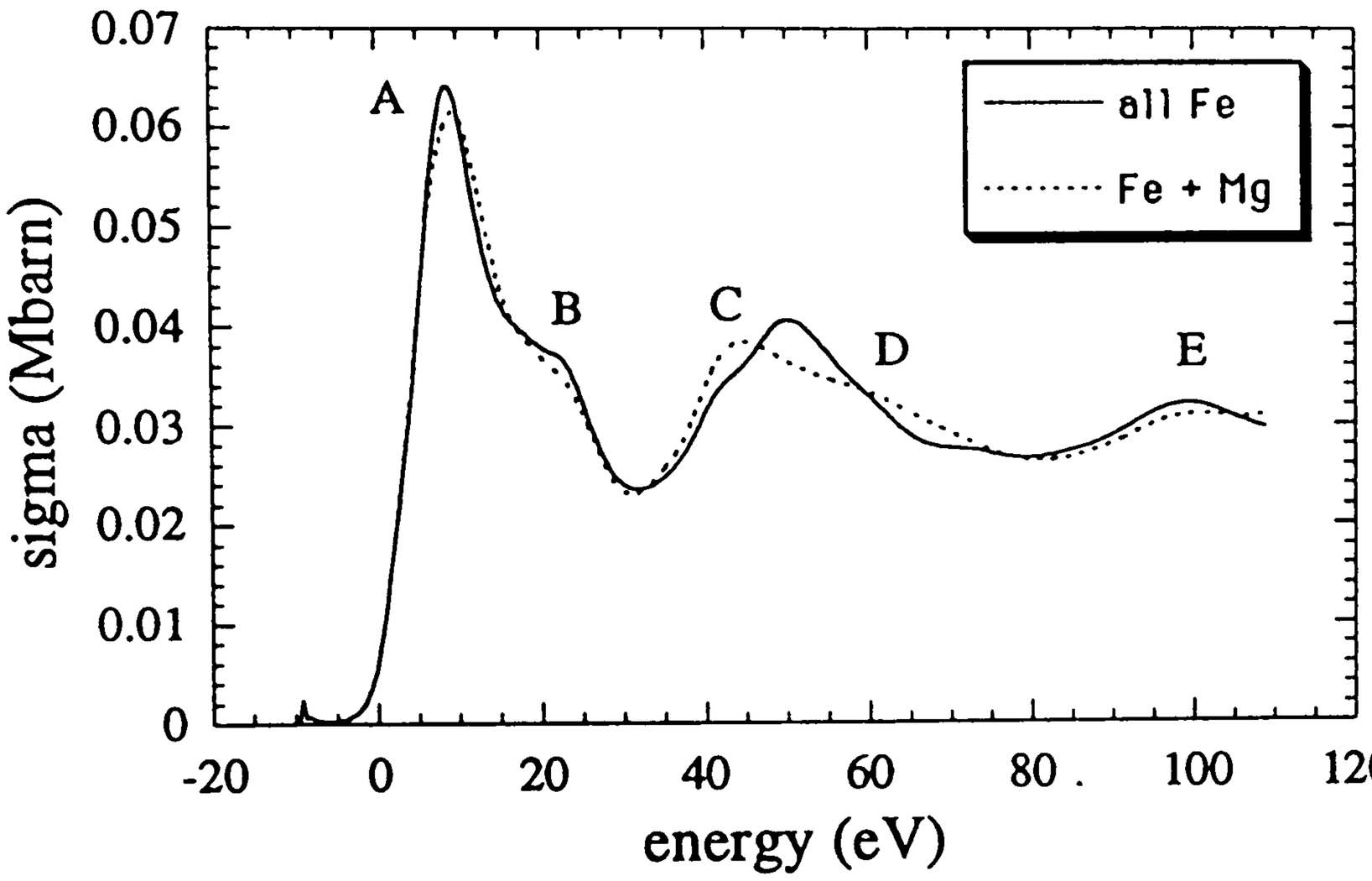

Fig. 4.1.8 Orthopyroxene M1 cluster MS calculation for ferrosilite (solid line) showing that the substitution of iron atoms in M1 (except the central absorber) with Mg (broken line) produces a main change in the region around 50 eV leaving the spectral region around the main absorption edge mostly unaffected (see text for explanation).

of the main absorption feature. Also, since XAS is an element-specific technique, only the sites occupied by iron are investigated and therefore the calculations are the average of those only. The sphere of oxygens around the absorber in *M1* has almost the same type of geometry as it has in ferrosilite since the crystallographical distortion parameters do not vary significantly with varying the amount of iron, as it turns out from XRD crystal structure refinements carried out on orthopyroxenes of intermediate composition (Domeneghetti et al., 1985). Therefore, variations in the shape of the near edge structures cannot be expected, and this is in fact the case. The second point concerns the choice of substituting certain iron atoms instead of others: this is an arbitrary choice, but supported by the general idea that it is not known which site is filled by Fe or Mg. However, considering that all the iron atoms in *M2* in the second cluster are comprised within a range of 0.27Å, the difference in scattering power between Mg and Fe, more than the difference in distance from the absorber is the factor most strongly affecting the spectrum. For all these reasons, the approximation used in this work can be considered as a good reproduction of the region comprising the peaks A and A', i.e. the edge region itself, whereas when considering the features at higher energies this approximation is inapplicable due to the influence of the outer spheres of atoms around the absorber.

4.1.7 Conclusions

Multiple scattering theory has been used to interpret the experimental XANES spectra of Fe-bearing minerals. The results obtained for FeO and orthopyroxene point out some information on the local geometry of iron atoms that will be useful for further applications of theoretical MS calculations to crystalline materials as well as to unknown complex structures (both inorganic and organic) and amorphous materials (e.g. glasses).

The spectra calculated using different type of clusters around the Fe absorber and the comparison between calculated and experimental spectra for the materials used in this study support the following conclusions:

1) the shape of the spectrum in the region of the absorption maximum is strongly dominated by the geometry of the oxygens around the absorber;
2) information on the presence and degree of polyhedral distortion can be quantified by experimental and calculated XANES spectra. These data complement those obtained from EXAFS on bond distances and coordination numbers;
3) the degree of distortion of the polyhedron and the grouping of Fe-O bonds influence the presence of split peaks in the XANES spectrum, where even minor distortion effects can be seen in derivative spectra;
4) each polyhedral site in a structure can be modelled by MS calculations and the influence of the local polyhedral geometry on the total absorption spectrum verified;

5) as a consequence, it is possible to discriminate the preference of an atom for a specific site(s), provided that the sites are sufficiently different (for symmetry, distortion, volume).

Although in the case of Mg-Fe orthopyroxenes other methods are certainly - at least now - more suitable for structural and crystal chemical characterization (e.g. XRD, Mössbauer spectroscopy) the present study has shown the feasibility of extracting such data from X-ray absorption spectra also; this will prove to be important for other elements occurring at high dilution and/or which cannot easily be distinguished by XRD techniques such as for instance isoelectronic elements.

CHAPTER 5. CA ENVIRONMENT IN CLINOPYROXENES

5.1 CALCIUM ENVIRONMENT IN OMPHACITIC PYROXENES: XANES EXPERIMENTAL DATA VERSUS ONE-ELECTRON MULTIPLE SCATTERING CALCULATIONS.

5.1.1 Abstract

One-electron multiple scattering calculations are used to model the local environment of calcium in three pyroxenes (diopside, intermediate ordered omphacite, and jadeite-rich disordered omphacite) starting from their crystal structure data. The calculated Ca K-edge spectra agree well with the experimental X-ray absorption XANES spectra. The overall comparison of theory and experiment supports the model that Ca in omphacite is distributed over two non-equivalent sites, one having the same geometry as the Ca site in diopside, and a second one that of Na in jadeite. I stress the need of comparing the measured XANES spectra with *ab-initio* calculated spectra in order to gain a full understanding of experimentally observed features and deduce from them the crystal-chemical behaviour of individual cations present in a mineral structure.

5.1.2 Introduction

The crystal chemistry of Ca-Na pyroxenes has been studied extensively over the last two decades, mainly on the basis of single-crystal structure refinements of natural samples (for a review see Rossi *et al.*, 1983). More recently, the character of the order-disorder transition occurring in this join has also been explained using Landau theory (Carpenter *et al.*, 1990a,b). Ordering occurs in two distinct sets of sites: (i) Mg (+Fe^{2+}) and Al (+Fe^{3+}) are partitioned over two slightly distorted octahedral sites (M1 and M11) which are edge-connected so as to form a chain parallel to the tetrahedral T chain; (ii) Na and Ca are ordered over two large eight-coordinated sites (M2 and M21) that are separated from each other by the interposition of the O2A and O2B oxygens that link the octahedra with the tetrahedra. In fact, only the ordering of the two M2 cations Na and Ca can be directly measured by X-ray single crystal diffraction because of their sufficient difference in electronic density; ordering in the M1 and M11 (*i.e.* between Mg and Al) is largely inferred (Rossi *et al.*, 1983).

Ordering in the M2 and M21 sites has been independently confirmed by Davoli *et al.* (1983, 1987) by the chemically selective XAS (X-ray Absorption Spectroscopy) technique. These authors measured the Ca K-edge of various Ca-Na pyroxenes by XANES (X-ray Absorption Near-Edge Structure) spectroscopy and found that Ca was located in two distinguishable sites, differing in their absorption energy and environment. However, their interpretation of XANES spectra was largely subjective and dependent on

models derived from a general knowledge of the structure. Recently, *ab-initio* calculation methods have been developed based on one-electron multiple scattering theory which enables precise computation of absorption spectra and their comparison with experimental data, thus making it possible to explain the observed XANES resonances in a far less subjective way. By performing such calculations on three samples of the Ca-Na pyroxene series measured by Davoli *et al.* (1987), for which full structural data are available, the initial interpretation can be here confirmed, and also provide independent support for Davoli *et al.*'s crystal-chemical model of solid-solution and ordering in the Ca-Na pyroxene series.

5.1.3 Methods

The samples investigated here are natural pyroxenes having different calcium contents: a nearly-pure diopside (MMR18362, with Ca 0.982 and Na 0.018); an ordered *P2/n* omphacite of intermediate composition (M.1, with Ca 0.493 and Na 0.436); and a jadeite-rich disordered *C2/c* omphacite [or impure jadeite] (P1-25, with Ca 0.202 and Na 0.762) (Davoli *et al.*, 1987). The crystal structures of the three samples were investigated by G. Rossi (personal communication, 1987) to *R ca.* 0.02-0.03. Such structural refinements constitute the starting data for the calculations (Table 5.1.1). Identical results were found for diopside when using the positional parameters given by Cameron *et al.* (1973), and these are used in preference to show that the calculated spectra are not affected by small differences in the positional parameters of the atoms, but are influenced rather by the chemistry of the cluster used. The experimental XANES spectra were collected in transmission mode at the PULS X-ray line of the Frascati synchrotron radiation facility (Italy). All the details concerning the experimental line and the measurements are reported in Davoli *et al.* (1987).

The computation of XANES spectra is based on the one-electron multiple-scattering (MS) theory of Lee & Pendry (1975), and takes advantage of refinements to the theory as well as to the computational methods introduced over a number of years by Natoli *et al.* (1980), Durham *et al.* (1982), Natoli & Benfatto (1986) and Durham (1988). The cluster density was constructed following the method of Mattheiss (1964), and the Coulomb component of the potential by superposition of neutral atomic charge densities using the Clementi & Roetti (1974) basis set. In order to simulate the charge relaxation around the core hole in the photoabsorber of atomic number Z, I use the well-screened Z+1 approximation (final state rule) of Lee & Beni (1977). In metallic and (nearly) covalent systems, this method is known to provide charge distributions relatively close to those obtained by self-consistent calculations, at least within the muffin-tin model. For more details, the reader is referred to the description of multichannel MS theory given by Natoli *et al.* (1990). To obtain the exchange-correlation component of the potential, I use the energy- and position-dependent complex Hedin-Lundquist potential (Tyson *et al.*,

Table 5.1.1. Structural and chemical data of the pyroxenes used for MS calculations

sample space group	chemistry		positional parameters x	y	z
(a) *C2/c*	Ca 0.982 Na 0.018	M2	0.0000	0.3015	0.2500
		M1	0.0000	0.9082	0.2500
		T	0.2862	0.0933	0.2293
		O1	0.1156	0.0873	0.1422
		O2	0.3611	0.2500	0.3180
		O3	0.3505	0.0176	0.9953
cell parameters a (Å) 9.510(4); b (Å) 8.686(4); c (Å) 5.238(3); β (°) 107.09(3)					
(b) *P2/n*	Ca 0.493 Na 0.436	M2	0.2500	0.9504	0.7500
		M2	0.2500	0.5526	0.2500
		M1	0.2500	0.3480	0.7500
		M1	0.2500	0.1598	0.2500
		T1	0.5394	0.3481	0.2266
		T2	0.5372	0.1631	0.7309
		O1	0.3634	0.3382	0.1232
		O2	0.3621	0.1767	0.6475
		O3	0.6138	0.5090	0.3091
		O4	0.6063	0.9974	0.8054
		O5	0.6057	0.2663	0.0037
		O6	0.5981	0.2398	0.4984
cell parameters a (Å) 9.552(9); b (Å) 8.780(8); c (Å) 5.209(5); β (°) 106.59(5)					
(c) *C2/c*	Ca 0.202 Na 0.762	M2	0.0000	0.3000	0.2500
		M1	0.0000	0.9048	0.2500
		T	0.2897	0.0928	0.2292
		O1	0.1115	0.0807	0.1422
		O2	0.3610	0.2578	0.3180
		O3	0.3522	0.0112	0.9953
cell parameters a (Å) 9.7496(4); b (Å) 8.9206(3); c (Å) 5.2509(2); β (°) 105.81(3)					

(a) diopside, structural refinement by Cameron *et al.* (1973); (b) ordered intermediate omphacite, structural refinement by G.Rossi (pers. comm., 1987); (c) jadeite-rich disordered omphacite, structural refinement by G. Rossi (pers. comm., 1987

1992). The calculated spectra are further convoluted with a Lorentzian-shaped function to account for the core-hole lifetime. The muffin-tin radii was chosen according to Norman (1974), allowing 10% overlap between contiguous spheres to simulate the atomic bond. For further applications of the theory, the reader is referred to Tyson *et al.* (1992) and Wu *et al.* (1992, 1994).

5.1.4 Results

The XANES experimental spectra at the Ca K-edge of the three studied pyroxenes are shown in Fig. 5.1.1. In diopside (curve (a)), the spectrum is composed of a strong absorption peak (labelled A) and minor resonances both on the low-energy side (A' and A") and on the high energy side (B, C, D) of the edge. In intermediate pyroxene, the spectra are similar in shape to that of diopside, but the single resonances differ in energy position and intensity. In fact, peak A shifts by 1.3 eV to higher energy passing from diopside (Fig. 5.1.1, curve (a)) to impure jadeite (curve (c)), while peaks A' and A" merge to form only one peak in jadeite. Furthermore, peak B decreases in intensity with decreasing Ca content (from (a) to (c)) and shifts to higher energy as well. On the basis of the experimental spectra, the absorption features can be interpreted in terms of a variation of the local environment around calcium atoms: in diopside the CaO_8 cluster has a 4-2-2 configuration (*i.e.* four short, two intermediate and two long Ca-O bonds, distributed nearly symmetrically distributed around the central M2 cation), whereas in jadeite the configuration of the M2 site (ideally centered by Na) is 6-2 (six short and two very long bonds) (Table 5.1.2). The shift in energy of peak A supports the idea that Ca in jadeite assumes the same configuration as Na with slightly shorter average bonds relative to diopside but, more important, with 6 bonds at almost the same distance assuming therefore a more "regular" configuration. This is consistent with the increase in relative intensity of peak A from a) to c) being due to increased resonance within the more "regular" ligand configuration. However, the chemistry of the cluster may also have a marked effect on resonance intensities.

The MS calculations were carried out using clusters of increasing number of atoms (over 90 atoms) and taking into account all atoms within 6 Å from the absorber (Ca) as the center of the cluster. In this way, the structural significance of the cluster is assured, although a comparison with spectra obtained from smaller clusters shows that no large changes occur in this structure if the cluster size is increased from 58 to 95 atoms (Fig. 5.1.2). This is probably due to the fact that the majority of the atoms involved in the clusters are low-Z atoms. The energy alignment between the spectra shown in Fig. 5.1.2 is made referring to the first feature (P).

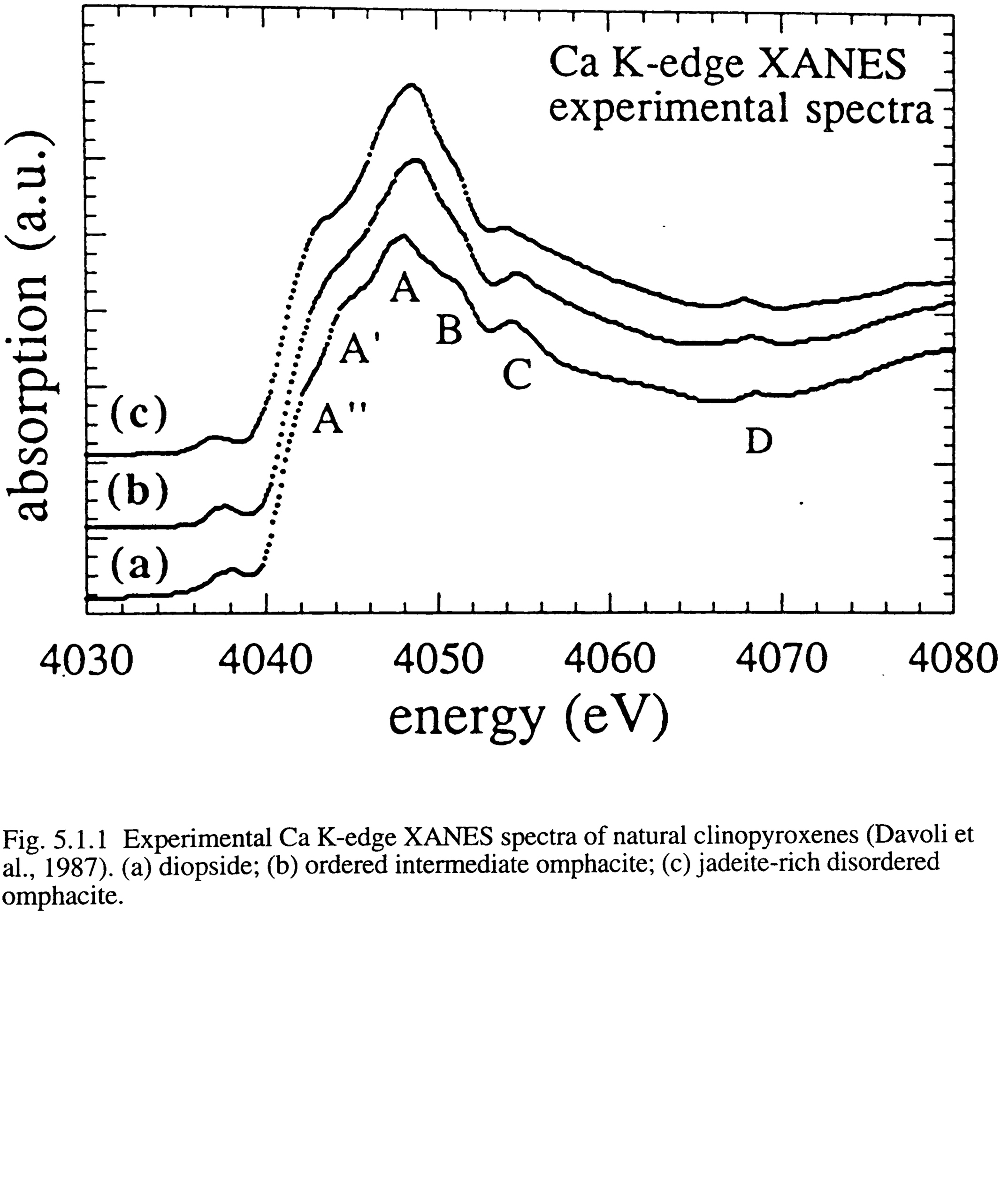

Fig. 5.1.1 Experimental Ca K-edge XANES spectra of natural clinopyroxenes (Davoli et al., 1987). (a) diopside; (b) ordered intermediate omphacite; (c) jadeite-rich disordered omphacite.

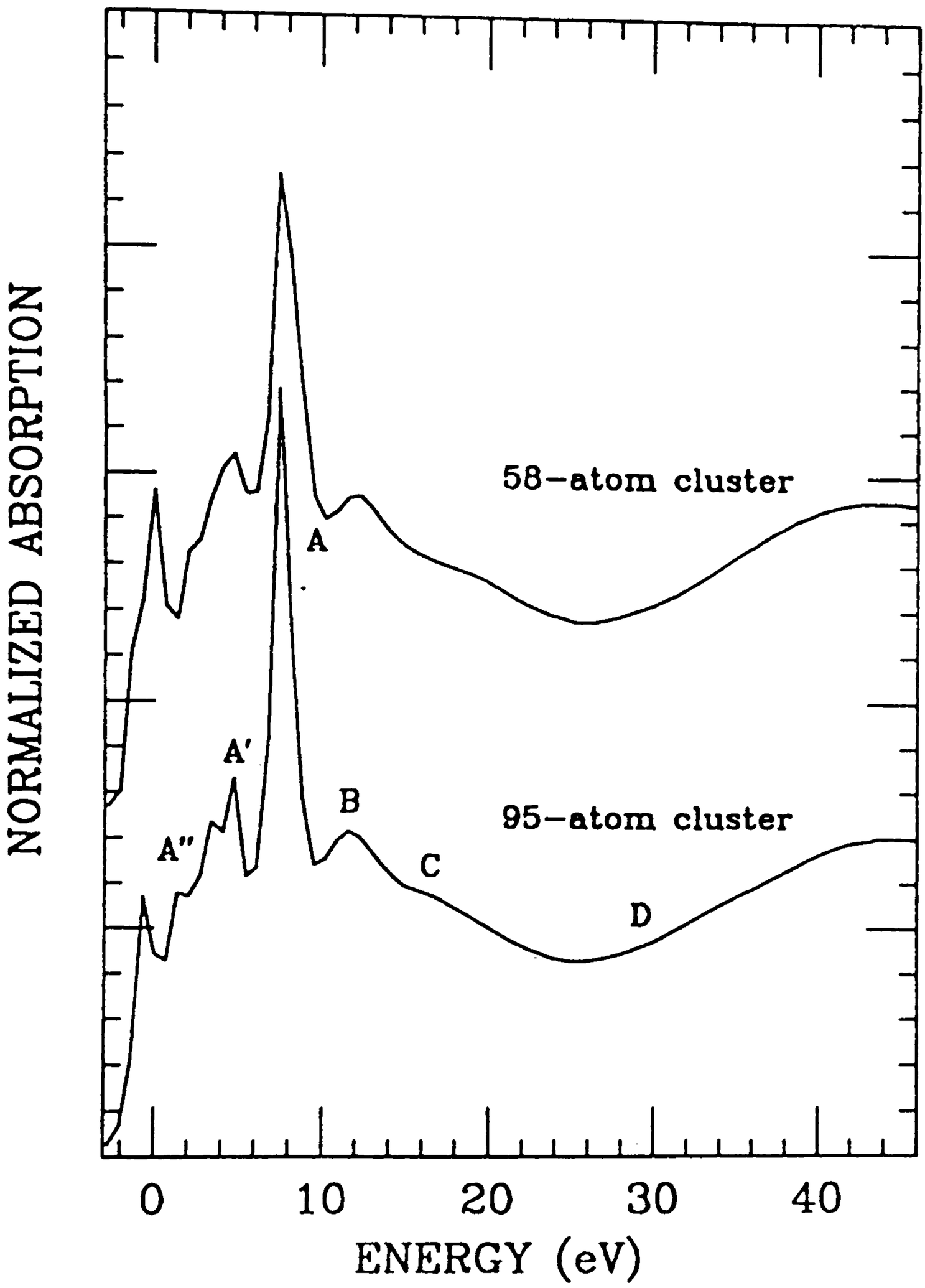

Fig. 5.1.2 Diopside spectra calculated using two clusters of different sizes.

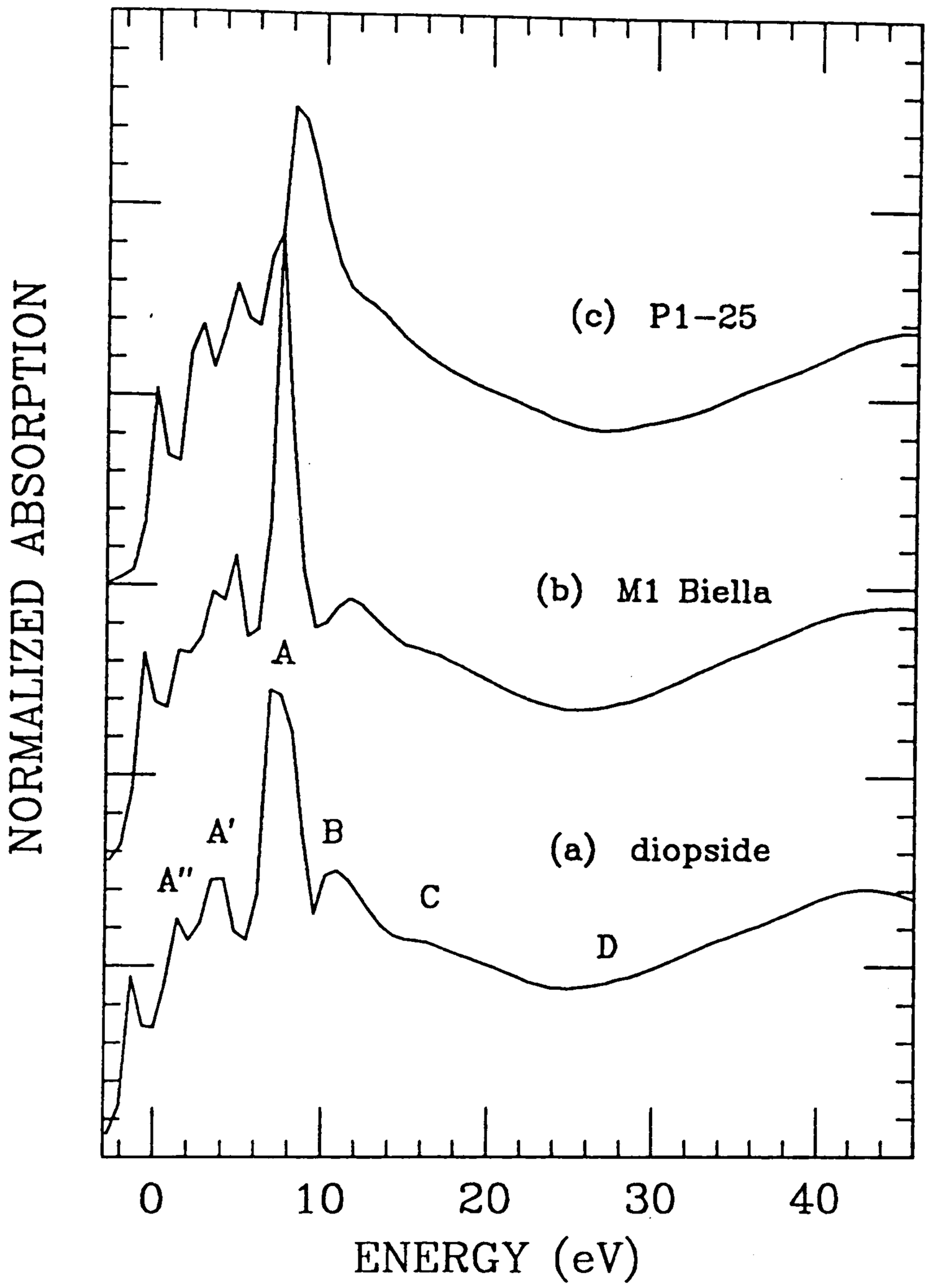

Fig. 5.1.3 Theoretical MS calculations of the clinopyroxenes at the Ca K-edge. (a) diopside; (b) ordered intermediate omphacite; (c) jadeite-rich disordered omphacite.

Fig. 5.1.3 shows the calculated spectra of the three samples under investigation, using clusters of the same size for better comparison. All the spectra show a strong main peak A that compares well with the experimental one. In agreement with the experimental data, this peak shifts by 1 eV toward high energy when passing from diopside (curve (a)) to impure jadeite (curve (c)). Peaks A' and A" display a more complex behavior: they both shift to higher energy from curve (a) to curve (c). Peak C is very weak in the theoretical spectra, although it has the same energy position in all three spectra. However, peak C shows a peculiar type of behavior: when the chemical composition of the cluster is changed, *i.e.* by substituting some Mg atoms in M1 site with Al (in diopside, Fig.5.1.3 (b) and of Ca atoms in M2 with Na (in impure jadeite, Fig. 5.1.4 (d)), peak C shows some shift in energy position and intensity compared with the starting clusters (Fig. 5.1.3 (a) and (c)). These effects are not related to changes in the first coordination shell (since Ca is always the absorber at the center of the cluster) but to second-shell effects; they point out how changes in the chemistry of atoms well away from the absorber can affect the XANES resonances. In this regard, peak B (Fig. 5.1.3) is particularly interesting since it has the same energy position in all the three samples and shows the same trend as seen in the experimental spectra (Fig. 5.1.1). In diopside (curve (a), Fig. 5.1.3), however, its intensity is slightly stronger compared with the peak in the experimental spectrum (Fig. 5.1.1(a)). This fact has a simple explanation: the calculated spectrum is based on Cameron *et al.*'s (1973) structure for a synthetic diopside crystal of pure $CaMgSi_2O_6$ composition, whereas the experimental spectrum was taken on a gem-quality natural diopside that, although very pure, contains minor Al_2O_3 (0.51 wt%) and Fe (Fe_2O_3 1.94 wt% and FeO 1.16 wt%) substituting for Mg (see Fig. 5.1.4(b)). The presence of Al and/or Fe in the M1 site introduces detectable changes in the XANES spectrum, since the substitution of a chemical species with another having different atomic number strongly affects the charge density and, consequently, the potential calculated for the cluster. On the other hand, small differences in atomic position do not have much influence on the features in the calculated spectra, making it possible to use structural refinements obtained on different crystals for a general calculation of the spectra. The effects identified on the basis of these calculations reveal the extremely high sensitivity of XANES to even minor chemical variations in the cluster around the absorbing atom, although the sensitivity limit is still difficult to quantify. Thus, XANES could be suitable for applications in the crystal-chemistry of known and unknown structures. Indeed, the results of calculations indicate that the trend in increased relative intensity of the main peak A (Fig. 5.1.1) may be related to the presence of Al, Fe and Na in the cluster surrounding the Ca absorber.

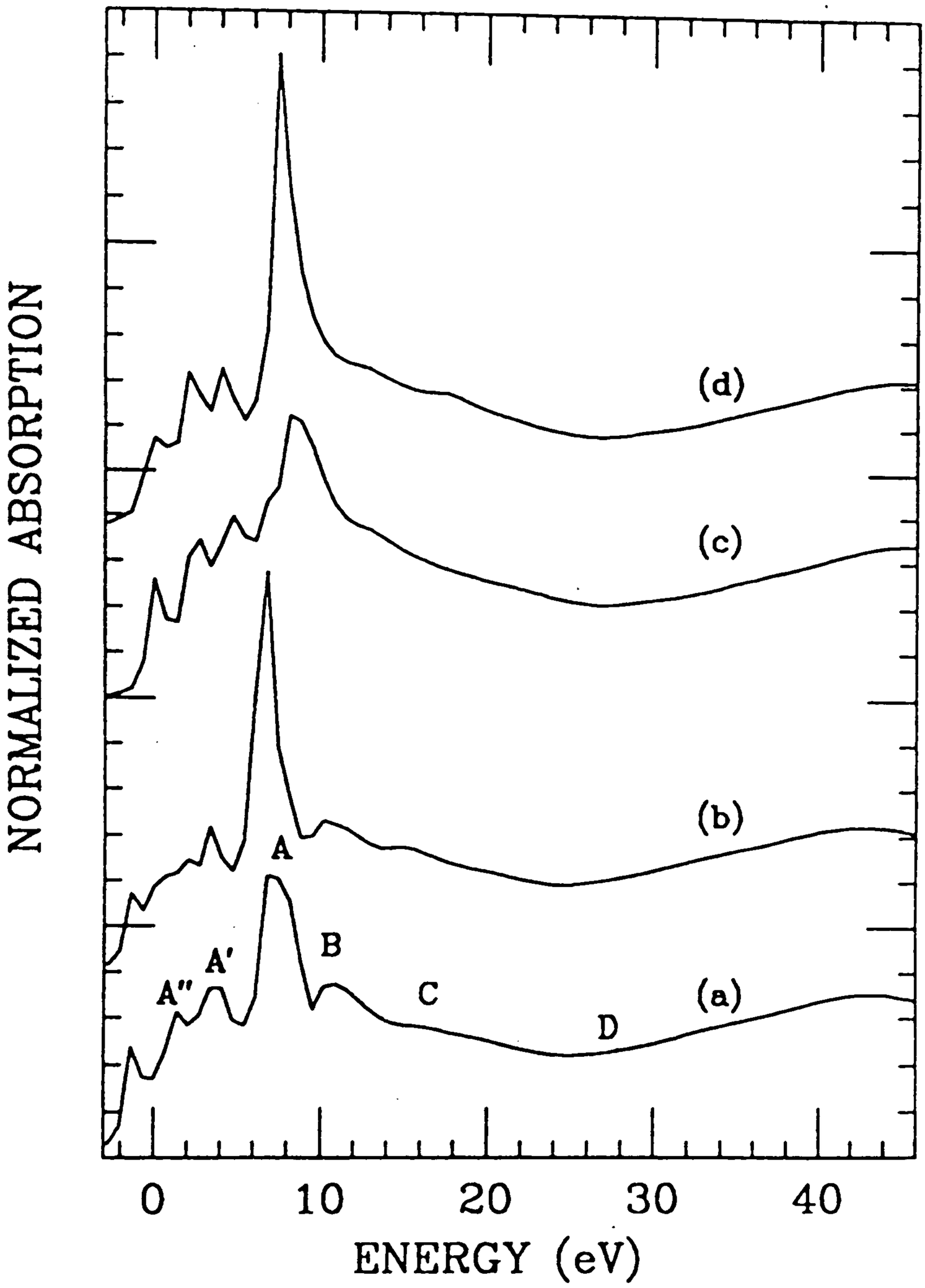

Fig. 5.1.4 Effect of chemical composition of the cluster on the XANES resonances. (a) diopside, (b) same cluster with 2 Mg atoms substituted by Al; (c) jadeite-rich disordered omphacite, (d) same cluster with all the Mg atoms substituted by Al and all the Ca atoms substituted by Na, except the central absorbing atom.

Table 5.1.2. Ca-O bond length distribution for the three pyroxenes

(a)		**(b)**		**(c)**	
Ca		Ca		Ca	
O2	2.3489	O4	2.3840	O2	2.3132
O2	2.3489	O4	2.3840	O2	2.3132
O1	2.3647	O2	2.3904	O1	2.3265
O1	2.3647	O2	2.3904	O1	2.3265
O3	2.5633	O5	2.4800	O3	2.4480
O3	2.5633	O5	2.4800	O3	2.4481
O3	2.7223	O6	2.7748	O3	2.7174
O3	2.7223	O6	2.7748	O3	2.7174

(a),**(b)**,**(c)** as in Table 1. Numbers refer to the distance in Å from the absorber.

5.1.5 Conclusions

1. The interpretation of XANES spectra is greatly facilitated when it is possible to compare the experimental and calculated spectra by using one-electron multiple-scattering theory starting from the crystal-structural data of the minerals.
2. The use of MS calculations allows study of the geometry and bond distribution of the first shell of atoms around the absorber and enables investigation of the influence of chemical variation in the cluster under study.
3. The combination of experimental and calculated spectra makes XANES a powerful tool for testing the local crystal-chemical properties of minerals, which generally show deviations from ideal, end-member compositions.
4. MS calculations confirm the interpretation of XANES spectra of intermediate Ca-Na pyroxenes (omphacites) proposed by Davoli *et al.* (1987): Ca is distributed over two M2 sites, one close in geometry to that of Ca in diopside, and the other close to that of Na in jadeite. The average structure of omphacite is a mosaic of two different polyhedra (M2 and M21) that remain essentially the same throughout the series but vary in their relative proportions. The stability of the overall structure is made possible by the fact that the octahedral and tetrahedral chains are flexible enough to bend around these relatively rigid eight-fold coordinated units.

Dedicated XANES studies at the Na, Mg and Al K-edges need to be undertaken to confirm these findings and elucidate further the crystal chemistry of omphacitic pyroxenes.

CHAPTER 6. MG AND FE IN OLIVINES

6.1 THEORETICAL ANALYSIS OF X-RAY-ABSORPTION NEAR-EDGE STRUCTURE AT THE Mg K-EDGE IN FORSTERITE, Mg_2SiO_4 - Pbnm, UNDER EXTREME CONDITIONS

6.1.1 Abstract

The Mg K edge X-ray absorption spectra of forsterite for the M1 and M2 sites and for the overall edge have been calculated using the one-electron multiple-scattering theory. The validity of the theoretical model is illustrated by good agreement between calculations and experimental data at the Mg K edge of MgO (periclase). Based on these results, XAS experiments at the Mg K edge of forsterite are suggested, in as much as calculations performed up to 1020°C and 149 kbar indicate variation of fine structures in the multiple scattering region. These variations can be related to structural changes in forsterite and these results demonstrate how information obtained by theoretical modelling of XANES spectra can lead to deeper knowledge of structures relevant to the Earth's upper mantle.

6.1.2 Introduction

The structure and electronic properties of forsterite, Mg_2SiO_4 (Pbnm), are of considerable interest both in geophysics and crystal-chemistry. Forsterite is the Mg end-member and structural prototype of the olivine solid-solution series, α-$Mg_{2-x}Fe_xSiO_4$, one of the members of which (with $x \approx 0.1$) is the predominant phase throughout the Earth's upper mantle. Furthermore, forsterite is the precursor of two other polymorphic phases (wadsleyite, β-$(Mg,Fe)_2SiO_4$ (Imma), with modified spinel structure, Horiuchi and Sawamoto, 1981; and ringwoodite, γ-$(Mg,Fe)_2SiO_4$ (Fd3m), with spinel structure, Sasaki et al. 1982) which are believed to be stable deeper in the mantle across the 400 and 650 km seismic discontinuities (e.g. Ringwood and Irifune, 1988; Akaogi et al., 1989; Katsura and Ito, 1989; Fei et al., 1991; Jeanloz, 1991).

It is well known that X-ray absorption near-edge structure (XANES) spectroscopy provides direct information on the structural arrangement around a selected atomic site. For olivines, theoretical analysis of XANES has not been carried out so far, and thus a set of one-electron multiple scattering calculations of XANES spectra of the Mg K edge in pure forsterite at ambient and under extreme P, T conditions is reported here. As for the relevant measurements, they must be deferred to a later time: the Mg K edge can hardly be recorded with the set-ups presently available at synchrotron radiation sources. Furthermore X-ray absorption spectroscopy (XAS) measurements at high

temperature and pressure can now be performed only at much higher energy than the Mg K edge.

6.1.3 Theoretical methods

The crystal structure of forsterite is well-known, both for natural material (Bragg and Brown, 1926; Birle et al., 1968; Fujino et al., 1981), and for synthetic material of essentially pure composition (Smyth and Hazen, 1973). Furthermore, Smyth and Hazen (1973), Hazen (1976) and Tak'euchi (1984) carried out refinements of the forsterite crystal structure as a function of temperature up to 1020°C and Hazen (1976), Hazen and Finger (1980) and Kudoh and Tak'euchi (1985) determined it as a function of pressure up to 149 kbar. The atomic coordinates given by these authors were the starting data used to perform the calculations. Table 6.1.1 summarizes the different unit cells, average first shell Mg-O bond distances and P and T conditions used for calculations.

Simulation of the XANES spectra is based on the one-electron multiple-scattering (MS) theory of Lee and Pendry (1975), and takes advantage of the refinements to the theory, as well as to the computational methods, progressively introduced by Natoli et al. (1980), Durham et al. (1982), Natoli and Benfatto (1986) and Durham (1988). I use Mattheiss (1964) prescription to construct the cluster density and I obtain the Coulomb part of the potential by superposition of neutral atomic charge densities using Clementi and Roetti (1974) tables.

In order to simulate the charge relaxation around the core hole in the photoabsorber of atomic number Z (12 in the case of Mg), I use the well screened Z+1 approximation (final state rule) of Lee and Beni (1977). This involves taking the orbitals of the Z+1 atom and constructing the charge density by using the excited electronic configuration of the photoabsorber with the core electron promoted to a valence orbital. In metallic and (nearly) covalent systems, this method is known to provide reasonable approximation to the relaxed charge distributions. This is obtained by self-consistent calculations, at least within the muffin-tin (MT) model and for the purposes of calculating absorption spectra in the MS scheme. For more details, the reader is referred to the multichannel MS theory description of Natoli et al. (1990).

For the exchange-correlation part of the potential I use the energy- and position-dependent, complex Hedin-Lundquist (H-L) self-energy S(r,E), as described by Tyson et al. (1992). The imaginary part of H-L gives the amplitude attenuation of the excited photoelectron due to inelastic losses, and takes into account the photoelectron mean free path in the final state of the absorber. The calculated spectra are further convoluted with a Lorentzian shaped function with a full width G_h to account for the core hole lifetime, as given by Krause and Oliver (1979). For the sake of the argument presented here, substantially similar results are obtained with a calculation using a X-a type of exchange followed by a Lorentzian convolution to account for inelastic losses of the photoelectron in the final state and the core hole width (Penn, 1987). I have choosen the muffin-tin

TABLE 6.1.1 Crystal structure parameters and bond distances of Mg_2SiO_4 – *Pbnm*

Sample	1[a]	2[b]	3[b]	4[c]
a($\dot{A}$)	4.7535	4.7977	4.7125	4.6519
b($\dot{A}$)	10.1943	10.3520	9.9710	9.7701
c($\dot{A}$)	5.9807	6.0588	5.9556	5.7441
T(°C)	23	1020	23	23
P(kbar)	0.001	0.001	50	149
$\langle M1\text{-O}\rangle$	2.0938	2.1188	2.0595	2.0521
$\langle M2\text{-O}\rangle$	2.1314	2.2003	2.1094	2.0504
Q.E.($M1$)	1.0001	1.0005	1.0002	1.0005
Q.E.($M2$)	1.0011	1.0018	1.0038	1.0010

[a]Fujino et al., 1981.

[b]Hazen, 1976.

[c]Kudoh and Takéuchi, 1985.

radii according to the criterion of Norman (1974), and allowed a 10% overlap between contiguous spheres to simulate the atomic bond.

6.1.4 Results

The theoretical model has been tested to reproduce the available experimental data at the Mg K edge of MgO(periclase) (Wong, 1993) which has Fm3m symmetry. Comparison of different cluster calculations for periclase in normal condition is illustrated in Fig.6.1.1. Good agreement is obtained for a cluster of 93 atoms around Mg. However, even better agreement with the experimental XANES spectrum of periclase is obtained when calculating a cluster comprising more than 100 atoms, i.e., extending to 7 Å distance from the Mg absorber taken as origin.

The structure of forsterite comprises three independent sites: T, with coordination number (C.N.) 4 occupied by Si; M1, with C.N. 6 occupied by Mg, and M2, again occupied by Mg with C.N. 6. The two metallic sites differ in mean size(2.094 Å vs. 2.129 Å at room temperature, RT), but are substantially equivalent in shape. The actual point symmetry is 1 for M1 and m for M2 but the quadratic elongations (Q.E.: Robinson et al., 1971) are nearly the same (Table 6.1.1).

To start with, the XANES spectra for each individual site were calculated using atomic clusters having increasing number of atoms until convergence. The convergent clusters include over 50 atoms within 5.03Å from the Mg atom taken as the center and have the Pbnm symmetry of forsterite as a whole. Larger clusters containing up to 89 atoms do not show any significant differences in the MS region as shown by (d) curves in Fig.6.1.2. The first-shell spectra for the M1 and M2 sites, as reported by curves (a) in Fig.6.1.2, are almost identical to the spectrum calculated for periclase (see Fig. 6.1.1). With increasing size of both clusters built around the M1 and M2 sites, definite differences arise between the calculated spectra of the two clusters which depend both on the average lengths of their bonds, and on their individual point symmetries. Such differences are not seen as clearly at the edge itself (where calculation certainly gives abrupt swings due to the muffin-tin effect problem) as in the MS region (in this system located between 10 and 40 eV). The convergent M1 cluster spectrum has ripples that are more sharply defined than the M2 cluster spectrum, besides being shifted to higher energies (approx 3 eV).

An experimental Mg K edge XANES spectrum of forsterite would consist of the superimposed contributions of all the Mg atoms present in the structure, i.e. of both clusters. A weighted combination of the calculated Mg-M1 and Mg-M2 cluster spectra in 1:1 proportion, as in the forsterite stoichiometry, is shown in Fig.6.1.2, right panel; the curve (d) is the spectrum that should be compared with the experimental Mg K edge XANES spectrum of forsterite at room temperature, when it becomes available.

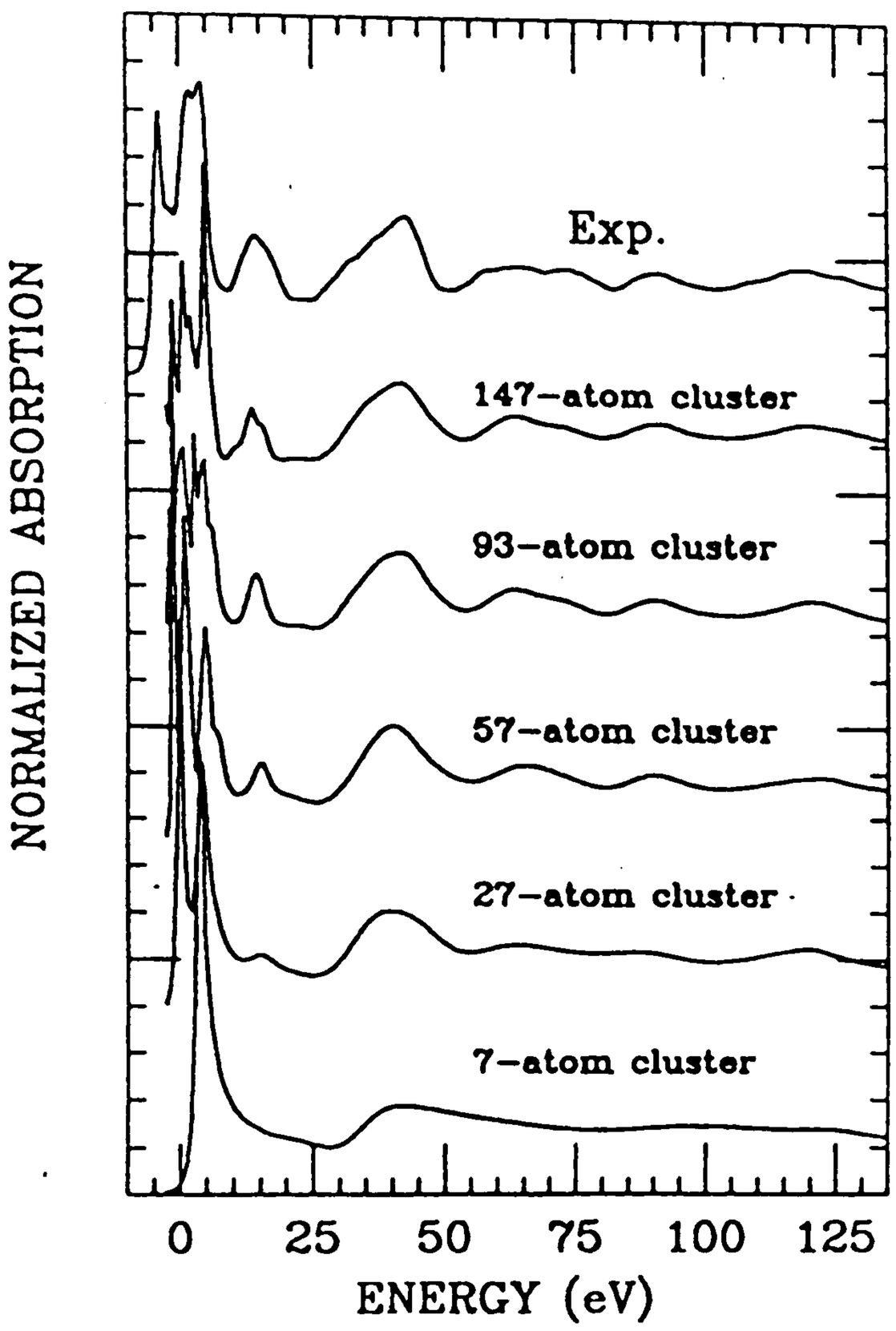

Fig. 6.1.1 Mg K-edge in MgO (periclase). The top curve is the experimental spectrum (Wong, 1993). From bottom to top the spectra show calculation results for clusters of 7, 27, 57, 93 and 147 atoms around the photoabsorber. Good agreement is obtained for the two largest cluster sizes.

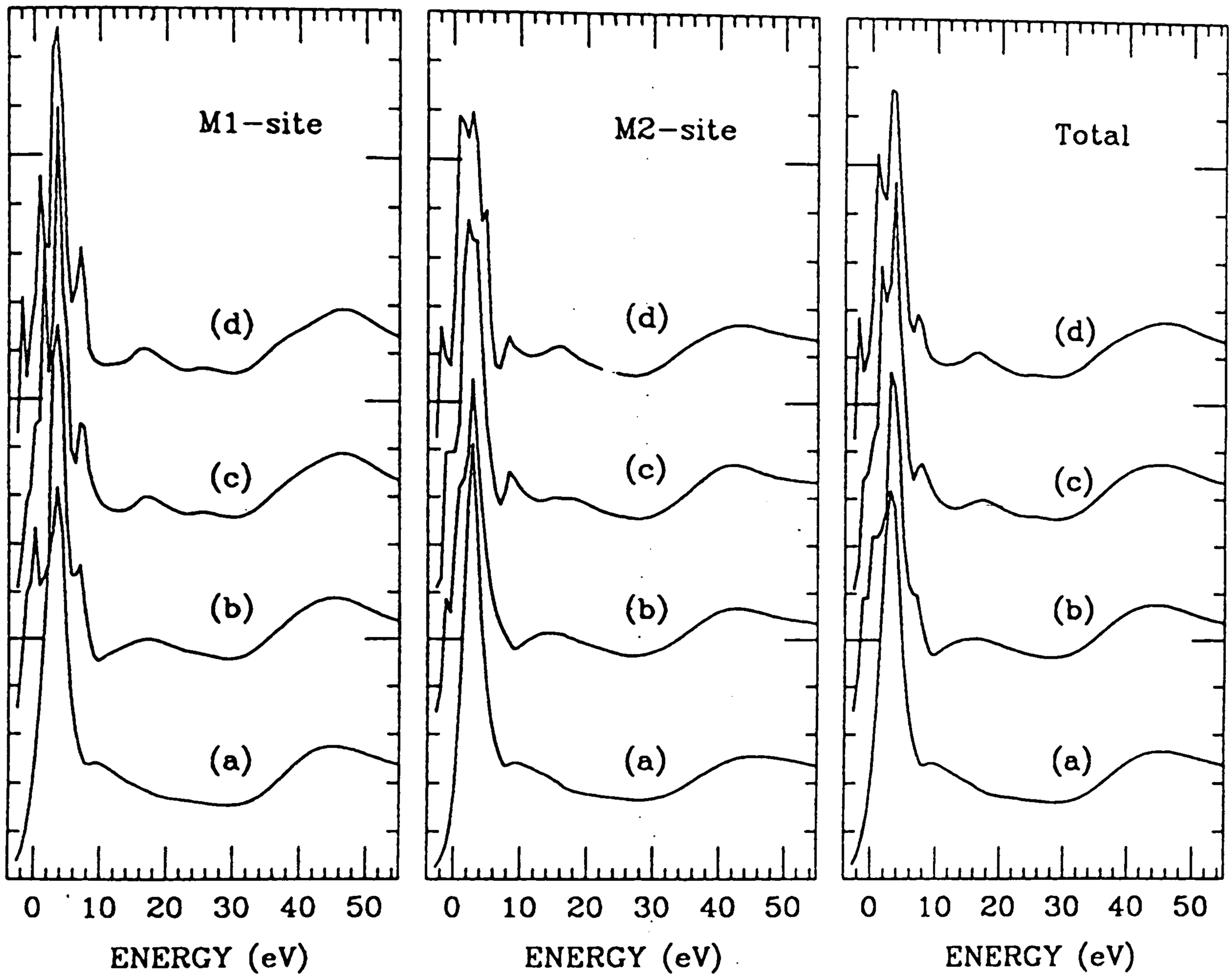

Fig. 6.1.2 Mg K-edge calculations for forsterite at ambient conditions for the M1-site cluster (left panel), the M2 site cluster (center panel) and the sum of these two contributions (right panel) - see text for details. Curves a, (b), (c), (d) refer to cluster calculations with increasing number of atoms: 14, 31, 55, 89, respectively, around the central photoabsorbing Mg.

The spectra to be expected for forsterite when submitted to extreme conditions, namely at high temperature (1020°C, from the in situ crystal structure determinations of Hazen (1976)), and at high pressure (at 50 kbar from the structure determinations of Hazen (1976), and at 149 kbar from the data of Kudoh and Tak'euchi (1985)) were also calculated. It appears that a temperature increase of 1000°C affects the spectrum only in the MS region (≥~40 eV above the edge; Fig. 6.1.3). There is a shift with respect to RT forsterite of approx 3 eV, that could be easily detected with standard experimental resolution at this energy. Moreover, it is important to underline that the changes in the spectra depend mainly on the contribution of the M2 site, because the M1 cluster spectrum calculated at 1020°C is almost identical to the RT spectrum (Fig. 6.1.3).

The effect of pressure on the calculated spectra is as significant as the temperature effect, but in the opposite direction: the ripples in the MS region are shifted by approx 3 eV while the whole spectrum becomes better defined and sharper than it is at room conditions (Fig. 6.1.4). However, changes of the MS structures are now due also to minor contributions coming from M1 site as well. This behaviour is consistent with the energy shift - bond distance relationship (Bianconi et al., 1983). The validity of the rule is verified by the calculations both at HP (= contraction) and HT (= expansion), and holds as long as the variation of the bond length does not modify the atomic potential. Indeed can be shown that the constrained site M1 is unaffected while the unconstrained site M2 is affected on a local scale by the variation of P and T conditions. Therefore, XANES is a local probe that should be used to check HT-HP structural modifications, in connection with X-ray diffraction studies which reveal the average structural changes on a much longer scale.

6.1.5 Conclusions

The main results of this study may be summarized as follows:

1. Calculations performed using the models based on the one-electron multiple-scattering theory result into computed XANES spectra that reproduce quite well the experimental spectrum of MgO-Fm3m (periclase).
2. The calculated Mg K edge XANES spectrum of forsterite is the averaged sum of two clearly recognizable contributions: one from the M1 site and the other from the M2 site. M2 gives most contribution to the total spectrum.
3. Calculated spectra corresponding to high temperature conditions indicate that shifts up to approx 3 eV towards low energy occur. They should easily be detected in the experimental spectra when it is possible to perform in situ measurements at the Mg K edge.
4. Calculated spectra at high pressure conditions indicate similar significant shifts, but in the opposite energy direction (approx +3 eV).

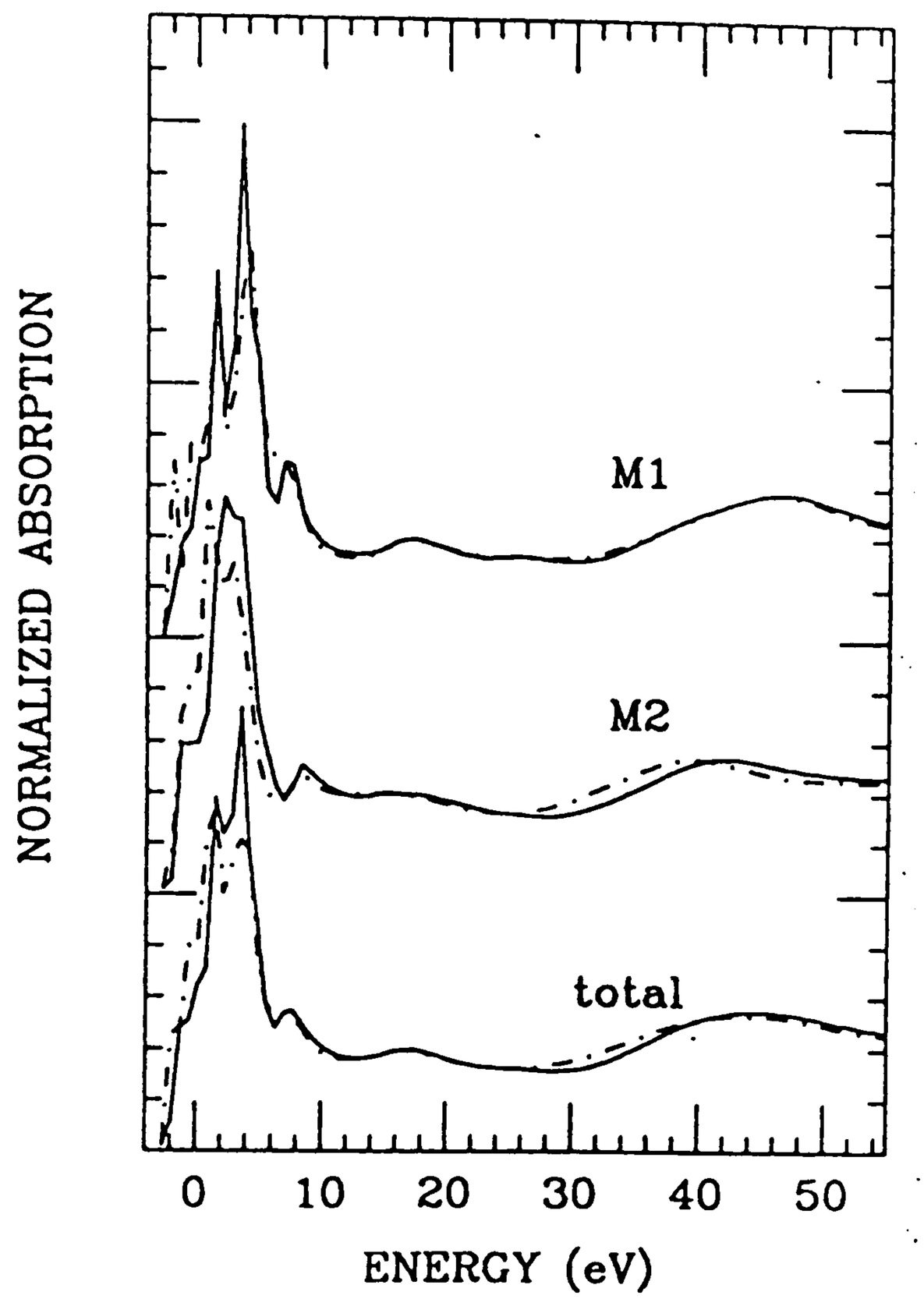

Fig. 6.1.3 Comparison of calculated Mg K-edge XANES for the forsterite structure at 1020°C (dot-dash line) and the forsterite structure at room T (solid line). Upper curves are for M1 site, middle curves are for M2 site. The bottom curves represent the sum of the M1 and M2 contributions. The dependence on T of the total spectrum (bottom) is mainly due to the M2 site contribution.

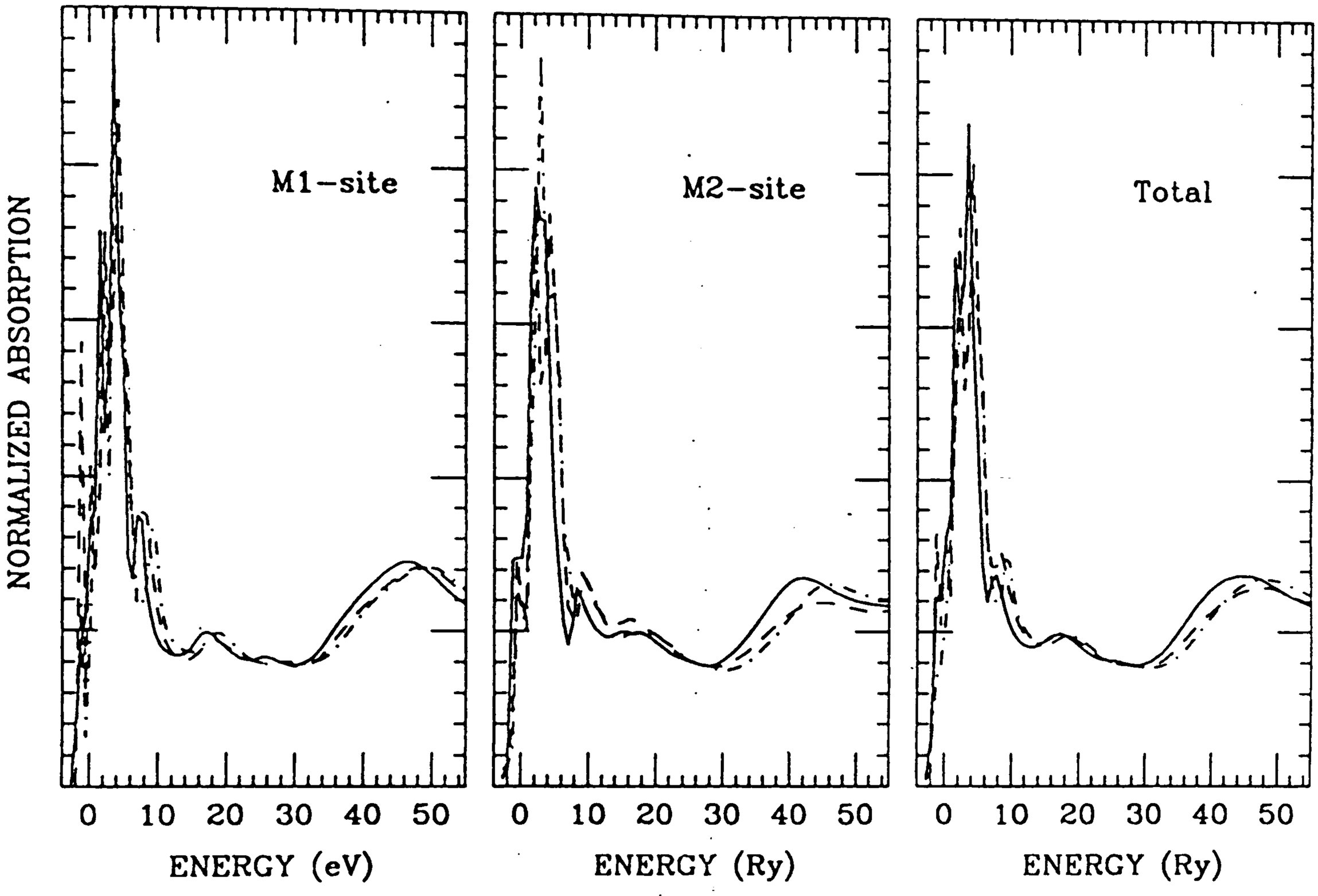

Fig 6.1.4 Comparison among Mg K-edge XANES calculations for forsterite at ambient conditions (solid line), 50 kbar (dash line) and 149 kbar (dot-dash line). The dependence on P of the total contribution to the cross section (right panel) is evident in the sum. Again it is mainly due to the M2 site contribution (center panel), but some differences also derive from the M1 site contribution (left panel).

Consequently, variations in structural properties at high P and T such as those occurring in forsterite can be studied by this method; conversely, pure forsterite appears to be a promising phase to be studied in situ at HP and HT. However, this indication needs to be verified by investigating the changes intervening in the spectra when Fe is partly substituted for Mg since this stoichiometry is closer to the composition of the olivine constituent of the upper mantle. Actually, Fe K edge can be measured at synchrotron radiation sources under extreme conditions whereas XAS experiments at Mg K edge are extremely difficult to perform, due mainly to the low energy of the Mg x-rays. Furthermore, given the high-field strength character of Fe, the XANES spectra may undergo changes that would make in situ XAS measurements of Fe at high pressure and temperature a promising project to better understanding the crystal-chemistry of olivines and the geophysical characters of the mantle.

6.2 THEORETICAL ANALYSIS OF THE X-RAY ABSORPTION NEAR-EDGE STRUCTURE (XANES) OF FAYALITE AT ROOM TEMPERATURE AND UNDER EXTREME CONDITIONS.

6.2.1 Abstract

The Fe K edge X-ray absorption spectra of fayalite have been calculated both for the constituting M1 and M2 sites and for the overall edge using the one-electron multiple scattering theory. Comparison with the experimental spectrum confirms the validity of theoretical model and of the calculation scheme. Starting from these results at room conditions, the Fe K edge X-ray absorption spectra of fayalite at low (-196°C) and high (+900°C) temperatures and at high (42 kbar) pressure have been calculated. The edge varies little with T, but shows well defined changes with P. Attempts to calculate the high-P edge for Fe^{2+} in low-spin using a different occupation of valence electrons show that if a change in spin state really occurs in fayalite, then it could easily be resolved by XAS, even with low resolution.

6.2.2 Introduction

Fayalite, Fe_2SiO_4 (Pbnm), is the ferrous analogue of forsterite, the Mg-endmember of the olivine solid solution series. As a mineral, fayalite is a rare constituent of certain felsic alkaline volcanics and granites, and of metamorphic iron formations. However, fayalite is by far more important for being the ferrous component (Fa) of the Mg-Fe-olivine solid solution series $(Mg_{2-x}Fe_x)[SiO_4]$-Pbnm. In fact, it is widely acknowledged that an olivine of composition $Fo_{88-90}Fa_{(10-12)}$(i.e., with x = 0.20-0.24) is the predominant phase in the Earth's upper mantle, and it is generally believed that the elastic and magnetic properties of such an intermediate Mg-Fe phase mostly depend upon its ferrous component (e.g., Drickhamer, 1965; Dietrich and Arndt, 1982; Graham et al., 1988; Sherman, 1988). Thus, knowledge of the structure and electronic properties of fayalite s.s. is essential, because endmember properties are boundary conditions to the properties of the geophysically-relevant solid solutions which contain them.

X-ray absorption near-edge structure (XANES) spectroscopy provides direct information on the shell of neighbours around a selected atom and can provide valuable insights into the structure and electronic properties of fayalite. Following the previous work on the Mg K edge of forsterite at room temperature and under extreme conditions (sec. 6.1), a similar analysis of fayalite Fe K-edge XANES has been done using the same modelling procedures. These calculations are another step towards the goal of eventually being able to calculate XANES spectra for olivine solid solutions of greater geophysical significance.

The theoretical analysis is based on the one-electron multiple-scattering (MS) theory of Lee and Pendry (1975) as implemented and developed by Natoli et al. (1990).

Calculation of the electronic properties of Fe in fayalite are done first with the crystal structure at room temperature (RT), and then extended to extreme P,T conditions. Contrary to the study of the Mg K edge of forsterite, where the calculations could not be supported with experimental evidence, the Fe K edge of fayalite is easily measured. Consequently, the theoretical calculation of the fayalite XANES spectrum has been verified by comparison with RT experimental spectra (Waychunas et al., 1983; Calas et al., 1988), and found to be consistent, thus supporting the applicability of the calculation procedure.

6.2.3 Theoretical Methods

The multichannel MS theory is well described by Natoli et al. (1990) and will only be summarized here in very general terms. I use Mattheiss' (1964) prescription to construct the cluster density, and Clementi and Roetti's (1974) tables to obtain the Coulomb part of the potential by superimposition of neutral atomic charge densities. Relaxation around the core hole in the photoabsorber with atomic number Z is simulated by the well screened Z+1 approximation of Lee and Beni (1977); for the exchange correlation part of the potential I use the Hedin-Lundquist self energy. Finally, the muffin-tin radii are chosen according to Norman's (1974) criterion, with a 10% overlap between contiguous spheres to simulate the bond among atoms. The general strategy followed in the calculations is similar to what was done for forsterite. Variations due to the special electronic properties of Fe, a transition element, are outlined below.

6.2.4 The structure of fayalite

The orthorhombic structure of fayalite (e.g., Fujino et al., 1981) comprises three independent cation sites: T, with coordination number (C.N.) 4 occupied by Si; M1 and M2, with C.N. 6 occupied by Fe^{2+}. The two M sites differ in mean bond length (2.161Å for M1 and 2.177Å for M2, at RT: Fujino et al., 1981) and point symmetry (1- and m), and even more so in shape (quadratic elongations Q.E., (Robinson et al., 1971) are nearly identical, 1.0379 and 1.0370, but octahedral angular variances, O.A.V. (Robinson et al., 1971) are 130.1 and 124.9, respectively). With respect to forsterite, fayalite not only has a greater unit-cell size, but it also has a more distorted structure, mainly in the individual octahedra, because the mean bond length difference between them is in fact less than halved (0.016 Å, against 0.035 Å in forsterite, which however is more regular as a whole, because it has O.A.V. 95.3 and 89.5). Furthermore, while the Mg-O bonds of forsterite are almost totally ionic and equal in their degrees of ionicity so as to force a nearly perfect octahedral shape onto the M1 and M2 coordination polyhedra, the Fe-O bonds of fayalite always display significant degrees of covalency, the Fe ion occupying the distorted M1 site being much less ionic than Fe located in the more regular M2 octahedron (Fujino et al., 1981; Gonschorek, 1986). Structural data and the atomic

positional parameters of fayalites used as input for the calculations are reported in Table 6.2.1.

At low temperature (-196°C: Hazen, 1977) the structure of fayalite contracts slightly; the size of the octahedra reduces and the SiO_4 tetrahedron expands somewhat. Moreover, the octahedra become more regular, as shown by their decreasing O.A.V., and conversely the tetrahedron becomes more deformed, as shown by its increasing tetrahedral angle variance, T.A.V. (Robinson et al., 1971). With temperature increasing to 900°C (Smyth, 1975; Hazen, 1977), the M2 octahedron expands much faster than the M1 octahedron does, and both become more irregular, as shown by their larger O.A.V., although both keep their point symmetries, 1- and m, respectively. By contrast, again the tetrahedron shrinks slightly while T.A.V. decreases. Therefore, it appears that expansion and contraction of the fayalite structure with temperature is controlled by a rather simple interplay in deformation between octahedra and tetrahedron.

When submitted to pressure, the structure of fayalite (Hazen, 1977) contracts substantially, and essentially at the expenses of the tetrahedron T and of octahedron M1; by contrast, the M2 octahedron increases in size and irregularity. Again, therefore, the deformation of the fayalite structure as a whole is controlled by the interplay existing between the individual polyhedra, but in this case octahedron M1 and tetrahedron T play the same role, and it is octahedron M2 that compensates for their changing sizes. The high-P structure was solved by Hazen (1977) with Fe in high-spin state, as no indication was available for pressure-induced spin state changes (see later).

6.2.5 Results

6.2.5.1 *Room temperature spectrum*

The XANES spectrum of each individual M cation site at room temperature (RT) was first calculated, using the positional parameters determined by Hazen (1977) on a synthetic fayalite (Table 6.2.1); this fayalite, as determined by Mössbauer spectroscopy (Santoro et al., 1966; Schaefer, 1985; Stanek et al., 1986; Hayashi et al., 1987)has all Fe as divalent and in high-spin final state $[Ar]3d^84s^1$. Spin state as above is not strictly rigorous, as electron spin cannot introduced in the calculation. Fujino et al.'s (1981) structure parameters are more recent and probably superior to Hazen (1977), but Hazen (1977) were used in order to make the RT calculation consistent with the subsequent calculations at different P and T. Calculations were carried out on atomic clusters containing increasing numbers of atoms till convergence, which implies that adding a larger number of atoms does not affect the spectra. The convergent clusters were found to include 52 (M2) to 55 (M1) atoms (Fe, Si, O), respectively, and to extend to slightly more than 5 Å from the Fe atom taken as the center of the cluster.

The calculated spectra for the two clusters (Fig.6.2.1: top and middle row) show differences which depend both on the average lengths of their bonds, and on their point

Table 6.2.1 . Crystal structure parameters of fayalite, $Fe_2SiO_4 - Pbnm$

Sample	1^a	2^a	3^a	4^b
$a(\AA)$	4.8142	4.8181	4.8014	4.8601
$b(\AA)$	10.4483	10.4735	10.2210	10.5592
$c(\AA)$	6.0762	6.0862	6.0496	6.1501
T(°C)	-196	23	23	900
P(kbar)	0.001	0.001	42	0.001
$\langle M1\text{-O}\rangle$	2.1504	2.1520	2.1062	2.1804
$\langle M2\text{-O}\rangle$	2.1780	2.1674	2.1973	2.2159

[a]Hazen, 1977.

[b]Smyth, 1975.

symmetries and polyhedral shapes. The M1 cluster spectrum (top) is richer in fine structure than the M2 cluster spectrum (middle row). In the edge region *sensu stricto*, both spectra have a small shoulder at +2 eV, but only the M1 spectrum shows three well separated features: note in particular feature A at +4 eV from the edge inflection; the M2 spectrum has two only features and a second shoulder on the higher part of rising edge that replaces peak A. The middle XANES region is also best resolved in the M1 spectrum: ripple E, at +25 eV in M1, cannot be seen in the M2 spectrum.

The Fe K edge XANES spectrum of a fayalite consists of the superimposed contributions of all Fe atoms present in the structures. To simulate this, a weighted combination of the calculated M1 and M2 cluster spectra in the stoichiometric 1:1 ratio should best reflect the experimentally determined spectrum. Fig. 6.2.1 shows such a combined (total) calculated spectrum and compares it with the experimental XANES spectrum of a synthetic fayalite (bottom spectrum, dashed curve: Calas et al., 1988). Unfortunately, the experimental spectra reported by Waychunas et al. (1983) could not be used, mainly because they are of poor quality, but also because they do not extend to high enough energies. Most if not all of the calculated features, including ripple E, are visible in the fayalite XANES spectrum of Calas et al. (1988): due to the good experimental resolution, the maximum is clearly composed of two features similar to the calculated B and C, the first one being the edge top. Furthermore, shoulder A is also reproduced. However, calculated and experimental spectra differ in the middle XANES region where the calculated D and E features are substituted by a single peak. In spite of this minor difference, the calculation can give insights into the complex configuration of the Fe K-edge of fayalite.

6.2.5.2 *Temperature effect*

For calculation of fayalite spectra at temperatures other than ambient, the starting data were the crystal structure positional parameters determined by Hazen (1977) at -196°C and 1 atm, and by Smyth (1975) at 900°C and 1 atm (Table 6.2.1). The latter have been determined on the same material, and are considered by Hazen (1977, p. 287) to be fully consistent with his own. Iron was again assumed to be in the final state electronic configuration $[Ar]3d^84s^1$. The calculated spectra are reported in Fig. 6.2.2 in the same order as the RT spectra; i.e.,M1 (top) and M2 (middle) clusters and combination of the two (bottom row). No experimental spectra are available for comparison.

The -196°C M1 and M2 cluster spectra (left panel) are not markedly different from the corresponding RT cluster spectra (*cf.* Fig. 6.2.1). Essentially, the M1 cluster spectrum looses peak A, which transforms into a shoulder at +2 eV, while peaks B and C appear to merge. Oscillations at higher energy do not change or show any shift. The M2 cluster spectrum at first sight is identical to the RT spectrum; in fact the major peak B shifts negatively to +5 eV, assuming the same energy position as shoulder A in the RT

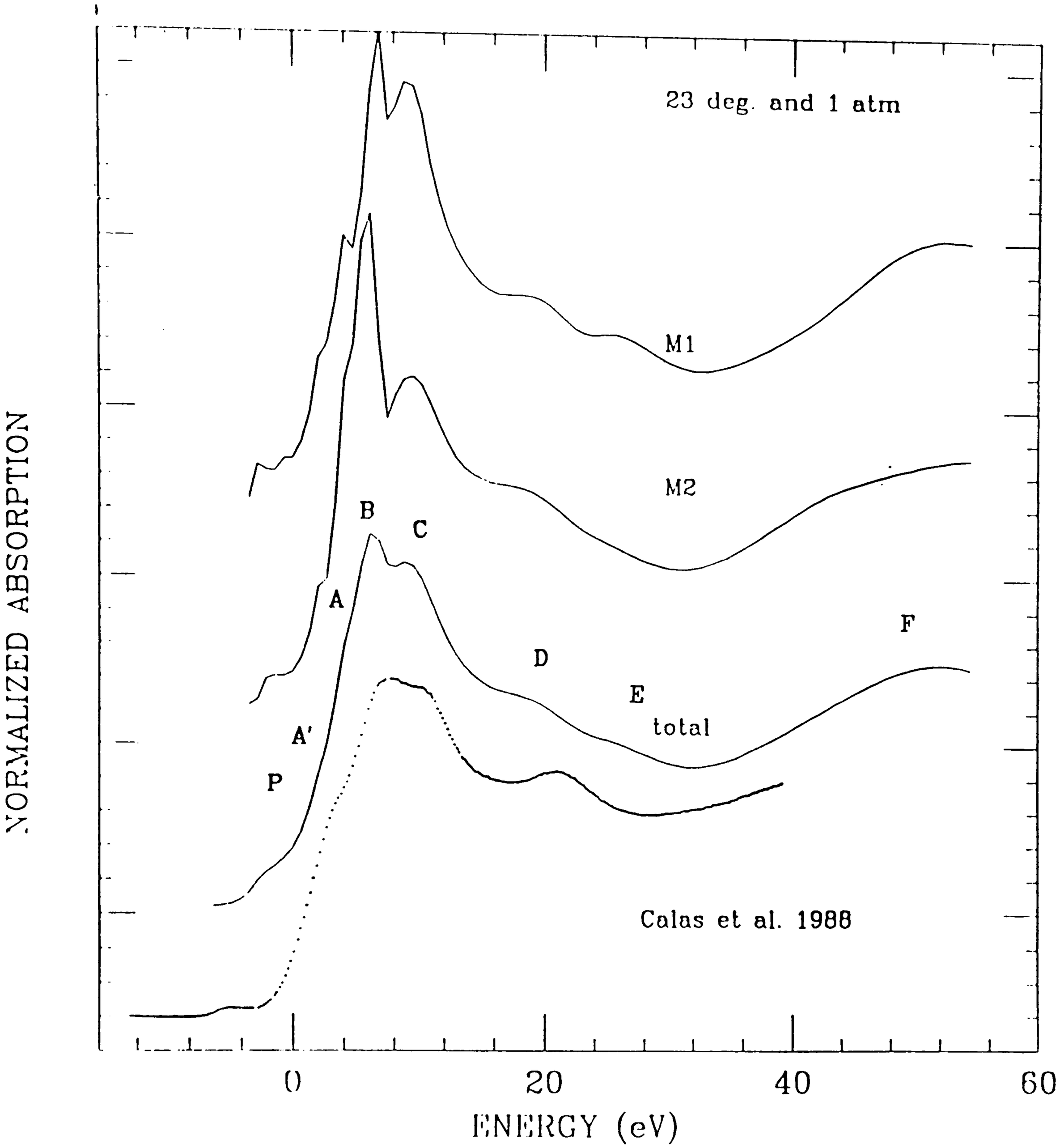

Fig. 6.2.1 Fe K-edge in Fe2sio4 at ambient conditions. The top and middle curves are M1- and M2-cluster contributions with Fe in high spin final state; the third curve gives the sum of M1 and M2. THe last curve is the experimental data of Calas et al. (1988)

spectrum. Consequently, the -196°C combined 1:1 spectrum (bottom row) is less well-defined than the RT spectrum in the edge region: feature A disappears, and peaks B and C almost merge into one; by contrast, in the middle XANES region the combined spectrum has peak D a little better defined than the RT spectrum.

When temperature is increased to 900°C, the situation changes drastically (Fig. 6.2.2: right panel): the M1 cluster spectrum (top) looses definition with respect to the RT M1 spectrum, particularly in the region just above the edge, where peak C becomes a shoulder to peak B; however, the spectrum gains somewhat in definition in the middle XANES region: ripples D at +19 and E at +26 eV are more marked than at RT, although they do not change in position. The M2 cluster spectrum (middle row) also shows major changes: the change in shape with respect to the RT spectrum is limited to the disappearance of the shoulder in the raising limb of the edge, substituted by a small but clear peak, but the energy position of edge B shifts negatively to +5 eV. Given these contrasting changes in contribution by the two clusters, it is not surprising that the 900°C combined 1:1 spectrum (bottom row) is practically identical to the -196°C combined spectrum. Apparently, therefore, a change in temperature of almost 1100°C would not appreciably change the total fayalite XANES spectrum: if changes occur, they will be difficult to detect, the more so as experimental spectra to be compared with the calculated ones are unlikely to show a good fine structure as a result of the poor resolution inherent in the thermal vibrations acquired on heating (*cf.* Seifert et al., 1993).

6.2.5.3 *Pressure effect*

The effect of pressure was determined by a calculation performed using as starting parameters Hazen's (1977) crystal structure refined at 23°C and 42 kbar (Table 6.2.1). The structures determined up to 140 kbar by Kudoh and Takeda (1986) have not been used because their natural fayalite is in fact a solid solution deviating significantly from the endmember. Again Fe was initially considered to be in the same spin configuration as Fig. 6.2. 2, but calculation was also repeated for Fe in low spin configuration (i.e., with electronic configuration $[Ar]3d^74s^2$). This possibility is considered because Fe^{2+} at high pressure may turn to spin configuration $[Ar]3d^74s^2$, despite the fact that at 1 atm it is constantly referred to be in the high spin state with the possible exception of some sulfide minerals (cf. Jagadeesh et al., 1981).

The HP spectra for fayalite with Fe in the high-spin state are reported in Fig. 6.2.3 in the same order as the previous ones. The M1 cluster spectrum (top) appears to be considerably richer in fine structure and better resolved than the corresponding RT spectrum: the three features A B C on the edge are clearly separated, and both ripples in the middle XANES region are strong and well defined. With the exception of peak A, which shifts by *ca.* -4 eV, the entire spectrum appears to be shifted to higher energies by +2 eV at least. The M2 cluster spectrum (middle row) is definitively poorer in fine

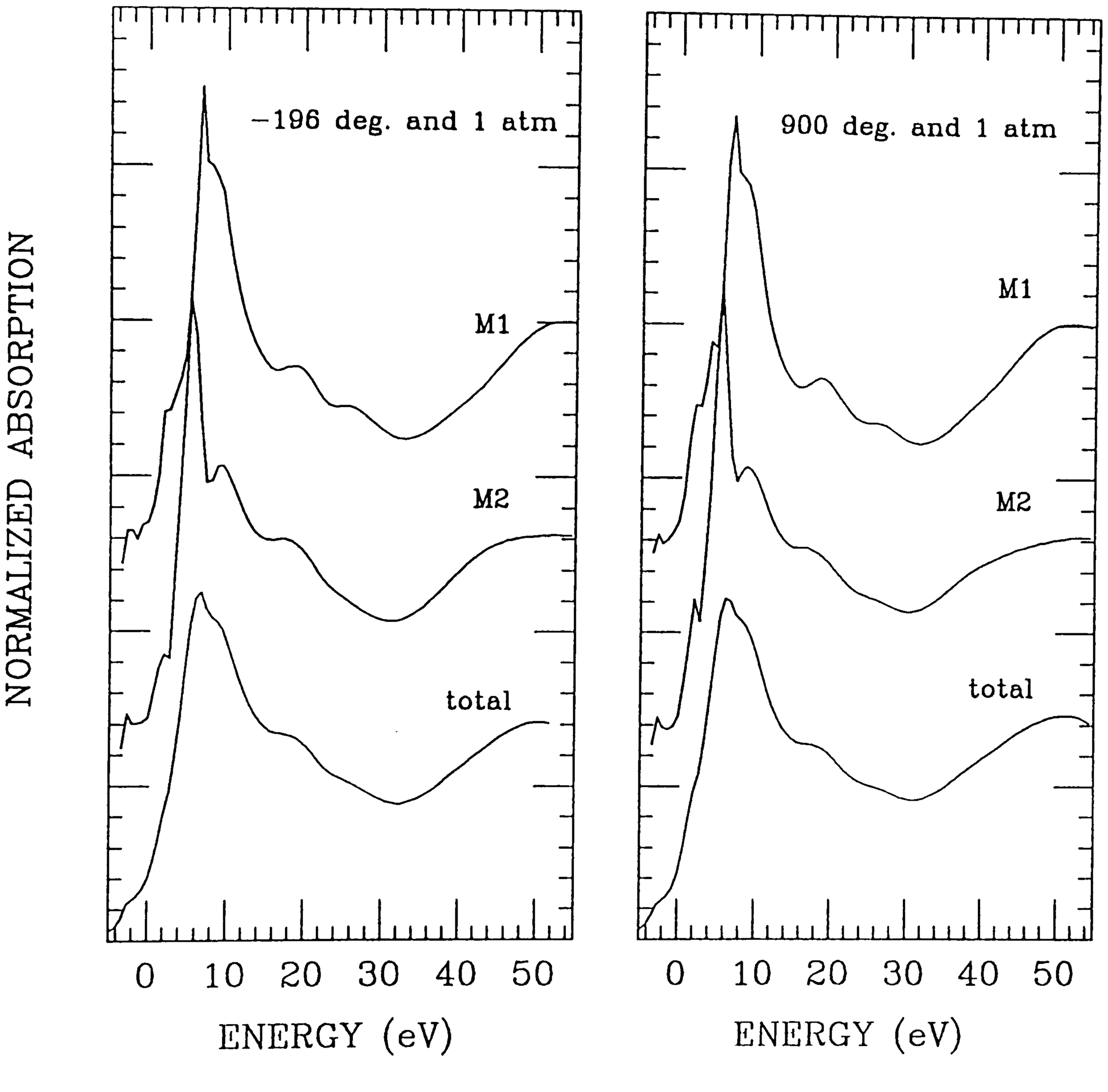

Fig 6.2.2 Fe K-edge XANES calculations at -196°C (left panel) and 900°C (right panel) with Fe in the high spin final state. From top to bottom: M1 cluster, M2 cluster and total contribution, respectively.

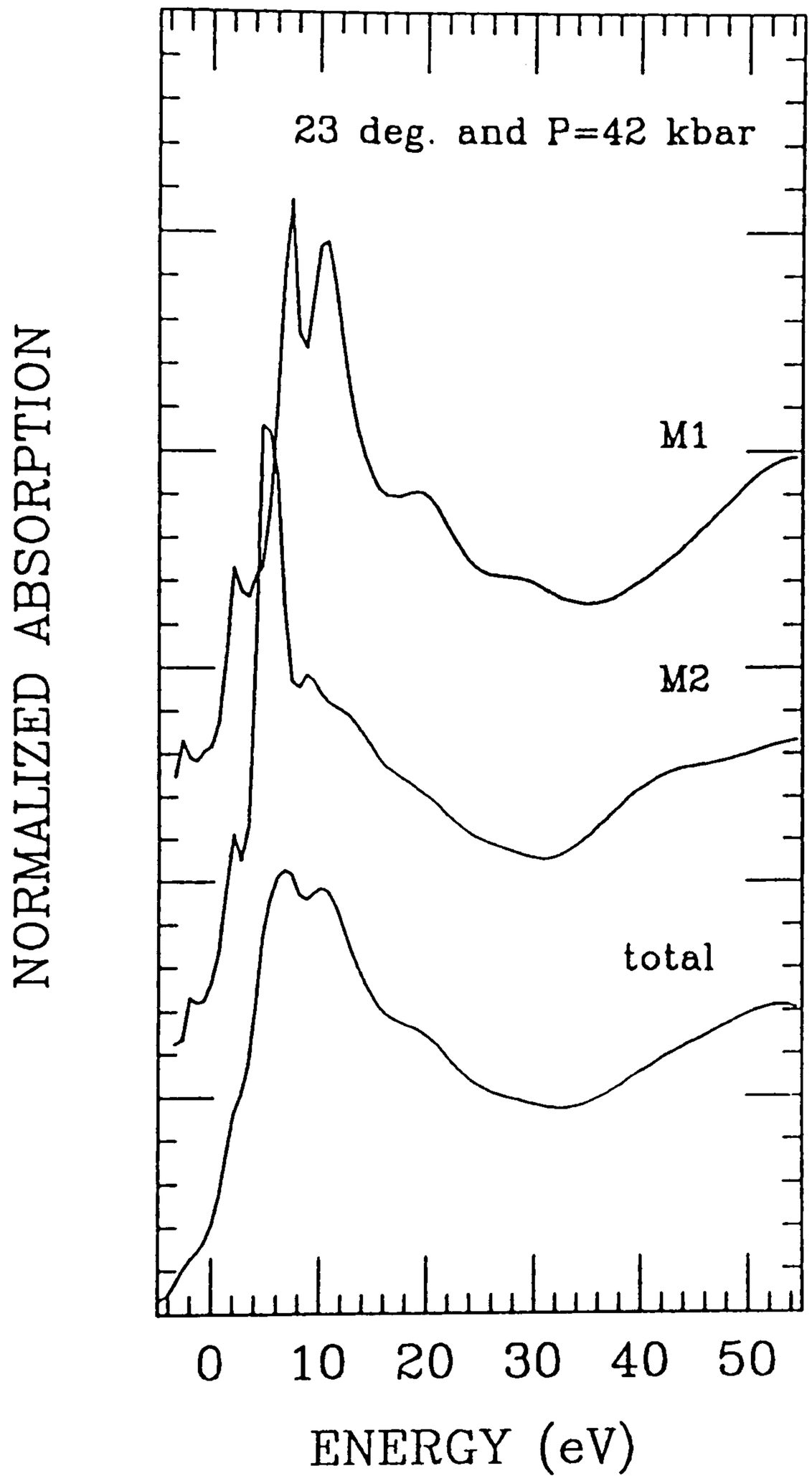

Fig 6.2.3 Fe K-edge XANES calculations at 23°C and 42 kbar with Fe in high spin final state. The order of the curves is the same as in Fig 6.2.2. The increase in P produces marked changes in both the M1 and M2 spectra. In particular, M2 shows a negative shift in energy position, related to an increase in the mean Fe-O bond length with pressure. In contrast, the M1 site decreases in size with increasing P and this reflects on the edge region of the spectrum M1, yielding a split of the peaks and a shift towards higher energy.

structure than the M1 cluster spectrum; however, it shows a systematic negative shift and is better resolved and richer in features than the corresponding RT spectrum (cf. Fig. 6.2.1): the loss in definition of peak C (shifted negatively to +10 eV) is compensated by the better definition of peak A at +2 eV; peak B is very strong and shifted to +5 eV, i.e., in the position that A had in the RT spectrum; moreover the two weak peaks D and E in the middle XANES region are clearly negatively shifted to +13 and +20 eV. The combined spectrum in the 1:1 ratio (Fig. 6.2.3: bottom row) appears to reflect mostly the appearance of the M1 cluster spectrum, and shows therefore a well resolved double edge with a shoulder in the raising limb of the edge, and a ripple in the middle XANES region. When compared to the RT spectrum, the 42 kbar model spectrum appears to be better resolved, especially in comparison with the low-T or high-T spectra.

As mentioned before, Fe may undergo a transition at high pressure from the high-spin to the low-spin state $[Ar]3d^74s^2$. This transition was first documented in Fe-doped manganese sulfide (Bargeron et al., 1971) and then extensively studied in oxides (e.g., Gaffney and Anderson, 1973; Sherman, 1988). However, the reported transition pressures are in the order of 100 kbar or greater, and may not apply to the fayalite case: e.g., Williams et al. (1990) specifically ruled out this possibility on the basis of the observed strong semiconducting electrical conductivity maintained by fayalite even at such high pressures, which contrasts with the band insulator character to be expected in a low-spin Fe-bearing mineral under those conditions. Nevertheless, it is useful to calculate the low-spin spectra, in order to investigate the predicted difference from high-spin Fe spectra.

In order to do this, the RT spectra of fayalite from the data of Hazen (1977) was first calculated, but with Fe in the low-spin final state, $[Ar]3d^74s^2$ as element, or $(t_{2g})^6(e_g)^0$, S=0 as divalent cation using the ligand field theory formalism (Verdaguer et al., 1990). These results are given in Fig. 6.2.4 as shown in left panel. Although this calculation is not based on a "rigorous" low-spin configuration, which rather would be similar to that acquired by Fe^{3+}, cannot be achieved, within this computation scheme, any better form to approximate the low-spin state.

The spectra calculated according to this model differ strongly from the corresponding RT high-spin spectra (*cf.* Fig. 6.2.1). The calculated low-spin Fe spectrum for the M1 cluster (top) is systematically negatively displaced by -4 eV in the edge region with respect to the high-spin Fe spectrum, as well as being better resolved. As seen previously, three main features define the edge, but in the low-spin spectrum A is a definite peak rather than a shoulder, and the edge maximum B displays an asymmetry toward the high energy side, suggesting a feature (B') which is undetectable in the high-spin spectrum; the broad peak C changes into a rather sharp peak. The ripples observed in the middle XANES region occur at the same or slightly higher (+1 eV) energy, and there is a final broad feature F with maximum at +48 eV. The low-spin-Fe M2 cluster

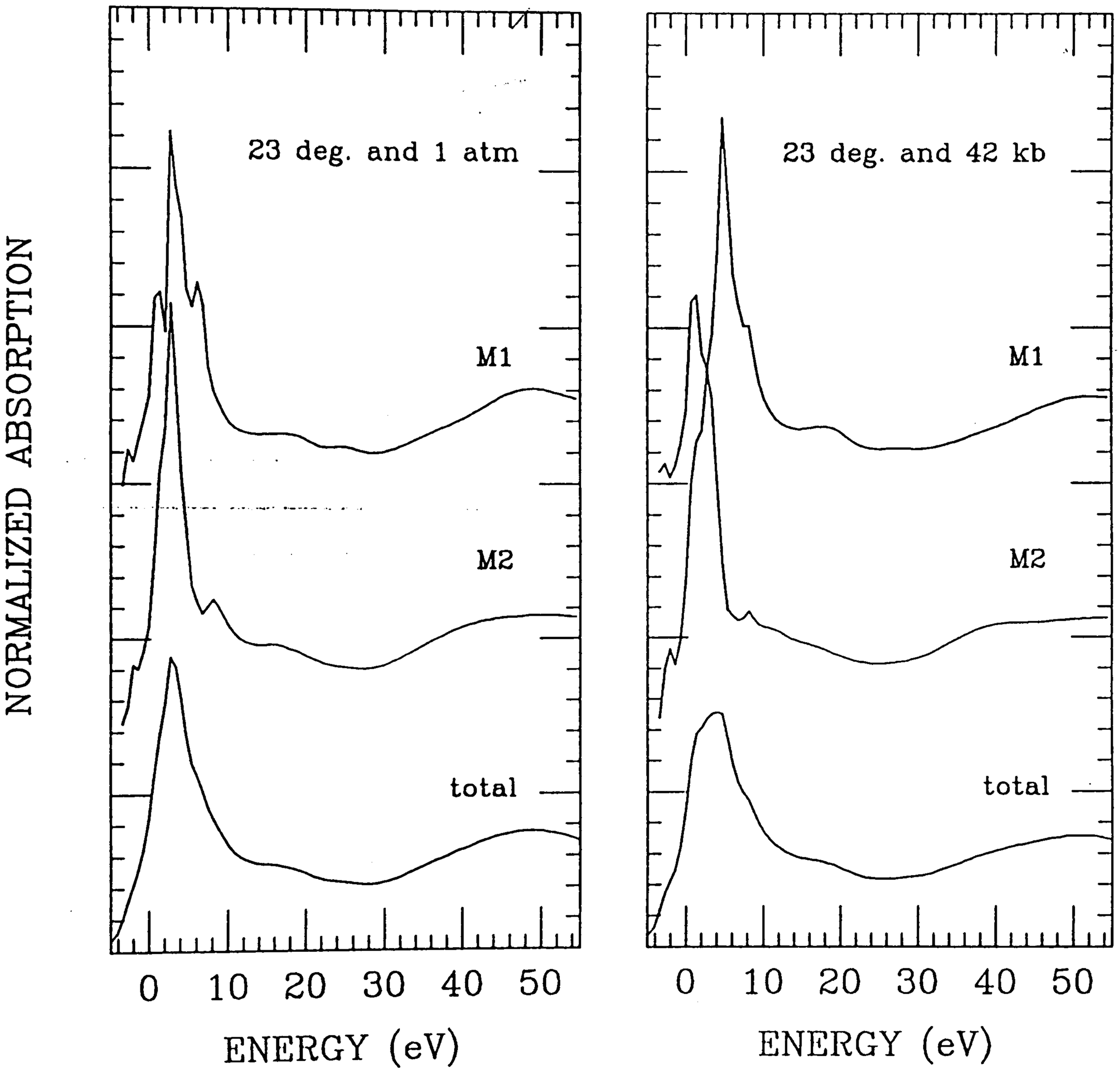

Fig. 6.2.4 Fe K-edge XANES spectra calculated at RT conditions (left panel) and at 42 kbar with Fe in low-spin final state. The order of the curves is same as in previous Figure.

spectrum (Fig. 6.2.4: left panel, middle row) shows less structure than the M1 spectrum; one can easily detect all features recognised in the M1 spectrum, but peak A and B now merge into a single strong peak with a shoulder on the rising limb, and peak C becomes rather weak. In the middle XANES region one of the ripples is lost, and the remaining one is very faint. As a result, the combined RT low-spin-Fe spectrum (Fig. 6.2. 4: left panel, bottom row) is almost featureless, with only the central peak sharp and strong, and with a weak ripple at +17 eV. This total spectrum has nothing in common with the experimental one (*cf.* Fig. 6.2.1).

The calculated low-spin-Fe spectrum for fayalite at P = 42 kbar, again from the atomic positional data of Hazen (1977), is shown in Fig. 6.2.4 (right panel). The results show the large differences arising from the pressure effect, both in the M1 and M2 cluster spectra (top and middle, respectively), and in the combined 1:1 spectrum (bottom row). All spectra loose definition with pressure, despite preserving the main features, but more important is the observed anisotropy in the changes. The 42 kbar M1 cluster spectrum has peak A enhanced because it maintains its energy position at +1 eV whereas peak B shifts considerably to higher energy (+6 eV) and almost overlaps peak C, even in spite of a small shift of the latter to +8 eV; the ripples present in the middle XANES region are reduced in number, but their intensities increase. The 42 kbar M2 cluster spectrum (Fig. 6.2.4: right panel, middle) gains somewhat in resolution, because A now appears as a shoulder just before the edge top B; however, peak C becomes even weaker and all ripples at high energy despair. As a result of these differences, the combined low-spin-Fe spectrum for fayalite at P = 42 kbar (Fig. 6.2.4: right panel, bottom row) has little structure: a shoulder near the edge top, another shoulder at +8 eV and a ripple at +18 eV. It compares unfavourably experimental RT spectrum of Calas et al. (1988) as well as with the calculated 42 kbar high-spin-Fe spectrum and both the RT spectra.

6.2.6 Discussion

The fayalite spectrum published by Calas et al. (1988, Fig. 2) is much better resolved, see Fig. 6.2.1 (bottom): the pre-edge at 7097 eV, the shoulder at 7106 eV, the double edge with its two features at 7110 eV and 7113 eV, and even the high-energy ripple at 7127 eV, are all features that compare favourably with the calculated total spectrum. Because Calas et al. (1988) gave no experimental details, the remaining discrepancy with the calculated spectrum could lie either in the resolution of their measurements, or in the quality of the fayalite used. However, even the calculated spectrum cannot be properly understood unless it is deconvoluted into the separate contributions given by the two clusters M1 and M2. In these, seven features have been identified and labelled: P, A', A, B, C, D, E and F. Features A' and A are particularly significant for considerations which will appear in the following; features B and C, on the

other hand, are the features defining the actual edge, which is split into two tops with uneven intensities.

An improved understanding of the fayalite XANES spectrum follows from evaluation of the spectrum calculated from -196°C structure data (Hazen, 1977) . The essential features of the calculated spectrum confirm the RT spectrum, but are everywhere better defined (as expected) except at the edge crest: besides the pre-edge, the separation of the edge top into two contributions B and C is indeed confirmed in spite of the overlap, as are the two ripples D and E in the middle XANES region. Moreover, on the rising limb of the edge a weak shoulder now supports the existence of a contribution from A that was not visible in the RT spectrum. The different contributions are better seen in the cluster spectra, where however there is no trace of A' detected at the RT. Furthermore, the -2 eV shift to lower energy of feature B in the M2 cluster spectrum confirms Natoli's (1984) law on the inverse relationship existing between average bond length and energy position of the edge. This shift is the cause of the broadening of the corresponding feature in the total XANES spectrum, and can be interpreted therefore as the best indicator of the contribution to the XANES spectrum arising from the relationships between Fe^{2+} and its next-nearest-neighbour oxygen. Ripples D and E, on the other hand, are second-shell contributions i.e., interactions between the ejected photoelectron and Si (or/and Fe in M1). The results of the calculation using the high temperature (900°C) structure determined by Smyth (1975) on the same fayalite confirm this interpretation: the two spectra at -196°C and +900°C are practically indistinguishable, both in overall shape and in energy position of the features. However, deconvolution of the 900°C spectrum into the contributions of the M1 and M2 clusters suggests some complementary ideas: the edge top due to the B feature becomes broad because this feature in the M2 cluster is shifted with respect to M1; furthermore, the shoulder on the rising slope of the edge is still due to the superimposition of the contributions of feature A. This feature still remains immobile with temperature (i.e., it does not change energy position) and, in order to account for the expansion of the structure, another feature develops, seen only in the M1 cluster spectrum: in fact, this is the cluster attaining the largest distortion (as indicated by O.A.V. = 152: Smyth, 1975, Fig. 3D), whereas the M2 octahedron tends to become more regular with increasing temperature. Together, these observations allow definition of the different structural contributions to the observed spectral features and give us confidence in the ability to model the major features of the XANES spectra.

The high-pressure spectrum needs experimental verification not only because of its significance in the interpretation of the electronic structure of fayalite, but because it can provide information about the pressure-dependent transition from high- to low-spin of Fe; this question would be easily answered by high P XANES spectra, as the model results show the resulting spectra would be easily distinguishable. Despite contrary

suggestions (Williams et al., 1990) the best way to determine whether such a transition is possible at P *ca.* 40 kbar still is a quick scan of the edge. Nowadays, new experimental apparatus would immediately solve the ambiguity: the high-P XANES spectrum would show a double edge in the case that Fe^{2+} is in high-spin, but it would appear broad and featureless in the case that pressure pushes the state of Fe^{2+} into low-spin.

6.2.7 Conclusions

Calculations of the Fe K edge of fayalite under different P,T conditions, and with iron approximating in the high- or low-spin state, lead to several interesting conclusions:

1) the experimental fayalite XANES spectra of Waychunas et al. (1983) conceal, probably because of their poor resolution, a number of interesting features which appear instead in the much better resolved XANES spectrum of Calas et al. (1988); these features can be used to understand the structural and electronic properties of this geophysically interesting endmember phase via computation performed on the basis of the MS theory of Natoli et al. (1990);
2) a XANES spectrum must be deconvoluted into the calculated contributions by the two Fe-bearing cation sites present in fayalite in order to be made understandable. Only in this way can the observed, often subtle, changes in experimental spectra be understood;
3) deconvolution points out that it is possible to extract two types of information from the spectrum: (i) those related to atomic contribution i.e., atomic coordination of Fe, from the energy position, and (ii) the structural contribution arising from the environment of Fe within the fayalite structure. The latter contribution is responsible for most features observed, and in particular for the double edge crest; the former is mostly concealed under the latter, and can be seen only occasionally in the form of a shoulder on the raising limb of the structural edge;
4) contraction due to cooling fayalite down to -196°C, and expansion due to its heating up to 900°C, reflect on the edge shape very little. They can be recognised only when the total spectrum is deconvoluted into its composing cluster spectra, but the effect of temperature on the fayalite absorption spectrum is bound to be minor, and possibly will defy resolution even when experiments will be attempted e.g., using in situ HT-cells (cf. Seifert et al., 1993);
5) contraction of the structure due to pressurizing fayalite to 42 kbar yields a total XANES spectrum with clearly different overall shape, although deconvolution into the two cluster spectra shows that it is composed of the same essential features as in the RT spectrum;
6) if a change in the spin state of Fe occurs with pressure, by using this computational scheme the low-spin Fe K edge XANES spectrum of fayalite becomes immediately recognisable because it is completely different from the high-spin Fe spectrum.

Experimental verification would be easy using appropriate HP-cells (cf. Shimomura and Kawamura, 1982), even though their resolution may be poor, since the Fe edge is at the very limit of detection when pressure is applied in situ in a large volume cell (O. Shimomura, personal communication, 1994).

CHAPTER 7. Ni/Mg DISTRIBUTION IN AMPHIBOLES

7.1 Ni-Mg DISTRIBUTION IN SYNTHETIC POTASSIUM-RICHTERITES: AN EXPERIMENTAL AND THEORETICAL XAS STUDY.

7.1.1 Abstract

The crystal-chemistry of synthetic amphiboles (potassium-richterites) along the join $K(CaNa)Mg_4Ni[Si_8O_{22}(OH)_2]$-$K(CaNa)MgNi_4[Si_8O_{22}(OH)_2]$ has been investigated by XAS (X-ray Absorption Spectroscopy). Experimental XANES spectra recorded at the Ni K-edge show a variation of the spectral features which can be related to the Ni-Mg substitution at the M sites of the studied amphiboles. Comparison with theoretical XANES spectra calculated on the basis of the multiple scattering theory aids interpretation of the observed experimental XANES features in terms of changes in the chemical and structural environments around the photoabsorbing ion. This combination of XAS experiments and theoretical calculations generates information on Ni partitioning between the three octahedral sites of richterites that compares favourably with site-occupancy determinations made by the Rietveld methods.

7.1.2 Introduction

X-ray absorption spectroscopy (XAS) is an element-selective method which can give information about the structural environment of elements present even in dilute amounts in both crystalline and amorphous materials (Brown et al., 1988). Combined EXAFS (Extended X-ray Absorption Fine Structure) and XANES (X-ray Absorption Near Edge Structure) spectroscopy gives data on bond distance and coordination number as well as on site geometry and degree of polyhedral distortion. Until recently, the structural information contained in the XANES spectra was not eaily interpreted and they were mostly used as a fingerprinting method to determine valence and coordination. The development of a rigorous theoretical model (Natoli et al., 1990; see also Davoli and Paris, 1990) has improved considerably the interpretation and allowed a much more quantitative use of XANES spectra (Paris and Tyson, 1994).

The basic features of the *C2/m* amphibole structure of richterites are described in Hawthorne (1981,1983). In particular, data on the structure of the octahedral strip in end-member fluor-potassium-richterite are to be found in Cameron et al. (1983) and are reported in Table 7.1.1. In this study it will be shown that the Ni and Mg distribution between the three octahedral sites obtained by Rietveld powder refinement on synthetic Ni-Mg-potassium-richterites (Della Ventura et al., 1993) can be independently determined by XAS. To this aim, experimental and theoretically-calculated spectra will be compared

Table 7.1.1. Crystal data for the octahedral sites of synthetic fluor-potassium-richterites*

	M(1)	M(2)	M(3)
M-O1 (Å)	2.060 (2x)#	2.181 (2x)	2.059 (4x)
M-O2 (Å)	2.027 (2x)		2.085 (2x)
M-O3 (Å)	2.070 (2x)	2.014 (2x)	
M-O4 (Å)		1.998 (2x)	
M-O average distance (Å)	2.052	2.088	2.044
polyhedral volume (Å^3)	11.299	11.940	11.133
quadratic elongation §	1.0135	1.0127	1.0144

* data taken from Cameron et al. (1983)

numbers in brackets indicates the bond multiplicity

§ as calculated following Robinson et al.(1971)

following methods similar to those used for orthopyroxenes (Chap. 4) and olivines (Chap. 6).

7.1.3 Methods

The characteristics of the experimentally synthesized Mg-Ni potassium-richterite samples (Della Ventura et al. 1993) used for this study are summarized in Table 7.1.2. Ni K-edge XANES experimental spectra were collected at the PULS X-ray beam line of the ADONE synchrotron of INFN-LNF, Frascati (Italy). A Si (111) monochromator was used, and the spectra recorded in transmission mode over an energy range of 150 eV across the Ni K-edge, with a step of 1.2 eV. EXAFS spectra of two samples were also collected over a range of 600 eV, with an energy step of 2 eV. Energy calibration was made by comparison with a standard Ni metal foil (8333 eV). Additional spectra were recorded using a Laboratory EXAFS apparatus equipped with a Rigaku 18 KW rotating-anode source at CIGA, University of Camerino (Italy). Sample preparation involved thorough mixing of the finely ground samples with BN, so as to ensure homogeneity and good signal-to-noise ratio. Data reduction of the XANES spectra consisted of background subtraction using linear function, and normalization of the spectra to the high energy side. The reduction of the EXAFS spectra has been performed using the GNXAS program (Di Cicco et al., 1992).

Theoretical XANES and EXAFS spectra were obtained using the GNXAS program package which is based on the multichannel one-electron multiple scattering theory (Natoli et al., 1990). GNXAS calculates both XANES and EXAFS theoretical spectra from a model structure (Filipponi et al.,1991; Di Cicco et al., 1992; Filipponi and Di Cicco, 1993) and includes the following steps:

1) building of an atomic cluster of suitable dimension, using the crystallographic coordinates of a structurally-refined material as close as possible to the sample under investigation;

2) automatic search of all the two-, three- and four-body photoelectron paths in the cluster;

3) phase-shift calculation;

4) calculation of the frequencies and amplitudes related to the scattering paths;

5) reduction of the experimental EXAFS spectrum, and comparison between calculated and experimental spectra;

6) calculation of the XANES spectrum.

For EXAFS spectra, the calculated spectrum is compared with the experimental one in such a way that each frequency and Debye-Waller factor of the calculated spectrum can be modified iteratively to obtain the best fit between the calculated and experimental spectrum. The result is a set of frequencies, each corresponding to a refined distance,

which allows determination of the contribution to the total spectrum due to an atom or a group of atoms.

7.1.4 Results

7.1.4.1 *EXAFS experimental spectra*

EXAFS spectra at the Ni K-edge were recorded for two samples representing the extremes of the Ni-Mg-potassium-richterite solid solution: $Ni_{20}Mg_{80}$ and $Ni_{80}Mg_{20}$. Their Fourier transforms are shown in Fig.7.1.1. Both spectra show two main contributions (A and B: Fig.7.1.1) localized within 4.0 Å from the photoabsorber. The main difference between the spectra is in the peak related to the contribution of the second coordination-shell (B). In the $Ni_{80}Mg_{20}$ spectrum B is more intense, and shifted to radial distances lower (by 0.08 Å) with respect to the $Ni_{20}Mg_{80}$ spectrum.

The observed difference in intensity can be explained by considering the different backscattering amplitude functions of Ni and Mg atoms. Ni has a higher backscattering function than Mg atoms do; thus, in sample $Ni_{80}Mg_{20}$, in which the photoabsorber (Ni) is surrounded mainly by Ni in the second coordination-shell, the corresponding peak is more intense than in sample $Ni_{20}Mg_{80}$, where the photoabsorber is more likely to be surrounded by Mg. The fact that the peak related to the second coordination-shell in sample $Ni_{20}Mg_{80}$ is less intense than in $Ni_{80}Mg_{20}$ suggests, moreover, that there is no nickel clustering (i.e. preferential like-neighbours distribution) in this amphibole.

The spectra in Fig.7.1.1 show no appreciable difference in the radial position of the first peak (A), which is related to photoelectron scattering from the nearest neighbours i.e. to the Ni-O bond distance; the difference in<M-O> distances in these samples must be virtually identical, given that the EXAFS resolution is ~0.02 Å. As a result, the EXAFS spectra cannot give any useful information on site population of these richterites. For this reason, major attention is focused on interpreting the XANES spectra.

7.1.4.2 *XANES experimental spectra*

The Ni K-edge XANES spectra are shown in Fig.7.1.2 and energy values for the major features are listed in Table 7.1.3. All spectra are characterized by a low intensity pre-edge peak (A), by a shoulder in the low-energy side of the edge region (B), by having the main absorption feature (D) accompanied by a pronounced shoulder (C) at the low-energy side, by another small shoulder (E) at higher energy, a peak (F), and a final broad peak (G) which, in some spectra, is split into two distinct peaks (G' and G").

Note that the spectrum of end member Ni-potassium-richterite Ni_{100} has been recorded with the Rigaku Laboratory XAS machine equipped with a 18 KW rotating anode. Although lacking in resolution in the edge region (note features A to C in Fig.7.1.2), the spectrum has a reasonably good resolution in the XANES region (10-50

Table 7.1.2. Formulas and unit-cell parameters of the synthetic Ni-Mg potassium-richterites under study.

SAMPLES	FORMULAS *a* (Å)*	*b* (Å)*	*c* (Å)*	ß (°)*
$Ni_{20}Mg_{80}$	$K(CaNa)Mg_4NiSi_8O_{22}(OH)_2$			
	10.0536(7)	17.982(1)	5.2702(4)	104.879(5)
$Ni_{40}Mg_{60}$	$K(CaNa)Mg_3Ni_2Si_8O_{22}(OH)_2$			
	10.0492(7)	17.975(1)	5.2661(4)	104.904(4)
$Ni_{60}Mg_{40}$	$K(CaNa)Mg_2Ni_3Si_8O_{22}(OH)_2$			
	10.0436(7)	17.962(1)	5.2633(3)	104.936(4)
$Ni_{80}Mg_{20}$	$K(CaNa)MgNi_4Si_8O_{22}(OH)_2$			
	10.0382(7)	17.954(1)	5.2610(3)	104.954(5)
$Ni_{100}Mg_0$	$K(CaNa)Ni_5Si_8O_{22}(OH)_2$			
	10.0297(7)	17.942(1)	5.2576(3)	104.982(5)

* data from Della Ventura et al. (1993), numbers in brackets indicate the error

Table 7.1.3. Energy position (eV) of Ni K-XANES relevant spectral features for the Ni-Mg potassium richterites

	A	D	F	G	G'	G''
$Ni_{20}Mg_{80}$	8324.1	8343.7	8357.7		8383	8395
$Ni_{40}Mg_{60}$	8325.0	8343.2	8357.7		8383	8395
$Ni_{60}Mg_{40}$	8324.1	8343.7	8358.4	8391.1		
$Ni_{80}Mg_{20}$	8324.6	8343.2	8358.4	8390.3		
$Ni_{100}Mg_0$	n.d.	8343.2	8358.2	8389.1		

n.d. peak not detectable

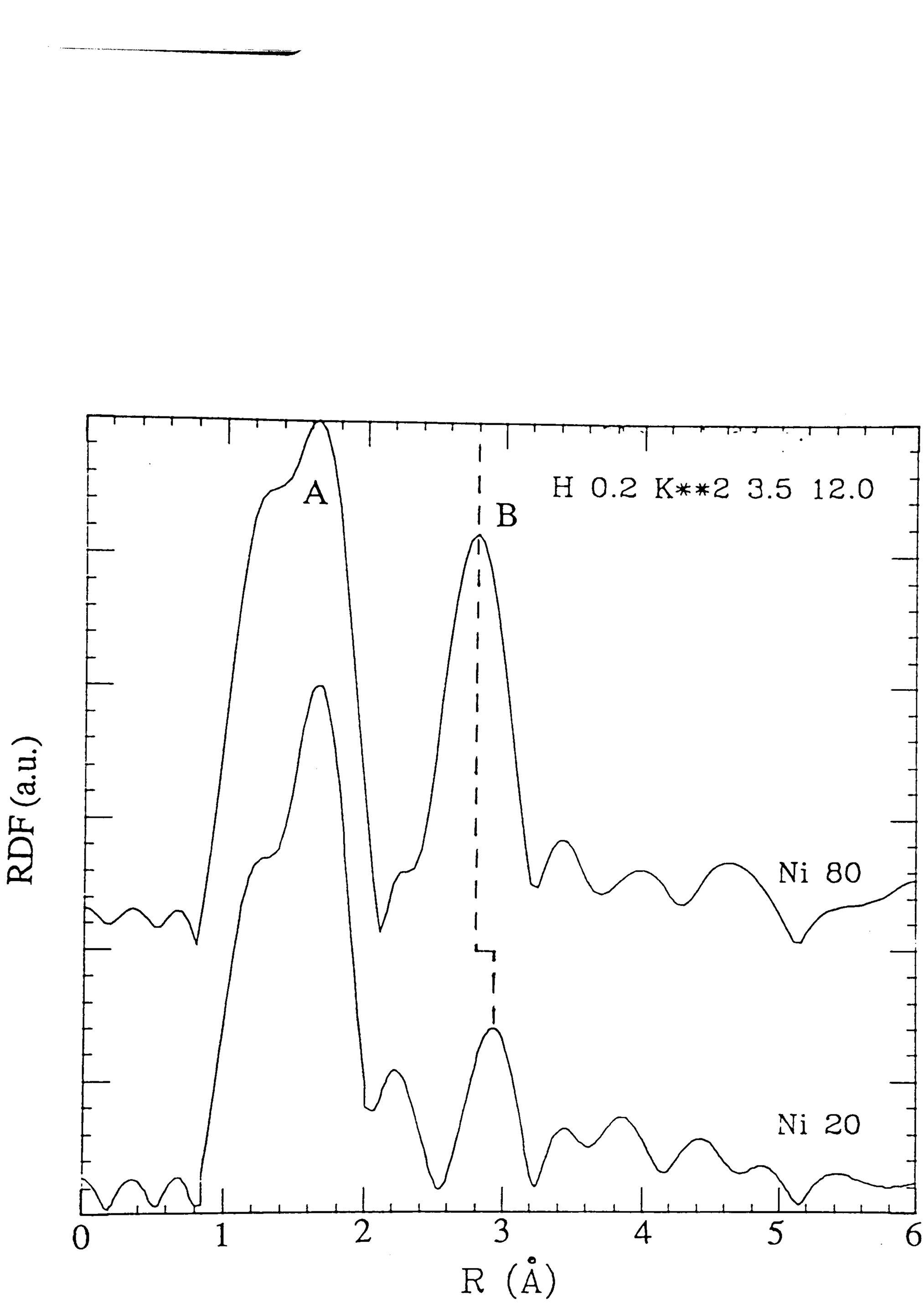

Fig. 7.1.1 Comparison between the Fourier transforms of the $Ni_{20}Mg_{80}$ and the $Ni_{80}Mg_{20}$ spectra.

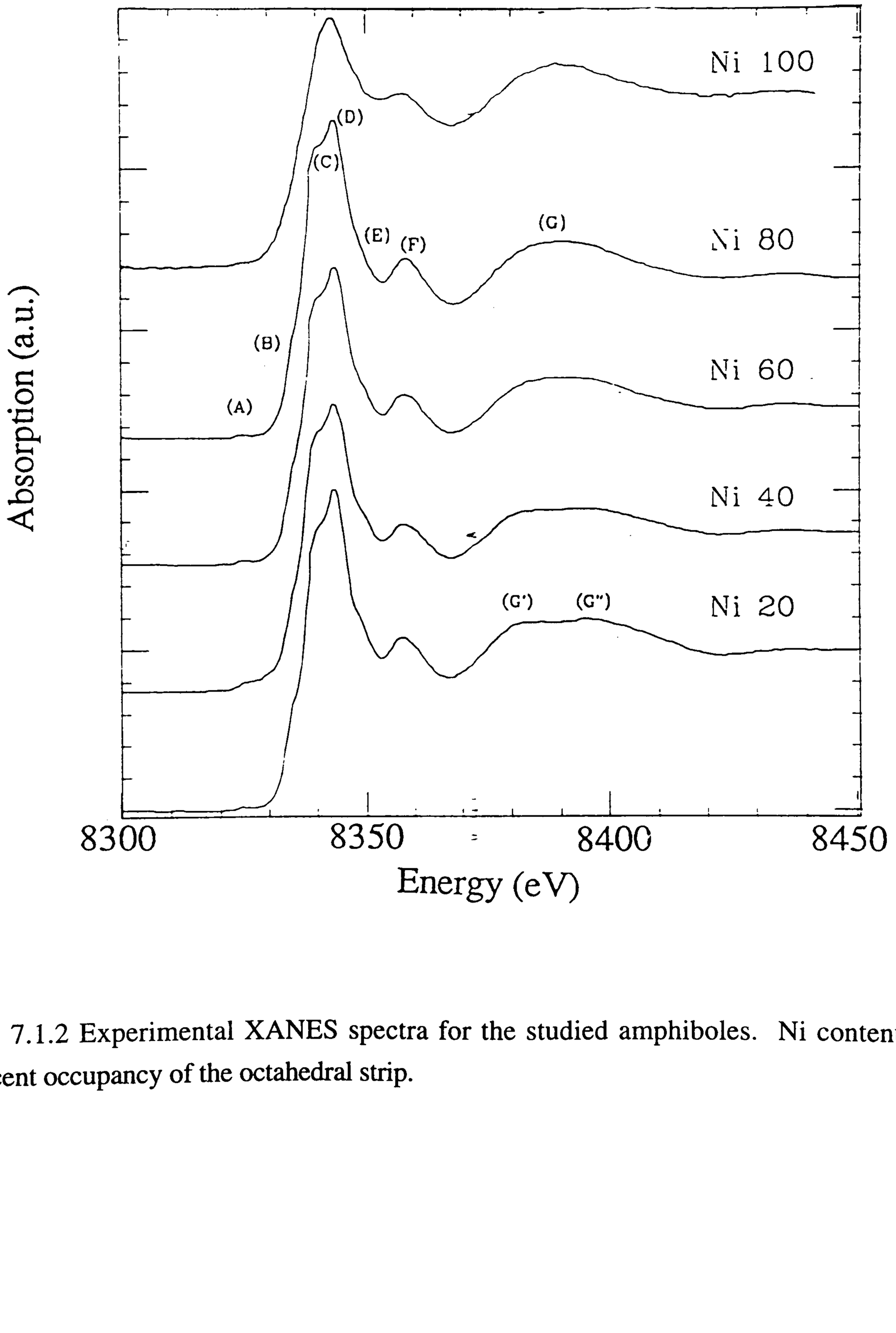

Fig. 7.1.2 Experimental XANES spectra for the studied amphiboles. Ni contents in percent occupancy of the octahedral strip.

eV above the threshold: features D to G in Fig.7.1.2) and therefore is useful to the following discussion of features in the XANES region.

The variations occurring in the spectra with increasing Ni-Mg substitution include the following:

1) the intensity of shoulder C with respect to the most intense peak D decreases with decreasing Ni content;
2) peak F slightly shifts to higher energy with increasing Ni content (Table 7.1.3);
3) peak G increasingly splits into two separate peaks (G' and G") with decreasing Ni content.

The changes in the spectra, in particular (1), the decreasing intensity of shoulder C, and (3), the splitting of peak G, correlate with the variation in the Ni/Mg ratio. Thus it seems reasonable to assume that (1) and (2).are related to a change in the structural and/or chemical environment around the photoabsorber (Ni).

7.1.4.3 *XANES theoretical spectra*

In order to test the above-mentioned factors, two sets of theoretical spectra were calculated: one for Ni_{100}, and one for $Ni_{20}Mg_{80}$. The structural parameters used in these calculations are those of Cameron et al. (1983), and the cell parameters are those of Della Ventura et al., (1993). It is worth noting that, while the complex potentials used in these calculations improve the results in the middle XANES region, they are discontinuous in the edge region, thus producing unreliable results in that part of the spectrum. Therefore these results will be considered only in the region 10-50 eV above the edge.

7.1.4.3.1 **Richterite Ni_{100}.** For this composition, the octahedral sites are occupied only by Ni. The EXAFS spectrum (Fig.7.1.1) shows that relevant contributions to the spectra are confined to within 4.0 Å from the photoabsorber, thus indicating the suitable number of atoms to be included in the calculation.

To simulate the experimental spectrum three different calculations were performed, with the photoabsorber at the M(1), M(2) and M(3) sites, respectively. The results of each independent calculation were then summed up together with a weight equal to the multiplicity of the site in the structure (i.e. M(1) : M(2) : M(3) = 2 : 2 : 1). For each site, three calculations were done, that included all atoms to within 2.1 Å, 3.3 Å, and 4.0 Å from the photoabsorber; this allowed testing how the size of the cluster affects the spectral features. The results are shown in Fig.7.1.3. In each set of calculation, the G peak is reproduced by including just the first coordination-shell, composed only by oxygens; when introducing the second and the third shells, peak G is slightly shifted to higher energies, but shows no splitting. Conversely, peak F is correctly reproduced only when introducing the third coordination shell.

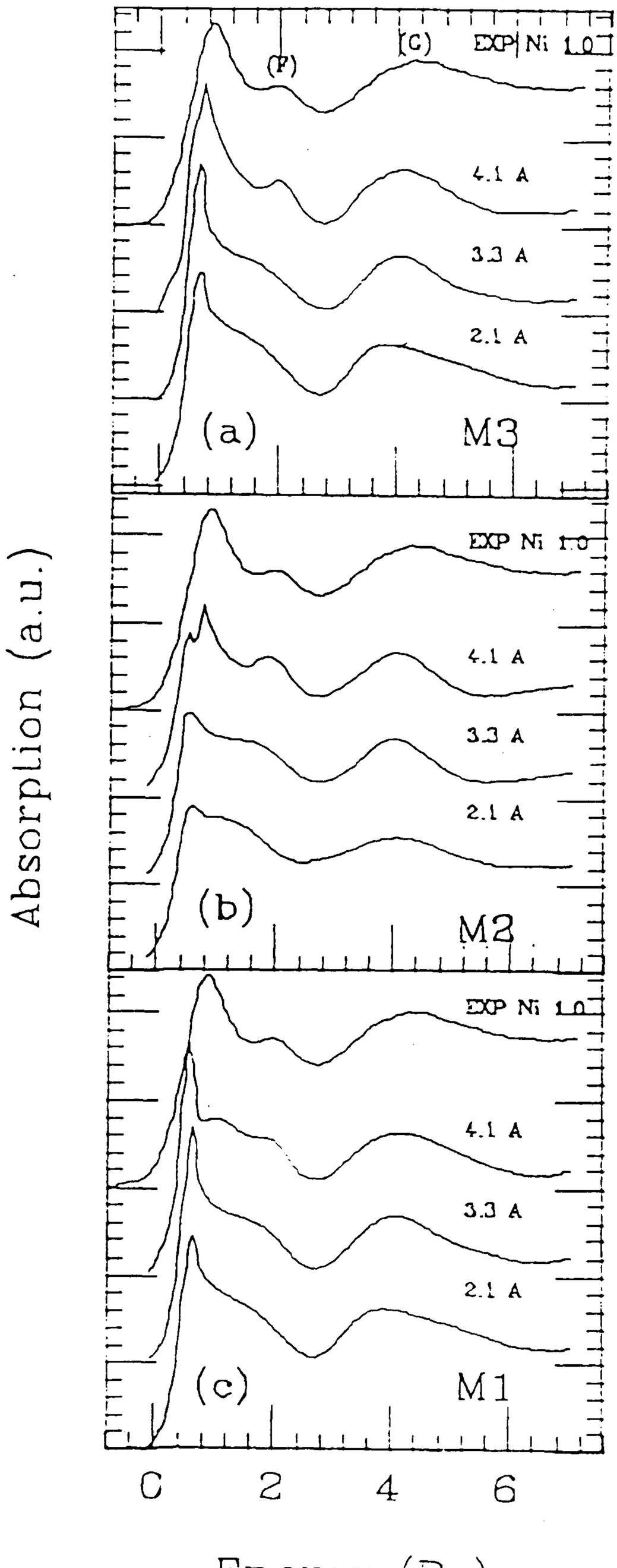

Fig. 7.1.3 Theoretical XANES spectra calculated for Ni_{100} richterite, with the photoabsorber located at (a) M3, (b) M2, or (c) M1. The experimental spectrum for Ni richterite is shown at the top of each panel for comparison.

The final spectrum obtained from the weighted sum of the three sites is given in Fig.7.1.4. The agreement with the experimental spectrum is excellent: the energy positions and the relative intensities of the peaks are well reproduced, suggesting that the choice of the model structure and the number of atoms included in the calculations (up to 4.1 Å) are satisfactory.

7.1.4.2 **Richterite $Ni_{20}Mg_{80}$.** This is the sample with the lowest Ni content of the series, and Rietveld refinement (Della Ventura et al., 1993) showed Ni to be strongly enriched in M(1) and M(3) respect to M(2). For this sample, three different cases were simulated, with Ni localized exclusively at only one of the M(1), M(2) and M(3) sites, and with the remaining octahedra occupied by Mg. For each case a set of three calculations were performed.

When Ni is located in M(3) (Fig.7.1.5a), peak G is well reproduced already by the smallest cluster used in this calculation (composed by 7 atoms). Upon introducing all atoms to within 3.3 Å from the photoabsorber (i.e. 6 Mg + 4 Si), peak G splits into two components as observed in the experimental spectrum. As a result of this, I tried to calculate a spectrum using a cluster including all atoms of the first coordination-shell plus the six Mg atoms only of the second coordination shell, in order to verify independently the effect of the Mg and Si contribution on the splitting of the G peak. The splitting of peak G was correctly reproduced by just including the 6 Mg atoms of the second coordination shell, whereas peak F can be reproduced only when including all atoms within 4.0 Å of the photoabsorber.

When Ni is only in M(2) (Fig.7.1.5b), a single G peak is produced by including the first coordination shell in the calculation. However even when including the second shell (i.e. 3 Mg + 2 Ca + 6 Si atoms), and the third coordination shell no splitting is reproduced. The introduction of all atoms to within 4.0 Å from the photoabsorber just enhances peak F.

In the case of the calculation with Ni in M(1) (Fig.7.1.5c), peak G is reproduced when using the smallest cluster (7 atoms). Introduction of the five Mg atoms of the second coordination shell is needed to obtain the splitting of peak G. Introduction of all atoms to within 4.0 Å distance from the photoabsorber only enhances peak F.

The experimental spectrum can be reproduced by summing the calculated spectra of the three clusters weighted according to the Ni-site populations of M(1), M(2) and M(3). Fig.7.1.6 shows that if using three increasing weights (site populations) for M(2) the splitting of peak G tends to disappear. Thus, comparison with the experimental spectrum suggests a low Ni-occupancy of the M(2) site, in agreement with the Rietveld data (Della Ventura et al., 1993). Good agreement between calculated and experimental spectra was achieved when using the values M(1) : M(2) : M(3) = 0.49 : 0.17 : 0.33 obtained via Rietveld refinement (Della Ventura et al., 1993) (Fig.7.1.7) .

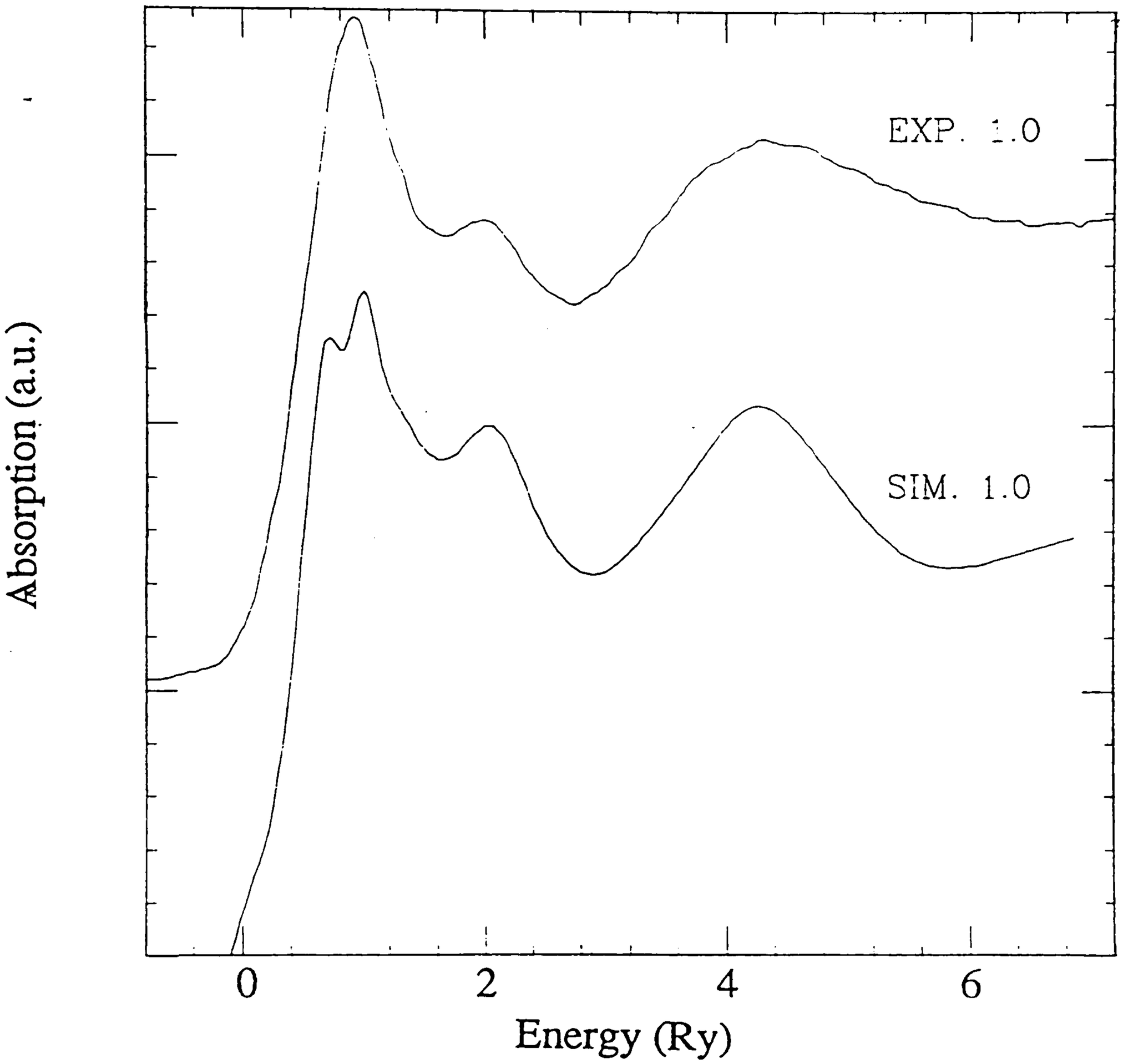

Fig. 7.1.4 Comparison between the experimental Ni_{100} XANES spectra and the theoretical total spectrum.

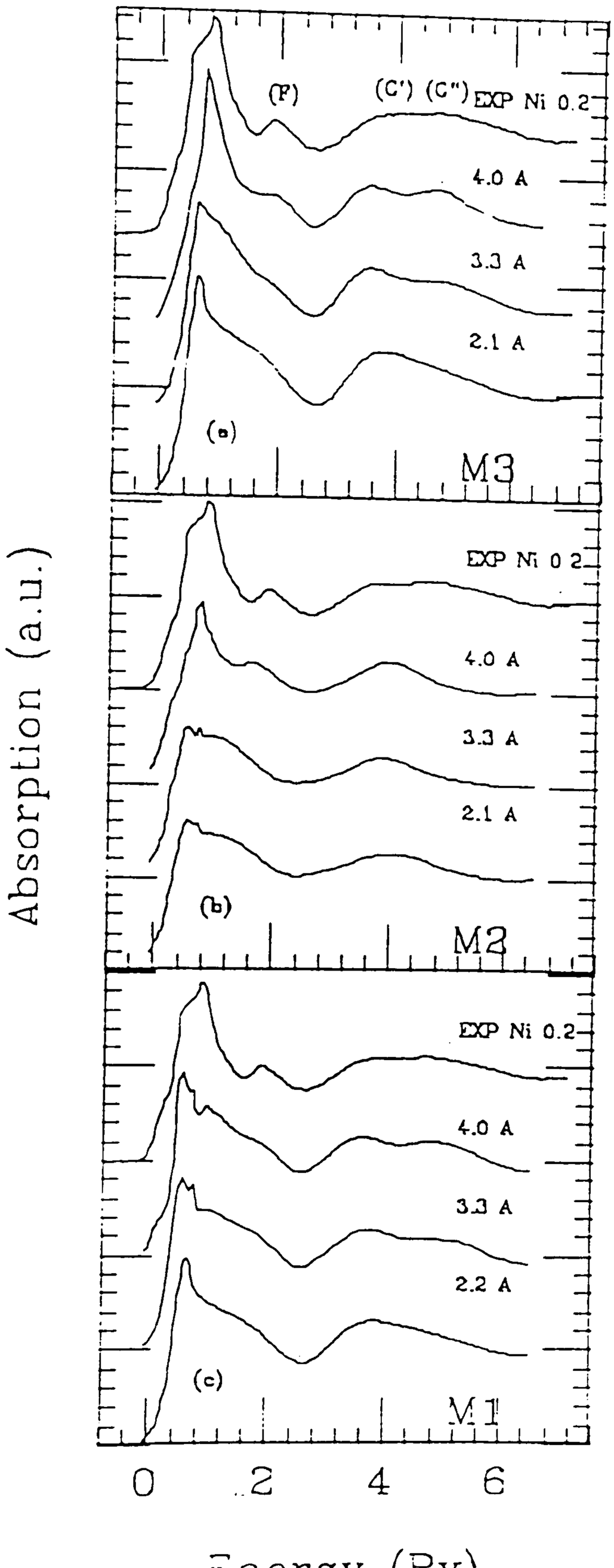

Fig. 7.1.5 Theoretical XANES spectra calculated for richterite $Ni_{20}Mg_{80}$. The experimental XANES spectrum (EXP) is shown for comparison.

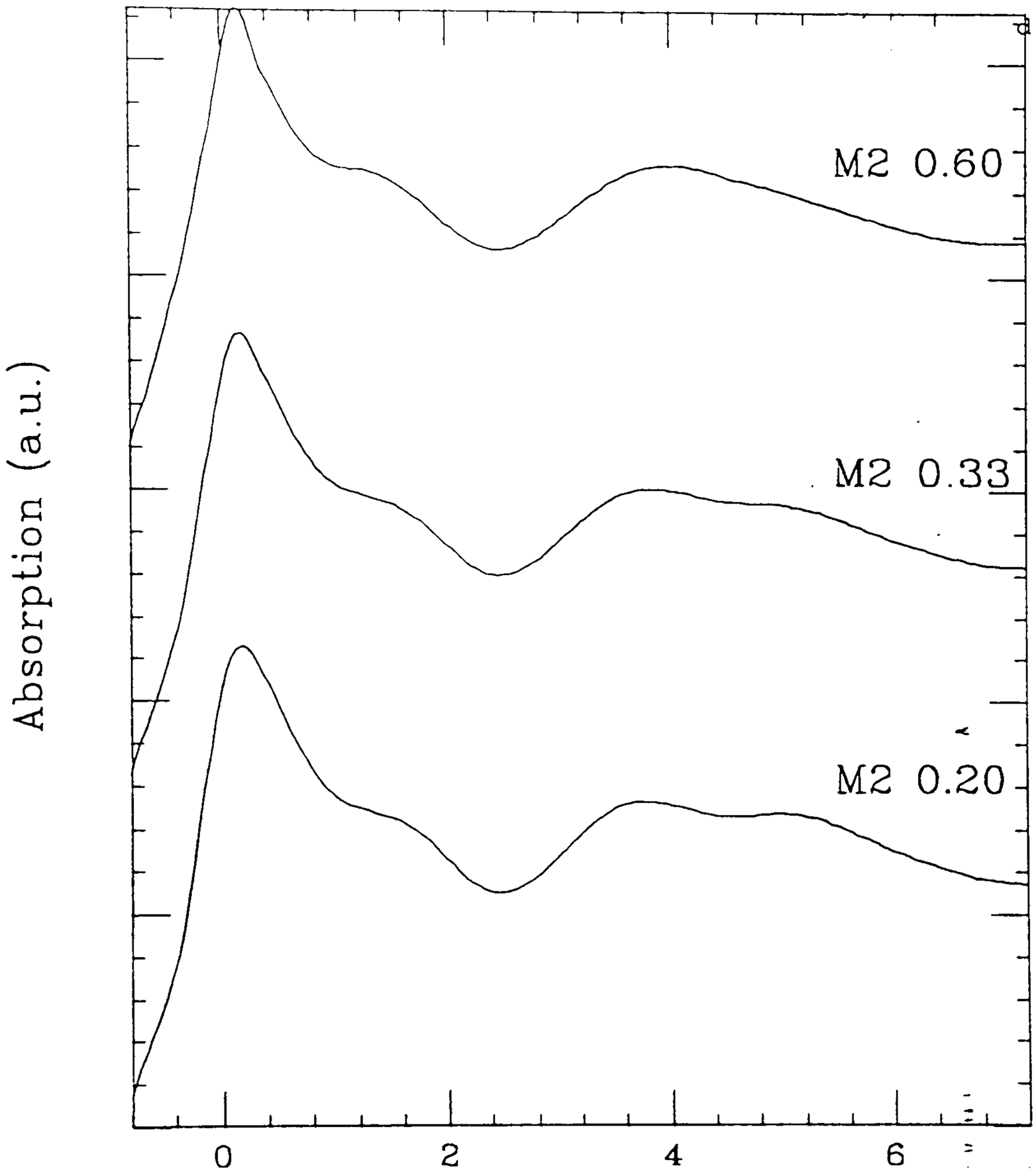

Fig. 7.1.6 Comparison between the $Ni_{20}Mg_{80}$ richterite experimental spectrum and theoretical spectra obtained by summing the contributions of M1, M2 and M3 site spectra with different weights (reported at right side of each spectrum).

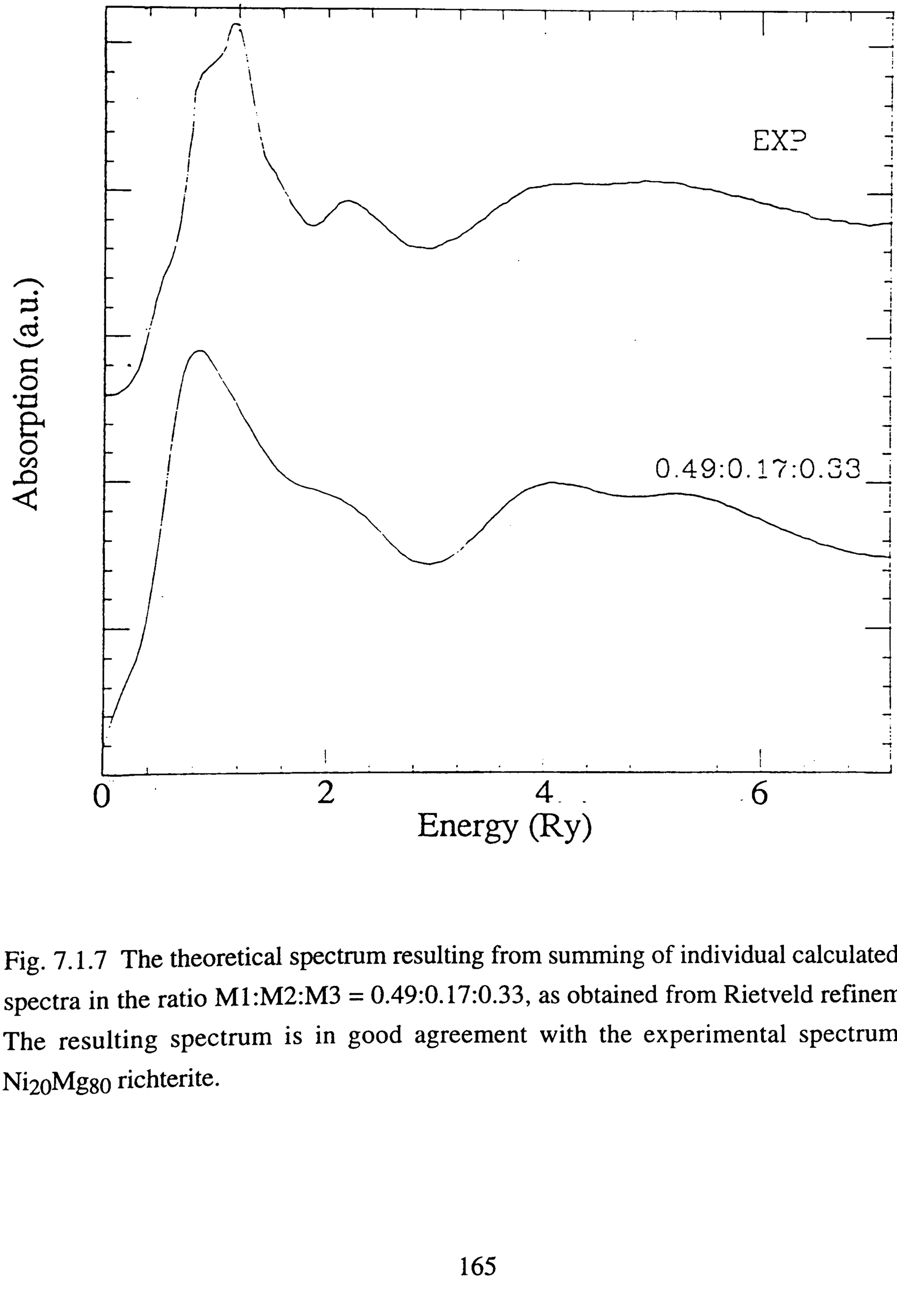

Fig. 7.1.7 The theoretical spectrum resulting from summing of individual calculated site spectra in the ratio M1:M2:M3 = 0.49:0.17:0.33, as obtained from Rietveld refinement. The resulting spectrum is in good agreement with the experimental spectrum for $Ni_{20}Mg_{80}$ richterite.

This result shows that this methods of determining site-distribution is promising as shown already for the simpler case of orthopyroxene (Chapter 4) and as it turns out now for a well-known complex structure such that of richterite.

7.1.5 Discussion

The precision in the determination of Ni site-occupancy by comparing theoretical and experimental XANES spectra is gratifying but needs additional comments. The physical processes behind XAS and XRD are very different: XAS mainly reflects short-range order phenomena, whereas XRD strictly depends on long-range ordering in the sample. Thus, the approximation based on theoretical calculation by the multiple scattering theory leads to an information about the studied sample that is different from that given by the Rietveld refinement, although the comparison is satisfactorily. In the XAS case the local distribution around the photoabsorber over a sphere of about 4 Å can be obtained; in the XRD case the average distribution among the three octahedral sites over the entire sample on a long-range basis can be obtained.

In the simplest case, in which Ni can be accommodated only in two sites, the resulting XAS spectrum is a linear combination of the theoretical spectra of these two sites, such as the case of orthopyroxenes and olivines (Chap. 4, Chap. 6). The calculated partition depends upon the extent of the difference between the spectra of the two sites: the more different are the two sites, more different are the respective partial spectra and more detectable are the changes determined by small differences in site occupancies. Thus, calculations depend strongly upon the geometrical differences between the two sites, and this in turn reflects upon the coherence between the calculated total spectrum and the experimental spectrum.

In a more complex case, when the photoabsorber (Ni in this case) can be located at three distinct octahedral sites, the total spectrum results from the weighted sum of three contributions, each related to a single site; consequently, a quantitative evaluation can be expected to be very difficult. However, in the case of richterites, the two-sites case is approached by degeneracy, because the M(1) and M(3) sites are similar in symmetry and chemical surroundings, whereas the M(2) site differs for both distortion degree and closest chemical environment (Table 7.1.1). Thus, the theoretical spectra of the three sites reflect this situation, as both the M(1) and M(3) site spectra present the splitting of peak G into two components G' and G", whereas no such splitting occurs in the M(2) spectrum. The major difference between spectra resides therefore in the presence/absence of the splitting of peak G, whereas shape and energy position of peak F are roughly the same throughout all the spectra. The similarity between the M(1) and M(3) spectra makes it impossible at the present time to discriminate the distribution of Ni between these two sites. On the other hand, since peak G is single in the M(2) spectrum alone, detectable changes in the combination of the three spectra are obtained only when varying the

weight of the contribution of the M(2) spectrum to the total spectrum, thus making possible to obtain a determination of the Ni partition coefficient expressed as $K_D = Ni_{[M(2)]} / (Ni_{[M(1)]} + Ni_{[M(3)]} + Ni_{[M(2)]})$, i.e. with respect to the M(2) site. Therefore, even in a very complex case as the amphiboles undoubtedly are, variations in the Ni distribution between the three sites of the octahedral strip produce changes in the XANES spectra, which can be understood.

7.1.6 Conclusions

XANES spectra collected at the Ni K-edge on synthetic richterites with different Ni-Mg octahedral compositions show several changes related to variation in the chemical and structural environments around the photoabsorber (Ni). The presence in the amphibole structure of three different octahedral sites where Ni may be located makes a XAS study particularly difficult. However, XANES calculations based on the position parameters of a model structure greatly help to clarify the relationships existing between the observed spectral features and the varying environments that surround Ni with increasing Ni contents along the join. In particular:

1) The splitting of peak G into two components G' and G", observed in the experimental spectra is reproducible in the calculations only when Ni is located either in the M(3) or M(1) sites. Such a splitting is produced by the presence of a sufficient number of Mg atoms located in the second coordination shell around Ni; therefore, it is typical of low-Ni compositions.

2) The decreasing of the peak G splitting with increasing Ni content is not directly related to the Ni site occupancy, but it is produced by the fact that, along the join, the second coordination shell around Ni becomes increasingly enriched by other Ni atoms replacing the Mg atoms.

3) In $Ni_{20}Mg_{80}$ richterite, the Ni atoms are mainly surrounded by Mg in the second coordination shell, rather than by Ni atoms; yet some splitting of peak G is detectable. This suggests the absence, or the very minor presence, of Ni clustering in this sample, which therefore needs to be investigated further.

4) In spite of the structural complexity of the amphibole samples studied here, the validity of this method of investigating site preferences of the absorber is demonstrated. However, a constraint to the method is that sites must be sufficiently different as for symmetry or for degree of distortion. In the more favourable case of a structure in which only two sites are present, this method can be used to obtain an adequate quantitative determination of site occupancy, as it was demonstrated for orthopyroxenes (Chapter 4).

CHAPTER 8. HIGH TEMPERATURE XANES

8.1 A HIGH TEMPERATURE DEVICE FOR *IN SITU* MEASUREMENT OF X-RAY ABSORPTION SPECTRA

8.1.1 Abstract

A new high temperature cell has been designed and built for the purpose of allowing measurement of the X-ray absorption spectra of samples heated in situ up to 1500° C under the vacuum (10^{-4} torr) of a synchrotron X-ray beam line. The cell is described and new results are presented on the determination of the transition (at ca.220°C) from incommensurately-modulated to normal structure in $Ca_2Co[Si_2O_7]$ melilite and the coordination of Ti on K_2O-TiO_2-SiO_2 melts.

8.1.2 Introduction

For a characterization of materials undergoing unquenchable phase transitions or for following the kinetics of a phase change or reaction, measurements under in situ conditions at elevated temperatures are essential. Moreover, geologically as well as technologically-significant transitions from the solid to the liquid state that cannot be studied by the conventional X-ray diffraction techniques can be studied continuously by X-ray absorption spectroscopy, provided a suitable in situ high temperature cell (HTC) is available. This paper presents the design and first applications of a HTC especially conceived for XAS which has been tested successfully for both XANES and EXAFS measurements at the PULS X-ray line of the synchrotron radiation facility of Frascati (Italy).

8.1.3 Design requirements

A high-temperature cell to be used for XAS spectroscopy has to fulfil the following technical requirements:

- homogeneous temperature distribution;
- negligible heating of surrounding parts such as windows, vacuum seals etc.;
- remote control of sample position;
- operation in vacuum;
- good transparency to X-rays in the energy region of interest;
- sample holders that minimize the problem of contamination and/or X-ray absorption, but maximize heat transfer;
- accommodation of several samples, or of samples with different thicknesses.

8.1.4 Experimental set-up

To achieve these goals, the furnace depicted in Fig.8.1.1 has been constructed. The entire furnace assembly is mounted to a 150mm vacuum flange containing the feed-throughs for cooling water, heating power (rated to 10A maximum), and thermocouple, and it is then inserted into the experimental vacuum chamber of the X-ray beam line. Vertical movements of the assembly relative to the vacuum chamber are made possible by a motor-driven stainless-steel bellows. Depending on the temperature range and/or number of samples required, three different designs for the heating element and sample holder have been developed. They all fit the same furnace shell surrounded by water-cooled jacket, and can easily be exchanged.

For the temperature range up to about 800° C stainless-steel tube is used onto which an Inconel-coated, MgO-insulated heating wire (rated to 1000° C) is firmly wound and fixed. The interior sample-holder consists of a central nickel block (Ni) sandwiched by sintered boron nitride plates (BN) and steel end-caps. The outer two boron nitride layers serve for the heat transfer to the nickel block and to the samples (S). Temperatures are measured and controlled by a sheated NiCr/Ni thermocouple placed inside the nickel block. Typical power consumption at 800°C in a 10^{-4} torr vacuum is about 500 W. End plates of the furnace with slits 100 mm wide x 40 mm high (corresponding to the total sample area) prevent excessive thermal radiation to the outside of the furnace.

The central nickel block (Fig.8.1.1, right) contains five slits (3mm high x 10mm wide x 4mm thick) which serve as sample compartments. In the high-energy application (e.g. for the study of Fe or Co edges) the appropriate amount of sample (several mg, depending on the type and concentration of the element studied) are intimately mixed with about 50 mg of boron nitride powder to ensure a homogeneous thickness, pressed into the slits of the nickel block, and covered on both sides by thin (1 mm) sheets of boron nitride to hold the sample in place. In the low-energy region (e.g. for study the Ti K-edge), or if reaction might become a problem, the samples are mounted on a fine metal mesh grids (see below) and attached to the nickel block without the sintered boron nitride cover sheets.

In the temperature ranges up to 1200°C or 1500°C, Kanthal A1 or a $Pt_{90}Rh_{10}$ (d=0.35 mm, 5 m long) heating wire, respectively, is wound directly onto a Al_2O_3 ceramic tube (d_o=25 mm, d_i=20 mm) and fixed by ZrO_2 cement. A radiation shield of Pt foil between the heating tube and the water-jacket minimize thermal losses. Maximum current is 8 A and power consumption is 850 W at 1500°C. The sample holder, made from BN or Al_2O_3 machinable ceramic, can accommodate two 3x10 mm samples. For these high-temperature applications, the finely powdered samples are pressed into a metal mesh grid (stainless steel, tantalum or platinum). Even rather fluid melts were found to be held in place on the vertically mounted mesh by surface tension. This arrangement gives minimal intensity losses (ca. 20%) and contamination.

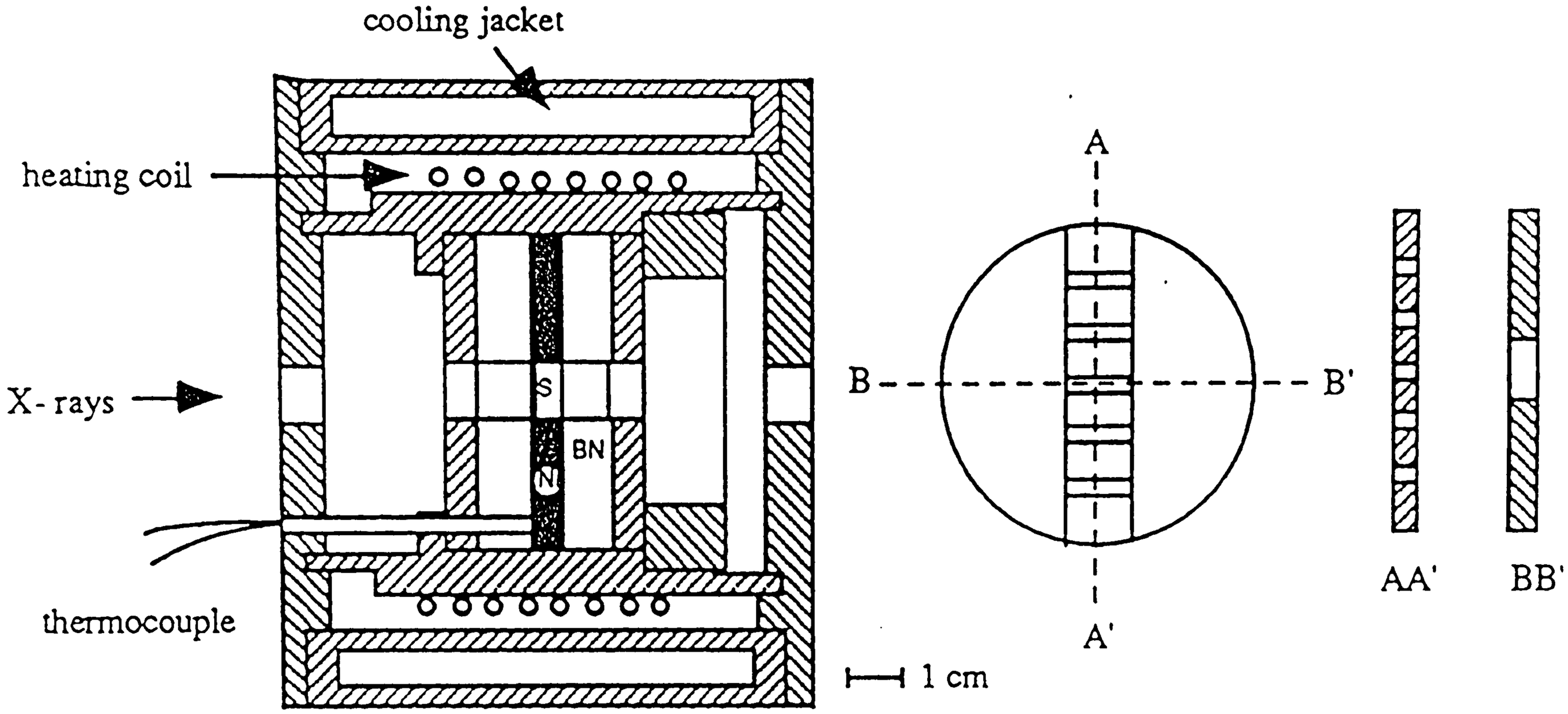

Fig.8.1.1 Cross-section through the 800 °C furnace. The symbol S designates the sample compartment, Ni the nickel heating block, BN the boron nitride plates, ruling to the left the stainless-steel caps and jackets, ruling to the right the brass frame of the cell. Right: detail of the nickel block that serves as sample holder. Samples are placed into the five rectangular slits.

In the high-temperature set up, temperature controlled is achieved by a $Pt_{90}Rh_{10}$ thermocouple and ramped (maximum 1500°C/h) Eurotherm controller operating in phase angle firing mode and power control. Typical temperature stability over extended periods of time (hours) is ±1°C.

8.1.5 Phase transition in melilite

The 800°C cell has been used for a study of the phase transition in synthetic $Ca_2Co[Si_2O_7]$ melilite by Co K-edge XANES and EXAFS spectroscopy. The high-T structure of this melilite consists of 4-fold coordinated CoO_4 polyhedra linked with Si_2O_7 dimers to form a sheetlike arrangement and Ca atoms occupy the 8-fold coordinated sites between the sheets. It is well known from TEM, Mössbauer, X-ray diffraction, NMR and DTA studies (Rothlisberger et al., 1990) that many melilite -type compounds, and the $Ca_2Co[Si_2O_7]$ phase in particular, undergo a non-quenchable hysteresis-free phase transition from a high temperature normal phase to a low-temperature, incommensurately modulated phase in which the Si_2O_7 dimers are rotated and kinked. For $Ca_2Co[Si_2O_7]$, the phase transition temperature is at 210-200°C (Rothlisberger et al 1990). As the phase transition is approached from lower temperatures, the structure changes by a decrease in modulation amplitude and increases in modulation wavelength in the direction towards the high-T normal structure, but nevertheless the final phase transition is sharp and of the lambda type. Local fluctuations of the structure may persist to temperatures above the phase transition.

As to be expected for a phase transition in which only subtle changes of the structure occur (e.g. no change in coordination number or valence, but only changes in angular and bond-length distortion), the changes in XANES and EXAFS spectra as a function of temperature are only slight. Fig.8.1.2 shows the normalized 261°C Co K-XANES spectrum (i.e. above the phase transition, in the field of the normal melilite structure) and the room-temperature spectrum (in the stability field of the modulated phase).

Energy changes of the XANES features are related to changes in the structural environment around the absorbing atom (Bianconi 1983). In $Ca_2Co[Si_2O_7]$ melilite, first attempts to evaluate the peak positions (Fig.8.1.3) indicate minor but rather systematic trends for the strong first peak (b) and the weaker second peak (d), but no changes for the pre-edge peak (a), and just weak changes for the third peak (c). For both peaks b and d, the energy reaches minima close to the phase transition, near 220°C.

For a final assessment, the recording of the spectra with higher energy resolution and the fitting of the spectral envelope to sums of Lorentzians will be required. However, the trends observed so far can tentatively be referred to the anomalous thermal expansion of the structure near the phase transition (Webb et al., 1992).

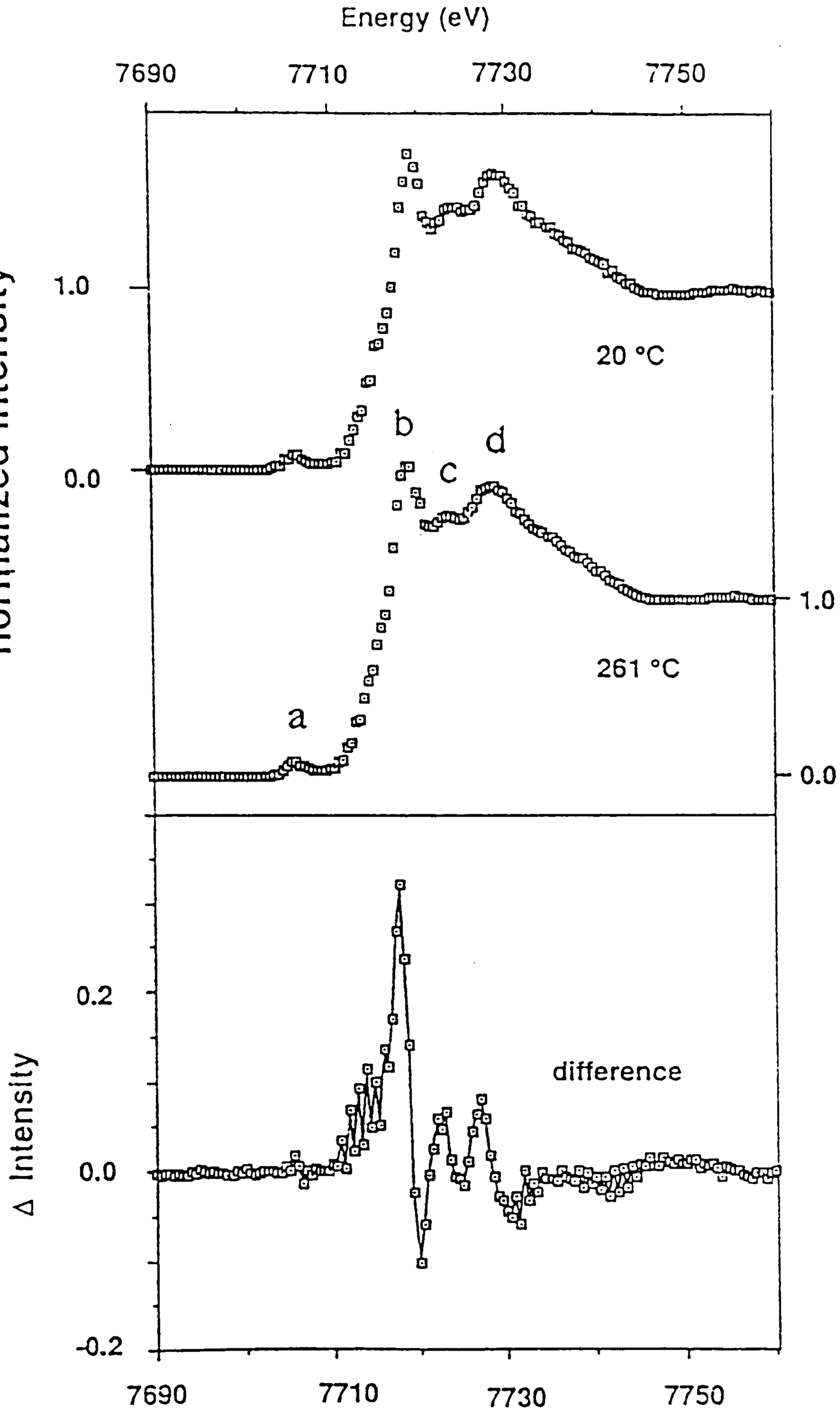

Fig. 8.1.2 Normalized Co K-edge XANES spectra of $Ca_2Co[Si_2O_7]$ melilite taken at room temperature (top) and at 261°C (middle), and their difference spectrum (bottom).

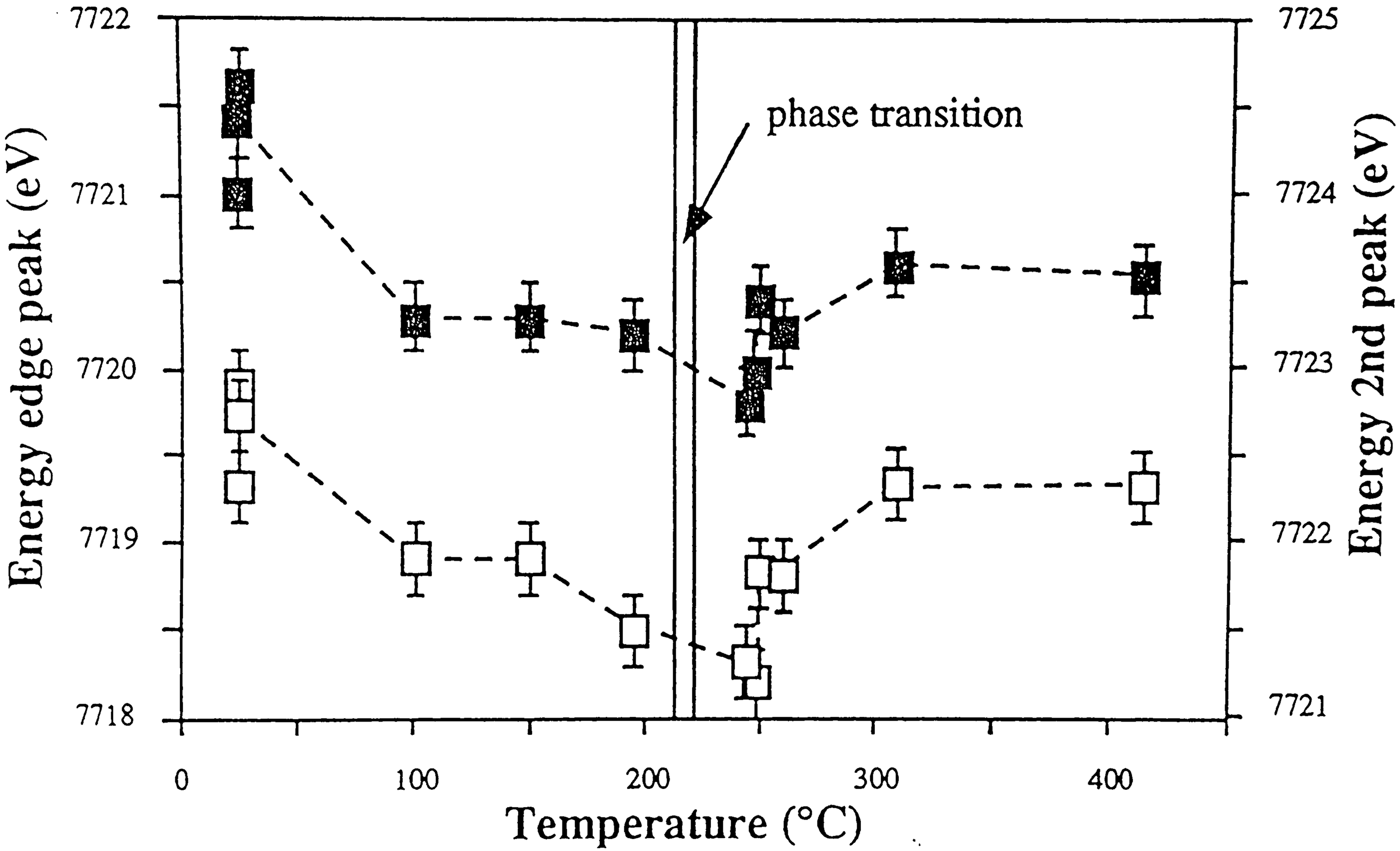

Fig.8.1.3 Energy positions of the Co K-edge peak b (bottom) and of the peak d (above) of melilite $Ca_2Co[Si_2O_7]$ as a function of temperature. The vertical bars indicate the experimental uncertainty in energy. Temperature uncertainty is less than the width of the plotted square.

8.1.6 TiO_2 coordination in silicate melts and glasses

TiO_2 is a crucial component of terrestrial and lunar magmas, high temperature slags and modern melt-based ceramic materials. The growth of high-purity TiO_2 crystals from the melts is also of industrial importance. The concentration of TiO_2 in natural melts ranges up to 16% and ceramic materials can even be richer in TiO_2. Thus, the effects of this major component on transport properties as well as its partial molar properties are important input for the modelling on crystal-melt interaction.

The coordination of Ti^{4+} in silicate glasses has been little investigated to date, but the existing data point to features which can be interpreted as a mixture of 4, 5, and 6-coordinated Ti^{4+}. Among the clearest distinctions between 4- and 6-coordination are XANES data showing the presence of a strong pre-peak for the 4-fold coordination as opposed to a weaker one for the 6-fold coordination (Mottana et al., 1990). XAS studies on quenched silicate glasses (Dumas and Petiau 1986) indicate the presence of either 4-, 5- or 6-coordinated Ti^{4+}, or a mixture of 4- and 6-fold coordination. These results suggest that Ti coordination is sensitive to chemical or physical parameters and that, at a given composition, Ti might behave differently in a melt compared to that observed in glass (quenched melt).

The XANES spectrum of a melt of $K_2Si_4TiO_{11}$ composition, obtained at 1300°C following heat treatment in the HTC temperatures up to 1450°C is compared with the room temperature spectrum of the glass in Fig.8.1.4. The broad features of the spectra are similar but significant differences are present. The relative intensity of the pre-peak remains high in the high-temperature liquids, consistent with the coordination number intermediate between 4 and 6 for Ti^{4+} in the liquid as in the glass.

These examples testify the broad application field of *in-situ* high-temperature XAS analysis. Especially regarding the study of melts, of geological as well as technological relevance, this device will allow to obtain structural information not suitable to be obtained by other methods.

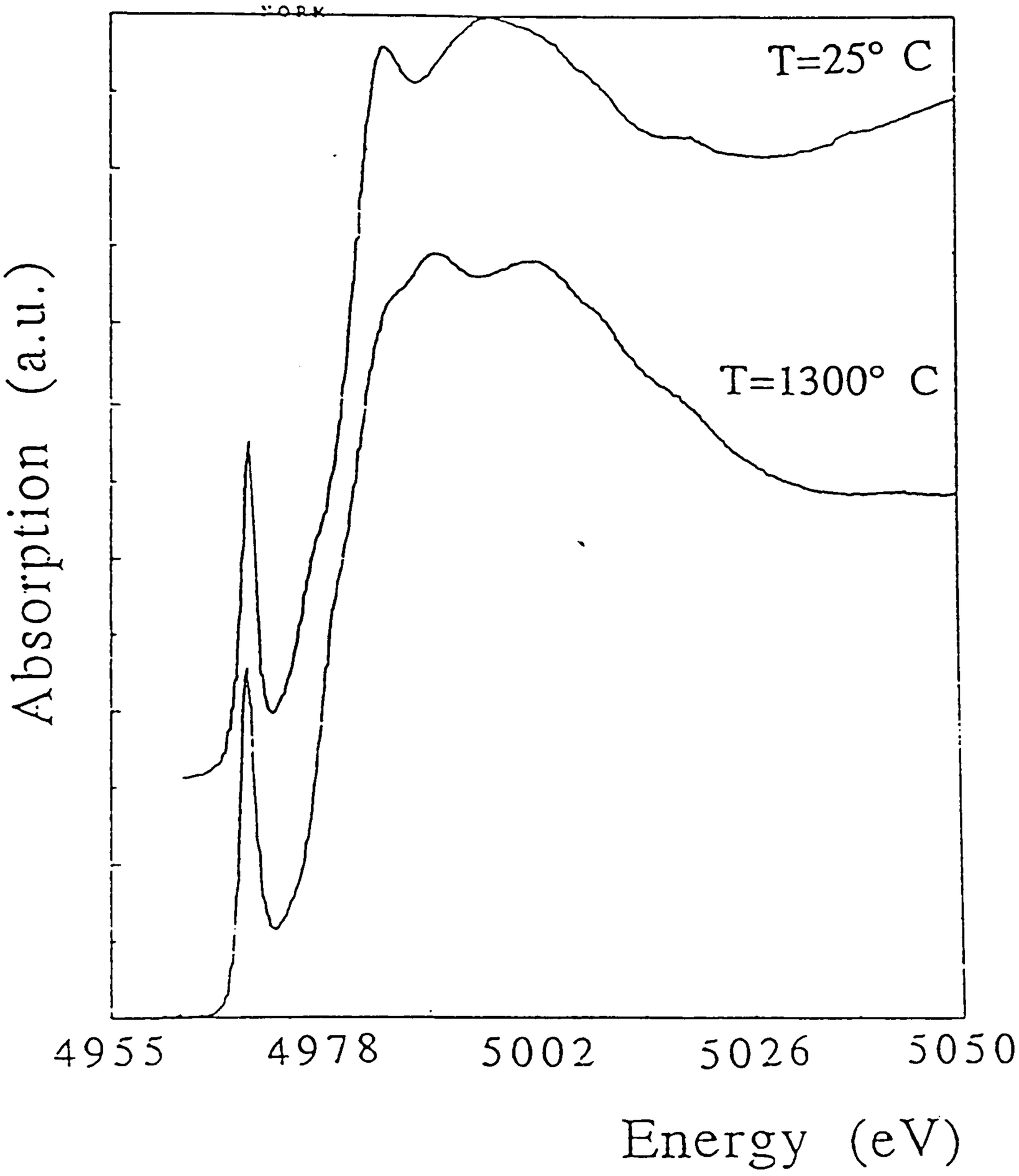

Fig. 8.1.4 XANES spectra of $K_2Si_4TiO_{11}$ composition as quenched glass at room temperature (top) and as liquid at 1300°C (bottom).

8.2 *IN-SITU* HIGH TEMPERATURE STUDY OF TITANIUM COORDINATION IN Rb-SILICATE GLASS AND LIQUID TO 1400°C

8.2.1 Abstract

In-situ high-temperature XANES spectra at the Ti-K edge demonstrate that the coordination number of Ti in $Rb_2TiSi_4O_{11}$ in the glassy, supercooled and stable liquid regimes remains essentially unchanged at a mean value close to 5 up to a temperature of 1400 ^oC. A slight increase in the intensity of the pre-edge peak with temperature can be taken as evidence for a minor decrease in the average coordination number of Ti, from *ca.* 5.0 in the glassy state to *ca.* 4.75 at 1400 ^oC.

8.2.2 Introduction

Most studies of melt structure have been performed on glasses quenched from high T melts, with the assumption that the results give information on the melt near the glass-transition temperature (cf. Mysen, 1988). A limited temperature range (on the order of several tens of degrees) is accessible for such studies by changing the quench-rate (Dingwell and Webb, 1990). For covering a wider temperature range, in particular into the region of stable liquids, *in-situ* techniques are required. Such studies are rare, mostly because of methodological difficulties. It has been shown, however, that the main structural features such as the topology of the network remains unchanged with temperature in fully polymerized melts such as GeO_2 (Seifert et al., 1981) and that, in depolymerized melts, only rather subtle changes occur, such as in the connectivity of SiO_4 tetrahedra (i.e. the distribution of Q-species) via disproportionation reactions of the type $Q^3 = Q^4 + Q^2$ (Brandriss and Stebbins, 1988; Mysen and Frantz, 1992; Seifert et al., 1981). Furthermore, minor coordination changes of Si and Al have been found (e.g. Poe et al., 1992 a,b).

It is the purpose of the present note to describe *in-situ* measurements on a $Rb_2TiSi_4O_{11}$ glass and melt via Ti-K-edge XANES in the temperature range of 25 to 1400 ^oC. This composition has been chosen as a result of a general comparison of $X^{n+}_{2/n}TiSi_4O_{11}$ glasses (where X is Li, Na, K, Rb, Cs, Ca, Sr, Ba, and Al) (Dingwell et al., 1993). This melt is expected, for reasons to be discussed below, to have an intermediate coordination number of Ti between 4 and 6 and therefore to be susceptible to variation with temperature. The need of *in-situ* spectroscopic data for explaining anomalous macroscopic properties in Ti-bearing melts has been emphasized recently by Lange and Navrotsky (1993).

8.2.3 Experimental

Starting materials for the preparation of a glass of $Rb_2TiSi_4O_{11}$ composition were powder mixtures of SiO_2 (99.95%), TiO_2 (99.8%) and Rb_2CO_3 (99%) which were

fused and homogenized at 1400°C in air in a $MoSi_2$ box furnace in a Pt crucible and then poured onto a steel plate for cooling. An analysis is provided by Dingwell et al. (1993)

The X-ray absorption spectra of the glass and liquid sample have been measured at temperatures between 25 and 1400 °C in a high-temperature cell at the PWA line of the National Synchrotron Radiation Facility, Frascati, Italy, at the Ti K-edge (4966 eV) using a (111) channel-cut Si monochromator with an energy resolution of 1 eV, at steps of 0.2 eV. The powdered glassy starting material was pressed into a Pt mesh (mesh size ca. 0.3 mm) and this mesh was then mounted between two MgO blocks held together by Pt wires. The MgO blocks were drilled in such a way as to ensure unattenuated passage of photons. This assembly was then inserted into a horizontal Pt-wound tube furnace. The surface tension of the melt was sufficient to keep a film of appropriate thickness suspended vertically for the period of the measurements (several hours). Temperature was measured and controlled by a Pt-$Pt_{90}Rh_{10}$ thermocouple and held constant to ±1°C. Between individual scans, temperature was allowed to equilibrate for ~30 minutes. A Ti metal foil (EXAFS Materials, 4966.0 eV) was used for energy calibration at room temperature. Experimental XANES data have been reduced by subtraction of background and normalisation of the spectra at the absorption edge.

8.2.4 Results and Discussion

Fig. 8.2.1 shows a (normalized) comparison of the spectra obtained. It should be noted that all spectra except the room temperature spectrum are in the region of the relaxed (stable or metastable) liquid, i.e. above the glass transition temperature T_g which, for this composition, lies between 550 and 600 °C (Takahashi et al., 1977). At these elevated temperatures rapid structural relaxation and consequently an equilibrium structural state are assumed. The overall shape of the absorption spectra is nearly independent of temperature, although with increasing temperature a general broadening of the features just above the edge can be observed, as well as increasing noise. The most important result is, however, that the relative height of the pre-edge peak only varies marginally with temperature, from 45% (normalized) height at room temperature (corresponding to a structural state near T_g at 550 - 600 °C) to 52 - 53 % at the highest temperature employed. Therefore the conclusion is that the overall structure of the melt shows little change with temperature. In detail, however, a systematic temperature dependence is observed: although the variation in pre-edge intensity with temperature is not much larger than the mean standard deviation of the individual determinations, a trend of increasing pre-edge height with temperature is apparent from the data (Fig. 8.2.2).

It has been shown (Waychunas, 1987; Paris et al. 1993; Dingwell et al., 1993) that the height of the Ti^{4+} pre-edge is inversely correlated with coordination number (CN) of titanium. It is also clear however, that appreciable ranges are observed at a given

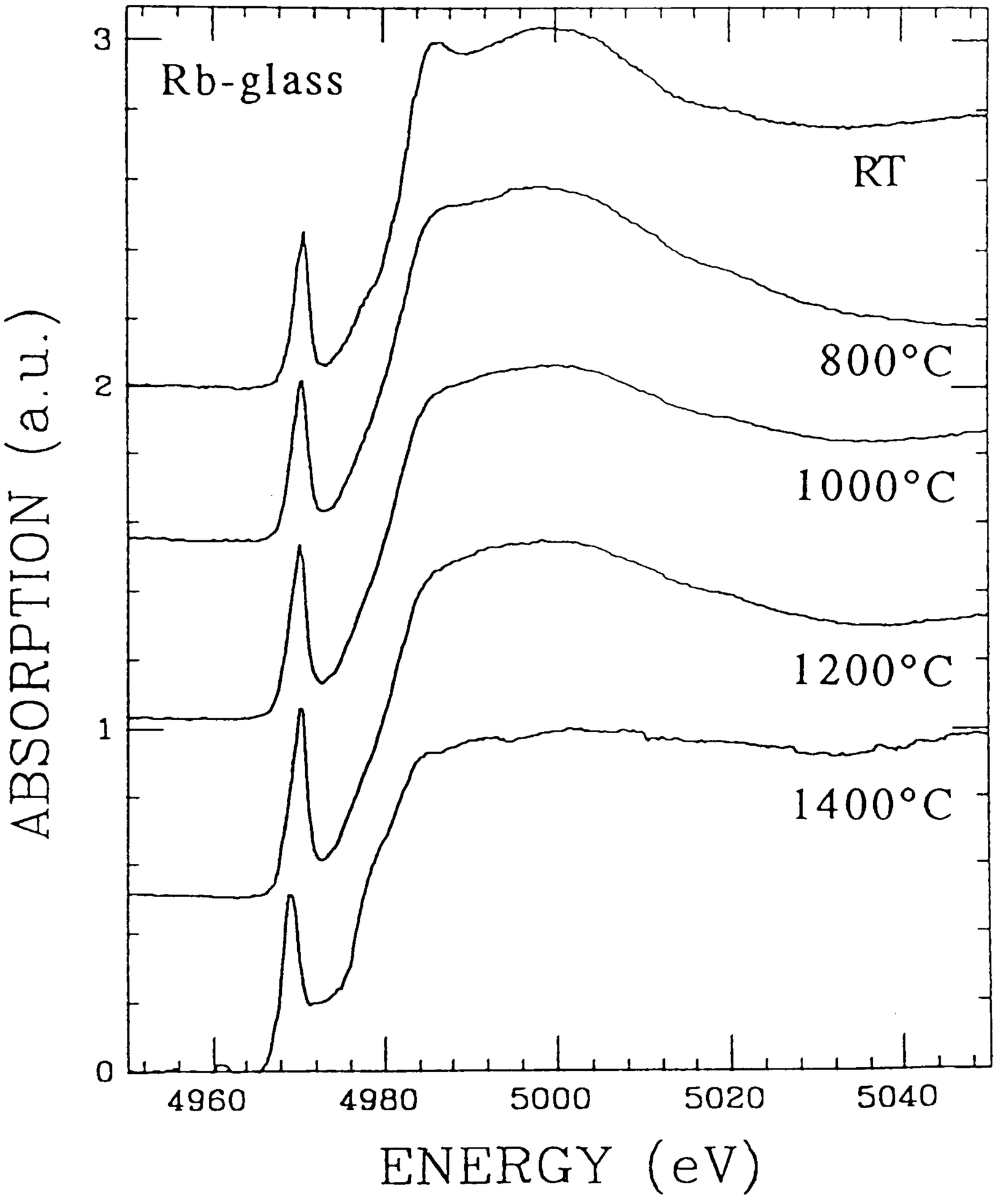

Fig. 8.2.1 XANES spectra of $Rb_2Si_4TiO_{11}$ melt and glass, normalized to the maximum height of the absorption edge. Note general similarity of topology of the spectra

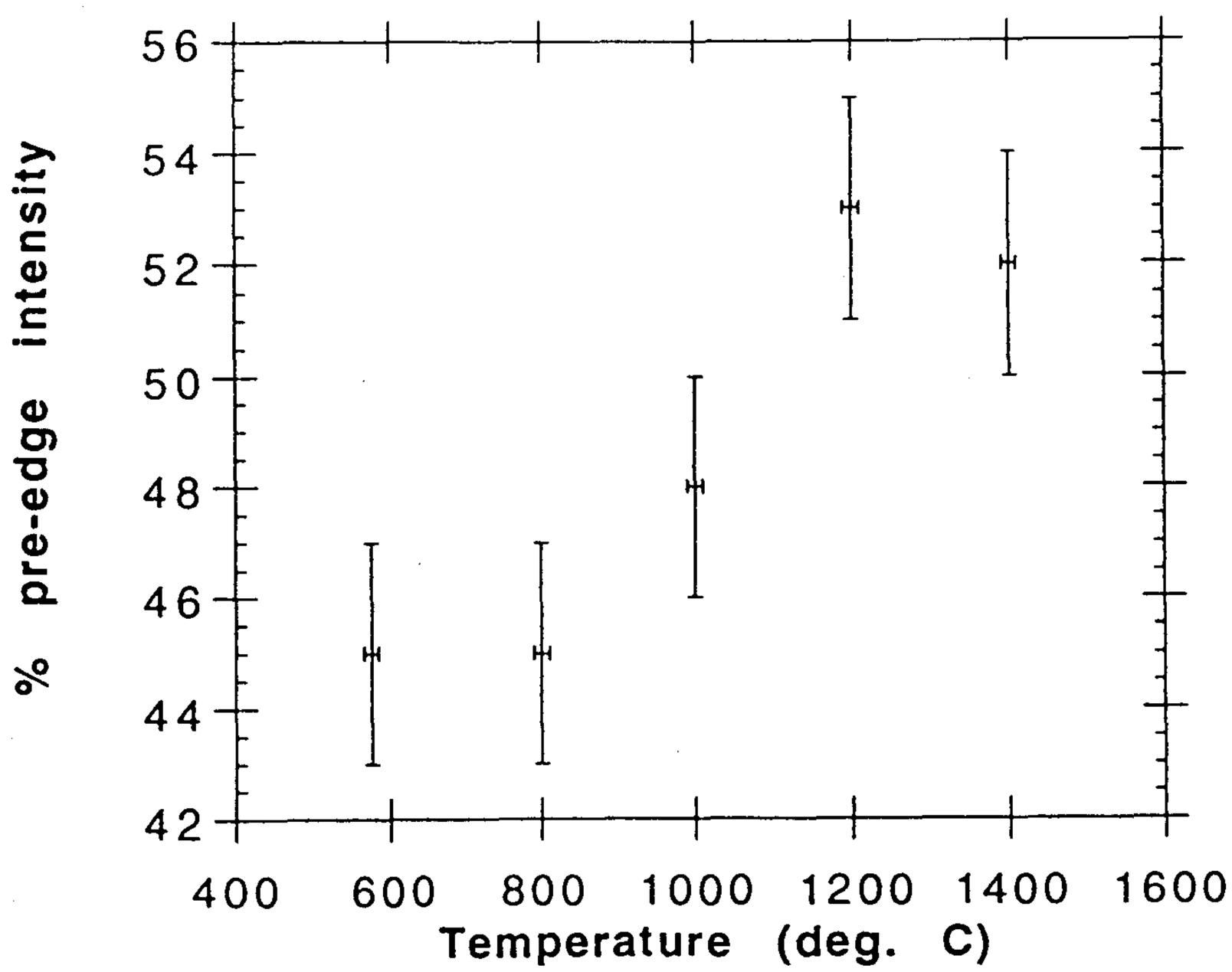

Fig. 8.2.2 Height of the pre-edge peak (expressed as % of the maximum peak height at the edge) versus temperature in $Rb_2Si_4TiO_{11}$ glasses. Note that the room temperature datum has been plotted at 575°C which represents its fictive temperature.

coordination number, most likely related to varying degrees of distortion of the polyhedra. The intensity of the pre-edge peak changes from 1–29 % for CN=6, to 40–45% for CN=5, to 57–84% for CN=4 in the crystalline state. Applying the least-squares fit of the variation of pre-edge intensity as a function of coordination number obtained by Paris et al. (1993) for crystalline standards to the present liquid data indicates that the *average* coordination number of Ti in the $Rb_2TiSi_4O_{11}$ glass is close to 5.0, and the change in pre-edge height reported in Fig. 8.2.2 thus corresponds to a decrease in *average* coordination number on the order of 0.25 in the temperature range between T_g and 1400°C. Such a decrease of CN with temperature may be expected on very general crystal chemical grounds; what is surprising, however, is that the magnitude of this effect is so small. It should be emphasized that, given the lack of energy resolution in the XANES absorption spectra, it is difficult to distinguish between a fivefold and a mixed 4+6-fold coordination of titanium, i.e. determine the width of the distribution curve of coordination numbers which may also change with temperature.

Given the ranges of pre-edge intensity at constant coordination numbers, the subtle variation with temperature could, in principle, also reflect a change of site distortion at constant coordination number. Because there are large variations in the volume per oxygen attributed to titanium in these melts, evident from the melt density data (Dingwell, 1992), the interpretation is fauvored that the observed spectroscopic variations reflect a variation in average coordination number of Ti.

CONCLUSIONS

The studies presented in this thesis comprise a series of investigations which exploit the utility of using synchrotron radiation to probe the structure of crystalline and glassy materials of geological interest. The use of X-ray absorption spectroscopy, and in particular XANES, as the method to investigate the structural role of specific elements in both amorphous and crystalline materials has proved to be of significant value in obtaining quantitative information on oxidation state and local coordination environments. Whereas most previous studies using XANES spectroscopy were limited to a largely qualitative interpretation of the experimental data, based on comparison with materials of known structure, the work described in this thesis has involved a major component of theoretical calculations based on multiple scattering theory. This approach allows calculation of theoretical XANES spectra for specific structural environments and therefore allows a much better understanding and interpretation of the origins of specific features observed in the experimental spectra.

The problems investigated in this work involved a variety of compounds having a wide range in structural complexity, with a major goal being to demonstrate the power of a combined experimental and computational approach to derive useful structural information from measured XANES spectra. In particular, Chapter 2 contains results from a study of densified silica glass by XANES, utilizing absorption spectra for both oxygen and silicon. A decrease in the mean Si-O-Si angle in vitreous silica upon densification from 2.20 to 2.36 g cm-3 is supported by multiple scattering calculations using clusters of two shells around the oxygen and silicon atoms; the calculated spectra are in good agreement with the experimental data and confirm mean Si-O-Si angles between 130 and 144° for these samples, with a decrease of the mean angle with increasing densification. Chapter 3 provides a comprehensive examination of Ti XANES for richteritic amphiboles and for a variety of glasses. The unusual occurrence of tetrahedral Ti in amphibole was discovered, and the glasses were shown to have Ti in a mixture of tetrahedral to octahedral sites. It was also shown that Ti coordination varies systematically with both glass composition and pressure of synthesis. Multiple scattering calculations on Ti K-XANES spectra reveals important effects of both coordination number and degree of polyhedral distortion on the resulting spectra and allows improved interpretation of the variations observed in the experimental spectra.

Chapter 4 concentrates on Fe site geometry in orthopyroxene, and shows the importance of considering contributions from both the M1 and M2 sites in understanding the experimental spectra. The results from this study also demonstrate the ability to

quantify site occupancies in orthopyroxene from measured XANES spectra. The calcium environment in clinopyroxene is the subject of Chapter 5, again involving both measurements and theoretical models of the factors affecting the XANES spectra. The overall comparison of theory and experiment supports the model that Ca in omphacite is distributed over two non-equivalent sites, one having the same geometry as the Ca site in diopside, and a second one that of Na in jadeite. Investigation of the sites of iron and magnesium in the olivine structure are the subject of Chapter 6, with the theoretical results showing how differences in site distortion, and the effects of pressure (compression) and temperature lead to changes in the XANES spectra. Based on these results, XAS experiments at the Mg K edge of forsterite are suggested, in as much as calculations performed up to 1020°C and 149 kbar indicate variation of fine structures in the multiple scattering region. These variations can be related to structural changes in forsterite and these results demonstrate how information obtained by theoretical modelling of XANES spectra can lead to deeper knowledge of structures relevant to the Earth's upper mantle.

Chapter 7 focuses on Ni distribution in synthetic potassium richterites, with result showing how XANES data and theory may be combined to understand Ni distribution in the different crystallographic sites in amphiboles which are too fine grained to be studied by conventional single crystal x-ray diffraction studies. The final Chapter (8) documents the development of a new furnace which allows in-situ x-ray absorption measurements at high temperatures. the application of this new development is illustrated with brief studies of unquenchable phase transitions in Co-melilite , and measurement of Ti XANES spectra in high temperature silicate melts.

In conclusion, the combination of measured x-ray absorption spectra with theoretical spectra produced using multiple scattering calculations provides greatly improved opportunities to extract valuable structural information from measured spectra. This approach has been shown to be much more powerful that which has been followed by numerous previous studies that relied simply on spectra of reference compounds to aid interpretation of features observed in the spectra of 'unknown' materials. The information obtainable from combined experimental and theoretical XANES spectroscopic studies of a variety of geologically relevant compounds and structures can be summarized as follows:

(1) it is possible to obtain structural data (mainly involving oxidation state and coordination environment) on specific elements in amorphous as well as crystalline materials; this is particularly important for studying geological materials with ordering ranging from long-range to short range as well as for in-situ studies of melt structure at high temperatures;

(2) the polyhedral distortion in the surroundings of specific atoms can be studied and used to provide evidence concerning differences between different coordination environments and consequent effects as shown in specific absorption features in measured XANES spectra;

(3) the use of theoretical models involving multiple scattering calculations allows clear distinction in measured spectra of the contributions to the total spectrum from atoms in different crystallographic sites, which in turn can be used to obtain insights into the site preferences of different species in different mineral structures;

(4) site occupancies can be determined in structures where the absorbing atom occupies multiple sites if the sites are of different coordination number or differ in their degree of distortion and symmetry.

REFERENCES

Akaogi M, Ito E, Navrotsky A (1989) Olivine - modified spinel - spinel transitions in the system Mg_2SiO_4-Fe_2SiO_4: calorimetric measurements, thermochemical calculation, and geophysical application. J Geophys Res 94:15671-15685

Anovitz LM, Essene EJ, Dunham WR (1988) Order-disorder experiments on orthopyroxene: Implications for the orthopyroxene geospeedometer. Amer. Mineral. 73:1060-1073

Balzarotti A, Comin F, Incoccia I, Piacentini M, Mobilio S, Savoia A (1980) K-edge absorption of titanium in the perovskites $SrTiO_3$, $BaTiO_3$, and TiO_2. Solid State Commun 35:145-149

Bargeron CB, Avinor M, Drickamer HA (1971) The effect of pressure on the spin state of iron (II) in manganese (IV) sulphide. Inorg Chem 10:1338-1339

Baur WA (1961) Atomabstände und Bindungswinkel im Brookite. Acta Cryst.14:214-216

Behrens P, Aßmann S, Felsche J, Vetter S, Schulz-Ekloff G, Jaeger NI, Niemann W (1990) Metal-atom substituted microporous materials - X-ray absorption spectroscopic studies. Proc VIth Int Conf X-ray Absorption Fine Structure York

Belli M, Scafati A, Bianconi A, Mobilio S, Palladino L, Reale A, Burattini E (1980) X-ray-absorption near edge structure in simple and complex Mn compounds. Solid State Comm. 35, 355-361

Benfatto M, Natoli CR (1987) A unified scheme of interpretation of the X-ray absorption spectra used as a structural probe. J. Non-Cryst. Solids 95, 96: 319-326

Benfatto M, Natoli CR, Bianconi A, Garcia J, Marcelli A, Fanfoni M, Davoli I (1986) Multiple scattering regime and higher order correlation in x-ray absorption spectra of liquid solutions. Phys.Rev.B 34, 5774-8.

Bianconi A (1981) X-ray Absorption Near Edge Structure (XANES) and their applications tp the local structure determination. In "EXAFS for inorganic systems" Garner C.D. & Hasnain S.S. (eds), Daresbury Laboratory SERC DL / SCI / R17, 13-23

Bianconi A (1983) XANES spectroscopy for local structures in complex systems. In "EXAFS and Near Edge Structure" (Eds. A.Bianconi, L.Incoccia and S.Stipcich). Springer, Berlin 118-129

Bianconi A (1988) XANES spectroscopy. In: X-ray Absorption, Principles, applications, techniques of EXAFS, SEXAFS and XANES. Koningsberger D.C.and Prins R. Eds. Chemical analysis series vol.92, Wiley, New York, pp 573-662

Bianconi A, Dell'Ariccia M, Durham PJ, Pendry JB(1982) Multiple scattering resonances and structural effects in the X-ray absorption near-edge spectra of Fe II and Fe III hexacyanide complexes. Phys Rev B 26,12:6502-6508

Bianconi A, Dell'Ariccia M, Gargano A, Natoli CR (1983) Bond length determination using XANES. In "EXAFS and Near Edge Structure" Springer Series in Chemical Physics 27:57-61, Springer-Verlag (New York)

Bianconi A, Doniach S, Lublin D (1978) X-ray Ca K-edge of calcium adenosine triphosphate system and of simple Ca compounds. Chem.Phys.Lett. 59(1), 121-124

Bianconi A, Giovannelli A, Davoli I, Stizza S, Palladino L, Gzowski O, Murawski L(1982) XANES (X-ray Absorption Near Edge Structure) of V in vanadium-iron phosphate glasses. Solid State Comm.42, 547-555

Bianconi A, Garcia J, Benfatto M (1988) XANES in condensed systems. Topics in Current Chemistry 145:29-67

Binsted N, Greaves GN, Henderson CMB (1986) Fe K-edge absorption spectroscopy of silicate minerals and glasses. Journ. Physique C8, 47:837-840

Birle JD, Gibbs GV, Moore PB, Smith JV (1968) Crystal structures of natural olivines. Amer Mineral 53:807-824

Bland JA (1961) The structure of barium orthotitanate, Ba_2TiO_4. Acta Cryst. 14:875-881

Bottinga Y (1985) On isothermal compressibility of silicate liquids at high pressure. Earth Plan Sc Lett 74:350-360

Bottinga Y, Weill D, Richet P, (1982) Density calculations for silicate liquids. I. Revised method for aluminosilicate compositions. Geochim Cosmochim Acta 46:909-919

Bragg WL, Brown GB (1926) Die Struktur des Olivins. Z Krist 63:538

Brandriss ME, Stebbins JF (1988) Effects of temperature on the structures of silicate liquids: ^{29}Si NMR results. Geochim Cosmochim Acta 52:2659-2669

Brown FC, Bachrach RZ, Lien N (1978) The SSRL ultra-high vacuum grazing incidence monochromator design, consideration and operating experience Nicl.Instr.and Meth. 152:73

Brown GE, Calas G, Waychunas GA, Petiau J (1988) X-ray absorption spectroscopy and its applications in mineralogy and geochemistry. In: Hawthorne F.C. (ed.): Spectroscopic methods in mineralogy and petrology, Reviews in Mineralogy, 18, 431-512

Burham CW, Ohashi Y, Hafner SS, Virgo D (1971) Cation distribution and atomic thermal vibrations in an iron-rich orthopyroxene. Am Mineral 56:850-876

Burns RG (1970) Mineralogical application of crystal field theory. Cambridge University Press

Calas G, Brown GE Jr, Waychunas GA, Petiau J (1987): X-ray absorption spectroscopy studies of silicate glasses and minerals. Phys. Chem. Minerals 15:19-29

Calas G, Manceau A, Petiau J (1988) Crystal chemistry of transition elements in minerals through X-ray absorption spectroscopy. In: Synchrotron radiation applications in mineralogy and petrology (SS Augustithis, ed), Theophrastus Publ., Athens, 77-95

Calas G, Petiau J (1983) Coordination of iron in oxide glasses through high-resolution K-edge spectra: information from the pre-edge. Solid State Comm 48:625-629

Calas G, Petiau J (1983) Structure of oxide glasses: spectroscopic studies of local order and crystal chemistry. Geochemical implications. Bull Mineral 106: 33-35.

Cameron M, Sueno S, Papike JJ, Prewitt CT (1983) High temperature crystal chemistry of K and Na fluor-richterites. Am. Mineral., 68, 924-943

Cameron M, Sueno S, Prewitt, CT, Papike JJ (1973): High-temperature crystal chemistry of acmite, diopside, hedenbergite, jadeite, spodumene and ureyite. Am. Mineral., 58, 594-618.

Carpenter M, Domeneghetti MC, Tazzoli V (1990a): Application of Landau theory to cation ordering in omphacite. I. Equilibrium behaviour. Eur. J. Mineral. 2, 7-18.

Carpenter M, Domeneghetti MC, Tazzoli V (1990b): Application of Landau theory to cation ordering in omphacite. II. Kinetic behaviour. Eur. J. Mineral., 2, 19-28.

Chaboy JN, Paris E, Marcelli A, Mottana A (1992) Valence state and coordination of Mn in piemontites. Terra Abstracts 5,1:362

Chiaradia P, Fanfoni M, Priori S, De Padova P, Nataletti P, Davoli I, Modesti S (1986) The soft X-ray beam line of ADONE. Vuoto XVI,2:83-87

Clementi E, Roetti C (1974) Roothaan-Hartree-Fock atomic wave-functions: basis functions and their coefficients for ground and certain excited states of neutral and ionized atoms, Z<54. Atomic Data and Nuclear Data Tables 14:177-478

Czamanske GK, Atkin SA (1985) Metasomatism, titanian acmite, and alkali amphiboles in lithic-wacke inclusions within the Coyote Peak diatreme, Humboldt County, California. Am. Mineral.,70: 499-516

Da Silva JRG, Pinatti DG, Anderson CE, Rudee ML (1974) A refinement of the structure of vitreous silica. Philos Mag 31:713-717

Davoli I, Paris E (1990) Principles and recent developments of XANES spectroscopy. In: Absorption spectroscopy in mineralogy, A.Mottana and F.Burragato Eds., Elsevier, Amsterdam pp 206-24

Davoli I, Paris E, Mottana A (1988) XANES analysis of M1-M2 cations in monoclinic pyroxenes. In: Synchrotron Radiation applications in Mineralogy and Petrology, SS Augustitis Ed, Theophrastus Pubbl., Athens, 97-131

Davoli I, Paris E, Mottana A, Marcelli A (1987) XANES analysis on pyroxenes with different Ca concentration in M2 site. Phys Chem Minerals 14:21-24

Davoli I, Paris E, Stizza S, Benfatto M, Fanfoni M, Gargano A, Bianconi A, Seifert F (1992) Structure of densified vitreous silica: silicon and oxygen XANES spectra and multiple scattering calculations. Phys Chem Minerals 19:171-175.

Davoli I, Stizza S, Durazzo A, Mottana A (1983) Progress in EXAFS and XANES analysis of complex minerals (pyroxenes). Per. Mineral., 52, 637-638.

De Crescenzi M, Davoli I (1983) Spectroscopie EXAFS, SEXAFS and EELFS: aspect experimetaux et determination de strutures de surfaces. In: "Absorption et adhesion" 5eme Ecole d'Ete' Mediterranee. Les Edition de Physique, Pisa

Della Ventura G, Robert JL (1988) OH-stretching region IR study of synthetic Ti-rich hydroxy-richterites. Terra Cognita 8:60

Della Ventura G, Robert JL, Bény J-M (1991) Tetrahedrally coordinated Ti^{4+} in synthetic Ti-rich ptassic richterites: evidences fro XRD, FTIR and Raman studies. Am. Mineral. 76:1134-1140

Della Ventura G, Robert J-L, Raudsepp M, Hawthorne FC (1993) Site occupancies in monoclinic amphiboles: Rietveld structure refinement of synthetic nickel magnesium cobalt potassium richterite. Am. Mineral., 78, 633-640

Di Cicco A, Filipponi A, Natoli CR, Tyson TA (1992) Documentazione dei programmi usati per l'analisi dei dati di assorbimento dei raggi-X (GNXAS). Workshop "EXAFS da laboratorio e tecniche di analisi dei dati", Camerino 27-9/3-10/1992.

Dietrich P, Arndt J (1982) Effects of pressure and temperature on the physical behavior of mantle-relevant olivine, orthopyroxene and garnet: I. Compressibility, thermal properties and macroscopic Grueneisen parameters. In: High-pressure researches in geoscience, Schweitzerbart, Stuttgart, 293-306

Dingwell DB (1990) Experimental determination of some physical properties of iron-bearing silicate melts. Glastech Ber 63K: 289-297

Dingwell DB (1992) Density of some titanium-bearing silicate liquids and the compositional dependence of the partial molar volume of TiO_2. Geochim Cosmochim Acta 56: 3403-3407

Dingwell DB (1992) Density of some titanium-bearing silicate liquids and the compositional dependence of the partial molar volume of TiO_2. Geochimica et Cosmochimica Acta, 56, 3403-3407

Dingwell DB (1992) Shear viscosity of alkali and alkaline earth titanium silicate liquids. Amer Mineral 77:270-274

Dingwell DB, Paris E, Seifert F, Mottana A, Romano C (1994) X-ray absorption study of Ti-bearing silicate glasses. Phys Chem Minerals 21:501-509

Dingwell DB, Webb SL (1990) Relaxation in silicate melts. Eur J Mineral 2: 427-449

Domeneghetti MC, Molin GM, Tazzoli V (1985) Crystal-chemical implications of the Mg^{2+}-Fe^{2+} distribution in orthopyroxenes. Am Mineral 70:987-995

Domeneghetti MC, Steffen G (1992) M1, M2 site populations and distortion parameters in synthetic Mg-Fe orthopyroxenes from Mössbauer spectra and X-ray structure refinements. Phys Chem Minerals 19:298-306

Drickhamer HG (1965) The effect of high pressure on the electronic structure of solids. Solid State Phys (Adv Res Appl) 17:1-134

Dubeau ML, Edgar AD (1985) Priderite stability in the system $K_2MgTi_7O_{16}$-$BaMgTi_7O_{16}$. Mineral. Mag. 49:603-606

Dumas T, Petiau J (1986) EXAFS study of titanium and zinc environments during nucleation in a cordierite glass. J. Non-Cryst. Solids 81:201-220

Dupree R, Pettifer RF (1984) Determination of the Si-O-Si bond angle distribution in vitreous silica by magic angle spinning NMR. Nature 308:523-525

Durben DJ, Wolf GH (1991) Raman spectroscopic study of the pressure-induced coordination change in GeO_2 glass. Phys Rev B 43: 2355-2363

Durham PJ (1988) Theory of XANES. *in*: "X-ray absorption", Koningsberger D.C. and Prins, R. (eds.). Chemical Analysis Series, 92, 72-84, J. Wiley, New York

Durham PJ, Pendry JB, Hodges CH (1982) Calculation of X-ray absorption spectra based on the multiple scattering theory. Comput.Phys.Commun. 25:193

Fei Y, Mao H-K, Mysen BO (1991) Experimental determination of element partitioning and calculation of phase relations in the MgO-FeO-SiO_2 system at high pressure and high temperature. J Geophys Res 96:2157-2169

Filipponi A, Di Cicco A (1993) Investigating local three-body correlations by means of a novel XAS data-analysis method. Synchr. Rad. News 6:13-19.

Filipponi A, Di Cicco A, Tyson TA, Natoli CR (1991) Ab-initio modelling of X-ray absorption spectra. Solid State Comm. 78:265-268

Fischer K (1969) Verfeinerung der Kristallstruktur von Benitoit BaTi[Si_3O_9]. Zeits für Kristall 129:222-243

Fleet M, Herzberg CT, Henderson GS, Crozier ED, Osborne MD, Scarfe CM (1984) Coordination of Fe, Ga and Ge in high pressure glasses by Mössbauer, Raman and X-ray absorption spectroscopy, and geological implications. Geochim Cosmochim Acta 48:1455-1466

Foster PK, Welsh AJE (1956) Metal oxide solution: I. Lattice constants and phase relations in ferrous oxide (wustite) and in solid solutions of ferrous oxide and manganous oxide. Trans Faraday Soc 52:1626-1634

Fujino K, Sasaki Y, Tak'euchi Y, Sadanaga R (1981) X-ray determination of electron distributions in forsterite, fayalite and tephroite. Acta Cryst B 37:513-518

Furukawa T and White WB (1979) Structure and crystallization of glasses in the $Li_2Si_2O_5$-TiO_2 system determined by Raman spectroscopy. Phys Chem Glass 20:69-80

Gaffney ES, Anderson DL (1973) Effect of low-spin Fe^{2+} on the composition of the lower mantle. J Geophys Res 78:7005-7014

Galoisy L, Calas G (1993) Structural environment of nickel in silicate glass/melt systems. Part 1: Spectroscopic determination of coordination states. Geochim Cosmochim Acta 57:3613-3626

Garcia J, Benfatto M, Natoli CR, Bianconi A, Fontaine A, Tolentino H (1989) The quantitative Jahn-Teller distortion of the Cu^{2+} site in aqueous solution by XANES spectroscopy. Chem Phys 132:295-307

Garcia J, Benfatto M, Natoli CR, Bianconi A, Marcelli A, Davoli I (1986) Three particle correlation function of metal ions in tetrahedral coordination determined by XANES. Solid State Comm. 58:595-598

Garcia J, Bianconi A, Benfatto M, Natoli CR (1986) Coordination geometry of transition metal ions in dilute solutions by XANES. J Physique 47, C8:49-54

Gaskell PH, Tarrant ID (1980) Refinement of a random network model for vitreous silicon dioxide. Philos. Mag. B42:265-286

Giuli G, Paris E, Berrettoni M, Della Ventura G, Robert JL, Raudsepp M, Hawthorne FC (1993) XAS study of Ni in pyroxenes and amphiboles.Terra Abstracts 5,1:362

Goldman DS, Rossman GR (1977) The spectra of iron in orthopyroxene revisited: the splitting of the ground state. Am Mineral 62:151-157

Gonschorek W (1986) Electron density and polarized absorption spectra of fayalite. Phys Chem Minerals 13:337-339

Graham EK, Schwab JA, Sopkin SM, Takei H (1988) The pressure and temperature dependence of the elastic properties of single-crystal fayalite Fe_2SiO_4. Phys Chem Minerals 16:186-198

Greegor RB, Lytle WB, Sandstrom DR, Wong J, Schultz P (1983) Investigation of TiO_2-SiO_2 glasses by X-ray absorption spectroscopy. J Non-Cryst Sol 55:27-43

Greegor RB, Lytle FW, Ewing RC, Haaker RF (1984) Ti-site geometry in metamict, annealed and synthetic complex Ti-Nb-Ta oxides by X-ray absorption spectroscopy. Nucl. Inst. Methods in Phys. Res. B1:587-596

Grunes LA (1983) Study of the K edges of 3d transition metals in pure and oxide form by X-ray absorption spectroscopy. Phys. Rev. B27:2111-2131

Gunnella R, Benfatto M, Marcelli A, Natoli CR (1990) Application of a complex potential to the interpretation of XANES spectra. The case of Na K-edge in NaCl. Solid State Comm 76:109-114

Hanada T, Soga N (1980) Coordination of titanium in sodium titanium silicate glasses. J Non-Cryst Sol 38-39:105-110

Hartman, P. (1969) Can Ti^{4+} replace Si^{4+} in silicates? Mineral. Mag. 37:366-369
Hawthorne FC (1981) Crystal chemistry of the amphiboles. In: Veblen D.R. (ed.) Amphiboles and other hydrous pyriboles - Mineralogy, Reviews in Mineralogy, 9A, 1-101.
Hawthorne FC (1983) The crystal chemistry of the amphiboles. Can. Mineral. 21:173-480
Hayashi M, Tamura I, Shimomura O, Sawamoto H, Kawamura H (1987) Antiferromagnetic transition of fayalite under highpressure studied by Mossbauer spectroscopy. Phys Chem Minerals 14:341-344
Hazen RM (1976) Effects of temperature and pressure on the crystal structure of forsterite. Am Mineral 61:1280-1293
Hazen RM (1977) Effects of temperature and pressure on the crystal structure of ferromagnesian olivine. Am Mineral 62:286-295
Hazen RM, Finger LW (1980) Crystal structure of forsterite at 40 kbar. Carnegie Inst. Wash. Year Book 79:364-367
Heald SM, Stern EA (1977) Anisotropic X-ray absorption in layered compounds. Phys.Rev.B 16(12):5549-5559
Henderson CMB, Charnock JM, Helz GR, Kohn SC, Pattrick RAD, Vaughan DJ (1991) EXAFS in earth sciences research. in "X-ray absorption fine structure", S.S. Hasnain, ed., Ellis Horwood, New York, 573-578
Henderson CMB, Charnock JM, Smith JV, Greaves GN (1993) X-ray absorption spectroscopy of Fe, Mn, Zn and Ti structural environments in staurolite. Am Mineral 78:477-485
Hodgson KO, Hedman B, Penner-Hahn JE (eds)(1984): EXAFS and Near Edge Structure III. Proceedings in Physics 2. Springer - Verlag, Berlin-Heidelberg
Höfler S, Seifert F (1984) Volume relaxation of compacted SiO2 glass: a model for the conservation of natural diaplectic glasses. Earth Plan. Sci. Lett. 67:433-438
Horiuchi H, Sawamoto H (1981) α–Mg_2SiO_4: single crystal X-ray diffraction study. Am Mineral 66:568-575
Horn M, Schwertfeger CF, Meagher EP (1972) Refinement of the structure of anatase at several temperatures. Zeit. Krist. 136:273-281
Howard CJ, Sabine TM, Dickson F (1991) Structural and thermal parameters for rutile and anatase. Acta Cryst. B47:462-468
Ihinger PD, Stolper EM (1986) The colour of meteoritic hibonite: an indicator of oxygen fugacity. Earth Planet. Sci. Letters 78:67-79
Itie' JP, Polian A, Calas G, Petiau J, Fontaine A, Tolentino H (1989) Pressure-induced coordination changes in crystalline and vitreous GeO_2. Phys Rev Lett 63:398-401
Jackson WE, Brown GE Jr, Waychunas GA, Mustre de Leon J, Conradson SD, Farges J-M (1993) High temperature XAS study of Fe_2SiO_4 : evidence for reduced coordination of ferrous iron in the liquid. Science 262:229-233
Jackson WE, Knittle E, Brown GE jr, Jeanloz R (1987) Partitioning of Fe within high-pressure silicate perovskite: evidence for unusual geochemistry in the lower mantle. Geophys Res Lett 14:224-226
Jagadeesh MS, Nagarathna HM, Montano PA, Seekra MS (1981) Magnetic and Mossbauer studies of phase transitions and mixed valences in bornite ($Cu_{4.5}Fe_{1.2}S_{4.7}$). Phys. Rev. B 23:2350-2356
Jeanloz R (1991) Effects of phase transitions and possible compositional changes in the seismological structure near 650 km depth. Geophys Res Lett 18:1743-1746
Johnson T, Carmichael ISE (1987) The partial molar volume of TiO_2 in multicomponent silicate melts. Geol Soc Amer Abstr Prog 19:719
Jorgensen JD (1978) Compression mechanisms in alfa-quartz structures: SiO2 and GeO2. J.Appl.Phys.49:5473-5478
Katsura T, Ito E (1989) The system Mg_2SiO_4-Fe_2SiO_4 at high pressures and temperatures: precise determination of stabilities of olivine, modified spinel, and spinel. J Geophys Res 94:15663-15670
Keppler H (1992) Crystal field spectra and geochemistry of transition metal ions in silicate melts and glasses. Amer Mineral 77:62-84

Keppler H, Rubie D (1993) Pressure-induced coordination changes of transition-metal ions in silicate melts and glasses. Nature 364:54-56
Kitzler P (1992) X-ray absorption near-edge structure spectra for bulk materials; multiple scattering analysis versus a phenomenological approach. Phys Rev B 46:17 10540-10546
Kndig W, Cape JA, Lindquist RH, Contrabaris G (1967) Some magnetic properties of Fe_2SiO_4 from 4 K to 300 K. J Appl Phys 38:947-948
Kohn S, Charnock JM, Henderson CMB, Greaves GN (1990) The structural environments of trace elements in dry and hydrous silicate glasses; a manganese and strontium K-edge X-ray absorption spectroscopic study. Contrib Mineral Petrol 105:359-368
Krause MO, Oliver JH (1979) Natural widths of atomic K and L levels, K-α X-ray lines and several KLL auger lines. J Phys Chem Ref Data 8:329
Kubicki JD, Lasaga AC (1988) Molecular dynamics simulations of SiO2 melt and glass: ionic and covalent models. Amer Mineral. 73:941-955
Kudoh Y, Tak'euchi Y (1985) The crystal structure of forsterite Mg_2SiO_4 under high pressure up to 149 kb. Z Krist 171:291-302
Kudoh Y, Takeda H (1986) Single crystal X-ray diffraction study on the bond compressibility of fayalite, Fe_2SiO_4 and rutile, TiO_2 under high pressure. Physica 139-140B:333-336
Kuiper P.et al. (1989) Phys. Rev. Lett. 62:221.
Kusabiraki K (1986) Infrared spectra of vitreous silica and sodium silicates containing titanium. J Non-Cryst Sol 79: 208-212
Kutzler FW, Natoli CR, Misemer DK, Doniach S, Hodgson KO (1980) Use of one-electron theory for the interpretation of near edge structure in K-shell X-ray absorption spectra of transition metal comlexes. J.Chem.Phys.73(7), 3274-3288.
Lager GA, Armbruster T, Ross FK, Rotella FJ, Jorgensen JD (1981) Neutron powder diffraction study of defect spinel structures: tetrahedrally coordinated Ti^{4+} in $Ni_{2.62}Ti_{0.69}O_4$ and $Ni_{2.42}Ti_{0.74}Si_{0.05}O_4$. J. Appl. Cryst. 14: 261-264
Lange RA, Carmichael ISE (1990) Thermodynamic properties of silicate liquids with emphasis on density, thermal expansion and compressibility. Rev Mineral 24:25-64
Lange RA, Navrotsky A (1993) Heat capacities of TiO_2-bearing liquids: evidence for anomalous changes in configurational entropy with temperature. Geochim Cosmochim Acta 57:3001-3011
Lee PA, Beni G (1977) New method for the calculation of atomic phase shifts: Application to extended X-ray absorption fine structure (EXAFS) in molecules and crystals. Phys Rev B 15:2862
Lee PA, Pendry JB (1975) Theory of the extended X-ray absorption fine structure. Phys Rev B 11:2795
Levien L., Prewitt CT, Weider DJ (1980) Structure and elestic properties of quartz at pressure. Amer Mineral. 65:920-930
Lloyd P, Smith PW (1972) Multiple scattering theory in condensed material. Adv.Phys. 21, 69-142.
Lopez A, Tuilier MH, Guth JL, Delmotte L, Popas JM (1993) Titanium in MFI-type zeolites: A characterization by XANES, EXAFS, IR and $^{74.49}Ti$ and $^{17}OMAS$ NMR spectroscopy and H_2O adsorption. J Solid State Chem 102:480-491
Lytle FW, Greegor RB, Panson AJ (1988) Discussion of X-ray absorption near edge structure: application to Cu in high T_C superconductors. $La_{1.8}Sr_{.2}CuO_4$ and $YBa_2Cu_3O_7$. Phys Rev B 37:1550-1562
Maier V, Frahm R (1989) X-ray absorption studies of the short-range order in lithium aluminosilicate glass-ceramics. Glastech. Ber. 62:20-28
Marcelli A, Davoli I, Bianconi A, Garcia J, Gargano A, Natoli CR, Benfatto M, Chiaradia P, Fanfoni M, Fritsch E, Calas G, Petiau J (1985) Local structure in SiO2 glasses by oxygen K edge XANES. J Phys. 46:C8, 107-112
Mattheiss L (1964) Energy bands for the iron transition series. Phys Rev A 134:970.

McCammon CA, Price DC (1985) Mössbauer spectra of Fe_xO (x>0.95). Phys Chem Minerals 11:250-254
McGuire EJ (1970) K-shell Auger transition rates and fluorescence yields for elements Ar-Xe. Phys.Rev. A2:273-278
McMillan P, Piriou B, Couty R (1984) A Raman study of pressure-densified vitreous silica. J.Chem.Phys. 81:4234-4237
Mitra SK (1982) Molecular dynamics simulation of silicon dioxide glass. Philos Mag. B45:529-548
Mobilio S.,Comin F., Incoccia L.(1982): Analisi dei dati EXAFS. INFN LNF-82 /19 NT.
Mottana A, Paris E, Davoli I, Anovitz L (1991) Determining Fe-Mg intersite distribution in natural and heated orthopyroxenes by X-ray absorption spectroscopy. Rend Fis Acc Lincei 9,2:379-387
Mottana A, Paris E, Della Ventura G, Robert J-L (1990) Spectroscopic evidence for tetrahedrally-coordinated titanium in richteritic amphiboles. Rend. Lincei Sc. Fis. 9(1):387-392
Mottana A, Paris E, Seifert F, Marcelli A (1994) Fe-Mg order-disorder in synthetic orthopyroxenes: determination by the XANES method. Terra abstract 6,1:157
Mozzi RL, Warren BE (1969) The structure of vitreous silica. J.Appl.Crystall. 2:149-192
Müller JE, Jepsen O, Wilkins JW (1982) Xray absorptiomn spectra: K-edges of 3d transition metals, L-edges of 3d and 4d metals, and M-edges of Palladium. Solid State Comm 42:365-368
Murray RA, Ching WY (1989) Electronic- and vibrational structure calculation in models of the compressed SiO2 glass system. Phys. Rev. B39:1320-1331
Mustre de Leon J, Rehr JJ, Zabinsky SI, Albers RC (1991) Ab initio curved wave X-ray-absorption fine structure. Phys. Rev. B44:4146-4156
Mysen BO (1988) Structure and Properties of Silicate Melts. Elsevier 354pp.
Mysen BO, Frantz J (1992) Raman spectrscopy of silicate melts at magmatic temperatures: Na_2O-SiO_2, K_2O-SiO_2, and Li_2O-SiO_2 binary compositions in the temperature range 25-1475°C.Chem Geol 96: 321-332.
Mysen BO, Ryerson FJ, Virgo D (1980) The influence of TiO_2 on structure and derivative properties of silicate melts. Amer Mineral 65:867-884
Natoli C.R. (1984) Distance dependence of continuum and bound state of excitonic resonances in X-ray Absorption Near Edge structure (XANES). In "EXAFS and Near Edge Structure III" Hodgson K.O., Hedman B. and Penner-Hahn J.E. (Eds). Springer-Verlag. Berlin, 38-42
Natoli CR (1987) Inner shell X-ray photoabsorption as a structural and electronic probe of matter. Frascati Int.Report. INFN LNF 87/83 (PT)
Natoli CR, Benfatto M (1986): A unifying scheme of interpretation of X-ray absorption spectra based on the multiple scattering theory. J Phys 47 C8:11-23
Natoli CR, Benfatto M, Brouder C, Ruiz Lopez MZ, Foulis DL (1990) Multichannel multiple-scattering theory with general potentials. Phys Rev B 42:1944-1968
Natoli CR, Misemer DK., Doniach S., Kutzler F.W. (1980): First-principles calculation of X-ray absorption-edge structure in molecular cluster. Phys.Rev.A 22, 1104-1108
Norman JG (1974) SCF-Xα scattered wave calculation of the electronic structure of $Pt(PH_3)_2O_2$. J Amer Chem Soc 96:3327-3328
Nyman H et al. (1978) Acta Cryst. B34:905
Oberti R, Ungaretti L, Cannillo E, Hawthorne FC (1992) The behaviour of Ti in amphiboles. I. Four-and six -coordinated Ti in richterite. Eur.J. Mineral. 4:425-439
Ogata K, Takeuchi Y, Kudoh Y (1987) Structure of alfa-quartz as a function of temperature and pressure. Z.Kristall. 179:403-413
Ohtani E, Taulelle F, Angell CA (1985) Al^{3+} coordination changes in liquid silicate under pressure. Nature 314: 78-81

Paris E, Mottana A, Della Ventura G, Robert J-L (1990) Valenza e coordinazione del titanio in anfiboli sintetici della serie richteriteTi-richterite. Studio XANES in luce di sincrotrone. Plinius 3:81-82

Paris E, Dingwell DB, Seifert FA, Mottana A, Romano C (1994) Pressure-induced coordination change of Ti in silicate glass: a XANES study. Phys Chem Minerals 21:510-515

Paris E, Mottana A, Della Ventura G, Robert JR (1993) Ti valence and coordination in synthetic amphiboles of the richterite/Ti-richterite series. A synchrotron radiation XAS study. Eur J Mineral 5:455-464

Paris E, Romano C, Benfatto M (1992) Multiple scattering calculations and XANES data on titanium environment in minerals and glasses. Terra Abstracts 4:34

Paris E, Romano C, Wu Z. (1994) Application of multiple scattering calculations to the study of local geometry in silicate glasses of geological interest. XAFS VIII Conf. Proc. Berlin, 1994

Paris E, Tyson TA (1994) Iron site geometry in orthopyroxene: multiple scattering calculations and XANES study. Phys. Chem. Minerals 21:299-308.

Peacor DR, Buerger MJ (1962) The determination and refinement of the structure of narsarsukite, $Na_2TiOSi_4O_{10}$. Amer Mineral 47:539-556

Penn DR (1987) Electron mean-free-path calculations using a model dielectric function. Phys Rev B 35:482

Poe BT, McMillan PF, Angell A, Sato RK (1992) Al and Si coordination in SiO_2-Al_2O_3 glasses and liquids: A study by NMR and IR spectroscopy and MD simulations. Chemical Geology 96:333-349.

Poe BT, McMillan PF, Coté B, Massiot D, Coutures JP (1992) SiO_2-Al_2O_3 liquids: in-situ study by high-temperature ^{27}Al NMR spectroscopy and molecular dynamics simulation. Journ Phys Chemistry 96:8220-8224

Poumellec B, Marucco JF, Touzelin B (1986) X-ray K edge absorption of titanium and L edges of tantalum in (TiTa)O_2 rutile solid solutions. Phys. Status Solidi (b) 137:519-531

Prewitt CT, Shannon RD, White WB (1972) Synthesis of a pyroxene containing trivalent titanium. Contrib. Mineral. Petrol. 35:77-82

Quartieri S, Antonioli G, Artioli G, Lottici PP (1993) XANES study of titanium coordination in natural pyroxenes. Eur J Mineral 5:1101-1109

Richet P, Bottinga Y (1985) Heat capacity of aluminum-free liquid silicates. Geochim Cosmochim Acta 49:471-486

Richet P, Bottinga Y (1986) Thermophysical properties of silicate glasses and liquids. Rev Geophys 24:1-25

Riebling EF (1967) Volume relations in Na_2O-B_2O_3 and $Na_2O.SiO_2.B_2O_3$ melts at 1300°C. J Am Cer Soc 50: 46-53

Rigden SM, Ahrens TJ, Stolper EM (1984) Densities of silicate liquids at high pressures. Science 226: 1071-1074

Ringwood AE, Irifune T (1988) Nature of the 650-km seismic discontinuity: implications for mantle dynamics and differentiation. Nature 331:131-136

Robinson K, Gibbs GV, Ribbe PH (1971) Quadratic elongation: a quantitative measure of distortion in coordination polyhedra. Science 172:567-570

Ross NL, Akaogi M, Navrotsky A, Susaki J-I, McMillan P (1986) Phase transitions among the $CaGeO_3$ polymorphs (wollastonite, garnet and perovskite structures): studies by high-pressure synthesis, high-temperature calorimetry and vibrational spectroscopy and calculation. J Geophys Res 91(B5): 4685-4696

Ross NL, Navrotsky A (1987) The Mg_2GeO_4 olivine-spinel phase transition. Phys Chem Mineral 14: 473-481

Rossi G, Smith DC, Ungaretti L, Domeneghetti MC (1983) Crystal-chemistry and cation ordering in the system diopside-jadeite: a detailed study by crystal structure refinement. Contrib. Mineral. Petrol. 83:247-258

Röthlisberger F, Seifert F, Czank M (1990) Eur. J. Mineral. 2:585-594

Ruiz Lopez MF, Loos M, Goulon J, Benfatto M, Natoli CR (1988) Reinvestigation of the EXAFS and the XANES spectra of ferrocene and nickelocene in the framework of the multiple scattering theory. Chem.Phys. 121, 419-437

Sainctavit Ph, Calas G, Petiau J, Karnatak R, Esteva JM, Brown GE jr (1986) Electronic structure from X-ray K-edges in ZnS:Fe and $CuFeS_2$. Journ Phys 47,C8:411-14

Sandstrom DR, Lytle FW, Wei P, Greegor RB, Wong J, Schultz P (1980) Coordination of Ti in TiO_2-SiO_2 glasses by X-ray absorption spectroscopy. J Non-Cryst Sol 41: 201-207

Santoro RP, Newham RE, Nomura D (1966) Magnetic properties of Mn_2SiO_4 and Fe_2SiO_4. J Phys Chem Solids 27:655-666

Sasaki S, Prewitt CT, Sato Y, Ito E (1982) Single crystal X-ray study of γ-Mg_2SiO_4. J Geophys Res 87:7829-7832

Sasaki S, Takeuchi Y, Fujino K, Akimoto S (1982) Electron-density distributions of three orthopyroxenes $Mg_2Si_2O_2$, $Co_2Si_2O_6$ and $Fe_2Si_2O_6$. Z Kristall 158:279-297

Sayers DE, Stern EA, Lytle FW (1971) New technique for investigating noncrystalline structure: Fourier analysis of the Extended X-ray Absorption Fine Structure. Phys. Rev. Lett. 27:1204-1208.

Schaefer MW (1985) Site occupancy and two-phase character of "ferrifayalite". Amer. Mineral 70:729-736

Schreiber HD, Balazs GB, Carpenter BE, Kirkley JE, Minnix LM, Jamison PL (1984) An electromotive force series in a borosilicate glass-forming melt. J Am Cer Soc 67:C-106-108

Seifert F, Mysen BO, Virgo D (1981) Structural similarity betwen glasses and melts relevant to petrological processes. Geoch. Cosmoch. Acta 45:1879-1884

Seifert FA, Mysen BO, Virgo D (1982) Three-dimensional network structure of quenched melts (glass) in the system SiO_2-$NaAlO_2$,SiO_2-$CaAl_2O_4$ and SiO_2-$MgAl_2O_4$. Amer.Mineral 67:696-717

Seifert FA, Mysen BO, Virgo D (1983) Raman study of densified vitreous silica. Phys Chem Glasses 24: 141-145

Seifert F, Paris E, Dingwell DB, Davoli I, Mottana A(1993) A high-temperature device for in situ measurement of X-ray absorption spectra. Condens. Matter Mat. Comm. 1:115-121

Seifert F, Paris E, Dingwell DB, Mottana A, Romano C, Davoli I (1994) *In situ* high temperature study of Ti coordination in a Rb-silicate glass and liquid to 1400 °C. Glastech Ber (in press)

Shannon RD (1976) Revised effective ionic radii and systematic studies of interatomic distances in halides and chalcogenides. Acta Cryst. A32:751-767

Sherman DM (1988) High-spin to low-spin transitions of iron(II) oxides and their possible effect on the physics and chemistry of lower mantle. Adv Phys Geochem 7:113-128

Shimomura O, Kawamura T (1982) EXAFS and XANES study under pressure. In: High pressure research in mineral physics.(Manghnani MH and Syono Y, eds) Terra Sci Publ Co, Tokyo, 187-193

Shintani H, Sato S, Saito Y (1975) Electron-density distribution in rutile crystals. Acta Cryst. B31:1981-1982

Smyth JR (1975) High temperature crystal chemistry of fayalite.Amer. Mineral. 60:1092-1097

Smyth JR, Bish DL (1988) Crystal structures and cation sites of the rock-forming minerals. Allen and Unwin, Boston

Smyth JR, Hazen RM (1973) The crystal structures of forsterite and hortonolite at several temperatures up to 900°C. Amer. Mineral. 58:588-593

Stanek J, Hafner SS, Sawicki JA (1986) Local states of Fe^{2+} and Mg^{2+} in magnesium-rich olivines. Amer. Mineral. 7:127-135

Stebbins J (1991) NMR evidence for five-coordinated silicon in a silicate glass at atmospheric pressure. Nature 351:638-639
Stebbins J, McMillan P (1989) Five and six-coordinated Si in $K_2Si_4O_9$ glass quenched from 1.9 GPa and 1200°C. Amer Mineral 74:965-968
Steffen G, Langer K, Seifert F (1988) Polarized electronic absorption spectra of synthetic (Mg,Fe)-orthopyroxenes, ferrosilite and Fe^{3+}-bearing ferrosilite. Phys Chem Minerals 16:120-129
Stern EA, Kim K (1981) Thickness effect on the extended-X-ray-absorption-fine-structure amplitude. Phys. Rev.B 23:3781-3787.
Stohr J, Noguera C, Kendelewicz T(1984) Auger and photoelectron contributions to the electron yield surface extended X-ray-absorption fine structure. Phys.Rev.B 30(10):5571-5579.
Stolper EM Ahrens TJ (1987) On the nature of pressure-induced coordination changes in silicate melts and glasses. Geophys Res Lett 14: 1231-1233
Stolper EM, Walker D, Hager B, Hays J (1981) Melt segregation from partially molten source regions: the importance of melt density and source region size. J Geophys Res 86: 6261-6271
Tak'euchi Y, Yamanaka T, Haga N, Hirano M (1984) High temperature crystallography of olivines and spinels. In: Sunagawa I (ed). Materials science of Earth's interior.191-231, Terra Sci. Publ. Co., Tokyo
Takahashi K, Mochida N, Yoshida Y (1977) Properties and structure of silicate glasses containing tetravalent cations. J Cer Soc Jap 85: 330-340
Teo BK, Joy DC (1979) EXAFS spectroscopy: techniques and applications. Plenum Press, New York
Tyson TA, Hodgson KO, Natoli CR, Benfatto M (1992) General multiple-scattering scheme for the computation and interpretation of X-ray absorption fine structure in atomic clusters with applications to SF_6, $GeCl_4$ and Br_2 molecules, Phys Rev B 46:5997-6019
Uozumi T, Okada K, Kotani A, Durmeyer O, Kappler JP, Beaurepaire E, Parbelas JC (1992) Experimental and theoretical investigations of the pre-peaks at the K-edge absorption spectra in TiO_2. Europhysics Letters 18:85-90
Van Alboom A, De Grave E, Vandenberghe RE (1993) Study of the temperature dependence of the hyperfine parameters in two orthopyroxenes by ^{57}Fe Mössbauer spectroscopy. Phys Chem Minerals 20:263-275
Van Heurk C, Van Tendeloo G, Amelinckx S (1992) Phys. Chem. Minerals 18:441-452
Velde B, Couty R (1987) High-pressure infrared spectra of silica glass and quartz. J. Non-Cryst.Solids 94:238-250
Verdaguer M, Briois V, Cartier C, Gadet V, Michalowicz A, Villain F, (1990) Synchrotron radiation and coordination chemistry. Conference Proceeding "2nd European Conference on Progressin X-ray Synchrotron Radiation Research" A. Balerna, E. Bernieri and S. Mobilio (Eds.) SIF, Bologna, 25:889-902
Virgo D, Hafner S (1969) Fe^{2+},Mg order-disorder in heated orthopyroxenes. Mineral Soc Am Spec Paper 2: 67-81
Virgo D, Mysen BO (1985) The structural state of iron in oxidized versus reduced glasses at 1 atm: a ^{57}Fe Mössbauer study. Phys Chem Mineral 12: 65-76
Waff HF (1975) Pressure induced coordination changes in magmatic liquids. Geophys Res Lett 2:193-196
Wagner C, Velde D (1986) The mineralogy of K-richterite-bearing lamproites. Amer. Mineral. 71:17-31
Waychunas GA (1983) Mössbauer, EXAFS and X-ray diffraction study of Fe^{3+} clusters in MgO:Fe and magnesiowustite $(Mg,Fe)_{1-x}O$ - evidence for specific cluster geometries. J Mater Sci 18:195-207
Waychunas GA (1987) Synchrotron radiation XANES spectroscopy of Ti in minerals: Effects of Ti bonding distances, Ti valence, and site geometry on absorption edge structure. Amer Mineral 72:89-101

Waychunas GA, Rossman GR (1983) Spectroscopic standard for tetrahedrally coordinated ferric iron: γ-$LiAlO_2$:Fe^{3+}. Phys. Chem. Minerals 9:212-215
Waychunas GA, Brown GE Jr (1990) Polarized X-ray absorption spectroscopy of metal ions in minerals. Applications to site geometry and electronic structure determination. Phys. Chem. Minerals 17:420-430
Waychunas GA, Brown GE Jr, Ponader CW, Jackson WE (1988) Evidence from X-ray absorption for network-forming Fe^{2+} in molten alkali silicates. Nature 332:251-253
Waychunas GA, Brown GE, Apted MJ (1983) X-ray K-edge absorption spectra of Fe minerals and model compounds: near-edge structure. Phys Chem Minerals 10:1-9
Waychunas GA, Brown GE, Apted MJ (1986) X-ray K-edge absorption spectra of Fe minerals and model compounds: II EXAFS. Phys Chem Minerals 13:31-47
Webb S.L., Ross II C.R., Liebertz J. Phys. Chem. Minerals, 18, 522-525 (1992)
Webb SL, Dingwell DB (1994) Compressibility of TiO_2-bearing alkali silicate melts. Contrib Mineral Petrol (in press)
Williams Q, Knittle E, Reichlin R, Martin S, Jeanloz R(1990) Structural and electronic properties of Fe_2SiO_4-fayalite at ultra-high pressures: amorphization and gap closure. J Geophys Res 95:21549-21563
Winick H (1980) Properties of Synchrotron radiation. In: "Synchrotron radiation research". Plenum Press, New York
Wong J (1993) private communication
Wong J (1986) Extended X-ray absorption fine structure: a modern structural tool in materials science. Materials Science and Engineering 80:107-128
Wright AC, Yarker CA, Johnson PAV, Wedgwood FA (1977) Neutron scattering techniques for structural studies of amorphous solids. In: (G.H. Frischat, ed.) Non Crystalline Solids, TransTech, pp. 118-123
Wu ZY, Marcelli A, Natoli CR, Mottana A, Paris E(1995) Theoretical analysis of X-ray-absorption near-edgestructure at the Mg K edge in forsterite, Mg_2SiO_4-Pbnm, underextreme conditions. Phys Chem Minerals (submitted)
Wu ZY, Mottana A, Marcelli A, Paris E (1995) Theoretical analysis of the X-ray absorption near-edge structure (XANES) of fayalite at room temperature and under extreme conditions. Phys. Chem. Minerals (submitted)
Wu ZY, Benfatto M, Natoli CR (1992) Theoretical calculation of X-ray absorption near edge structure at Sr K-edge in $La_{2-x}Sr_xCuO_4$ compounds. Phys Rev., B45, 531-534.
Wu ZY, Natoli CR, Benfatto M (1994) X-ray absorption studies of Sr, La and Nd in T- and T'-phases compounds. Physica B (in press)
Xue X, Stebbins JF, Kanzaki M, Tronnes RG (1989) Silicon coordination and speciation changes in a silicate liquid at high pressures. Science 245:962-964
Yarker CA, Johnson PAV, Wright AC, Wong J, Greegor RB, Lytle FW, Sinclair RN(1986) Neutron diffraction and EXAFS evidence for TiO_5 units in vitreous K_2O-TiO_2-$2SiO_2$. J Non-cryst Solids 79:117-36